

# Nuclear Magnetic Resonance

## Chemical Shift investigation of Protein Folding

**Jürgensen, Vibeke Würtz**

*Publication date:*
2006

*Document Version*
Publisher's PDF, also known as Version of record

# Nuclear Magnetic Resonance
# Chemical Shift investigation of Protein Folding

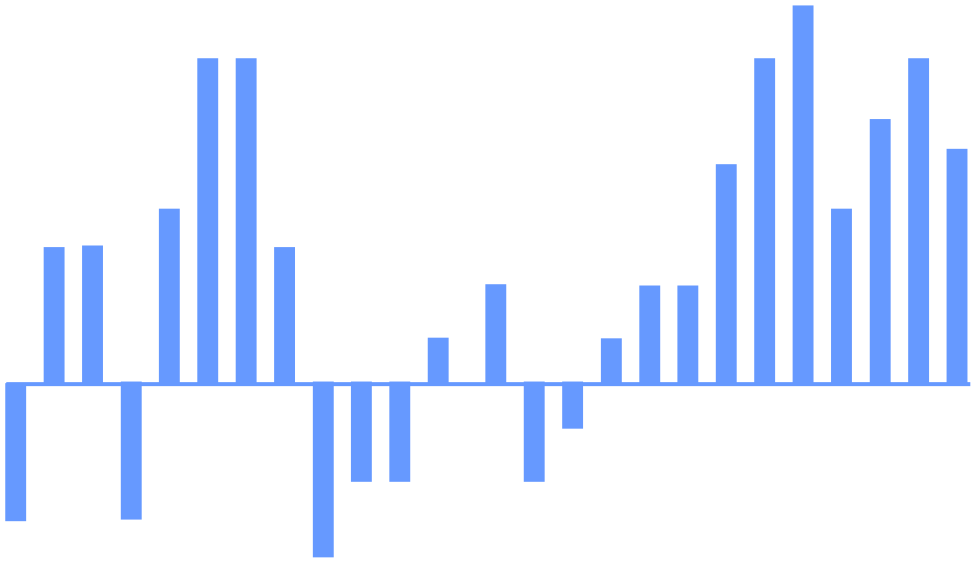

Ph.D.-thesis of

**Vibeke Würtz Jürgensen**

QUP-centre

Department of Physics

Technical University of Denmark

# Nuclear Magnetic Resonance
# Chemical Shift investigation of Protein Folding

The experiments leading to this thesis were carried out at the Department for Protein Chemistry, University of Copenhagen. At the same time research was undertaken at the QUP-centre, Department of Physics, DTU.


| | |
|---|---|
| PhD. programme: | Physics |
| Institute: | Department of Physics, QUP-centre |
| Name: | Vibeke Würtz Jürgensen |
| PhD number: | 020050 (PHD) |
| | |
| Supervisors: | |
| Henrik G. Bohr: | QUP-centre, Department of Physics, Technical University of Denmark (DTU) |
| Flemming M. Poulsen, | Department of Protein Chemistry (APK), Institute of Molecular Biology, University of Copenhagen |



The study was financed through a grant from the Danish National Research Foundation.


Vibeke Würtz Jürgensen Date

## Acknowledgment

I would like to thank all the people at the Department of Protein Chemistry (APK) and at the QUP-centre, DTU who have made this study possible. In particular I would like to thank Jens K. Thomsen, as well as Wolfgang Fieber for supplying protein for this study. A general thanks goes to Asger Batting Clausen, Karl Jalkanen, Kristofer Modig and Birthe Brandt Kragelund. A special thanks goes to Kresten Lindorff-Larsen for help with all the work on MD/MC simulations and in particular I would like to thank Wolfgang Fieber, who has helped me not only with all the practical details during the experiments at APK, but always was there to discuss and answer every question I might have had. Finally I would like to thank my supervisors Henrik Bohr and Flemming Poulsen, who have made this study possible.

Copenhagen, November 2005

Vibeke Würtz Jürgensen

Edition for ORBIT, the submitted article has been replaced by the printed version.

Copenhagen 2007

1 Introduction ..... 2
2 Residual secondary structure and the random coil state ..... 4
2.1 Acyl-coenzyme A binding protein ..... 6
2.2 Folding/Unfolding of ACBP ..... 7
3 The acid denatured state of ACBP ..... 10
Results ..... 11
3.1 High concentration pH titration ..... 11
3.2 Low concentration pH titration ..... 14
3.3 Differences between the two acid denatured titration series ..... 21
3.4 Discussion/Conclusion ..... 25
4 Urea and Guanidine hydrochloride denaturation ..... 27
4.1 The urea denatured state ..... 29
4.2 The Guanidine hydrochloride denatured state ..... 35
5 Assessing the ensemble of structures representing the denatured state ..... 41
5.1 Molecular Dynamics Simulations ..... 41
5.1.1 CHARMM Force Field ..... 42
5.2 Monte Carlo Simulations ..... 43
5.3 SHIFTX ..... 44
5.4 PALES ..... 44
6 Molecular Dynamics and Monte Carlo Simulations results ..... 45
6.1 Molecular Dynamic Simulation: Construction, energy minimization ..... 45
6.2 Monte Carlo simulations ..... 48
6.2.1 Monte Carlo simulations of pH 2.7 ..... 50
6.2.2 Monte Carlo simulations of pH 2.3 ..... 59
6.3 PALES ..... 65
6.4 Discussion/Conclusion ..... 68
7 Introduction to Met- and Leu-Enkephalin ..... 71
7.1 Residual dipolar couplings of denatured proteins ..... 72
8 Results for Met and Leu-Enkephalin ..... 75
8.1 NOESY ..... 75
8.2 Residual dipolar couplings ..... 75
8.3 Circular dichroism ..... 80
8.4 Discussion/Conclusion ..... 82
9 Methods and Materials ..... 84
9.1 NMR-spectroscopy: ..... 84
9.1.1 Chemical shift analysis ..... 84
9.1.2 Met and Leu-Enkephalin ..... 84
9.1.3 RDCs ..... 85
9.2 CD, refractive index etc. ..... 86
Appendix A ..... 87
Appendix B ..... 92
Appendix C ..... 103
Appendix D ..... 106
Bibliography ..... 110
10 Introduction to tri-L-serine ..... 116
10.1 Density functional theory ..... 116
10.2 Calculation of the vibrational spectra ..... 117
10.3 Bibliography ..... 118
Paper: The VA, VCD, Raman and ROA spectra of tri-l-serine in aqueous solution. 119

# 1 Introduction

It is the goal of this project to investigate the folding of acyl-coenzyme A binding protein (ACBP) by Chemical Shift Analysis and compare the results to data predicted by existing theoretical models and previously obtained data. That is, to characterize the unfolded state of ACBP by chemical shifts. The experiments are part of ongoing investigations at the Department for Protein Chemistry, University of Copenhagen (APK).
The unfolded state of bovine ACBP has been investigated in the presence of urea, guanidine hydrochloride, as well as low pH. Furthermore, another system of two small neuropeptides, Leu & Met-Enkephalin, has been investigated in order to characterize their preferred conformation in solution. Finally, a third part of this study included the characterization by density functional calculation of the tripeptide tri-L-serine.

Investigations of protein folding are important for understanding the mechanisms by which proteins fold into the correct three-dimensional structures, which in turn is necessary for its function. NMR together with computational chemistry methods can help solve or refine the structure and give insights into their functions, which ultimately may help in areas like drug design.

The main focus was Acyl-CoA binding protein (ACBP), which consists of four α-helices and is approximately 10 kDa (86 residues) large. This intracellular protein specifically binds acyl-CoA esters with high affinity. The protein is highly conserved from yeast to mammals and it is likely that ACBP carries out basal cellular functions. For instants Gaigg et al. [Gaigg01] suggested that ACBP from yeast appears to be necessary for proper vesicular trafficking and not, as generally believed, for general lipid metabolism.

The primary investigative method was nuclear magnetic resonance (NMR) spectroscopy, which is uniquely suited to provide information on for instance the structure of transient intermediates formed during protein folding. The observation of transiently populated folded structures, including turns, nascent helix, and hydrophobic clusters, in water solutions of short peptides have important implications for initiation of protein folding. Formation of elements of secondary structure probably play an important role in the initiation of protein folding by reducing the number of conformations that must be explored by the polypeptide chain, and by directing subsequent folding pathways. Thereby answering the Levingtal paradox by providing the energy bias necessary [RZwanz92].
The NMR spectra of denatured proteins lack dispersion and resemble spectra of mixtures of free amino acid. But fine deviations from random coil spectra have been measured, indicating some residual structure of the denatured state (e.g. by urea or thermally denatured) [YLiFPi05]. With uniform labelling of the NMR active nuclei, $^{13}C$ and $^{15}N$ (together with multidimensional hetereonuclear NMR experiments) it is possible to characterize the denatured state. The $^{15}N$ chemical shift dispersion remains large in denatured proteins, due to dependence on both residue type and sequence, and these spectra are hence well dissolved.
It is known that $H^{\alpha}$, $C^{\alpha}$ and $C^{\beta}$ chemical shifts vary with secondary structure of proteins. The $H^{\alpha}$ shift in average is for instance 0.3 ppm upfield for α-helical structure

and 0.3 downfield for β-sheet structures, i.e. large individual deviations can be expected especially for protons near aromatic rings. If several protons have consistent upfield shift this indicates a helix in the native protein, and consistent downfield shift indicates a β-sheet. Several methods exist for the purpose of secondary structure determination, e.g. Chemical shift Index (CSI). The method is reliable, but for error elimination chemical shift of $^{1}H$ are usually compared with CS information from e.g. $C^{\alpha}$ and $C^{\beta}$.
These shifts rely on accurate random coil values, measured for short peptides, typically hexapeptides [DWisha95]. It is, however, not clear if these values also apply for longer peptides and large proteins. A question that will be addressed here.

Through usage of existing programs for theoretical chemical shift prediction it might be possible to model experiments, e.g. pH dependence of conformational transitions such as unfolding events. Works on folding of peptide fragments from proteins and small proteins have been accomplished by some groups [VDagge03]. Here we tried to investigate the structure of unfolded ACBP by Chemical Shift Analysis and model the folding from the obtained data.

The study also covered Enkephalins, a family of neuro-peptides, involved in pain-perception. They are endogenous morphine-like neurotransmitter in the mammalian brain, which bind to the opiate receptors better than morphine. This is most probably due to their flexible nature. Drug design of selective opoid agonists are difficult. Proper folding is thought of as occurring only when the peptide is in complex with the receptor [RSpada01]. Ideally it would be best to study the bioactive conformation, i.e. the peptide in complex with its receptor, but this is not yet feasible for solution state NMR, since opioid receptors are large membrane proteins.
Peptides are normally void of secondary structure, but may have preferred conformations. The two pentapetides Met- and Leu-Enkephalin (Tyr-Gly-Gly-Phe-Met/Leu) are investigated in aqueous-solution by nuclear magnetic resonance spectroscopy to characterize the conformational distribution under such conditions. Here residual dipolar couplings have been used to elucidate an eventual conformational change as a function of pH for both Enkephalins.

Another way of approaching the question of conformations and structure in proteins and small peptides is by density functional theory (DFT). Contrary to NMR measurements and the computational approaches used to elucidate the unfolding of ACBP, DFT does not concern itself with ensemble averages, but focus on a single conformation. Here the structural properties for the small tripeptide tri-L-serine are investigated through its spectroscopic features of Infrared Absorption (VA), Vibrational Circular Dichroism (VCD) and Ramanspectra.

## 2 Residual secondary structure and the random coil state

Protein folding is concerned with the prediction of the three-dimensional, biological active, native structure of proteins from its sequence and how the native structure is reached from its denatured state. To circumvent the problem of to many folding pathways encompassed by Levinthal's paradox several mechanisms to reduce the number of possible conformations have been proposed. One mechanism is the stepwise rapid formation of secondary structure, which is followed by acquisition of tertiary structure. This again can be achieved in two ways. One way is diffusion-collision, which comprises the formation of secondary structure followed by diffusion, collision and coalescence to form tertiary structure. A second way is by nucleation, in which a nucleus is formed followed by fast formation of tertiary structure. Another theory for the folding pathway is that of the hydrophobic-collapse as an initial step in folding, which is followed by acquisition of secondary structure with subsequent correct packing.

The non-native states of proteins are of general interest to the study of protein folding, since intermediate or unfolded states may hold important insight about formation of local structure or key interactions that steer the folding process.
But a framework for interpreting experimental data from various experimental techniques of the non-native states is needed and a general consensus on what the random coil state comprises, i.e. a state characterised by the total absence of structure, other than inherent local interaction.
Several ways of characterising the local properties of the random coil exist. Tanford [CTanf68] defines the random coil state of a polymer as each bond of the molecule having the possibility of free internal rotation, to the same extent as a molecule of low molecular weight containing the same bond would have. While Shortle [DShort96] describes the random coil as a well-defined reference state where no sidechain-sidechain interactions take place, but never the less says proteins do not unfold to a simple reference state. In fact many denatured proteins show evidence of large amounts of residual secondary structure.
Models show transient population of secondary structure by a polypeptide chain behaving as a random-coil. For instance a model where the random coil was defined as a state where the $\Phi,\psi$ torsion angles of a given residue are independent of torsion angles of all other residues [LSmith96]. L. Smith et al. propose their model, i.e. where random coil is defined in terms of statistical distributions in $\Phi,\psi$ space, as a baseline with which regions of nonrandom structure can be recognized. In particular they have used it to predict spin-spin coupling constants $^3J_{HN\alpha}$ and NOE's for random coil structures. Several other studies also propose restrictions of the polypeptide chain solely due to sequence [NFitsk04], and assign conformational constraints with implications for the organization of the unfolded protein, and hence limiting possible protein domains.

The review by V. Daggett and A. Fersht [VDagge03] assesses three small proteins where theory and experiments have complimented each other and represent the three extremes of the folding behaviours. They draw some general conclusion about folding at the molecular and structural level. In such a way that small proteins most likely fold the same way in vivo as in vitro and are representative for individual domains of larger proteins. One of the proteins they review is the two state folder chymotrypsin

inhibitor 2 (CI2), which was investigated by Φ-values analysis. Structural characterisation of transition and intermediate states was achieved by MD-simulations. The combination of theory and experiment yielded a self-consistent view of the unfolding/folding pathway of CI2, where a single rate-determining transition state ensemble for folding and unfolding is found. This ensemble is native-like and exhibits considerable secondary structure with disrupted side-chain packing. The unfolding in silico leads to a poorly structured expanded denatured state, which is almost random coil, exhibiting some native, residual helical structure as well as a hydrophobic cluster. This by MD-simulations found denatured state ensemble is corroborated by NMR studies, and all in all leads to a folding/unfolding mechanism that is not defined by a single of the proposed theoretical mechanism, but could be called a nucleation-condensation/collapse. Another example is the three-state folder barnase, which is a multidomain protein that folds in a more complicated manner than CI2, through an experimentally detectable intermediate. The denatured state of Barnase contains considerable amount of residual structure, which again could be corroborated by both experiments and MD-simulations. The folding of Barnase in the main hydrophobic core is started by residual structure, which again aids formations of secondary structure in an adjacent structural motif. Again this cluster helps in the loose packing of the overall structure, forming the intermediate, further collapse leads to a transition state and to the native structure. They conclude [VDagge03] that combined theoretical and experimental studies suggest that proteins are programmed for efficient folding. The intrinsic conformational tendency for secondary structure and tertiary interactions guide the search through conformational space, from the denatured state to the native, down the folding pathways. Even minor residual structure in the denatured state can lead to nucleation, where the strength of the nucleation determines if folding is only guided down a pathway or leads to experimentally detectable folding intermediates.
Other work also indicates that the stabilization of intermediates via secondary structure contents enhances or hinders the folding process, depending on the secondary structures nature and contents of native-like interactions [FChiti99]. Corroborating results where intermediate states aid in the folding to the native state (ubiquitin), or hinder and have to be unfolded again (Che Y), as well as proteins where no intermediates are detected. Apomyoglobin is a globular protein that exhibits well-defined folding intermediates, P. E. Wright and R. L. Baldwin in [RPain00], and has similar structural features, secondary and tertiary structure, to the holo-form. The acid denaturing of apomyoglobin advances in two distinct stages: a compact intermediate with reduced α-helical contents at pH 4 and a denatured state at pH 2 with residual secondary structure. The pH 4 intermediate has the characteristic of a molten globule, just slightly less compact than the native apo- and holo-proteins, contains substantial secondary structure and lack of ordered tertiary structure. Hydrogen exchange trapping experiments indicated a model for folding where three helical regions constitute a folded compact hydrophobic core. $^{13}C^{\alpha}$ chemical shifts from random coil values of apomyoglobin at pH 4 indicated the tendency of the majority of residues to populate helical backbone conformations, and exhibits residual secondary structure in the acid-denatured state at pH 2. The intrinsic conformational propensities were also studied by isolated peptide fragments, and the results were for most segments in good agreement with the results obtained for the full length protein in the acid-unfolded state. The overall folding of apomyoglobin appears to occur through compactions of the polypeptide, which leads to progressive accumulation of secondary structure and increasing restriction of backbone fluctuations. After

formation of a hydrophobic core and progressively stabilised secondary structure, ordered tertiary structure is formed late in the folding process.

### *2.1 Acyl-coenzyme A binding protein*

The protein investigated in this study is bovine acyl-coenzyme A binding protein (ACBP). ACBP is a good model-system for the study of protein-folding, partly due to reversibility of the folding process and its lack of prosthetic groups. The protein is an 86 residue long, four α-helix bundle protein and binds thiol esters of long fatty acids and coenzyme A. Its structure consist of an up-down down-up 4-α-helix bundle with an overhand loop connecting helices A2 and A3, figure 2.1, and was determined by NMR and X-ray crystallography [KVAnde91], [KVAnde93], [DvAalt01] as well as its structure in complex with palmitoyl CoA [BBKrag93]. The arrangement of the helices is special in that helix A3 is tilted compared to A1 and A4 producing 4 helix-helix interfaces. The α-helices are defined as the following regions Ala3 - Leu15, Asp21 – Val36, Gly51 – Lys62 and Ser65 – Tyr84 for A1, A2, A3 and A4 respectively. Twenty-one highly conserved residues form three separate hydrophobic mini-cores and were present in more than 90% of the 30 sequences of acyl-coA binding proteins known at the time of the review by B. Kragelund et al. [BBKrag99]. These residues are mostly located at helix-helix interfaces. Today far more than 100 sequences of ACBP have been published. The gene for the protein is known for eukaryotic species from animals, plant and yeast, and the protein is believed to be important for intracellular transport of long chain acyl-CoA esters and their function as signal molecules. Particularly it is believed that ACBP acts as an intermembrane transporter of acyl-CoA [ASimon03].

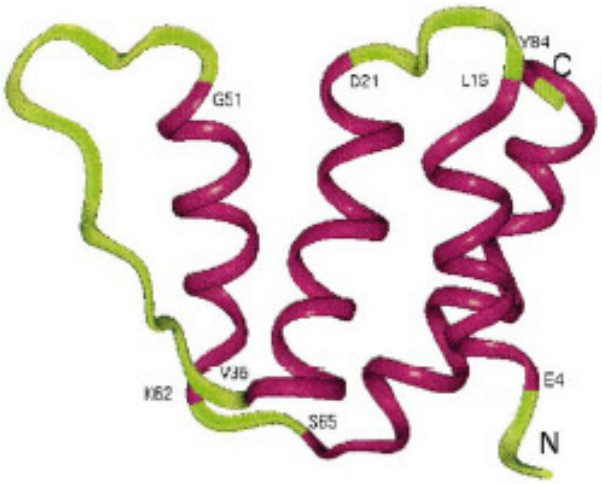


Figure 2.1: The structure of the four helix bundle protein ACBP (pdb code 2ABD). The helices are named A1, A2, A3 and A4 and encompass residues 3-15, 21-36, 51-61 and 65-84. Bovine ACBP contains two tryptophan residues (Trp-55 and Trp-58 in helix A3), two proline residues (Pro-19 and Pro-44 in loop-regions) and no cysteins. Figure from: Kragelund et al. BBA (1999), [BBKrag99].

In the native protein residues of helix A1 form strong contacts with residues of helix A2, which runs anti-parallel to A1 (with a 30° helix-helix angle) and together with the parallel running helix A4 (which forms an angle of 36°). A2 and A4, again, run anti-parallel with an angle of 30°, whereas A3 and A2 run parallel at an angle of

42°[MKjærK94]. The loop between A3 and A4 is identified as a type II-β turn formed by residues Leu61 - Lys64.

### *2.2 Folding/Unfolding of ACBP*

ACBP was originally assigned to the family that folds in a two-state process and has been investigated by a large variety of techniques. For instance fast-reaction techniques like Stopped-flow fluorescence, circular dichroism and mass spectrometry have all shown that ACBP is a fast folder, folding in less than 5 ms at 25° C and gave no indication of partially structured intermediates [BBKrag95]. Refolding kinetics appeared to be the same for proteins unfolded by pH or guanidine hydrochloride (GuHCl). The three mini-cores forming interactions between residues in helix A1 and A4, A2 and A3, A1, A2 and A4, together with conserved non-hydrophobic and not conserved hydrophobic residues are important for fast and effective folding [BBKrag96] and play an important role in the stabilization of ACBP [KAnder93]. Investigations of residues involved in rate-limiting native-like structure in the protein folding by the effect of single-site mutations on folding rates revealed a large influence by residues at the interface between A1 and A4. From this it was concluded that these residues (Phe5, Ala9 with Tyr73 and Ile74 and Val12, Leu15 with Val77 and Leu80) most probably form native-like interactions in the rate-determining folding step [BBKrag99*][BBKrag99†]. All these residues are part of the previously described min-cores, except for Ile74, and are also involved in the stability of the protein together with residues Leu25, Tyr28, Lys32, Gln33 (the only polar residue involved in stability) [BBKrag99†].

A study using quenched-flow in combination with site-specific NMR-detected hydrogen exchange revealed early burst phase intermediates (formation of partially structured intermediates within the deadtime of for instance the fluorescence instrument), by tracking the formation of hydrogen bonds of amide groups [KTeilu00]. The contradiction between NMR and results obtained by CD and fluorescence, are attributed to the disability of CD and fluorescence to detect hydrogen bonds formed during a burst phase. (This also implies that the tryptophan side-chains are not engaged in helix formation, thereby yielding no hydrogen bond protection in the burst phase). The experiments where performed in guanidine deuterocloride (GuDCl) and at pH 5.3 and showed that the same eight conserved residues involved in the formation of native-like structure in A1 and A4 that constituted a rate limiting step in the folding event [BBKrag99*], coincide with burst phase structures.
ACBP exhibited strong interactions between helix A1 and helix A4 and folding/unfolding in guanidine hydrochloride showed that more than 90% of the molecules follow the same two-state kinetics. Furthermore it was shown that the formation of specific interactions occurred during the rate-limiting step of folding. These interactions had to be formed for folding to occur and were shown to include the formation of helix structure in the N- and C-terminal parts of the peptide chain with successive formation of hydrophobic interactions between them.
This led to the assumption of a folding model starting with the formation of ordered but highly flexible structure in those areas constituting helices A1, A2 and A4 in the native structure. At this stage no tertiary interactions are formed, since no solvent molecules have been excluded. As more and more structured molecules are formed

later on, helix A1 and A4 form hydrophobic interactions forming the rate-limiting native-like structure, resulting in a cooperative formation of native folded structure. Analysis of the secondary chemical shift of backbone $^{15}N$ in a GuHCl denatured ACBP sample revealed high helix propensity in the C-terminal part of the protein [KTeilu02]. This prompted the idea that native-like structural elements develop transiently in the unfolded state and the investigation of ACBP denatured in GuHCl from 2.5 M to 5.5 M.

The interactions responsible for the unfolding of proteins at low pH has been shown to be of a electrostatic nature involving relatively few protons (2-5) in the unfolding to the $U_A$ state (acid-unfolded state) and the A-state (pH lowered further, properties similar to molten globule state) [SKim98]. This study also showed that this protein formed secondary structure elements in the acid-unfolded state and in an acid-induced intermediate state.
Hydrogen exchange studies, measuring the exchange rates between folded and unfolded states and their relaxation times, on ACBP showed that: “local unfolding took place in regions of the protein where hydrogen exchange is fast” [JThoms02]. The study indicated that helix A1 might be the trigger for an unfolding event, since the lifetimes in the closed state were very short, confirming a significance of the interaction between helix A1 and A4 for the stability of ACPB. Stability measurements of ACBP as a function of pH showed differences in pH transition midpoints between different spectroscopic methods. It was later made likely that this behaviour was a result of aggregation in the acid denatured state [WFiebe05]. Similar experiments in guanidine hydrochloride did not show this kind of difference, which suggests a difference between guanidine hydrochloride- and acid- unfolding.

Investigations of residual dipolar couplings (RDC) on ACBP under different denaturant conditions (pH and GuHCl), together with site-directed mutagenesis, also support the evidence of residual secondary structure formation in the unfolded protein. It was shown that ACBP in 2.5 M GuHCl did not assume a random coil state, whereas the N-H dipolar couplings of ACBP at pH 2.3 displayed a distinctive sequence-specific pattern, the magnitude of which scaled with the strength of the denaturant concentration. These results strengthen the findings about cooperative transitions between pH 2.4 and 3.6 [JThoms02] in the folding process of ACBP.

NMR diffusion experiments on ACBP, as well as NMR investigation of the peptide corresponding to α-helix A4 in the native protein, showed extensive dimerization properties under denaturing conditions [WFiebe05]. The peptide segment was exceptionally stable, as it also appears to be in the denatured protein and the structure could be represented by a homo-dimeric coiled-coil with a hydrophobic interface between two peptide segments. The diffusion experiments together with concentration dependent experiments at low pH, showed a cooperative stabilisation of helix A4 in the dimerization process. There seems to be fundamental differences in the folding and unfolding dependent on the denaturant in question. For instance, stability differences between acid and GuHCl denaturations were observed. Additionally the GuHCl denatured state does not exhibit dimerization. Furthermore, an inability to fit the acid denatured state to a two state model exist, while the GuHCl state could. W. Fieber et al. [WFiebe05] suggested that the inability to fit the data to the two-state equilibrium between folded and unfolded ACBP at low pH, originated due to the formation of the dimer. To investigate possible residual structure in transient states

and access its behaviour the acid-unfolded state was here investigated in the pH interval from 1.8 to 3.1 by chemical shifts analysis of $^{13}C^{\alpha}$, $^{13}CO$, $^{1}HN$ and $^{15}N$ and compared to random coil values.

The previous experiments suggest that folding of ACBP proceeds through the formation of a rate-limiting transition state with native-like contacts mainly between 8 hydrophobic residues in helices A1 and A4. Recent Φ-value analysis on new mutants also revealed the participation of Ile-27 in helix A2. This residue makes van der Waals contacts in the native state to V12 and V77, high Φ-value residues of helix A1 and A4, respectively [KTeilu05]. This suggests that bovine ACBP undergoes transient helix formation in the region comprising helix A4 and that hydrophobic interactions between residues in A1, A2 and A4 form a transition state. This proposes a transition state, which stabilize and make these interactions beneficial for folding, consisting of residues Phe-5, Ala-9, Val-12, Leu-15, Ile-27, Tyr-73, Ile-74, Val-77 and Leu-80.

# 3 The acid denatured state of ACBP

The acid denatured state of ACBP was investigated under mild denaturant conditions at low pH. Below pH 2.8 it was previously shown that 95 % of ACBP is denatured. It is generally believed that low pH is closer to physiological conditions as compared to unfolding by urea or guanidine hydrochloride, since the concentration of denaturant needed to unfold a protein by pH is tremendously lower than the two other denaturants. It is well known that e.g. $^{13}C^{\alpha}$, $^{13}C^{\beta}$ or $^{1}H^{\alpha}$ resonance exhibit an average shift away from random coil values for residues in α-helices, or β-sheet [SSpera91], [DWisha94]. And observation of chemical shifts can hence be used to observe residual secondary structure in denatured states.
The purpose of this investigation was to characterise the unfolded state of ACBP and consider the appearance of the chemical shifts under acid denaturant conditions.
The chemical shifts investigated were the backbone chemical shifts of $C^{\alpha}$, CO, amide nitrogen and amide hydrogen. The main NMR experiments used where HSQC, HNCA and HNCO. The sequential assignment for the acid-unfolded ACBP at pH 2.3 was made by Jens K. Thomsen. The pH titration's were made twice; once at an approximate concentration of 0.5 mM and once at a concentration of 58 μM for ACBP, since an investigation suggested the formation of extensive dimerzation at higher concentration under acid denaturant conditions [WFiebe05]. In order to obtain a greater understanding of the dimerization process the titration series was also measured for a high concentration of ACBP. In the investigated pH interval the unfolded and folded populations are in slow exchange and all measurements and evaluations are hence just made on the unfolded peaks.
The titration series obtained for the high concentration of ACBP was made at the following pH-values: 1.80, 2.00, 2.20, 2.40, 2.60, 2.80, 2.95 and 3.20.
For data-analysis pH-values 1.80, 2.00 and 3.20 were not included. The reason for this being, that ACBP at the highest pH-value was substantially refolded, which was seen by the appearance of multiple new peaks in the spectra, and loss of some unfolded peaks. The lowest pH-value of 1.80 was discarded since it showed a bigger chemical shift difference from random coil values, and in the opposite direction of the previous chemical shifts trend. This was interpreted as an acid induced refolding of the protein [YGoto90]. It could also, as was made likely later on, be an artefact due to an increased salt concentration in the sample (data not shown).
The titration series obtained for the low concentration of ACBP, were no appreciable dimerization occurred, was made at pH values: 2.30, 2.40, 2.50, 2.60, 2.70, 2.80, 2.90 and 3.01.
The chemical shifts were evaluated as secondary chemical shift, calculated by subtraction of random-coil values, generated for ACBP from chemical shift values of Schwarzinger et al. [SSchwa00], [SSchwa01], from the measured chemical shift data. The random coil values used here, where measured at pH = 2.3 at a temperature of 25° Celsius for the fully denatured (by 8 M urea) peptide sequence Ac-G-G-X-G-G-$NH_2$. These random coil chemical shift values take nearest neighbour effects into account. The high concentration series, however, was compared against random-coil values obtained from Wishart et al. [DWisha95], measured at pH = 5.0 ± 0.3 and at 25° C for the fully denatured (by 1 M urea) peptide sequence Ac-G- G-X-Ala- G- G-$NH_2$, also including nearest neighbour effects.

*Results*

### *3.1 High concentration pH titration*

Figures 3.1 and 3.2 show the secondary chemical shift measured for the high concentration pH titration series of $C^{\alpha}$ at pH 2.40 and 2.95 (excluding Aspartate residues 6, 21, 38, 48, 56, 68, 75, due to large pH dependencies of the $C^{\alpha}$ random-coil values).

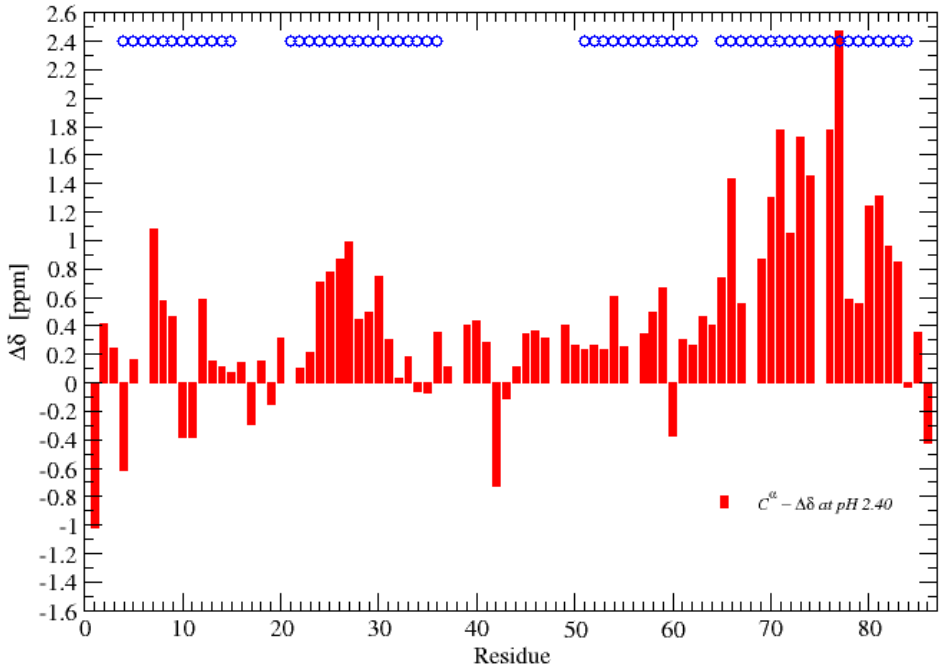


Figures 3.1: Secondary $C^{\alpha}$ chemical shift at pH 2.40. Concentration of ACBP ~ 0.5 mM. The blue circles indicate the location of helices A1 to A4 in the native structure.

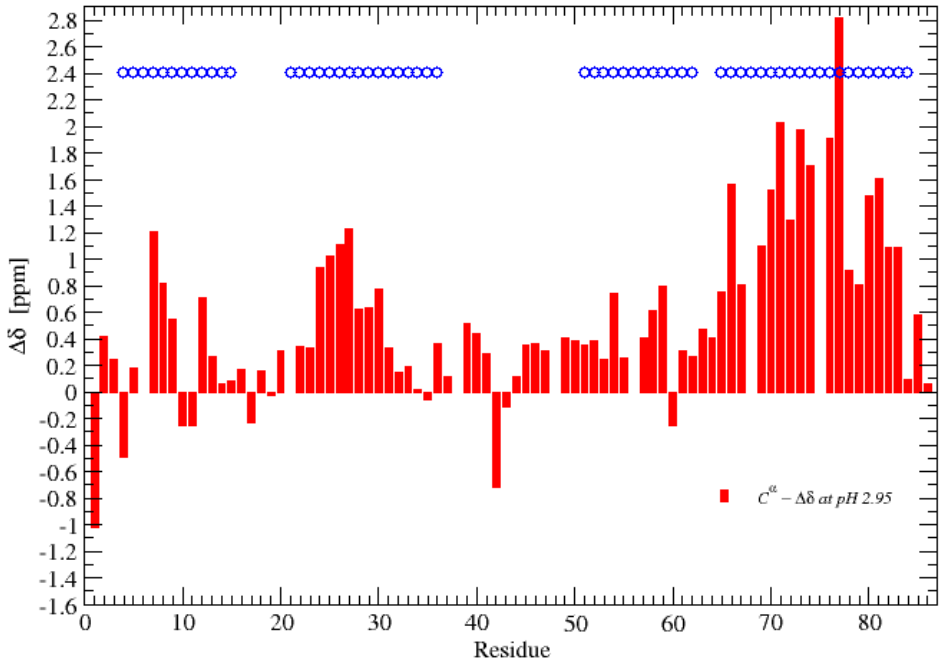


Figures 3.2: Secondary $C^{\alpha}$ chemical shift at pH 2.95. Concentration of ACBP ~ 0.5 mM. The blue circles indicate the location of helices A1 to A4 in the native structure.

The chemical shift analysis here suggests that more α-helix-like structure is formed, i.e. secondary structure, at higher pH, 2.95, compared to pH 2.4. The picture is clearest for the $C^{\alpha}$-shifts indicating helix-formation in regions of the polypeptide chain comprising helix A2 and A4 in the native protein. Furthermore, the $C^{\alpha}$-chemical shifts in the region of helix A3 in the native protein also indicate some residual helical structure at high pH. This picture is different for the CO shifts at this higher pH-value. Compared to the lower pH, the inclination for helix in the peptide segment, consisting of helix A4 in the native protein, is now pronounced. At pH 2.95 most residues, except the first half of the region A2 and A4, exhibit negative shifts. The residues of the peptide segment comprising A4 in the native structure have positive shifts away from random coil values in the order of 0.5 ppm and larger, whereas residues of the first half of A2 are positive with values of roughly 0.25 ppm. At pH 2.4 CO chemical shifts for almost all residues are negative, except again for residues in the regions of A2 and A4. Now however, the absolute values of these residues are decreased significantly, to almost zero for those residues of the first half of A2 and well below 0.5 ppm for those of A4. (The data for the CO chemical shifts are not shown here). CO-groups are in the native state expected to engage in hydrogen bond formation and their chemical shifts should change considerable when these bonds are lost. Thus, indicating a loss of these bonds over the course of the pH interval.
In order to illustrate the overall changes of the chemical shifts over the investigated pH-interval linear regression on the data for each residue was performed, providing a slope showing the chemical shift change per pH-unit for each residue. Figures 3.3 and

3.4 show the secondary chemical shift difference pr. pH unit for $C^{\alpha}$ and carbonyl carbon (CO) chemical shifts of the pH titration series at a high concentration of ACBP (Again without aspartate residues and tryptophan 55 and 58 due to large a large pH dependency of the random-coil values of the carbonyl carbon).

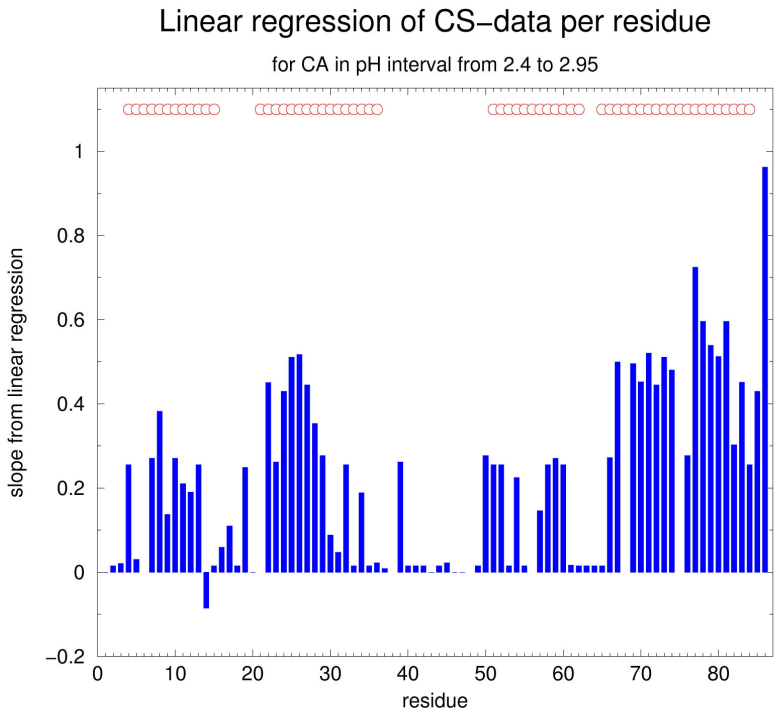


Figures 3.3: Linear regression on $C^{\alpha}$ chemical shifts in the pH interval from 2.40 to 2.95. Concentration of ACBP ~ 0.5 mM. The red circles indicate the location of helices A1 to A4 in the native structure.

The picture figure 3.3 clearly shows that over the course of the pH-interval from 2.4 to 2.95 there is an increasing amount of residual secondary structure being formed in the region of all four helices. Where, the largest tendency is seen in helix A4, to a lesser extent in A2, and even less in A1 and A3. It is also seen that the inter-helical regions (loop-regions) do not change and exhibit random coil values over the entire pH-interval.

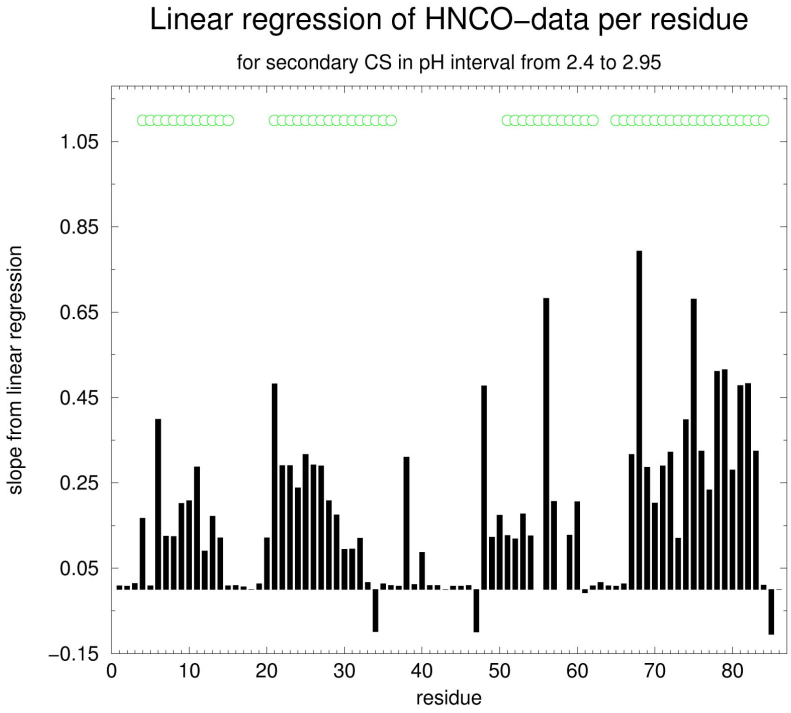


Figures 3.4: Linear regression on CO chemical shift in the pH interval from 2.40 to 2.95. Concentration of ACBP ~ 0.5 mM. The green circles indicate the location of helices A1 to A4 in the native structure.

The changes of the CO shifts also indicate a raising tendency for helix in all four helices, with the same order for inclination for helix as the $C^{\alpha}$-shifts. Also here, the loop regions seem disordered over the course of the pH interval.
The amide proton chemical shifts at high pH show a somewhat different picture. Although all residues have shift values away from random coil, the only region with several residues showing more than -0.2 ppm difference from random coil, seems to be region A3, and less clearly region A1 and A2. Surprisingly, the residues in region A4 seem to be the least ordered. The slope of the amide proton chemical shift over the course of the pH-interval shows that the chemical shift do not change as the pH value is lowered/raised (data are not shown here).
The amide chemical shifts are expected to be unstructured since they depend on both amino acid type and sequence. However, the linear regression data show that there is a correlated change towards α-helix formation over the range of the pH-interval in α-helix region A4 of the native structure, while there is no correlated change in the loop regions (data not depicted here).

### *3.2 Low concentration pH titration*

As mentioned the pH titration series was also measured with a lower concentration of ACBP. The low concentration of 58 μM was made possible due to the introduction of cryoprobes to the 750 and 800 MHz NMR-instruments. In the region from pH 2.3 to

3.0 a similar picture as was observed for the 0.5 mM titration series was seen. Figures 3.5-8 show the overall changes in $C^{\alpha}$, CO, $H^{N}$ and $N^{H}$ per pH unit.

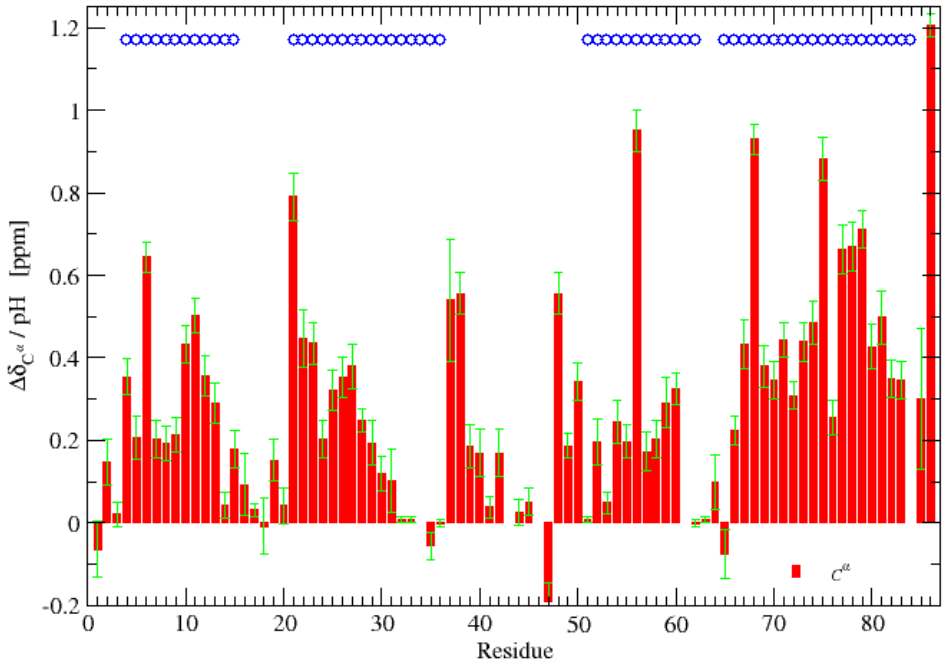


Figure 3.5: $\Delta C^{\alpha}$ chemical shift as function of pH with standard error. The blue circles indicate the locations of the four α-helices in the native structure. Concentration of ACBP 58 µM.

As can be seen from the figure 3.5, over the course of the pH-interval from 2.3 to 3.0, an increasing amount of residual secondary structure is formed in the region of all four helices. Where, the biggest tendency for helix-formation is seen in helix A4 of the native structure, to a lesser extent in A2, and even less in A1 and A3. It is also seen that the inter-helical regions (loop-regions), experience more chemical shift changes as are observed for the high concentration pH-titration series. The third loop-region poses one exception, which seems almost as unstructured (random coil) as was the case for the series where extensive dimerization was present.

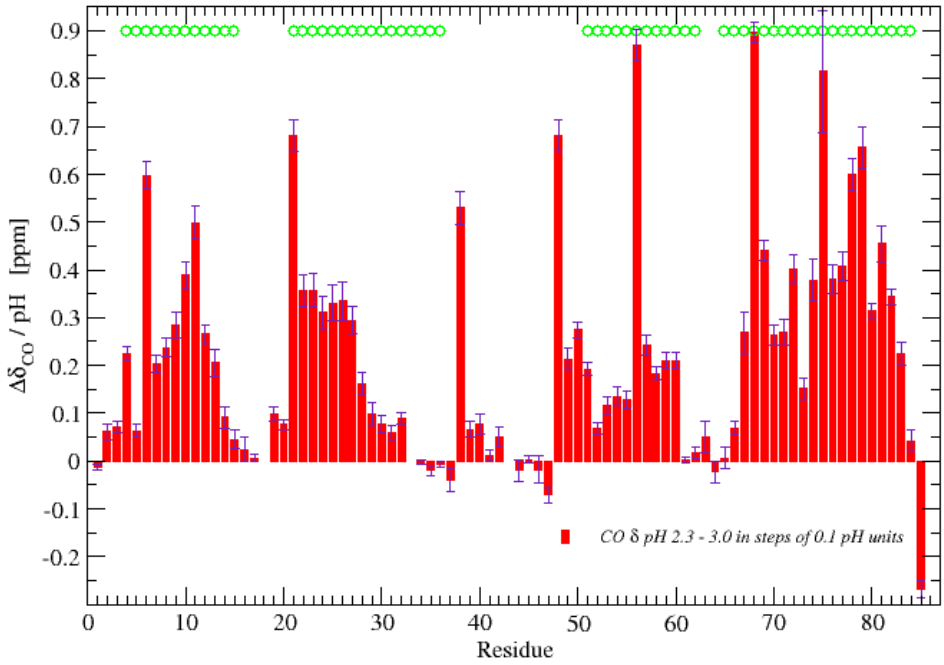


Figure 3.6: ΔCO chemical shifts values as function of pH with standard errors. The blue circles depict the location of the four α-helices in the native structure. Concentration of ACBP 58 µM.

The changes of the CO shifts over the pH- interval also indicate a raising tendency for helix formation in all four regions comprising helices in the native structure, again with increasing amount. The largest tendency for α-helix formation is found for the region of the peptide sequence making up helix A4 in the native structure, followed by A2 and A1 and least for A3. The loop regions seem disordered over the course of the pH interval, but show also more variation than was the case for the high concentration series.

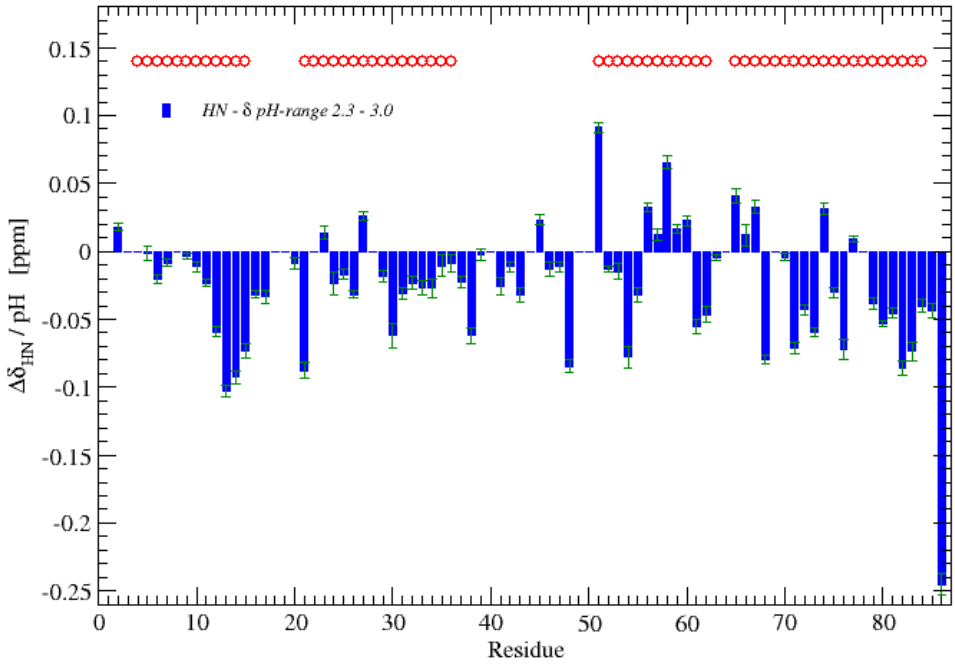


Figure 3.7: Change of $H^N$ chemical shift values as a function of pH with standard error. The blue circles indicate the location of the four α-helices in the native structure. Concentration of ACBP 58 µM.

The amide proton chemical shifts pr pH-unit are very much like the changes observed for the high concentration pH titration series, showing no change over the course of the pH interval. Again, the largest deviations from random-coil values are found in the region of helix A3 in the native structure. The lesser extent in the inclination for α-helix is expected, since hydrogen bonds in helices are not expected in the denatured state.

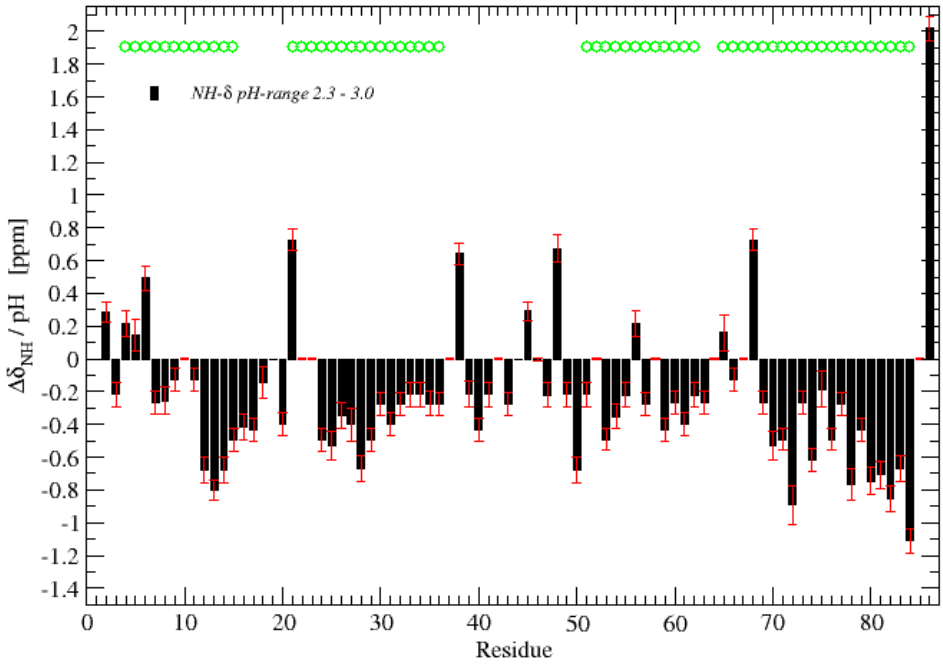


Figure 3.8: Change of $N^H$ chemical shift values as a function of pH with standard error. The blue circles show the location of the four α-helices in the native structure. Concentration of ACBP 58 µM.

The amide chemical shifts look somewhat different than was the case in the high concentration pH titration series. They are expected to be unstructured, since they are not expected to engage in α-helix bond formation in the acid unfolded state. However, negative correlations away from random-coil chemical shift values are observed in all regions except the loops, compared to the previously unstructured pattern (see figures A.5 and A.6 in Appendix A). The linear regression data, similar between the two trials, show that there is a correlated change towards α-helix formation over the range of the pH-interval in α-helix region A4 of the native structure, while there is no correlated change in the loop regions. Figures for all pH values can be seen in Appendix A, figures A.1 to A.4.

In order to show the different extent of conformation between low and high pH, scatter plots are made for the secondary chemical for both $C^\alpha$ and CO, where pH 2.3 and pH 2.4 are depicted against each other, as well as pH 2.3 and pH 3.0.
If the data is located on the diagonal, the corresponding residue is in the same "conformation" (secondary shift) at both pH-values. If however, a residue is situated above or below the diagonal, they exhibit different "conformational environments". As expected, see figures 3.6 – 3.9, conformations are more alike between the two low pH values, than between the two extreme pH values. k signifies the slope of the fitted line and the following regression values were found: $C^\alpha$: k = 1.17, std. error = 0.04 and correlation coefficient = 0.96 for pH 2.3 versus 3.0, and k = 1.01, std. error = $2.7 \times 10^{-9}$ and correlation coefficient = 0.99 for pH 2.3 versus 2.4, while carbonyl shifts

have values of k = 1.24, std. error = 0.03 and correlation coefficient 0.97, and k = 1.02, std. error = 0.01 and correlation coefficient of 0.998, for pH 2.3 against 3.0 and pH 2.3 against 2.4 respectively.

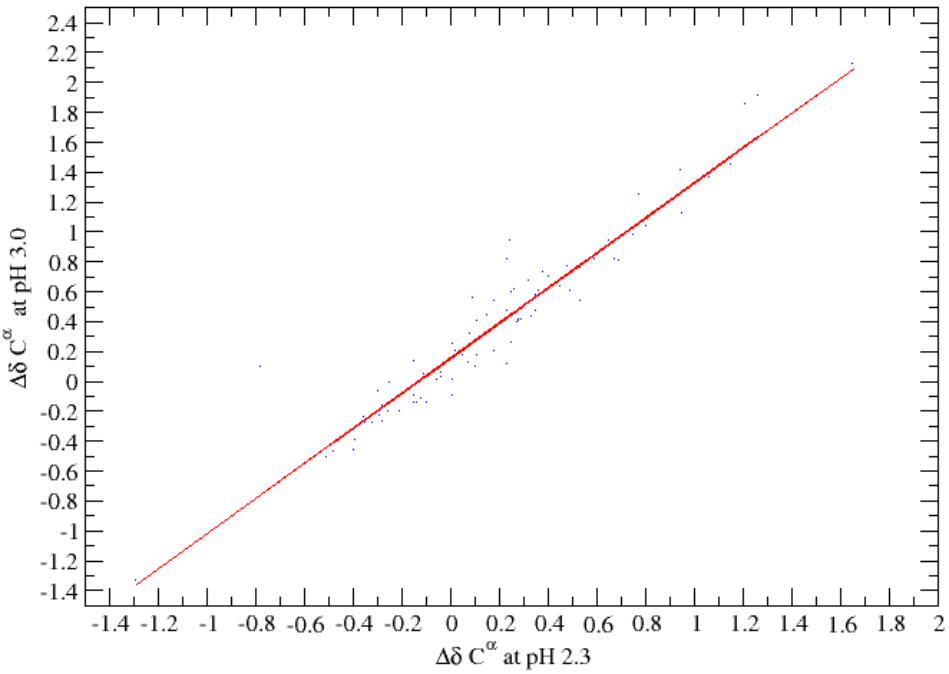


Figures 3.9: Scatter plot of $C^{\alpha}$ secondary chemical shift values at pH 3.0 against values at pH 2.3.

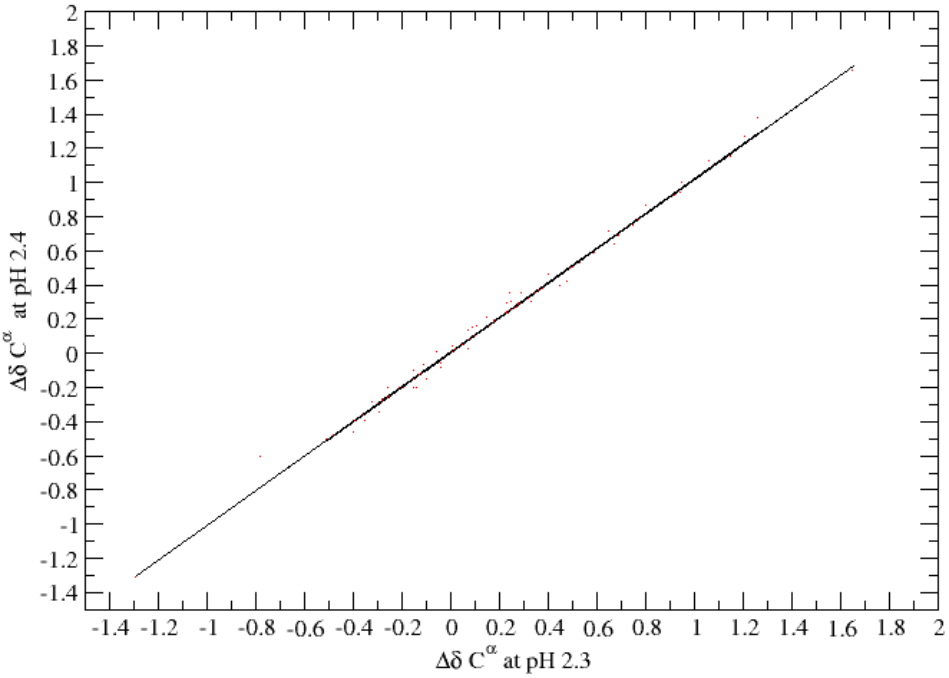


Figures 3.10: Scatter plot of $C^{\alpha}$ secondary chemical shift values at pH 2.4 against values at pH 2.3.

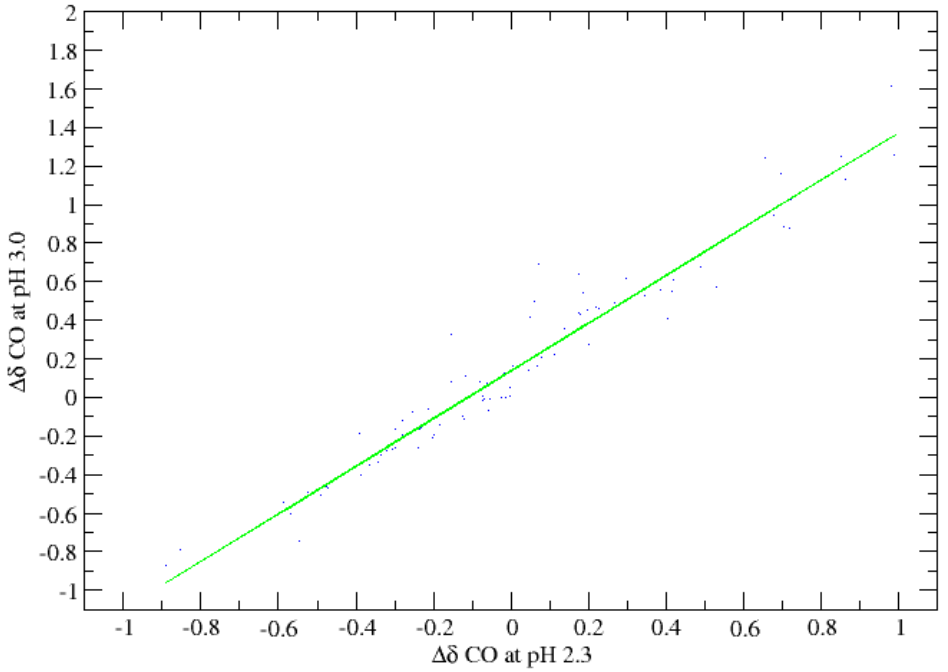

Figures 3.11: Scatter plot of CO secondary chemical shift values at pH 3.0 against values at pH 2.3.

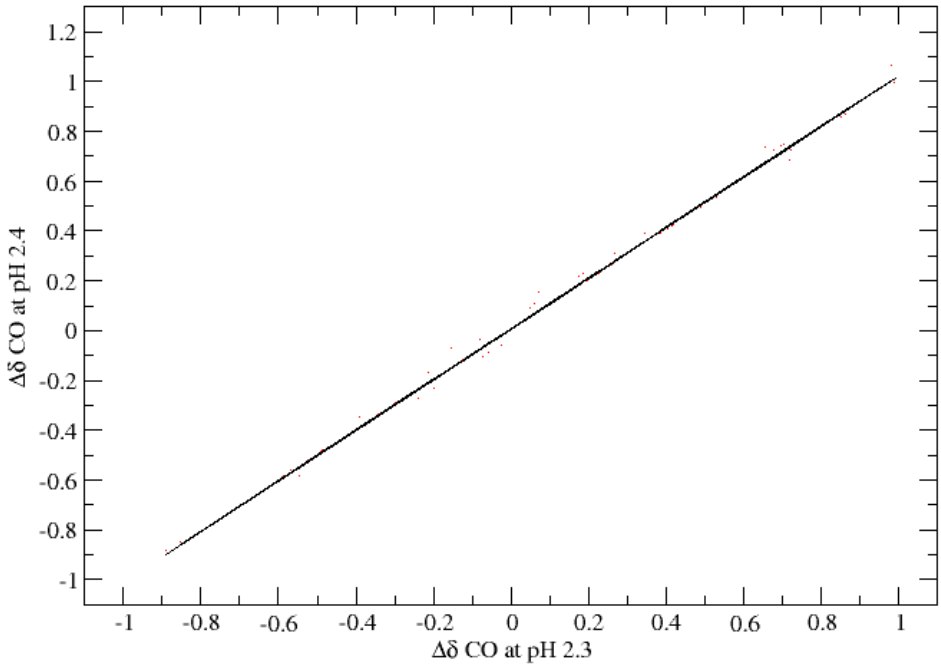


Figures 3.12: Scatter plot of CO secondary chemical shift values at pH 2.4 against values at pH 2.3.

### *3.3 Differences between the two acid denatured titration series*

If one compares the two data sets directly an indication of which parts of the structure are engaged in the dimerization process can be gained. In figure 3.13 the difference between the $C^{\alpha}$- chemical shifts measured with a concentration of approximately 0.5 mM and 58 µM is seen, both at pH 2.8. The data clearly points towards the participation of the residues from the region of helix A4 of the native structure in the dimerization process, since the largest difference is observed here. But also parts of the region of helix A2 in the native structure participate to some extent, since the $C^{\alpha}$ - chemical shifts of these residues have larger positive chemical shifts at high concentration as compared to the lower concentration. Yielding an absolute difference from random coil value that will be larger for samples with extensive dimerization and hence have a larger tendency for helix formation. This picture is reversed for helix region A1 of the native structure, where the lower concentration yields larger positive chemical shifts. The remaining sequence shows no particular correlation between the two sets.

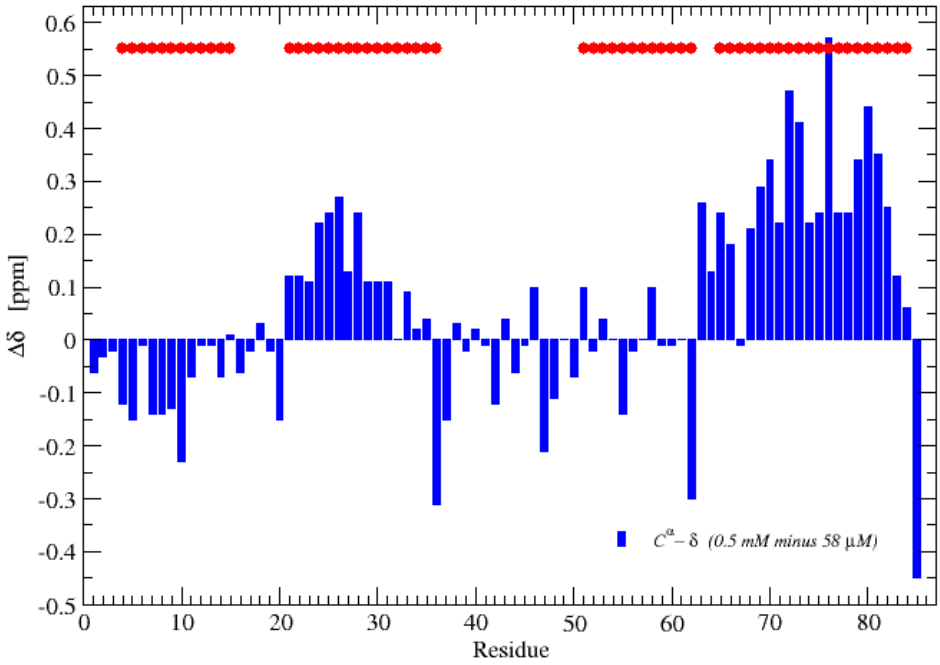


Figure 3.13: Difference between $C^{\alpha}$ chemical shifts from the two data-series (0.5 mM data-set minus 58 µM data-set) at pH 2.8.

This difference between the two sets converges as the pH gets smaller, indicating that the two sets move towards the same conformations, as the proteins get more unfolded, see figure A.7 in Appendix A, showing the difference between the two sets at pH 2.3, for both $C^{\alpha}$ and CO chemical shifts. The difference between the two titration series suggest that the extent in helix formation in the region of A4 and A2 would be over-estimated, while A1 would be underestimated in the high concentration pH titration series, as compared to the actual extent present with no dimerization.

The influence the two different random-coil data have on the chemical shifts, both values are obtained for small model peptides, but under different denaturant conditions, is evaluated. As previously mentioned, the two random coil value datasets were those from Wishart et al. [DWisha95] measured at pH = 5, in 1 M urea, and Schwarzinger et al. [SSchwa01], where the model peptides were evaluated at pH = 2.3 in 8 M urea, both including nearest neighbour effects. Figures 3.14 and 3.15 show the same data-set measured at low ACBP concentration obtained at pH 2.7 evaluated with random coil values from Wishart et al. and Schwarzinger et al., respectively. Differences are observed for the helix A1 region and the region from the middle of A2 to the centre of A3, differences which most probably can be attributed to pH effects on specific residues.

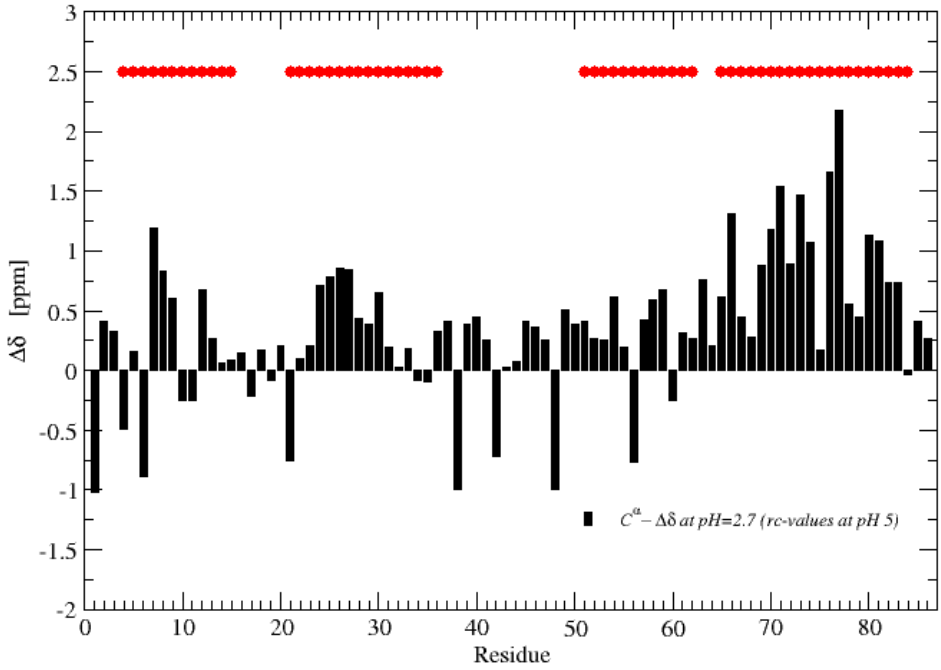


Figure 3.14: Secondary $C^{\alpha}$ chemical shift at 58µM ACBP and pH = 2.7 evaluated with random-coil values from Wishart et al.

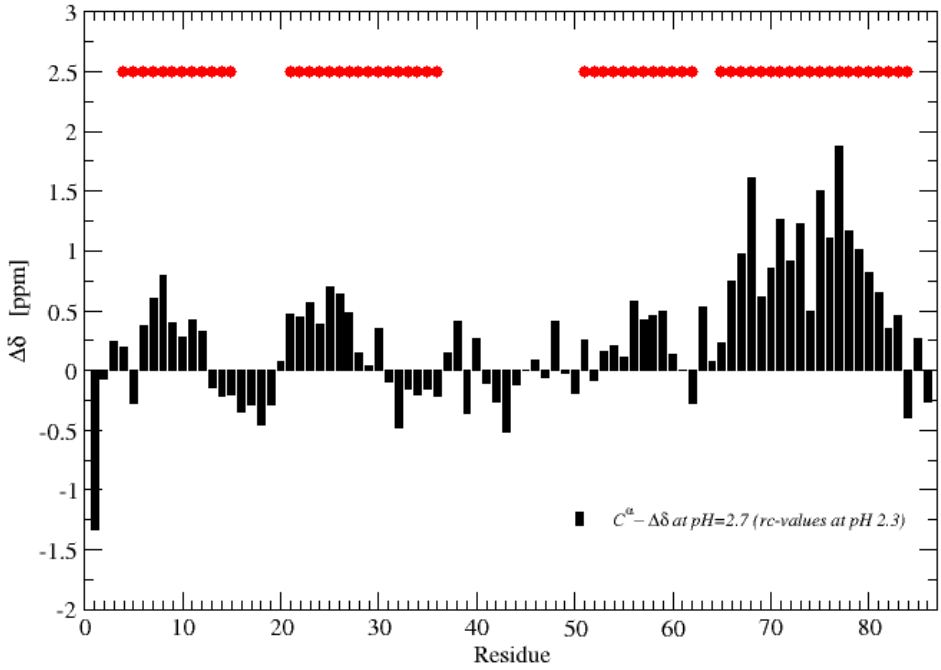

Figure 3.15: Secondary $C^{\alpha}$ chemical shift at 58µM ACBP and pH = 2.7 evaluated with random-coil values from Schwarzinger et al.

In order to evaluate the influence of the two different random coil values on ACBP it is possible to look at the difference the two datasets of random coil chemical shift values have on the sequence of ACBP. This gives rise to, what one could call an intrinsic pH dependency for ACBP, i.e. a sequence specific chemical shift dependency on nearest neighbours and the pH-values. There is of course also a difference in denaturant concentration. If one subtracts the random-coil values derived from Wishart et al. for each residue of ACBP, from those assigned by Schwarzinger a picture of the intrinsic pH dependency for ACBP emerges, see figures 3.16 and 3.17, for $C^{\alpha}$ and CO respectively.

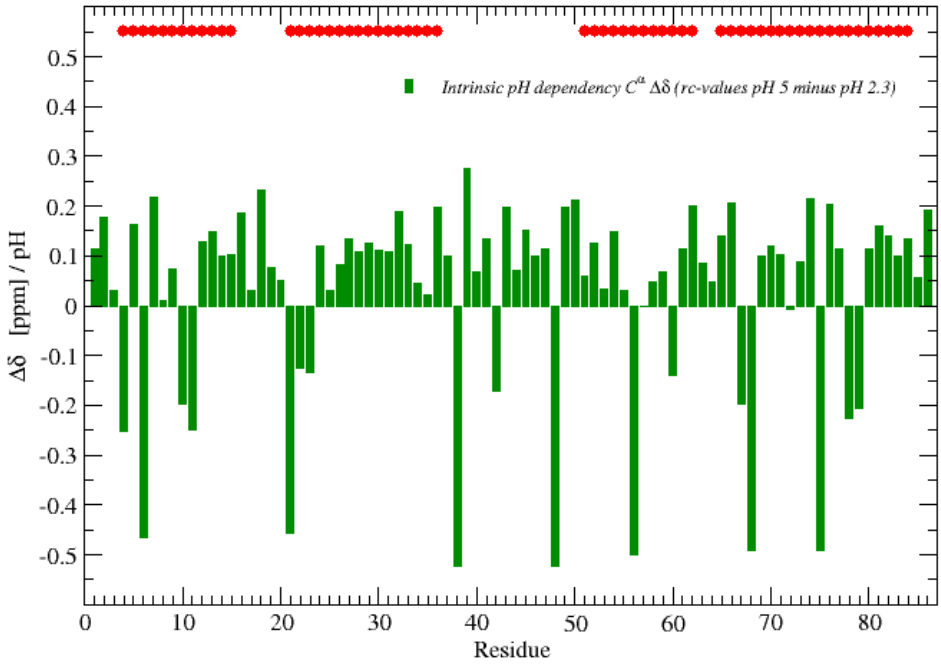


Figure 3.16: ACBP sequence specific random coil values for $C^{\alpha}$, representing the intrinsic pH dependency of ACBP (Wishart et al. minus Schwarzinger et al. random-coil values). All large negative values are Asp residues.

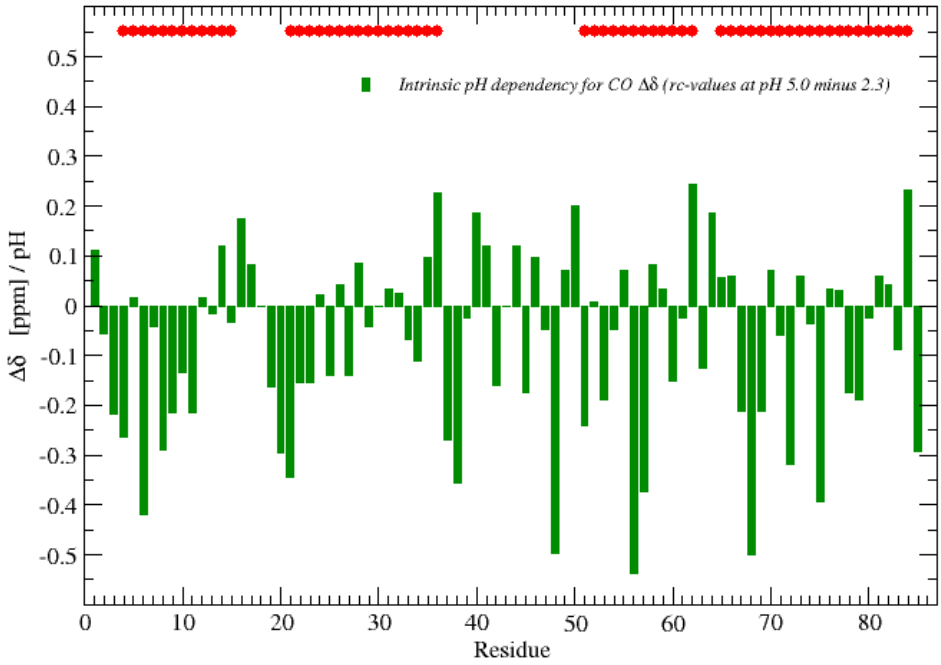


Figure 3:17: ACBP sequence specific random coil values for CO, representing the intrinsic pH dependency of ACBP (Wishart et al. minus Schwarzinger et al. random-coil values).

As is seen from figure 3.16, the dependency for $C^{\alpha}$ chemical shifts are evenly distributed throughout the sequence, but might display a small correlation for the second half of the A1, A2 regions and the loop in between, while CO exhibit a clustering around A1 and the beginning of A2, figure 3.17. The positive difference for residues, especially for the region from the middle of A2 to the centre of A3 for $C^{\alpha}$ chemical shifts, figure 3.16, can for instance explain the distinction in appearance observed in this region seen in figures 3.14 and 3.15. But also leads to a significant absolute difference in chemical shifts for the regions comprising the helices in the native structure. It is hence highly relevant which random coil values are used to estimate the secondary chemical shifts in order to avoid an over- or under-estimation of the extent of helix formation in the mentioned regions. For the data obtained here, under denaturing conditions at low pH the random coil values obtained by Schwarzinger et al. should be used, whereas data obtained around pH 5 should be evaluated against the random coil values of Wishart et al.

### *3.4 Discussion/Conclusion*

In summary ACBP forms more residual structure over the course of the pH-interval in all four helix regions, with A4 being the region with the largest tendency for helix formation in the acid unfolded state. To a lesser extent than helix A4, helix A2 is formed, and even less A1 and A3. Which of the two last helices has the larger tendency for helix is hard to determine, a feature that repeats itself for the CO chemical shifts. The $H^{N}$ chemical shifts show the highest tendency of occurring in the

region of helix A3, while A1 seems to be much less ordered for chemical shifts of this nuclei-species, but amide hydrogen chemical shifts experience almost no change over the course of the pH interval.
The $N^H$ secondary chemical shifts demonstrated negative correlations away from random-coil in all regions except the loops at low ACBP concentrations, which stood in contrast to the unstructured pattern for the values obtained at high concentration of ACBP. The linear regression data supported a change towards α-helix formation from low to high pH in α-helix region A4.
These data confirm the previously obtained information about the folding of ACBP (see chapter 2), which propose that folding of ACBP proceeds through the formation of a rate-limiting transition state [KTeilu05]. Calculation of secondary structure formation showed the highest propensity for α-helix to be in the peptide segment of α-helix A4 of the native structure [KTeilu02], which is clearly corroborated by the present chemical shift analysis, which even suggests residual secondary structure at pH 2.3. Also hydrogen protection in the early stages of folding supported the assumption of high α-helix propensity in A4 [KTeilu00] and further the view that bovine ACBP undergoes transient helix formation in the region comprising helix A4 and that hydrophobic interactions between residues in A1, A2 and A4 form a transition state.
Interestingly, the evaluation of the acid denaturing at two concentrations gave an indication of the participation of residues of helix A4 in the native structure and to a lesser extent A2, in the dimerization process. The increase in helical contents in A2 might be a passive effect due to presence of a more stable A4-region and not actually infer the participation of residues of A2 in the dimerization process. Samples with extensive dimerization will have a larger tendency for helix formation in those two regions of the peptide sequence. This picture is reversed for helix region A1 of the native structure, where there exists a bigger tendency for helix formation in samples with no significant dimerization. Previous investigation of the dimerization of ACBP and the peptide segment comprising helix A4, proved the cooperative association of two denatured ACBP molecules to a homodimer mediated by the peptide segment comprising helix A4 [WFiebe05]. Emphasising the role of A4 as a prime structural element, which operates to stabilize the denatured state of ACBP. For one, by native-like interactions with the region A2 and by non-native interactions like the formation of the homodimer at higher protein concentrations. The role of helix A4 is similar to that seen for helix H of apomyoglobin (see chapter 2, P. E. Wright and R. L. Baldwin in [RPain00]), which also participates in the structure of the denatured state, as well as in an intermediate state of the folding process and in the native state. But ACBP exhibits much more residual structure in A4 in the denatured state [JThoms02] than helix H.
In order to get a more quantitative measure of helix formation during the course of acid denaturing, the data was studied by theoretical means, in the form of Molecular Dynamic and Monte Carlo Simulations. For the evaluation of which helix has the largest propensity, more importance is placed in the $C^\alpha$-chemical shifts, since they mostly depend on the sidechain, while $N^H$, CO a very sequence depended (engage in bond formation). But since carbonyl carbon chemical shifts exhibit a similar picture to that obtained for $C^\alpha$ chemical shifts, emphasis in the Monte Carlo simulation is also put on this nucleus.

# 4 Urea and Guanidine hydrochloride denaturation

Two other major denaturants used in the study of protein folding are urea and guanidine hydrochloride (GuHCl). Both are considered less attractive than acid denaturing due to their ability to bind to proteins [ELiepi94], [DShort01].
The exact molecular mechanism by which urea unfolds is unknown, other than an altered protein-solvent interaction. It has, though, long been known that both denaturants act by favouring the stabilization of the unfolded state in preference to the native state [CTanfo68], [CNPace86]. I.e., raising the solubility of most parts of the protein compared to water and hereby stabilizing the denatured state compared to the native.
Denaturants like urea might bind directly to the protein surface or interrupt the hydrophobic interaction due to altered solvent properties or a combination of both. Both mechanisms are likely. The first requires the exposure of more binding sites in the denaturing protein, while the other should destabilize the hydrophobic interactions of the folded protein. Several studies have indicated the presents of short-lived binding of urea to proteins and the relatively high concentration of denaturant indicate the necessity of many binding sites [JSchel02], [ELiepi94]. Recently evidence for weak binding of urea and GuHCl as being directed towards the backbone has been seen for poly-glycine-serine chains [AMögli05]. The data indicated that both denaturants act by increasing solvent viscosity by indirectly slowing chain dynamics, as well as direct interaction with the polypeptide chain. The article additionally attributed the dissimilarity in their ability to denature to the difference in binding affinities, since they both exhibit the same number of denaturant binding sites along the polypeptide backbone.
Furthermore, experimental evidence has also been seen [KModig03] for long-lived (strong) binding of urea to intestinal fatty acid-binding protein, indicating site-specific binding of urea to both the native, as well as to the denatured protein. Thus, illustrating that strong binding adds to the unfolding. This in turn also gives that a simple extrapolation from a urea concentration, were residual structure still is present, to a higher concentration where the protein would be totally random coil, is not possible.
Also MD simulations on peptides in urea suggest the participation of both the direct and indirect mechanisms in the chemical denaturation process [ACabal05].

The interpretation of unfolded proteins is obscured by the use of chemical denaturants, since the denaturants may have an effect on the spectral characteristics of the unfolded protein, as well as on its conformational preference [CPace86]. This makes it difficult to separate effects on for instants chemical shifts arising due to residual structure from effects of the denaturant. Guanidine Hydrochlorides effect on random coil chemical shifts has previously been studied by investigating the peptide sequence GGXGG for all 20 amino acids in the case of proton chemical shifts [KPlaxc97]. While the effect on $^{13}C$ and $^{15}N$ chemical shifts was investigated on seven representative peptides, all at 20 degree, at pH 5 and referenced to internal DSS. This study provided correction factors, enabling to subtract the effect of GuHCl on the random coil chemical shifts.
They also showed that the intrinsic backbone conformational preferences of $\varphi$, $\psi$, and $\omega$ were not affected by GuHCl, but showed that GuHCl had an effect on the chemical shifts of referencing compounds, for instants that its effect on water was $\Delta\delta = -0.044$

ppm $M^{-1}$. The induced chemical shift changes were shown to be linearly dependent on the GuHCl concentration. The largest effect of the denaturant was shown to arise in $^{15}N$ chemical shifts, but exhibited relatively small residue specific dispersion. Of the carbon resonance, carbonyl carbons showed the largest sensitivity towards GuHCl, but also showed a small residue specific dispersion, $\Delta\delta = -0.086 \pm 0.016$ ppm $M^{-1}$, while the effect on aliphatic carbons was relatively small but revealed a large dependency on residue type. E.g. for $C^{\alpha}$ $\Delta\delta$ equalled $-0.038 \pm 0.044$ ppm $M^{-1}$. For this reason the $C^{\alpha}$ chemical shifts investigated in this study were just corrected for the seven investigated peptides, while carbonyl shifts were corrected for the seven known as well as with the mean value for the unknown amino acids. However, those seven peptides still comprised roughly $^{2}/_{3}$ of ACBP's amino acid sequence (Ala, Arg, Glu, Iso, Leu, Lys, Thr, Tyr and Val). Plaxco et al. also found that hydrogen's adjacent to carbonyl carbons, as well as $H^{\alpha}$ resonance's experienced relatively large changes, which, together with the lack of disturbance on the peptide conformation, they interpreted as evidence of GuHCl denaturant action as an effect on the hydrogen-bonding interactions between the carbonyl oxygen's, the amide protons and the surrounding water. That is, supporting the hypothesis of changes to solvation properties of water for GuHCl denaturing mechanism as opposed to specific binding. The perception that denatured proteins are fully solvated random coils, is slowly been revised due to extensive experimental evidence. Spectroscopic evidence mounts up that native-like topologies persist under strong denaturants conditions, e.g. for urea concentrations of at least 8 M [YLiFPi05], where residual structure also is observed for low pH. Also small angle X-ray scattering show that some proteins exhibit residual secondary structure even under strong denaturing conditions [JKohn04].

### *4.1 The urea denatured state*

In order to get and truly random coil data set for the interpretation of the acid denatured state, that is where ACBP has no residual secondary structure, a titration by urea was made at concentrations of 1.1, 2.1, 3.1, 4.1 and 5.1 M. The samples were adjusted to pH 2.3, in 10 mM Glycine buffer, 10% $D_2O$ and a concentration of ACBP of 60 μM. The urea concentration interval was decided on after a urea denaturation with CD-spectroscopy in the far UV-region from 195 to 230 nm, where ACBP was denatured in the interval from 0.86 M to 4.04 M urea at pH 2.3 and a concentration of ACBP of roughly 20 μM. Over this interval the characteristic minima of a α-helix secondary structure was reduced in magnitude by a factor of approximately four, and its features almost totally extinguished.
At the investigated field strengths in NMR spectroscopy, the water and urea peaks exchange, making a direct classification of the direct and indirect reference value impossible, since the proton transmitter offset frequency (tof) was shifted but appeared to be unchanged due to the exchange with urea. In order to subsequently calculate the correct reference values for the three nuclei, DSS (3-(Trimethylsilyl)-1-propanesulfonic acid Sodium salt) was used as an internal standard. See Appendix C for a table of measured and revised proton transmitter offsets (tof's), table C.1.
It was not possible to follow all residues from previously assigned peaks at pH 2.3 and 0 M to 1 M urea, therefore spectra of HNCOCA and HNCACB also were recorded.
Unfortunately the chemical shifts of $C^{\alpha}$ and CO did not completely go towards random coil values in the chosen urea concentration interval. Figure 4.1 shows a segment of CO chemical shifts of all 5 concentrations projected into one $^{15}N$ plane. As can be seen for the residues Glu-60 and Ala-57, they are located far from their respective random coil values, although they converge slightly towards them during the course from 1 to 5 M urea. Lys-66 and Ile-39 are just slightly off set from there random-coil value, and could therefore be regarded as moving closer to their random coil value, whereas Val-36 does not change much over the concentration range and hence does not converge towards its random-coil value. Val-36 could be considered totally unstructured and suggest an inherent random coil value for ACBP. It is, however, also just slightly offset from its random coil value, which could be due to binding of urea. Lys-52 is also offset from its random coil value, and does due to the offset not seem to move closer to it. This represents it self in figure 4.3 by a change in sign of the CO secondary chemical shift. A feature that is also observed for other residues, both carbonyl and $C^{\alpha}$ chemical shift, see figures 4.2 and 4.3, e.g. residues 10, 27, 47, 53 and 79. All in all it can be seen, that all values exhibit an offset from the standard random coil values, which can be both in the $^{13}C$ and/or $^{1}H$ chemical shift dimension. It is also noticed that this offset factor is not the same for each residue.

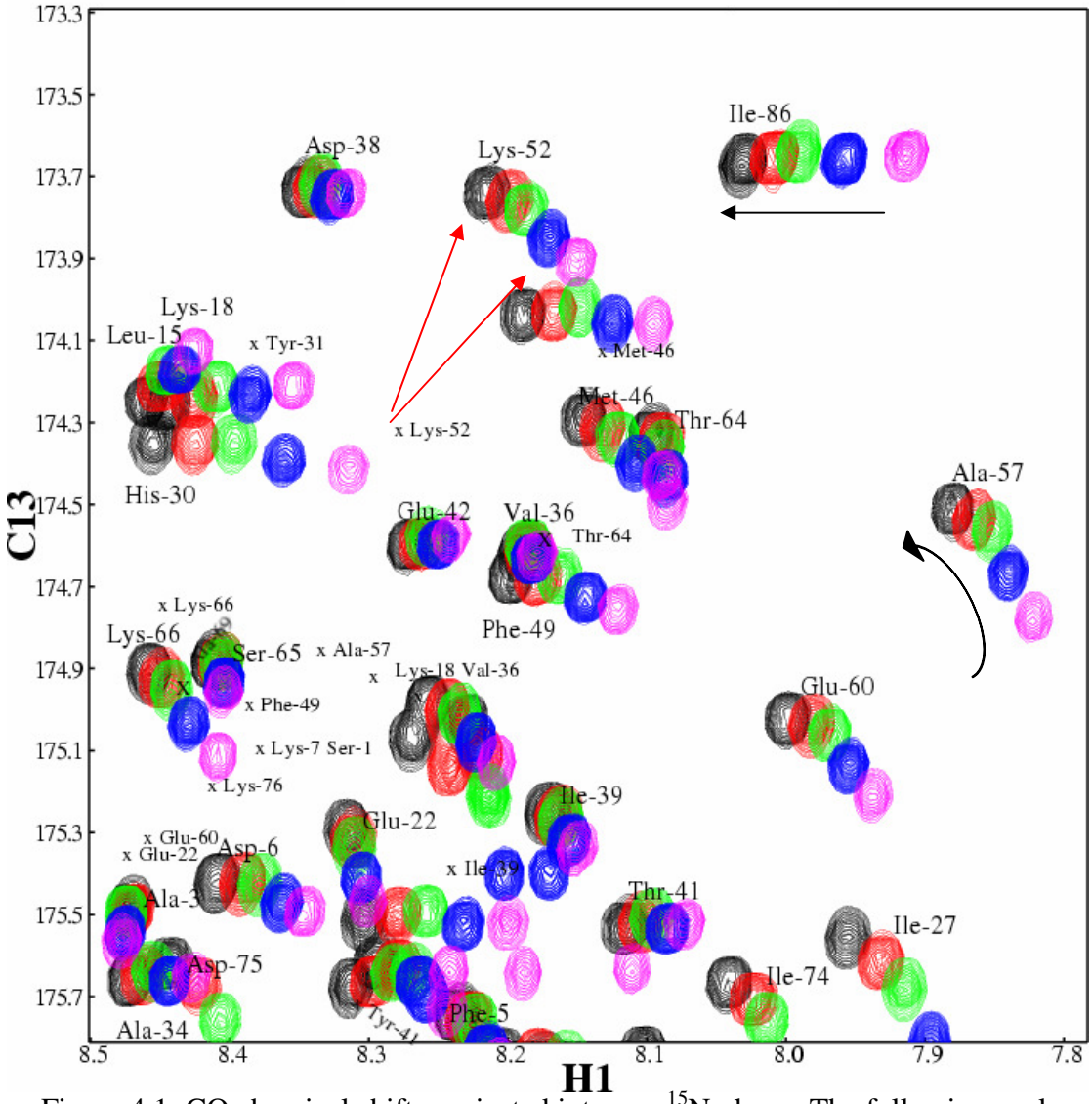


Figure 4.1: CO chemical shifts projected into one $^{15}$N plane. The following peak colours correspond to these different urea concentrations; black: 5 M, red: 4 M, green: 3M, blue: 2M and magenta: 1M. The different residues are denoted by there three-letter code and number in ACBP's sequence, with larger font compared to an "x" and Res-#, which denotes the location of that amino acids random coil value. Arrows indicate the movement of a particular amino acid during the urea titration; the two red arrows indicate Lys-52 movement passed its random-coil value.

Figure 4.2 and 4.3 show the secondary chemical shifts for $C^{\alpha}$ and CO, where again the random coil chemical shift values from Schwarzinger et al. were used. Figure 4.2 shows that there still exist offsets from random coil values at 5 M urea in the areas of helix A4, A1 and A2 in the native structure. The region of A4 is, as was also the case for the acid denaturation, the segment of the peptide sequence that exhibits the largest divergence from random-coil, followed by A1 and A2. As can be seen for several residues, the chemical shifts go pass the random coil value, shifting from positive to negative chemical shift differences, see for example residues 10, 11, 22, 45 and 78 to 82. Some segments of the peptide chain seem, however, not to change and might be considered to represent the unstructured chain, e.g. residues 13-20 and 38-44, but again the systematic offset should give rise to concerns.

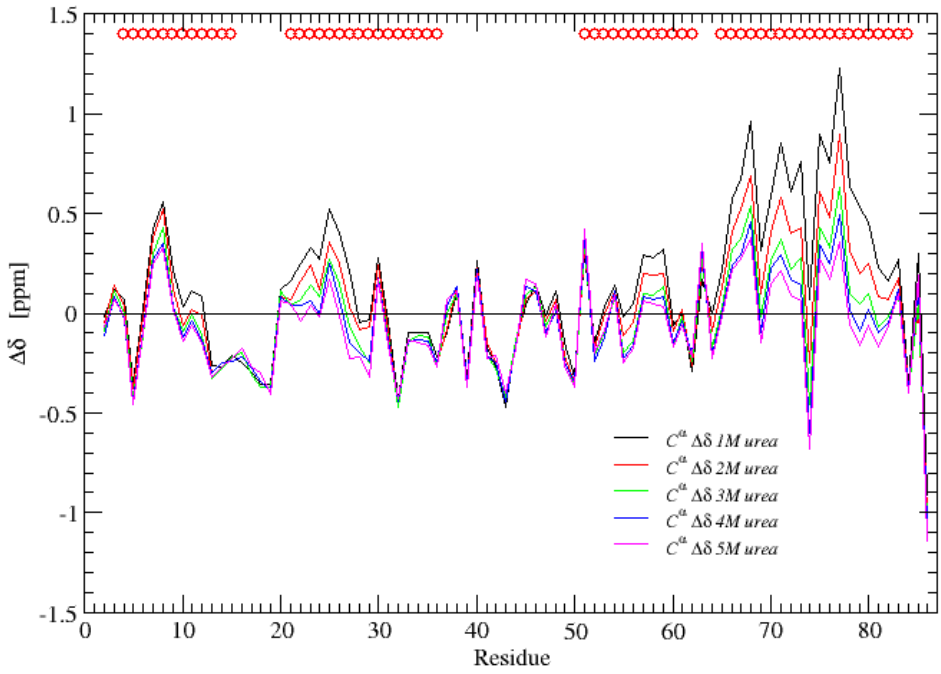


Figure 4.2: $C^{\alpha}$ secondary chemical shifts for urea concentrations from 1.1 to 5.1. black: 1 M, red: 2 M, green: 3 M, blue: 4 M and magenta: 5 M

A similar picture is seen for the carbonyl secondary chemical shifts, figure 4.3, where the peptide segment of helix A4 in native structure also has the largest offset from random coil and the largest change over the titration range, followed by A1. Interestingly, A2 and A3 move further away from random coil over the concentration range, whereas the loop region, especially around the start and end almost do not change at all. Again this can be due to the offset, as well as areas that might be regarded as unstructured.

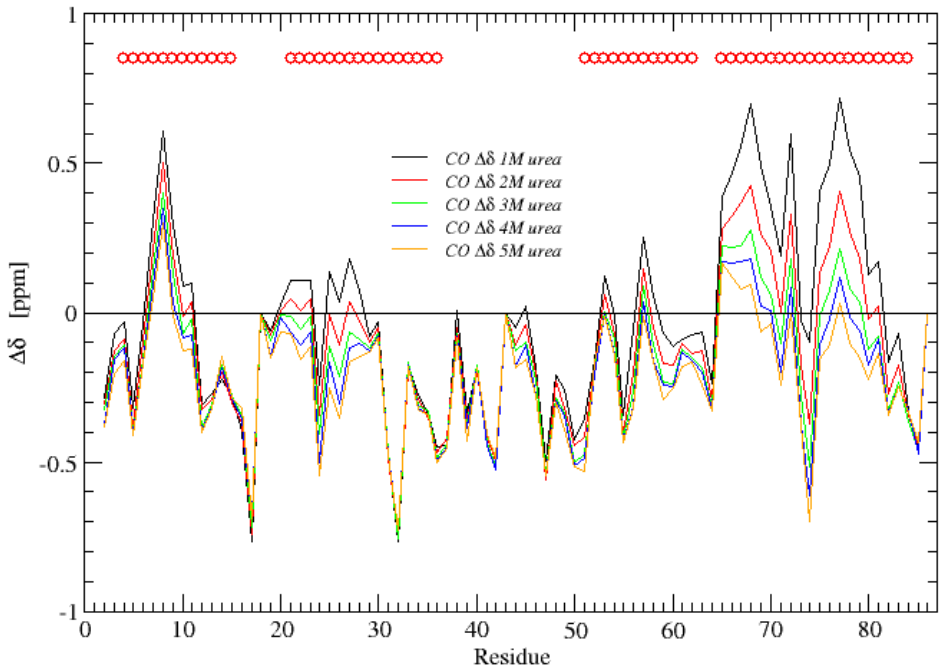


Figure 4.3: CO secondary chemical shifts for urea concentrations from 1.1 to 5.1. black: 1 M, red: 2 M, green: 3 M, blue: 4 M and yellow: 5 M

In Appendix C, figure C.1, a graph can be seen where the difference of $C^{\alpha}$ and CO chemical shifts between 1M and 5M urea as a function of residue is depicted. Indicating, that the largest changes over the titration range are seen in the region of A4, followed by A2 and A1. Note, there might exist a factor like binding, which could influence distinct areas of the peptide sequence differently, and hence make a straightforward interpretation impossible. Changes over the titration range seem to correlate relatively well between the two $^{13}C$ chemical shifts for the different segments of the polypeptide chain. It is such that the difference of CO chemical shifts from 1M to 5M urea depicted against those for $C^{\alpha}$ chemical shifts exhibit a correlation coefficient of 0.87, see figure 4.4.

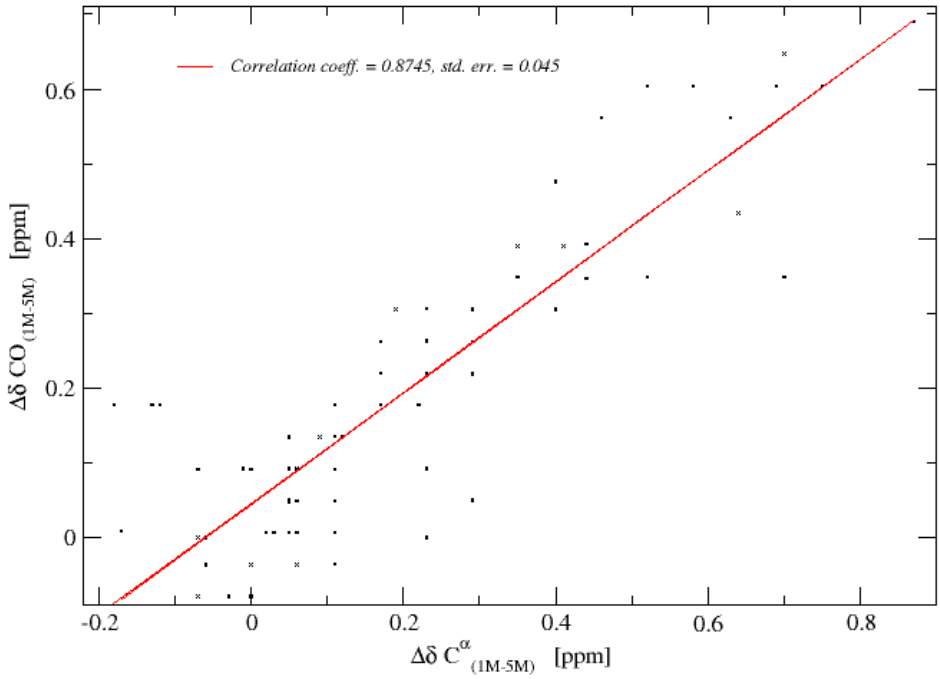


Figure 4.4: CO chemical shift differences (1M minus 5M urea) depicted against $C^{\alpha}$ chemical shift differences for the same interval. The correlation coefficient equals 0.87.

Several studies, as discussed in chapter 4, have indicated the presence of residual secondary structure in the presence of strong denaturant conditions of urea. But due to the apparent offset it cannot be clearly said, that there exist residual secondary structure at 5 M urea in the case of ACBP. It can, however, be concluded that the peptide segment corresponding to helix A4 in the native structure still changes over the titration range.
This offset can be interpreted as a binding effect of urea to the protein, as discussed in chapter 4. This behaviour, regrettably, makes it impossible to extrapolate the slope towards a 100 % denatured chemical shift distribution for ACBP.
If one measured the binding constant for urea to a random-coil model peptide, for instance the helical regions of ACBP, it might be possible to take the binding of urea to ACBP into account and extrapolate to random-coil values specific for ACBP.
Backbone chemical shift measurements on the peptide sequence comprising helix A3 in the native structure revealed that the chemical shifts in this peptide are very similar over the range of urea concentrations to the one of the full length protein measured here - except for some minor deviations in the N- and C- terminal residues (measurements made by BBK). So it seems that the intrinsic behaviour of the chemical shifts away from random coil values like Schwarzinger et al. are inherent even to smaller peptides comprising the helices. Therefore smaller peptides from ACBP's sequence cannot as such be used as "random coil" values.

In Appendix C figures of the behaviour of the amide proton and nitrogen chemical shifts during the titration experiment can be seen, figures C.2, C.3. The amide

nitrogen chemical shifts do not change much over the range of urea concentrations, but exhibit large off-sets up to ± 3 ppm from the random coil values of Schwarzinger et al., where the loop residues seem to be responsible for the largest positive off-sets. A feature that is not repeated for the amide proton secondary chemical shifts, figure C.3. The amide proton secondary chemical shifts show the same pattern with largest offsets from random coil in the regions of helices A4, part of A3, A2 and A1 in the native structure. These changes, however, are not huge over the interval form 1 to 5 M urea, but with the largest changes observed in the regions A4, A2 and A1.

### *4.2 The Guanidine hydrochloride denatured state*

ACBP was also denatured by guanidine hydrochloride (GuHCl). It is believed that the mechanism by which GuHCl disrupts the structure and unfolds a protein arises by changing the solvation properties of water as mentioned in chapter 4 [KPlaxc97]. Urea denaturation, on the other hand, is thought to arise both due to direct binding as well as a result of changed solvation properties. Here the unfolding of ACBP by GuHCl was investigated in order to compare different chemical denaturations of ACBP and reveal eventual differences in the unfolding of ACBP.
Again the backbone chemical shifts CO, HN, NH of $^{13}C$, $^{15}N$ double-labelled bovine ACBP in 10% $D_2O$, were measured. ACBP's concentration was approximately 0.5 mM, the same as the high concentration pH titration series. Investigations [WFiebe05] didn't reveal any dimerization effects of ACBP for denaturation in GuHCl, which made it possible to use a high concentration of the protein. The following concentrations were investigated: 2.5, 3.47, 4.06, 4.67, 5.15 and 5.51 M at a pH of 5.3 and every GuHCl concentration was verified by refractrometry [YNozak72].
As pointed out in chapter 4, GuHCl has a marked influence on random coil chemical shift of model peptides, as well as an evident effect on reference compounds. Therefore all chemical shifts were corrected for these effects. The chemical shift change of DSS was measured externally at O M and at 5.05 M GuHCl, under the same experimental conditions as the data collection, with a $^{13}C$-HSQC-spectrum. Due to the linear dependence of GuHCl on water and DSS, this gave rise to a correction factor for $^{1}H$ of 0.051 ppm $M^{-1}$ and by indirect referencing, 0.05 ppm $M^{-1}$ for $C^{\alpha}$ and 0.04 ppm $M^{-1}$ for CO. Interestingly, this is an effect of GuHCl on DSS and water and not an indirect effect of GuHCl due to instrumental/experimental set-up, as was the case for urea, were urea and water were in fast exchange hiding a change in the resonance frequency of water. GuHCl and water are under the investigated experimental conditions in slow exchange and the 5 labile protons exhibit one single peak at a frequency of 6.76 ppm in 5.05 M GuHCl.
Furthermore the secondary chemical shifts were corrected for the effect of GuHCl on the random coil chemical shifts, see chapter 4. As mentioned in the same chapter, carbonyl shifts were corrected for all amino acids in the peptide sequence of ACBP, where amino acids not investigated by Plaxco et al. [KPlaxc97] were approximated by the mean value of $\Delta\delta = -0.086 \pm 0.016$ ppm $M^{-1}$. Whereas, $C^{\alpha}$ secondary chemical shifts just were corrected for the known amino acids, due to their large residue specific dependence on GuHCl, $\Delta\delta = -0.038 \pm 0.044$ ppm $M^{-1}$. But these seven investigated residues still made up for roughly $^{2}/_{3}$ of the amino acids of ACBP.

Figures 4.5 and 4.6 show the secondary chemical shifts of $C^{\alpha}$ and CO at 3.47 and 5.5 M GuHCl. Both are corrected for the action of GuHCl on the random coil shifts, as well as on the referencing compound as described above. The secondary $C^{\alpha}$ chemical shift are almost all positive at 3.47 M and get smaller and some negative as the concentration rises to 5.51 M GuHCl, some thereby "surpassing" the random coil chemical shift, which in the case for the GuHCl titration series was based on Wishart et al. [DWisha95]. No apparent pattern, similar to the one found in acid denaturing series, is seen, see figure 4.5. The carbonyl shifts are almost exclusively negative at both concentrations and get more negative as the concentrations is raised, see figure 4.6. Again, no pattern is immediately evident, suggesting the same unstructured polypeptide chain.

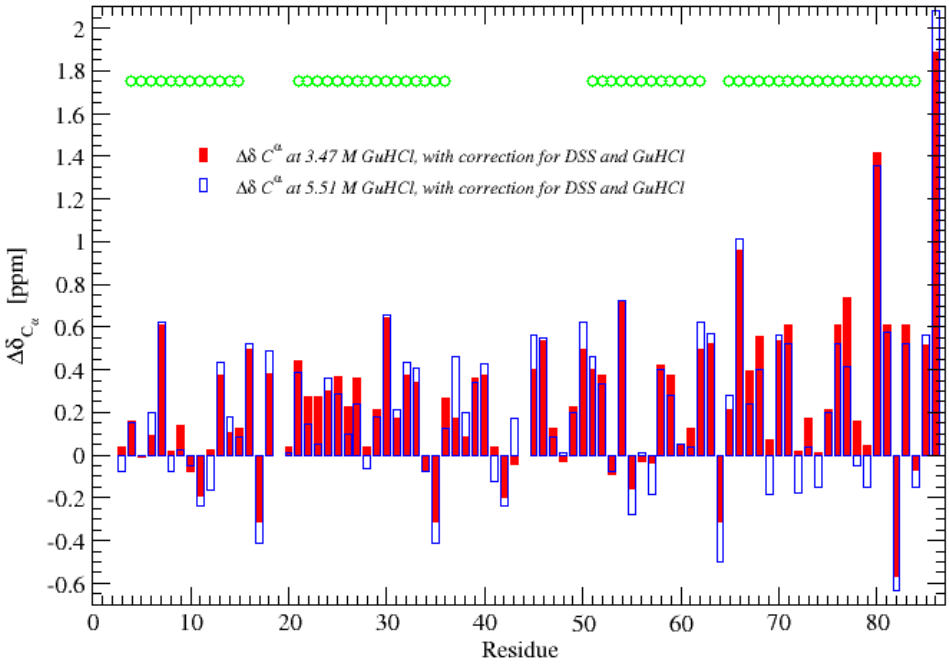


Figure 4.5: $C^{\alpha}$ secondary chemical shifts at 3.47 and 5.51 M GuHCl, red solid bars and open blue bars, respectively, as function of residue number. Corrected for the action of GuHCl on the random coil shifts, as well as on the referencing compound.

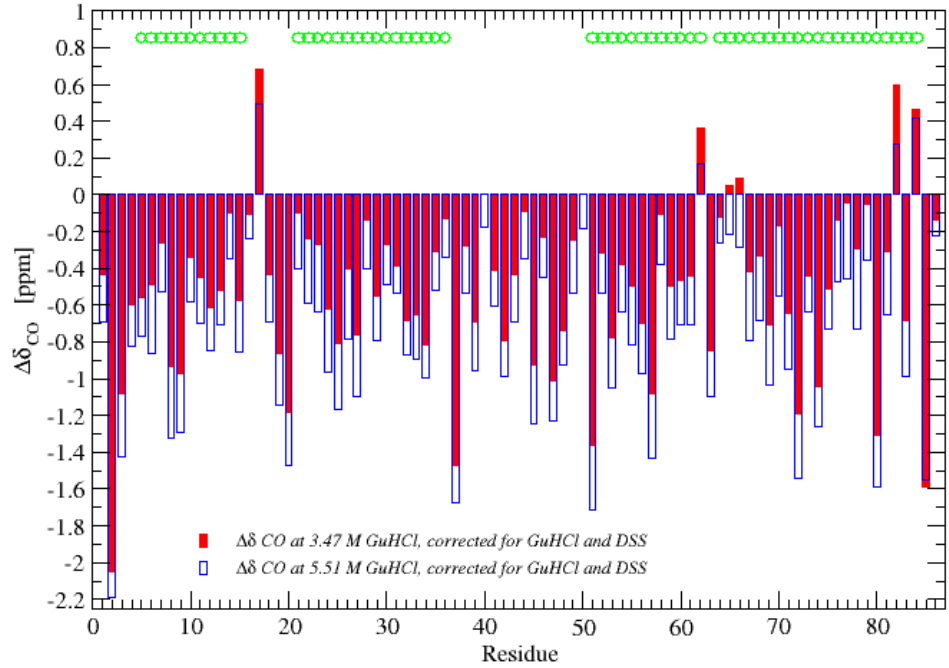

Figure 4.6: CO secondary chemical shifts at 3.47 and 5.51 M GuHCl, red solid bars and open blue bars, respectively, as function of residue number. Corrected for the action of GuHCl on the random coil shifts, as well as on the referencing compound.

Figures 4.7 and 4.8 show the chemical shift difference per molar GuHCl as found by linear regression for the aliphatic $C^{\alpha}$ carbon. In these calculations the x-axis had the same direction as was used for the pH-titration series, that is from most unfolded to less unfolded (5.5 M → 2.5 M). The error bars in figure 4.7 indicate the standard deviation from this slope for each residue and represent the raw data not corrected for the effect of GuHCl on the random coil values and its effect on DSS. Figure 4.8 shows the same data corrected for the effect of GuHCl. As is clearly seen, the chemical shift pattern between the two figures is quite dissimilar. The data in figure 4.7 encourages the perception of structural loss in the peptide segment of helix A4 in the native structure and figure 4.8 supports and strengthens this view, but also shows a reduction in the region A2. The data measured here supports the finding of residual structure in A4 and A2, but to a much lesser extent and not as obviously as the findings in the acid denatured state. For instance, the approximate change in $C^{\alpha}$ secondary chemical shift pr mole GuHCl is just 0.05 ppm, whereas the same change in the acid-unfolded state is roughly 0.4 ppm.

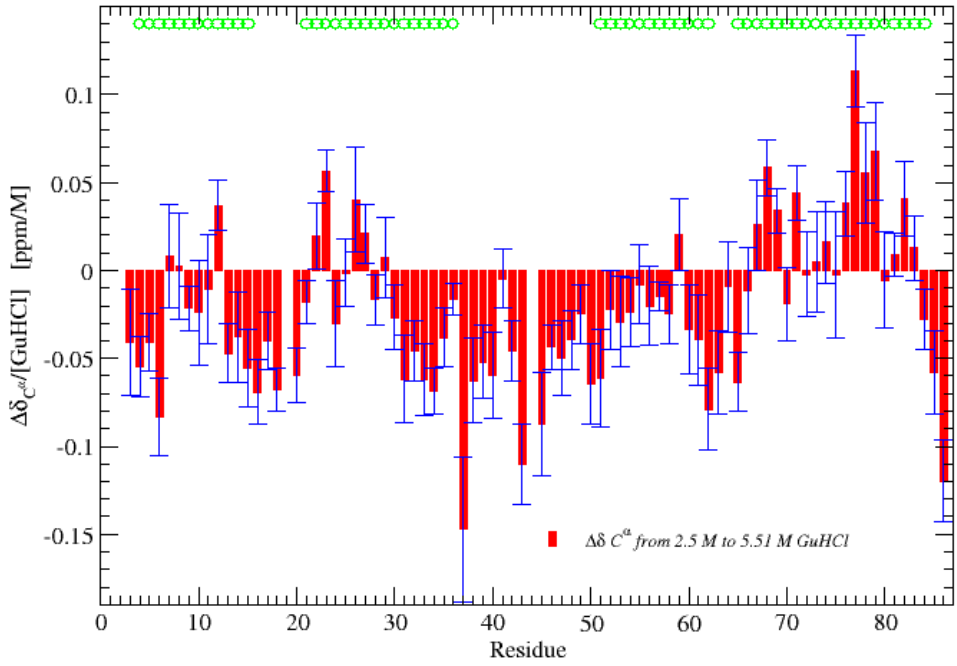


Figure 4.7: $C^{\alpha}$ chemical shift difference per molar GuHCl in the interval from 2.5 to 5.51 M with standard deviation, *not* corrected for the effects of GuHCl on the random coil shifts and DSS.

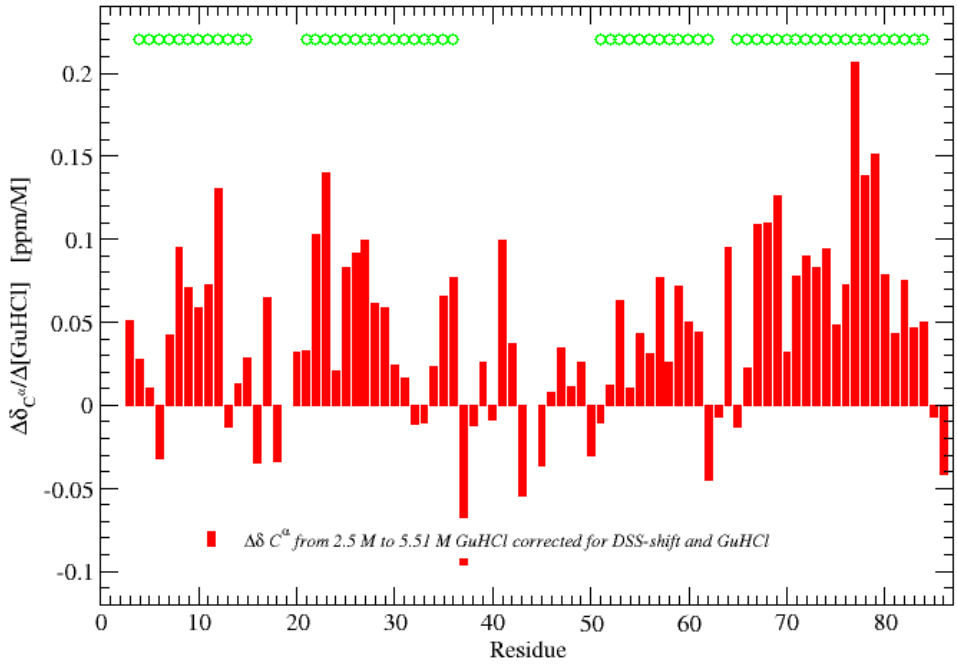


Figure 4.8: $C^\alpha$ chemical shift difference per molar GuHCl in the interval from 2.5 to 5.51 M, *corrected* for the effects of GuHCl on the random coil shifts and DSS.

The behaviour of the carbonyl shifts are actually quite different from those observed for the $C^\alpha$ chemical shifts. Figures 4.9 and 4.10 show the chemical shift difference per molar GuHCl as found by linear regression for the carbonyl shifts. The error bars indicate the standard deviation from this slope for each residue. Figure 4.9 shows the raw data, while figure 4.10 is corrected for the effect GuHCl has on the random coil values, as well as on DSS. The huge difference in appearance between the two figures makes the necessity of correction for GuHCl intrinsic effects on the polypeptide chain very clear. While the first figure may indicate apparent residual secondary structure in A2 and A4, figure 4.10 may just very vaguely indicate differences between the changes in chemical shifts over the investigated GuHCl concentrations. The changes in chemical shifts are fractionally more pronounced in the first half of A2, compared to the surrounding loops and helices. A very small difference compared to the surrounding residues can also be observed for the last two-third of helix A4.

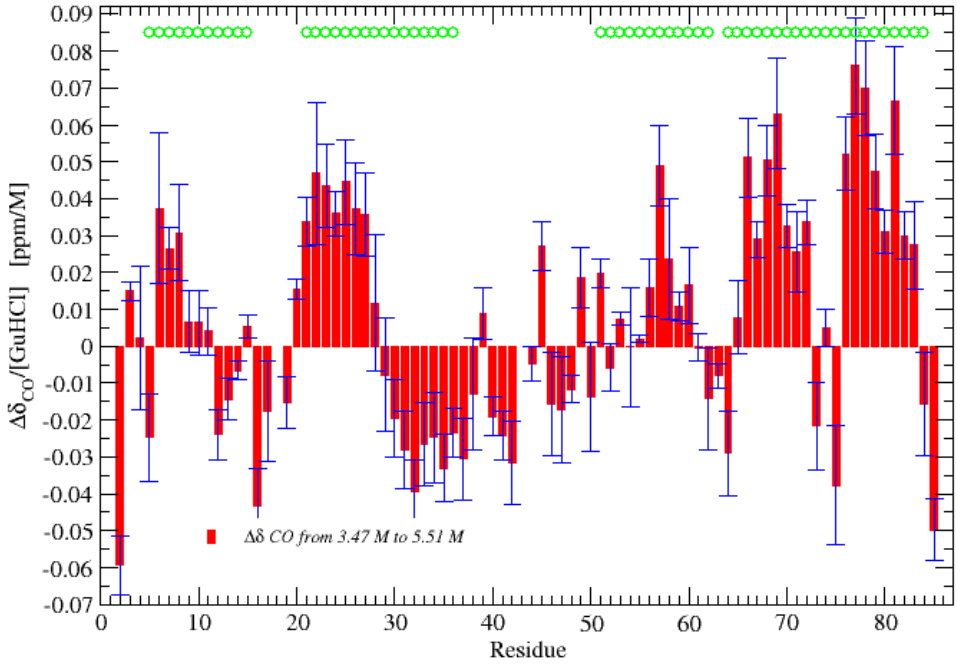


Figure 4.9: CO chemical shift difference per molar GuHCl in the interval from 3.47 to 5.51 M with standard deviation, *not* corrected for the effects of GuHCl on the random coil shifts and DSS.

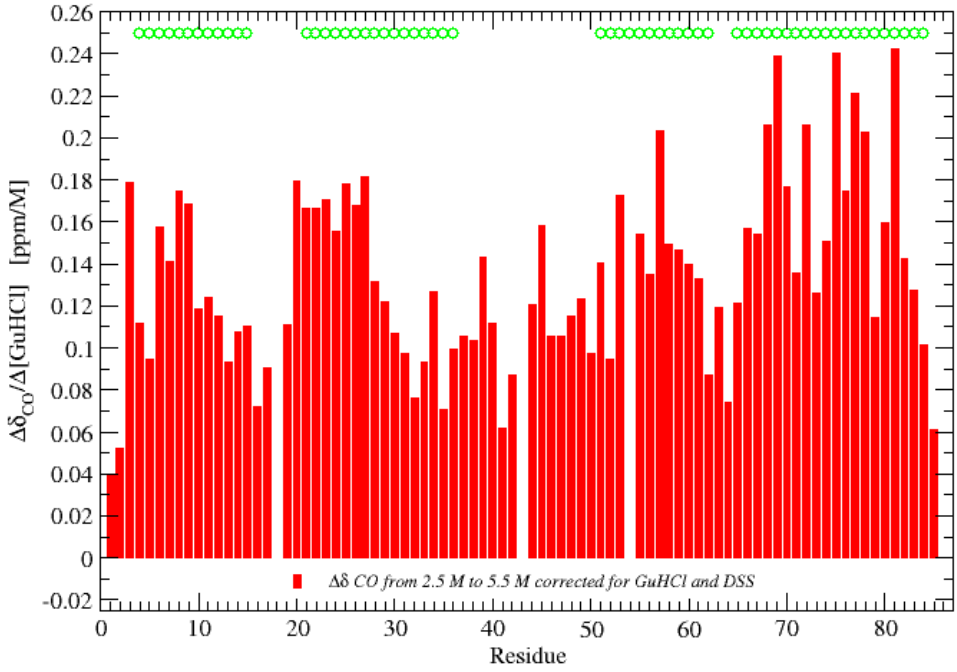

Figure 4.10: CO chemical shift difference per molar GuHCl in the interval from 2.5 to 5.51 M, *corrected* for the effects of GuHCl on the random coil shifts and DSS.

This striking difference between $C^{\alpha}$ and CO chemical shifts is not observed under the other denaturing conditions investigated. This could be an indication of a difference in denaturing mechanism and might even be attributed to a change in hydrogen-bonding interactions between the carbonyl oxygen's, the amide protons and the surrounding water, since the effect of GuHCl was believed to be one of changed solvation properties of the solvent [KPlaxc97]. Plaxco et al. also argues that the effect GuHCl has on the chemical shifts is not simply an effect of increased ionic strength, since sodium chloride at high concentration does not affect proton chemical shifts the way GuHCl does.
As mentioned in chapter 2, the unfolding/folding pathway of CI2 exhibits a single rate-determining transition state ensemble for folding and unfolding [VDagge03]. Chymotrypsin inhibitor 2 (CI2) unfolding by guanidinum chloride (6.4 M) showed most of the nuclei having chemical shifts close to random coil values except for two short peptides segments of a total of 10 residues, suggesting residual structure in a otherwise highly unfolded protein [SKazmi01]. MD-simulations support the findings of an expanded poorly structured denatured state with residual native helical structure in the denatured state of CI2. But CI2 seems to have much less pronounces residual structure in the GuHCl denatured state than the data for ACBP suggest (10 residues compared to the two regions A4 and A2 in ACBP).
Previously the backbone $^{15}N$ and $^{1}H^{N}$ chemical shifts of a mutant (I86C) of ACBP were investigated in GuHCl from 1.9 M to 4 M, indicating no cooperative transitions. However, these measurements were not corrected for the effects of GuHCl on the random coil values [KTeilu02]. The carbon resonance $C^{\alpha}$, $C^{\beta}$ and CO were evaluated at 1.9 M and revealed small deviation from random coil values, indicating small amounts of residual structure, but were again not corrected for the effect of GuHCl. The results here strengthen the view of residual structure in the peptide segments comprising helix A4 and A2 of the native structure even under strong denaturant conditions.

# 5 Assessing the ensemble of structures representing the denatured state

NMR-data obtained of the denatured states of macromolecules comprise of an average over a broad range of structures and it is hence, not possible to deduce something about the structures given rise to the experimental data without the use of computational approaches. That is, standard structure determination procedures cannot be applied to the denatured state.
Simple folding models, assuming that only interactions of the native state are favourable and ignoring non-native interactions, can predict folding rates, distribution of transition state ensembles and structures of the native state for small proteins relatively well [DBaker00]. These models are based on the assumption that the general path of the polypeptide chain during folding is determined by its topology rather than inter-atomic interactions [EAlm99].
Computational approaches on unfolded states have previously been implemented, where experimental data are compared to averages calculated over ensembles of structures [WChoy01]. Experimental data like paramagnetic relaxation enhancement have been use as distance restraints in computer simulation in order to determine the conformational ensembles representing the denatured state of ACBP. These simulations suggest the interaction of N and C-terminal parts of the protein sequence in the denatured state [SKrist05]. Paramagnetic relaxation enhancement derived distance restraints were also enforced on the average distance calculated across simulated ensembles, indicating the presence of residual structure and long-range interaction in the denatured state of ACBP [KLLars04].
The basic idea for the computational approach used here, is a two-stage approach were the experimental data are compared to averages calculated over an ensemble of structures. First an appropriate ensemble of initial structures is generated. This ensemble is generated by molecular dynamics simulations, where the equivalence between time and ensemble averages in sufficient long simulation is exploited. Different dihedral ($\varphi$, $\psi$) restraints on different areas of the unfolded structure of ACBP are applied, trying to encompass different aspects of the experimental data. For those structures, 140.000 in total, chemical shift data are calculated by the semi-empirical computer program SHIFTX [SNeal03], which again are used as restraints in Monte Carlo simulations, where the final ensemble is found by an energy minimization between the experimental and calculated chemical shift data. I.e. the initial ensemble of 140.000 structures is sampled by Monte Carlo simulations, which represent the second stage of the computational approach.
One problem of this approach is that the right ensemble comprising the experimental data, and hence simulating reality, is only found if adequate structures are present in the initial ensemble.

## *5.1 Molecular Dynamics Simulations*

Molecular Dynamics Simulations, MD-simulations for short, can be used for theoretical studies of biological systems. MD-simulations calculate time dependent behaviour and can hence give detailed information on fluctuations and conformational changes of for instance proteins. Molecular Dynamics Simulations produce information such as the systems atomic positions and velocities, were a time series yield an ensemble of structures, which exhibit the same thermodynamic state.

The theory behind Molecular dynamics simulations is based on Newton's second law, and yields position, velocities and acceleration of each particle. From an initial state and with the potential energy function the trajectory for the system can be calculated. The potential energy function is rather complex for large systems, and must therefore be solved numerically. Several algorithms exist for the integration of the equations for motion; here the Leap-frog algorithm (velocities and position are not calculated at the same time) were used in the simulations.

### *5.1.1 CHARMM Force Field*

The potential energy function, or force field, is a compromise between accuracy and computational cost (with respect to ab initio methods), and is often calibrated against experimental results and quantum mechanical calculations on small model compounds. A force field does not allow for changes in electronic structure, as bond making or breaking, as compared to quantum mechanical methods. For the simulations of unfolded ACBP the CHARMM force field (Chemistry HARvard Molecular Mechanics) was used. This potential energy function is calculated as a sum of internal terms ($E_{bonded}$) and external terms ($E_{non\text{-}bonded}$), equation 5.1. The first describes bonds, angles and bond rotations in the molecule, while the second represents the non-bonded atoms and atoms separated by three or more covalent bonds.

$$V(R) = \underbrace{E_{bonded}}_{E_{bond-stretching}+E_{angle-bending}+E_{bond-rotation}} + \underbrace{E_{non-bonded}}_{E_{electrostatic}+E_{van-der-Waals}}, \qquad 5.1$$

where R is the atom position.

$$V(R) = \sum_{bonds} K_b(b-b_0)^2 + \sum_{angles} K_\theta(\theta-\theta_0)^2 + \sum_{torsions} K_\phi[1-\cos(n\phi)] + \sum_{i=1,j=i+1}^{N}\left(\frac{q_i q_j}{Dr_{ij}}\right) + \sum_{i=1,j=i+1}^{N}\left(\frac{A_{ij}}{r_{ij}^{12}} - \frac{C_{ij}}{r_{ij}^{6}}\right) \qquad 5.2$$

*V(R)* is a function of the position of N particles and the first term models the interaction between pairs of bonded atoms via a harmonic potential, where the energy increases as the bond length *b* deviates from a reference bond length $b_0$ and where $K_b$ is a force constant, which depends on the type of atoms involved. The second term describes in the same way by a harmonic potential the alteration of the bond angles from an ideal value $\theta_0$, while the last of the bonded terms is modelled by a periodic function describing how the energy changes as a bond rotates (torsions), see equation 5.2.
In addition the CHARMM force field contains two terms representing an interaction based on the distance between atoms separated by two bonds (the Urey-Bradley term) and a term used to preserve planarity and chirality (the improper dihedral term).
The two non-bonded terms represent the electrostatic and van der Walls interactions of the atoms. The electrostatic interaction is given by the Coulomb potential, where *D* is the effective dielectric function and *r* is the distance between the two charges. The Van der Waals interactions are generally described by the Lennard-Jones 12-6 potential. In order to simplify calculations a fixed set of atoms types is used, e.g. an aliphatic carbon atom in sp3 bonding situation differs from a carbon in a ring, minimizing the number of possibilities. To facilitate faster computations a pair-wise additive approach is used as well, meaning a pair of atoms do not feel the interaction

energy of the other atoms in the systems. This leads to the neglect of certain polarization effects, for instance pK shifts of ionisable amino acid side chains induced by the electric field of the whole protein.
The solvent has a huge influence on biological molecules, but is just treated implicitly in the present calculations. One of the most significant effects of the solvent on the structure is screening of electrostatic interactions, and the simplest way of including its effect is by a distant dependent effective dielectric constant $\varepsilon_{eff}r$ (as opposed to the vacuumpermittivity $\varepsilon_o$). Here an excluded volume Gaussian solvation model (Lazaridis) is used [TLazar99], which assumes that the solvation free energy of a molecule is a sum of group contributions. These are determined from small model compounds. The solvent model is also called the Effective Energy Function 1 (EEF1).

### *5.2 Monte Carlo Simulations*

In a model where a change does not occur in a known way, but in a stochastic manner, it is possible to track this change with Monte Carlo Simulations. The next simulation will not yield the same result, but several will be similar within a margin of statistical error. For the study a simple Ising model, known as Metropolis importance sampling, was used. In this model the transition rate between two states is given by the Metropolis form:

$$W_{n\to m} = \tau_0^{-1} \exp\left(-\Delta E / k_b T\right), \qquad \Delta E > 0$$
$$W_{n\to m} = \tau_0^{-1} \qquad \Delta E < 0 \qquad (5.3)$$

Where $\Delta E$ is the energy difference between the two states *n* and *m*, $k_b$ is the Boltzmann factor, T the temperature and $\tau$ is the time required to attempt a transition, set to unity in this case. The algorithm is implemented simply by choosing an initial state (ensemble of structures). Next a site *i* is chosen (new ensemble with one structure changed) and $\Delta E$ calculated, which results if the new state is accepted. A random number *r* is generated, such that $0 < r < 1$. If $r < \exp(-\Delta E/k_b T)$, the new state is accepted, then a new site is chosen and $\Delta E$ calculated again. In this study the energy of an ensemble of calculated chemical shifts is compared, i.e. minimized against experimental chemical shift values:

$$\Delta E = \lambda(\delta^{\exp} - \delta^{calc})^2, \qquad \lambda = 1/a \times b \qquad (5.4)$$

$\lambda$ is a force constants for the particular chemical shifts, a factor calculated from the average of the experimental shifts (*a*) and a RMSD (*b*) for each of the calculated shifts obtained from the correlation coefficient between observed and calculated shifts on a test data set [SNeal03] (list of used force constants can be seen in Appendix B, table B.1). $\delta^{exp}$ and $\delta^{calc}$ are the chemical shift for the individual residues from the experimental and calculated data, respectively. In our scheme the energy is evaluated in a certain temperature interval until steady state is reached at each temperature. In practice a finite number of energy minimization for each temperature step is used (Monte Carlo steps). Several Monte Carlo simulations will not yield exactly the same result, i.e. the same ensemble of structures, but will be similar within a margin of statistical error.

### *5.3 SHIFTX*

The calculated chemical shift data was created on the basis of the program SHIFTX [SNeal03]. The program calculates the diamagnetic $^{1}H$, $^{13}C$ and $^{15}N$ chemical shifts for both backbone and sidechain atoms of proteins. Here the simulated structures derived from the MD simulations were used as input structures. The program predicts the chemical shifts from atomic coordinates by using classical and semi-classical equations for ring-currents, electric field, hydrogen bond and solvent effects as well as pre-determined empirically derived chemical shift hypersurfaces. The chemical shift hypersurfaces were created via a database of protein chemical shifts and high-resolution X-ray structures and describe effects such as nearest neighbour effects, secondary structure, sidechain orientations and dihedral angles, which are difficult to express analytically or predict classically. For folded proteins the program achieves very good correlations between calculated and observed shifts, making the program applicable for structure refinement in NMR (Correlation coefficients and RMSD for each atom type can be found in Appendix B, table B.1).

### *5.4 PALES*

The program PALES [MZweck00] can be used for the analysis of residual dipolar couplings, and mainly simulates the magnitude and orientation of a sterically induced alignment tensor from a solutes three-dimensional structure. PALES makes a systematic search of the solutes orientations that get obstructed by the alignment media and calculates the averages of all individual alignment tensors for the remaining non-obstructed molecules. In the PALES program it is assumed that alignment occurs in a liquid crystaline phase where no major attractive or long range repulsive interactions take place between the solute and the obstructing particles, i.e. only steric alignment. PALES calculates/predicts residual dipolar couplings (RDC) from pdb-files, and uses experimentally derived dipolar couplings as start values.

# 6 Molecular Dynamics and Monte Carlo Simulations results

In order to evaluate the chemical shift data obtained in the acid denaturing titration series Molecular Dynamic and Monte Carlo simulations where performed. The experimental data indicated the formation of secondary helical structure, see chapter 3. It is not believed that this residual secondary structure would appear in ordinary Molecular Dynamic simulations. It is therefore necessary to introduce secondary structure by means of restraining φ, ψ angles to appropriate values for helix. With Molecular Dynamics simulations (MD) a set of 140.000 structures were constructed with different extent of restrictions in different parts of the peptide sequence, including 10.000 structures with no restriction at all, an ensemble that as well served as random-coil values for the calculated data. This large ensemble thereby also contains structures that represent unfolded ACBP. For all of these structures the theoretical chemical shift (δ) were calculated by the program SHIFTX [SNeal03]. The approach used here is a two-stage approach, where the first part consists of the production of a large ensemble of 140.000 structures. In the second stage of the approach the large ensemble is sampled with simulated annealing (SA), a Monte Carlo method that enables "uphill" jumps out of local minima, see chapter 5 and equation 5.3. This Metropolis procedure generates an ensemble at some specific temperature; the SA approach "melts" the system at this temperature until no further changes occur, then proceeding to a lower temperature [SKirkp83]. At each temperature the simulation must continue long enough for the system to reach steady state, i.e. no changes in the energy happen, see chapter 5, MC-simulation. This energy is governed by the difference between experimental chemical shifts and calculated chemical shifts. The MC-simulations therefore produce a sub-ensemble that describes the experimental data. The found sub-ensemble is subsequently analysed, among other properties, for secondary structure contents.

## *6.1 Molecular Dynamic Simulation: Construction, energy minimization*

The initial unfolded structure of ACBP consisted of an all-atom ACBP peptide sequence, i.e. which contains all heavy atoms as well as hydrogen atoms bound to polar (O, S, N) heavy atoms. In order to construct the start ensemble of the 140.000 structures, 14 different MD-simulations were made, each sub-run comprising the restraining of different areas of the four α-helical regions of the native structure of ACBP. The different segments of the peptide sequence were restrained by forcing φ - and ψ - angles of specific residues to uphold values close to those observed for helices. The energy of each initial structure was minimized by methods of Steepest Descend and Adopted Basis Newton-Raphson. The MD simulations with the CHARMM19/EEF1 model were run for 40 ns and made at 573 K. The protein was previously heated from 0 to 573 K in steps of 10 K. During the simulation 10.000 structures were saved (every 2000 steps). For these pdb-files were calculated and used as input for SHIFTX.

For each MD-run both φ and ψ dihedral angles were constrained to values in the vicinity of helix as given by the Ramachandran plot (an example of a restraint input can be seen in Appendix B, table B.2). In order not to constrain the different parts too tightly, thereby forcing the peptide segment into a α-helix with something resembling

stable tertiary connections, the width of the angles, which the structures were allowed to adopt and the penalty for violation (Force), were optimized so that the resulting structures yielded an approximate α-helical content of 30%. The secondary structure contents were calculated with the program DSSPcont [WKabsc83], [CAnder02] over an average of 1000 structures. Figure 6.1 shows α-helical content, as calculated by DSSPcont, as a function of the force, for several restraint residues over an ensemble of structures from MD simulation where the dihedral angles φ,ψ were –62 ± 10 and –41 ± 7.5. Figure 6.2 shows the α-helical contents as a function of the width for the same residues at a force of 2.0 kcal/mol. In these simulations the four mid-residues in each helix were constrained.

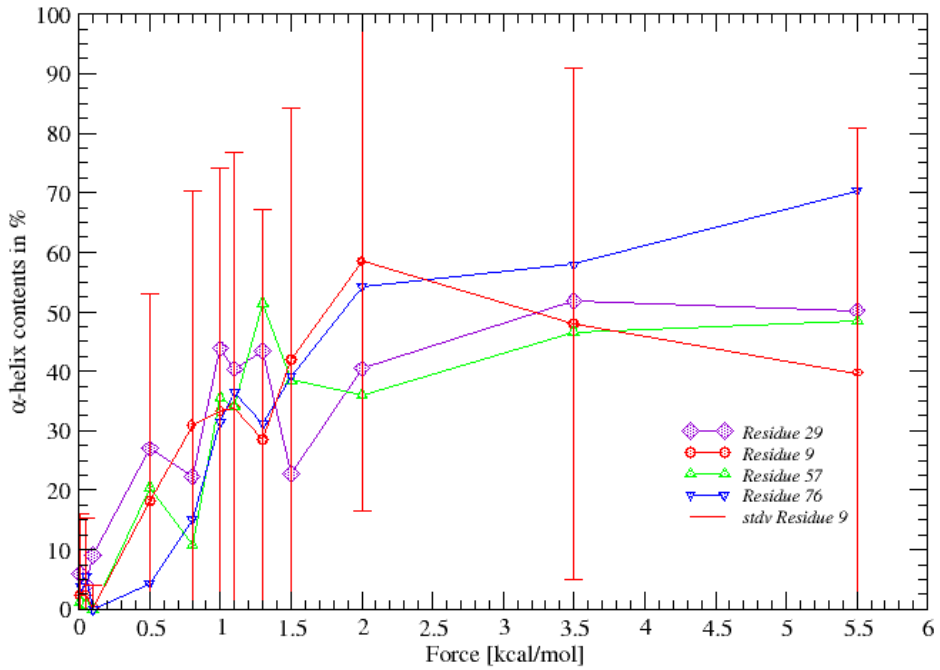


Figure 6.1: α-helical contents versus force for certain residues as found by DSSPcont. The four mid-residues in each helix of the native structure were constrained with dihedral angles φ,ψ [–62 ± 10] and [–41 ± 7.5]. The standard deviation for residue 9 is shown.

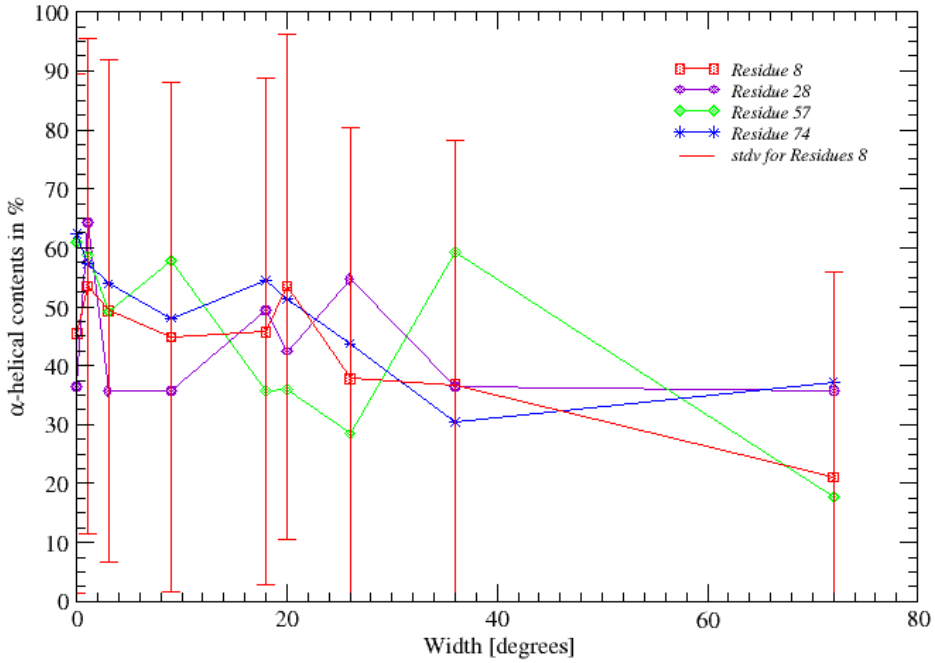


Figure 6.2 α-helical contents as a function of the width for φ[a] for certain residues as found by DSSPcont. The four mid-residues in each helix were constrained, and the force in each simulation was 2.0 kcal/mol.

[a]: the widths of φ,ψ were simultaneously increased proportionally ([0,0], [1,0.5], [3,2], [9,6], [18,12], [24,16], [36,24], [72,48])

All restraints were due to the above optimization consequently set to –62 ± 45 and –41 ± 30 for φ and ψ respectively, while the force was held at 2.0 kcal/mol, in order to obtain an approximate α-helical content of 30%. A picture of the secondary structure contents at φ,ψ [–62 ± 10] and [–41 ± 7.5] and a force of 2.0 kcal/mol can be found in Appendix B, figure B.1. The different areas that were constrained, in order to construct the start ensemble of 140.000 structures for a suitable representation of unfolded ACBP, can be seen in table 6.1.

The residues chosen to be restrained were selected on the bases of the chemical shift pattern obtained in the experimental data for $C^{\alpha}$ and CO chemical shifts. For instance, the first and last residues in each helix of the native structure were not in all cases restrained, since they did not seem to change over the course of the pH-interval and did not deviate much from random coil values. That is, the experimental results from the NMR experiments were used as a guide to decide which dihedral angles should be restraint in the MD-simulations, see for instance figures 3.5 and 3.6.
The resulting pdb-files were used as input for SHIFTX to calculated theoretical chemical shifts. Examples of the average chemical shift as calculated by SHIFTX for 1000 structures where 4 residues in each helix were constrained can be seen for $C^{\alpha}$ and carbonyl chemical shifts in Appendix B, figures B.2 and B.3.

Table 6.1.

| *Restraint-bin* | *Helix* | *Residues* |
|---|---|---|
| *1* | *A4* | *aa66 - aa83* |
| *2* | *A2* | *aa22 - aa35* |
| *3* | *A4 & A2* | *aa22 - aa35 & aa66 – aa83* |
| *4* | *A3* | *aa52 - aa61* |
| *5* | *A1* | *aa4 - aa14* |
| *6* | *A4, A2 & A3* | *aa22 - aa35, aa52 - aa61 & aa66 - aa83* |
| *7* | *½ A2* | *aa29 – aa35* |
| *8* | *¾ A4* | *aa66 – aa79* |
| *9* | *½ A2 & ¾ A4* | *aa29 – aa35 & aa66 – aa79* |
| *10* | *A4* | *aa65 – aa84* |
| *11* | *A2* | *aa21 –aa36* |
| *12* | *A4 & A2* | *aa21 –aa36 & aa65 – aa84* |
| *13* | *no restraints* | *-* |
| *14* | *½ A2* | *aa22 – aa26* |

The ensembles of the 140.000 structures hence include structures with helix in different parts of the peptide sequence. Each Restraint-bin of table 6.1 represents structures where a particular area of the peptide sequence 30 % of the time exhibits α-helical structure. I.e. 70 % of the time or rather 70 % of the structures, due to the equivalence between time and ensemble averages, exhibit other conformations. For a particular Restraint-bin the rest of the peptide sequence, apart from the residues restraint, do not represent specific structures as well. The start ensemble also includes at least 10.000 structures, which represent the unfolded peptide chain of ACBP.
In summary, the first stage comprised the construction of 140.000 structures of ACBP by 14 Molecular Dynamic simulations. In 13 MD-runs out of the 14, each generating 10.000 structures, specific regions of ACBP's sequence where constrained in order to yield an overall α-helical content of 30 %. For all 140.000 structures pdb-files where calculated and used as input for SHIFTX, thereby generating calculated chemical shift data for 140.000 structures.

### *6.2 Monte Carlo simulations*

The second stage of the computational approach comprised the sampling of the 140.000 structures by simulated annealing. The simulated annealing algorithm is implemented by choosing an ensemble; in this study the simulated ensemble comprised 10.000 structures. The energy for this state is calculated, where the energy is the difference between the experimental and calculated chemical shift for each residue, see equation 5.4. The next step is the replacement of one structure of this ensemble with another from the ensemble of 140.000 structures produced by the MD simulations and the calculation of the energy for this new state. If the energy difference between these two states fulfils the scheme describe in chapter 5 the new state is accepted. This sampling is repeated until the system reaches steady state at each temperature and the energy is converged.
For $C^{\alpha}$, CO, $H^{N}$ and $N^{H}$ chemical shifts the Monte Carlo simulations were optimized varying the temperature interval in which the energy was minimized and number of Monte Carlo steps at each temperature. I.e. the energy at each Monte Carlo step was calculated as the difference between experimental chemical shifts and those calculated

for 10.000 structures picked out of the 140.000 structure large start ensemble. This resulted in the energy stabilizing and minimization of the difference between the experimental and theoretical chemical shifts. In Appendix B examples of a trajectory of the energy and the difference between experimental and calculated shifts for CO and $C^{\alpha}$ are shown, figures B.4, B.5 and B.6. The optimal temperature interval for both $C^{\alpha}$ and CO was found to be from 0.1 to 0.00001 in steps of 40, with 60 million Monte Carlo steps at each temperature.
The simulated ensemble size was set to contain 10.000 structures, in order to sample a sufficient ensemble size, but at the same time contain the amount of CPU time used and make calculations feasible.
The experimental chemical shifts were those obtained during the pH-titration experiments at low ACBP concentration from chapter 3. Due to the slow exchange between peaks from the unfolded and folded populations, all simulations are hence performed against the unfolded population.
The chemical shifts used in the energy minimization where secondary chemical shifts, since the absolute chemical shifts yielded a bias producing much more helix all over the amino acid sequence in order to minimize the energy. Since, the difference between the experimental and calculated data were shifted toward positive values all over the amino acid sequence, it seemed to be a general problem for the simulation. It was believed that this arose due to an offset between the experimental chemical shifts and the random-coil values for the calculated ensemble, i.e. Restraint-bin 13. In the Monte Carlo simulations this would lead to more helical structures and no structures from the ensemble, which represents the random coil state in order to compensate for the large positive shift. The difference between experimental values and an average of Restraint-bin 13 structures, as well as the difference between random coil values from Schwarzinger et al. [SSchwa01] and a calculated ensemble can be seen in figure 6.3. A graph of the difference between the absolute chemical shift of experimental and calculated values can be found in Appendix B, figure B.7. Figure B.8, also in Appendix B, shows the distribution between the different Restraint-bins, were it was noted that the ensemble comprised no structures that were totally random coil, i.e. from Restraint-bin 13. This of course was a strong indication that something in the energy minimization was wrong.

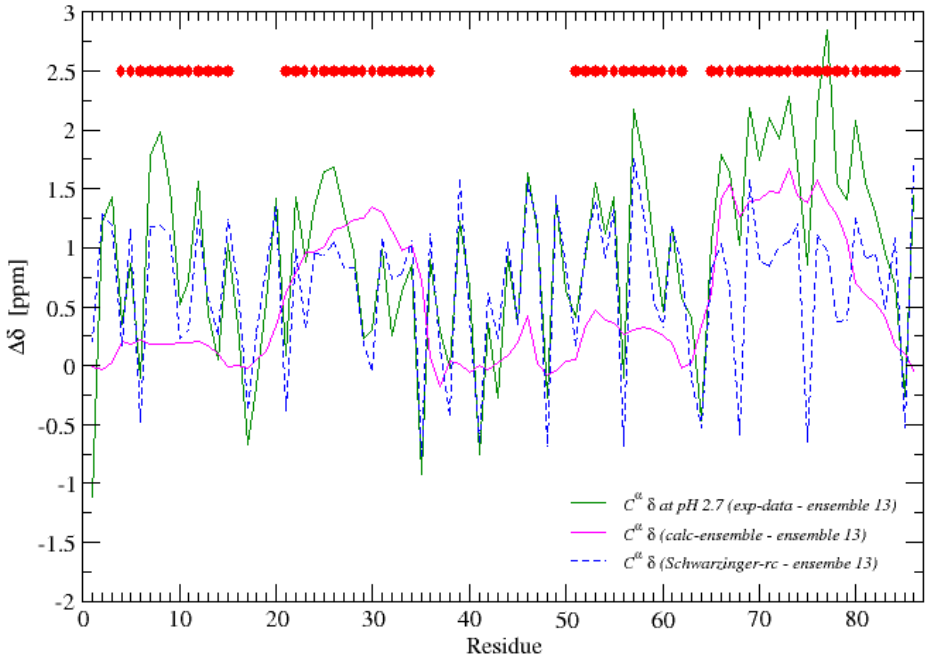


Figure 6.3: The difference between experimental values and an average of Restraint-bin 13 structures (green solid line), as well as the difference between random coil values from Schwarzinger et al. and an average of Restraint-bin 13 structures (blue dotted line). The solid line (magenta) represents the difference between a calculated ensemble and average of Restraint-bin 13 structures. The red circles denote the location of the four α-helices in the native structure of ACBP.

In order to compensate for this discrepancy the Monte Carlo simulations were performed on secondary chemical shifts. The experimental secondary chemical shifts were calculated by using the random coil values from Schwarzinger et al. at pH 2.3 [SSchwa01], whereas the theoretical calculated chemical shifts were hold up against the average chemical shift of the MD-simulation Restraint-bin 13 (see table 6.1). That is, a MD-run of the totally unfolded protein with no restraints at all.
Another difficulty in the simulations was the modelling of N and C-terminal residues. A much larger difference between the experimental and calculated values than observed for the rest of the amino acid sequence was seen and therefore those residues were removed from the MC simulations.
In summary, the second stage of the computational approach comprised the sampling of the 140.000 structures by simulated annealing, where the energy was the difference between the experimental and calculated chemical shift values. This yielded a final ensemble of 10.000 structures originating from the 14 Restraint-bins.

### *6.2.1 Monte Carlo simulations of pH 2.7*

The Monte Carlo simulations were performed for the four backbone chemical shifts measured by the NMR experiments, $C^{\alpha}$, CO, $H^{N}$ and $N^{H}$, i.e. where each nucleus by

itself was used as restraint for the simulation. I.e. is the energy difference between experimental and calculated chemical shifts were calculated for one nuclei species. The distributions between calculated values subtracted from the experimental chemical shift values over the amino acid sequence, varied substantially for the four nuclear species. The carbonyl shifts were shifted towards negative values along the sequence, figure 6.4, but with an average value of approximately – 0.0005 ppm. This however, is much better than the accuracy with which the peaks in the HNCO spectra can be set, which are roughly 0.01 ppm. The digital resolution for $^{1}$HNCO spectra was approximately 0.016 ppm (CO: 0.03 ppm) before zero-filling, see chapter 9.

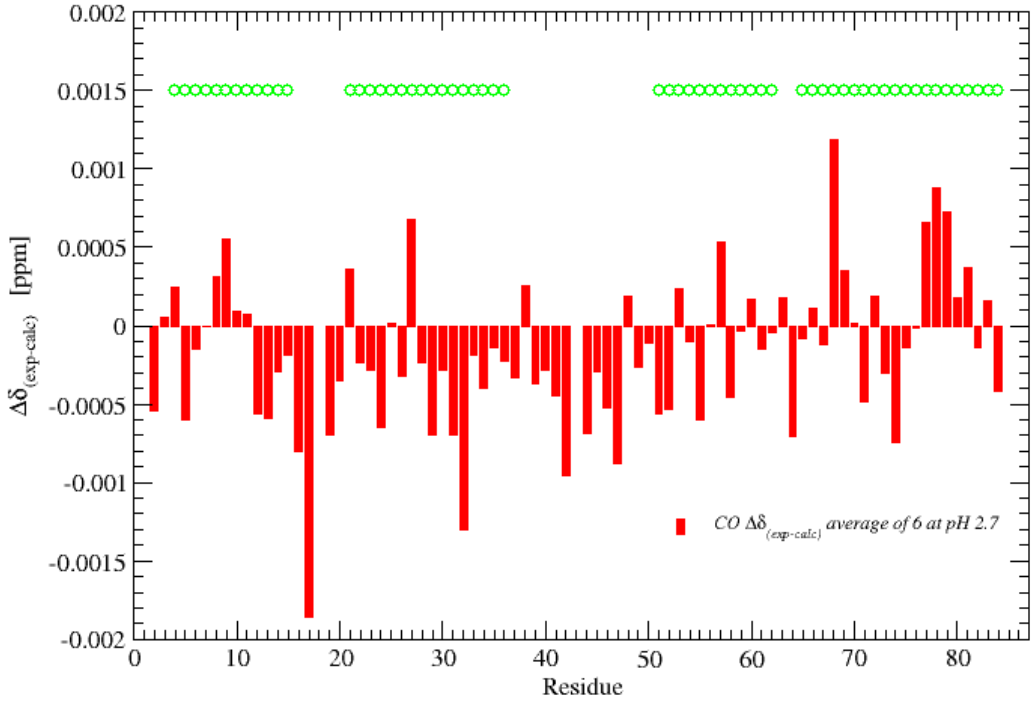


Figure 6.4: CO experimental secondary chemical shift values at pH 2.7 minus the calculated secondary chemical shifts, where the average of Restraint-bin 13 served as theoretical random-coil values for the calculated chemical shifts. The data represent an average of 6 Monte Carlo simulations cycles.

Unfortunately the data presented in figure 6.4 is not completely randomly distributed. Scattering of the same data in a histogram overlaid with a Normal distribution reveals that the spreading of the difference between experimental and calculated chemical shifts as a function of residue position is a little bit skewed, figure 6.5. But since the uncertainty with which the experimental peaks can be assigned in the experimental spectra are in the same order of magnitude or better than the average deviation of the simulated values from those data, this bias is believed to be of no consequence for the interpretation. The same data can be seen plotted in a Normal Probability and an auto-correlation plot in Appendix B, both illustrating a small deviation from randomness, figures B.9 and B.10.

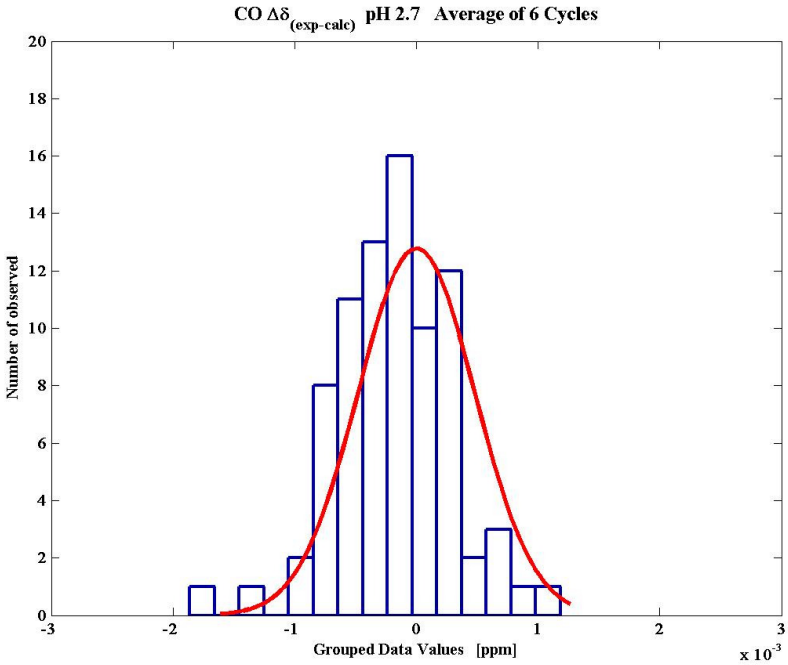


Figure 6.5: Histogram of CO $\Delta\delta_{(exp\text{-}calc)}$ data for pH 2.7, average over 6 Monte Carlo simulation cycles.

The amide nitrogen chemical shifts used as restraint in the MC-simulation had significantly larger differences than both $C^{\alpha}$ and CO between experimental and calculated chemical shifts values and were in the order of 0.1 ppm (see Figure B.11 in Appendix B). Furthermore, those simulations also exhibited an odd distribution between the different Restraint-bins, containing mostly structures from Restraint-bins 4, 5 and 6.
The deviation was not as large for the amide hydrogen chemical shifts, approximately – 0.05 ppm, but all residues were equally affected and the distribution was odd as well, with contributions mostly from Restraint-bin 6 and almost non from the random coil Restraint-bin (the distribution can be seen in figure B.12 of Appendix B). Due to these discrepancies and the nature of the experimental results for the $H^N$ and $N^H$ chemical shifts, it was decided that it was not worth pursuing these chemical shifts as restraints any further.

$C^{\alpha}$ chemical shifts had overall deviations between the experimental and calculated secondary chemical shifts of just around 0.0005 ppm, figure 6.6, which is an extremely good agreement compared to the certainty with which the $C^{\alpha}$ peaks can be assigned in the experimental spectra (HNCA), which is roughly 0.05 ppm. The agreement between the experimental and simulated data is much better, than it is possible to assign the peaks in the experimental spectra. The digital resolution for $^1$HNCA spectra was approximately 0.016 ppm ($C^{\alpha}$: 0.07 ppm) before zero-filling, see chapter 9. Therefore, once again, the fact that the differences along the amino acid sequence are not randomly distributed is ignored. Figure 6.7 shows the Normal probability plot for the data of figure 6.6, which in case of a random distribution should be evenly distributed around the straight line and exhibit no deflection at the end. Although not random, the deviation from a random distribution is very small. Figures B.13 in Appendix B shows the scattering of the same data in a histogram overlaid with a Normal distribution, while figure B.14 shows an autocorrelation plot.

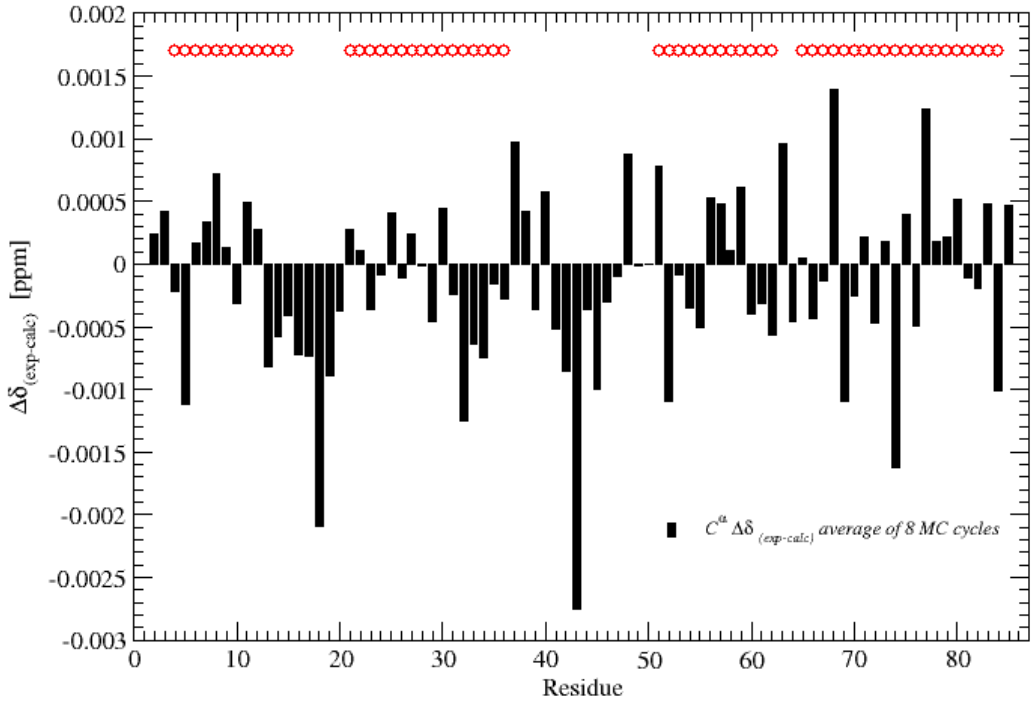


Figure 6.6: $C^{\alpha}$ experimental secondary chemical shift values at pH 2.7 subtracted from the calculated secondary chemical shifts. The data represent an average of 8 Monte Carlo simulation cycles.

Simulations were also made where both $C^{\alpha}$ and CO chemical shifts served as restraints. For these simulations the ensemble size was, exceptionally, chosen to encompass only 1000 structures due to the lengthiness of these simulations. Beforehand a simulation with an ensemble size of 10000 structures was run, and compared to a simulation containing only an ensemble size 1000 structures. This comparison revealed no major differences, neither for the secondary chemical shift values, nor for the ensemble distribution between the different Restraint-bins. Those simulations yielded also good correlations between experimental and calculated values in the order of 0.005 ppm for carbonyl shifts and 0.03 ppm for $C^{\alpha}$ shifts, figure 6.8. Strangely, the correlation for $C^{\alpha}$ shifts is not as good as it was for the simulations where the $C^{\alpha}$ chemical shifts were used as sole restraint. However, the distribution of the secondary chemical shifts (experimental minus calculated) for each residue remains similar to the ones observed in simulations with just one chemical shift used as restraint. The difference might indicate a difference in the information contained by the two datasets.

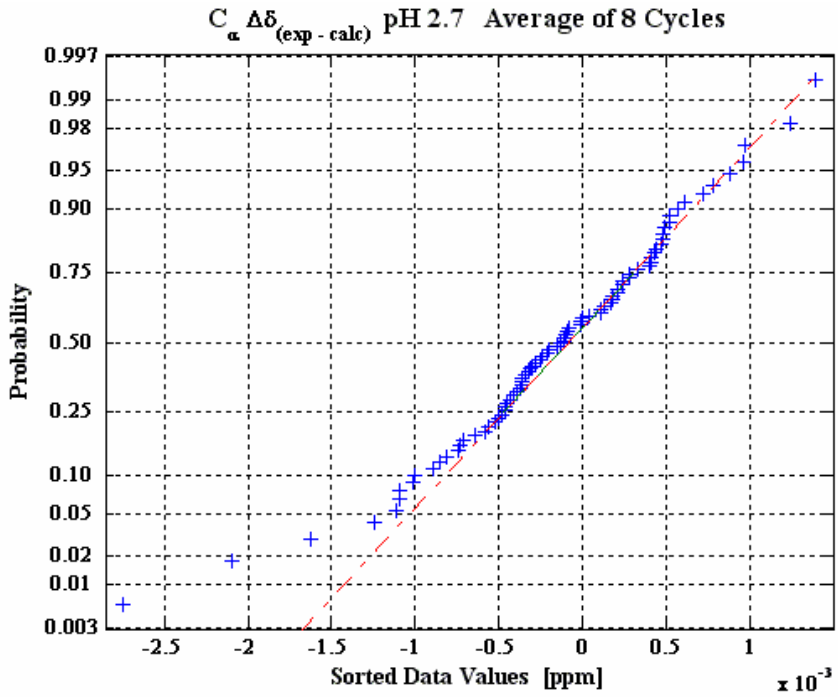


Figure 6.7: Normal Probability Plot for $C^{\alpha}$ $\Delta\delta_{(exp\text{-}calc)}$ pH 2.7, average of 8 Monte Carlo simulation cycles.

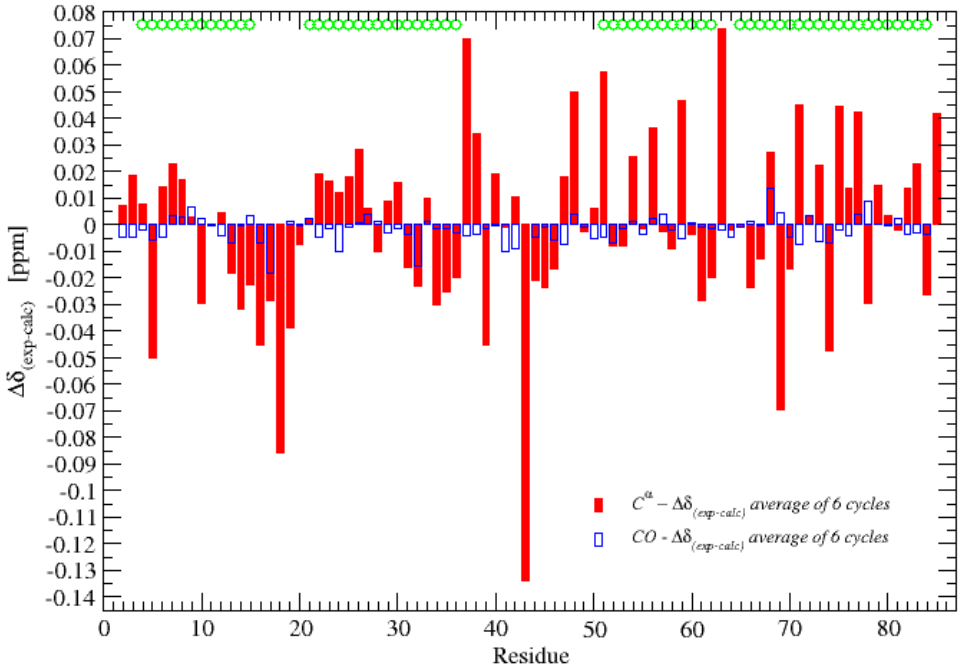


Figure 6.8: $C^{\alpha}$ (red) and CO (blue) experimental secondary chemical shift values at pH 2.7 subtracted from the calculated secondary chemical shifts. The data represent an average over 6 Monte Carlo simulation cycles where both $C^{\alpha}$ and CO chemicals shifts were used as restraints and made for simulations with an ensemble size of 1000 structures.

Looking at the distributions of the calculated ensembles between the different Restraint-bins, it was seen that regardless of which chemical shift was used as restraint for the Monte Carlo simulations, they are all approximately the same, figures 6.9a-9c.

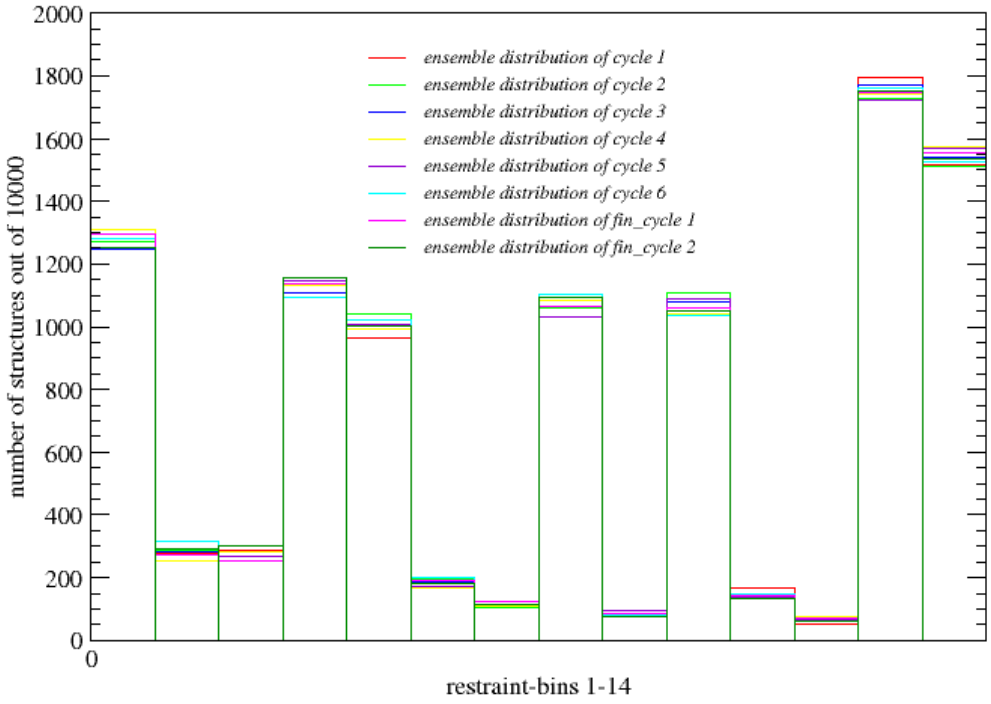


Figure 6.9a: Distribution for the ensembles found during MC-simulation, where $C^{\alpha}$ chemical shifts at pH 2.7 were used as restraint, between the different Restraint-bins of table 6.1. The number of structures in each Restraint-bin are out of a total of 10.000 possible structures for each Monte Carlo simulation cycle.

The MC-simulations minimize the energy between experimental and calculated chemical shifts values for an ensemble of 10.000 structures, were the start ensemble of 140.000 calculated structures served as a sampling pool. Among the 140.000 structures sub-ensembles with characteristics explained in table 6.1 exist. The original MD-simulations of the Restraint-bins had a probability for α-helix of just about 30 %, except for Restraint-bin 13, but the structures extracted from each Restraint-bin can represent a larger or smaller propensity.
From figure 6.9a it is seen that the final distribution contained roughly [12.5-13 %] of structures from Restraint-bin 1, [11-11.5%] from Restraint-bin 4, [9.5-10.5%] from Restraint-bin 5, [10-11%] from Restraint-bin 8, [10.5-11%] from Restraint-bin 10, [17-18%] from Restraint-bin 13 and [15-16%] from Restraint-bin 14. The remaining Restraint-bins contain less than 2-3 %. In other words the resulting ensemble contains approximately [40%] helix A4 at pH 2.7, while structures with helix A2 are represented at [27%]. Helix A1 and A3 are almost evenly represented with roughly

[10%] and [13%] respectively. It is also noted that the amount of random coil is roughly [18%].

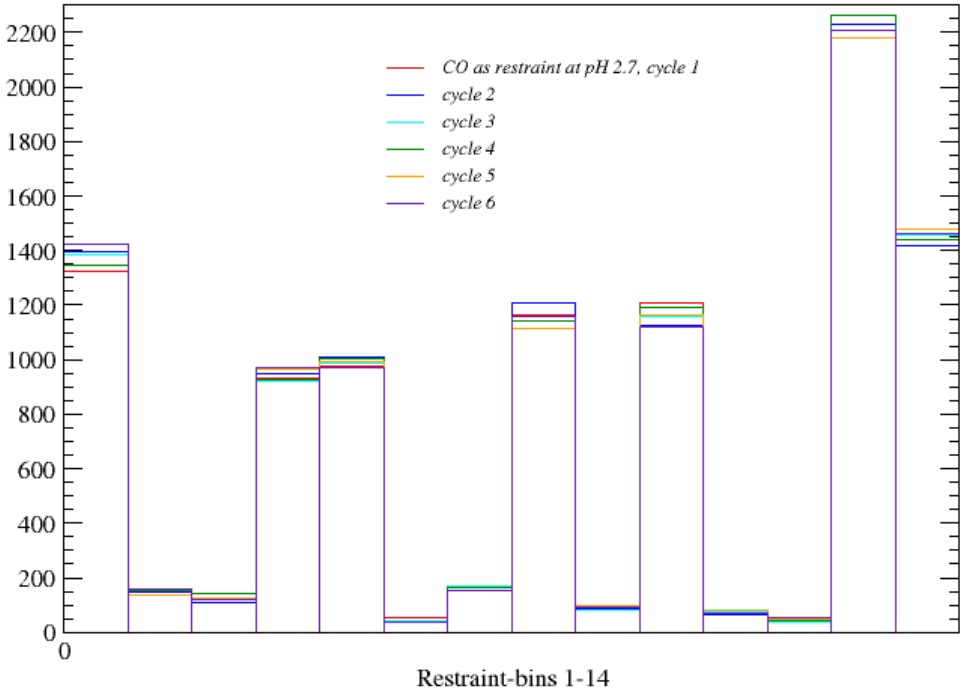


Figure 6.9b: Distribution between the different Restraint-bins, see table 6.1, of the ensembles found during MC-simulation, where CO chemical shifts were used as restraint at pH 2.7. The number of structures are out of a total of 10.000 possible structures for each Monte Carlo simulation cycle.

If CO chemical shifts were used as sole restraint in the Monte Carlo simulations, the distribution between the different Restraint-bins was roughly the same, figure 6.9b. Here A4 could be accredited about [40%] of the time present in the ensemble, while A2 accounted for [21%], A3 and A1 both for roughly [9.7%]. Notably the random coil was represented with approximately 22 %, i.e. a few present more than if $C^{\alpha}$ was used as a restraint. Another difference between the two simulations is that helix A2 exists to a lesser extent in this latest simulation, i.e. 21 % versus 27 %. So somehow something different is modelled or measured by the MC-simulation with the two restraints. For the Monte Carlo simulations where both $C^{\alpha}$ and CO were used as restraint, figure 6.9c, the picture is similar, but with minor differences. The distributions being spaced as followed; A4: [40%], A2: [24%], A3: [10%], A1: [7%] and random-coil [22%]. This seems to be a distribution that resembles features of both previous simulations; A4's occupation equals the simulation where $C^{\alpha}$ was used as restraint, while the amount of random-coil is similar to that seen for simulations where CO chemical shifts were used as restraints.

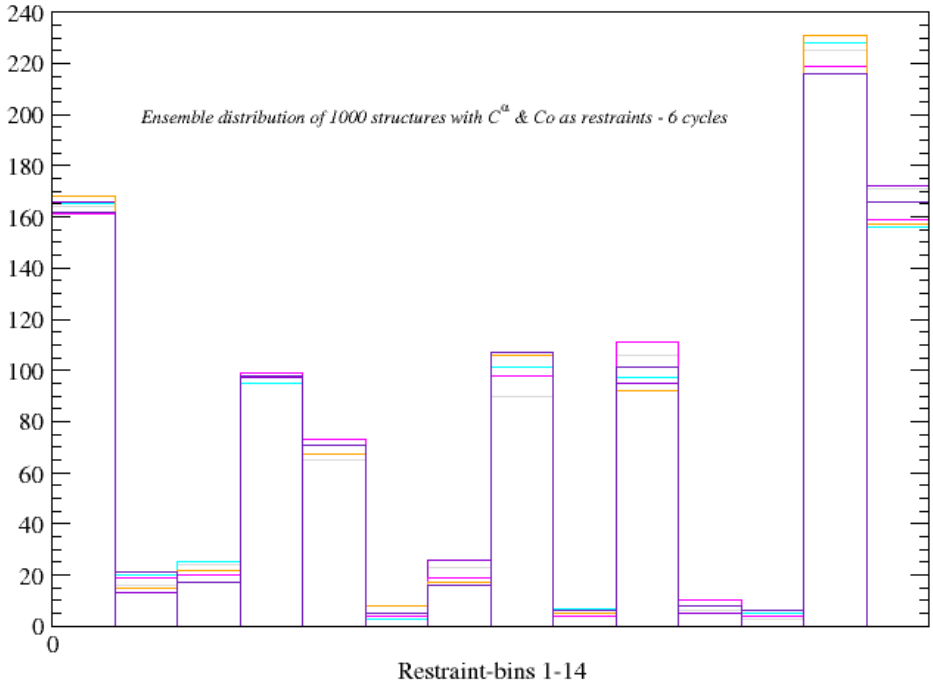


Figure 6.9c: Distribution between the different Restraint-bins, see table 6.1, of the ensembles found during MC-simulation where both $C^{\alpha}$ + CO chemical shifts were used as restraint. The number of structures are out of a total of 1.000 possible structures for each Monte Carlo simulation cycle.

The question is, if the structures extracted out of each Restraint-bin in the different Monte Carlo simulations represent the same amount of secondary structure. To check the absolute distribution of the final ensembles, the secondary structure contents of each Restraint-bin of the final ensembles were estimated with the program DSSPcont [CAnder02]. This was done for all ensembles found for the repeated MC-simulations, that is on approximately 60000 – 80000 structures. Figures 6.10 to 6.11 are examples of the different secondary structure contents under the different simulation conditions ($C^{\alpha}$, CO and $C^{\alpha}$ + CO used as restraints in the MC-simulations) for certain of the Restraint-bins.

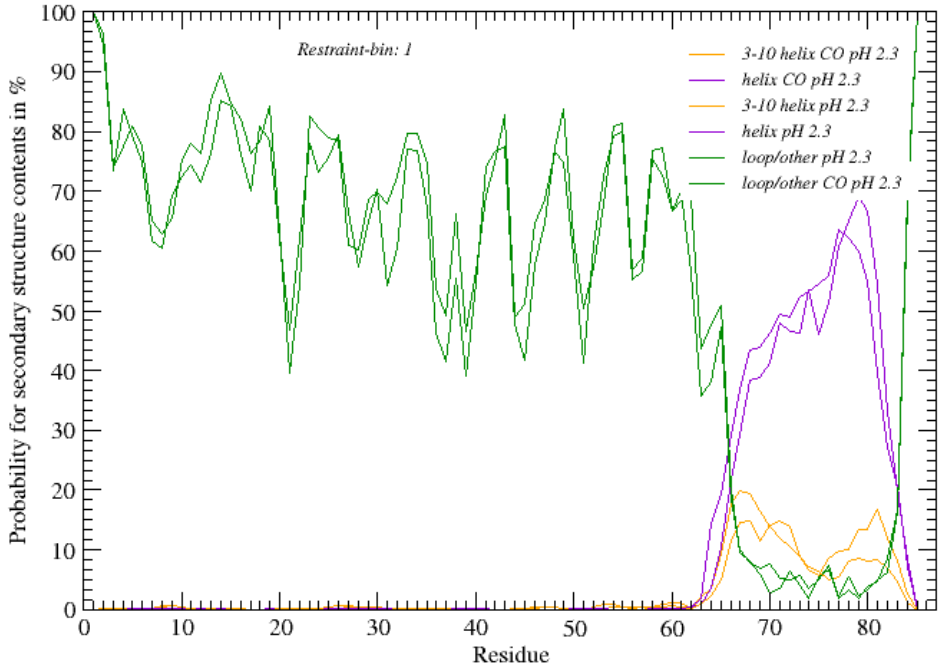


Figures 6.10: Calculated secondary structure contents for Restraint-bin 1, for simulations where CO or $C^{\alpha}$ chemical shifts were used as restraint, both at pH 2.3. Orange: probability for 3-10 helix in percent, Violet: probability in percent for α-helix and Green: probability in percent for loop.

Figure 6.10 shows the probability for α-helix in the region of A4, which is up to 70 % for the amino acids around residue 80. In the final ensemble of the MC simulation where $C^{\alpha}$ was used as restraint, 12.5-13 % of the structures originated from this Restraint-bin. These 12.5-13 % structures of the final ensemble represent, hence, 70 % α-helical structure in the region of A4 and not 100 %. The DSSPcont calculation were unfortunately not made on the entire ensemble found, but just for each Restraint-bin, wherefore it is not possible to access the total probability for helix.
As is seen in figure 6.10 only minor differences exist in the secondary structure contents between the simulations were $C^{\alpha}$ or CO chemical shifts were used as restraints. The overall "shape" and magnitude is the same. A similar behaviour is also found for the case where both $C^{\alpha}$ and CO chemical shifts were used as restraints, see figure 6.11.

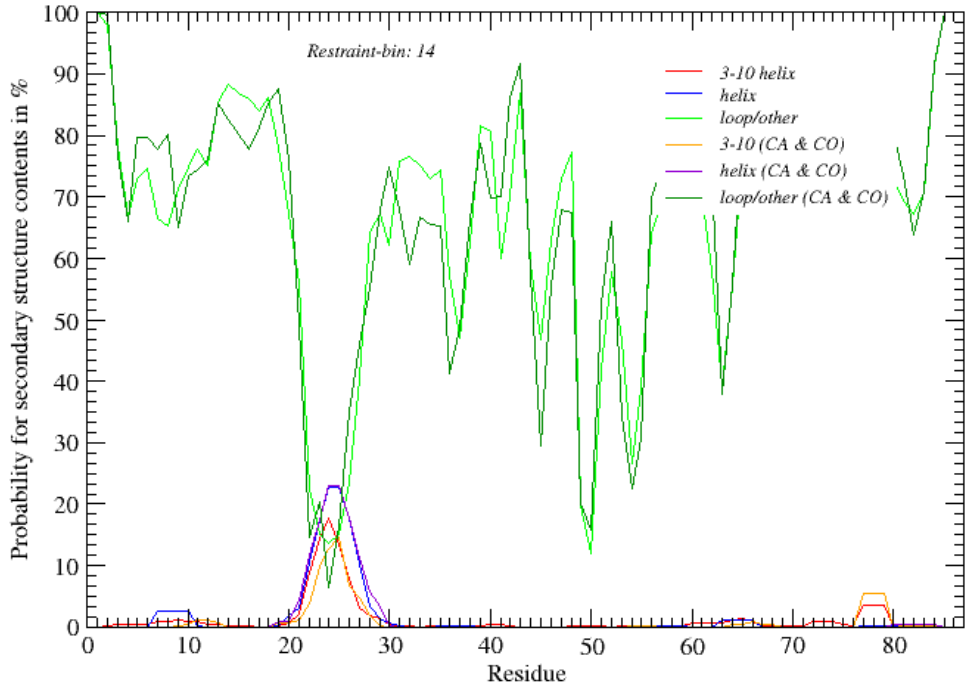


Figures 6.11: Calculated secondary structure contents for Restraint-bin 14 in percent, for simulations where $C^{\alpha}$ or ($C^{\alpha}$ + CO) chemical shifts were used as restraint, both at pH 2.7. Orange: probability for 3-10 helix, Blue: probability for α-helix and Green: probability for loop.

### *6.2.2 Monte Carlo simulations of pH 2.3*

The pH-titration experiments were performed to get quantitative information about the helical contents during the folding process using experimental chemical shifts. More so, if it was possible to get absolute differences in the tendency for helix formation between the distinct pH values. Therefore the Monte-Carlo simulations also included modelling of the experimental data obtained at pH 2.3. Here only simulations with $C^{\alpha}$ or carbonyl chemical shifts as restraint were performed and the results can be seen in figures 6.12 and 6.13.

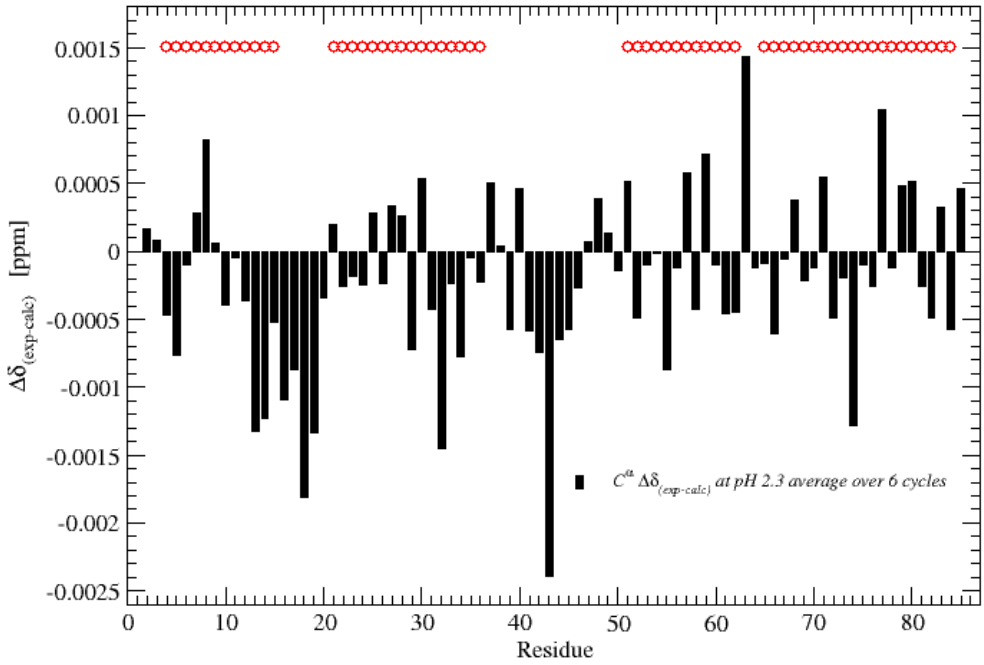


Figure 6.12: $C^{\alpha}$ experimental secondary chemical shift values at pH 2.3 subtracted from the calculated secondary chemical shifts. The data represent an average of 6 Monte Carlo simulation cycles. The red circles denote the location of the four α-helices in the native structure of ACBP.

The distribution of secondary chemical shift differences seems to be similar to the one obtained at pH 2.7: Both in overall magnitude and the areas that are distributed away from randomness, i.e. the second half of peptide segment comprising helix A1 of the native structure and the first loop, as well as in the middle of the large loop, figure 6.12. Also the differences for carbonyl shifts are comparable to those found at pH 2.7, and are again defined better than the experimental uncertainty for assignment of the peaks in the experimental spectra, figure 6.13.

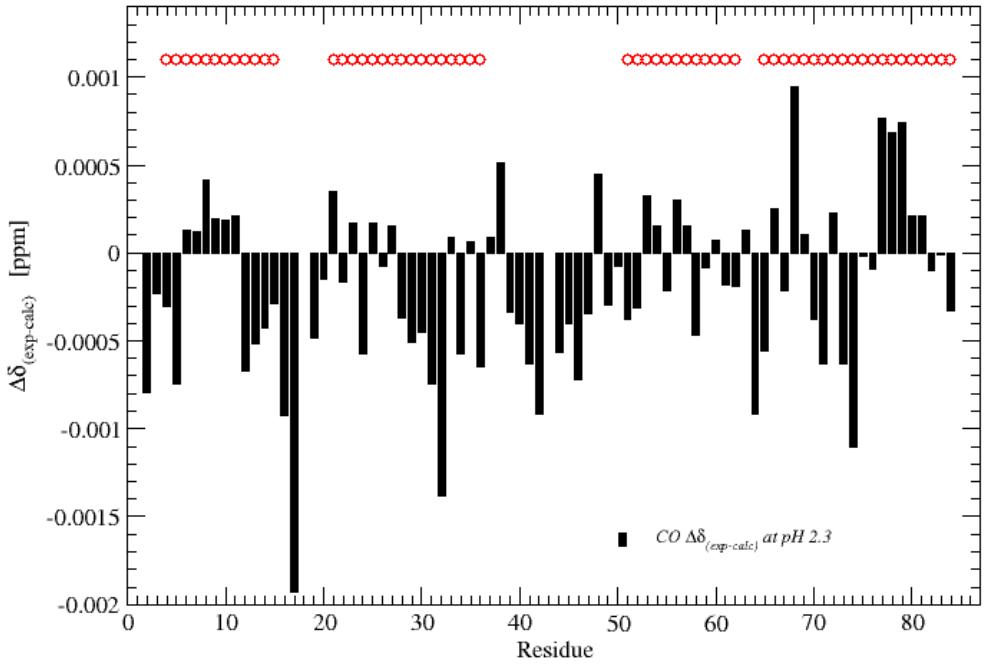


Figure 6.13: CO experimental secondary chemical shift values at pH 2.3 subtracted from the calculated secondary chemical shifts. As before, the calculated secondary chemical shifts were found by subtracting the average of Restraint-bin 13, which served as theoretical random-coil values. The data represent an average of 6 Monte Carlo simulations cycles. The red circles denote the location of the four α-helices in the native structure of ACBP.

As seen from figures 6.14 the distribution between the different Restraint-bins is very similar to that seen at pH 2.7. However, it is clearly seen that the amount of helical secondary structure is significantly reduced and the amount of random coil drastically increased by almost 6.5 %. At pH 2.3 the percentage of structures containing A4 helical propensity is reduced by 5.5 % compared to pH 2.7. A2 is not reduced as radically, and merely accounts for a loss of 1.6 %. A3 and A1 fall by roughly 2 and 3 percent, respectively.
Contrary to this clear behaviour the distribution between the Restraint-bins for MC-simulations were CO chemical shifts served as restraint do not change at all, figure 6.15. At this lower pH the distribution still is A4 ~ 40 %, A2 ~ 21 %, A3 and A4 still both 9.7%, and Restraint-bin 13 22 %. The overall distributions from all Monte Carlo simulations are summarized in table 6.2.

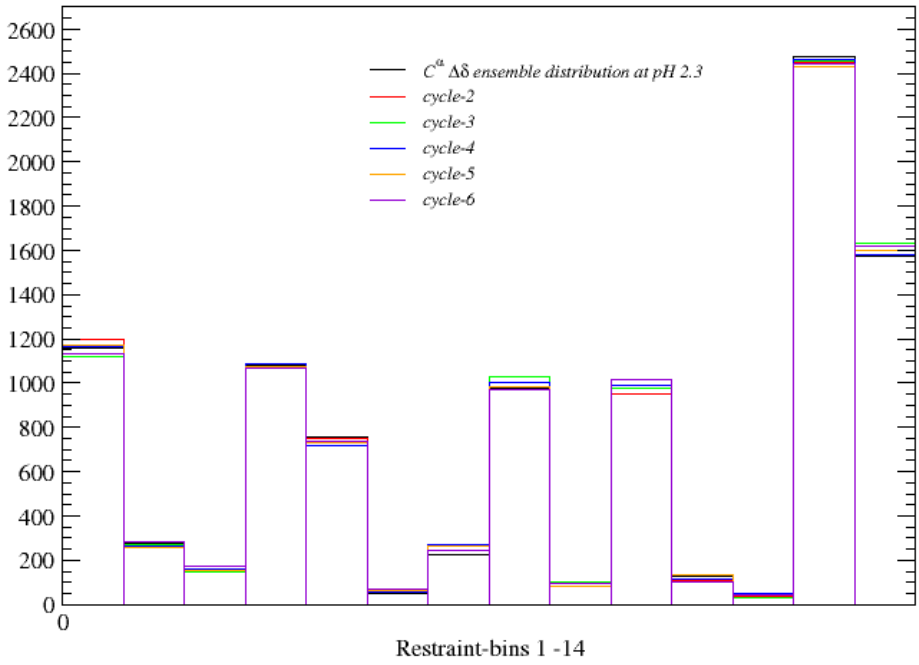


Figure 6.14: Distribution between the different Restraint-bins, see table 6.1, of the ensembles found during MC-simulations, where $C^{\alpha}$ was used as restraint at pH 2.3. The number of structures in each Restraint-bin are out of a total of 10.000 possible structures for each Monte Carlo simulation cycle.

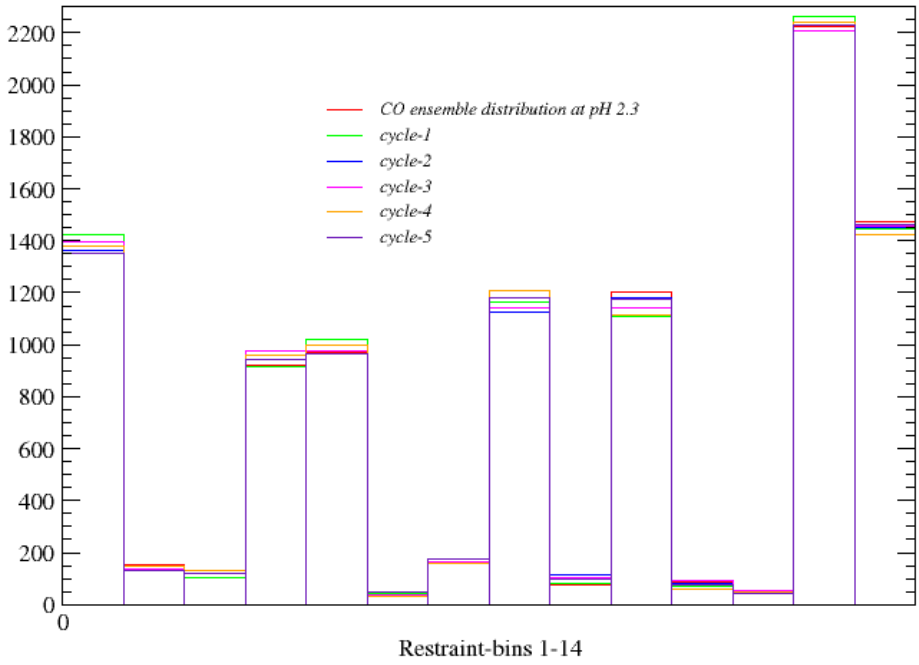


Figure 6.15: Distribution between the different Restraint bins of table 6.1 of the ensembles found during MC-simulations, where CO chemical shifts were used as restraint at pH 2.3. The number of structures in each Restraint-bin are out of a total of 10.000 possible structures for each Monte Carlo simulation cycle.

Table 6.2: Approximate average ensemble distributions in % for the different Monte Carlo simulations:

| *Bin* | *Helix* | *$C^{\alpha}$ (2.7)* | *$C^{\alpha}$ (2.3)* | *$C^{\alpha}$+CO* | *CO (2.7)* | *CO (2.3)* |
|---|---|---|---|---|---|---|
| *1* | *A4* | *12.7* | *11.5* | *17* | *13.5* | *13.9* |
| *2* | *A2* | *2.8* | *2.7* | *2* | *1.5* | *1.4* |
| *3* | *A4 & A2* | *2.7* | *1.5* | *2.5* | *1.1* | *1.1* |
| *4* | *A3* | *11.3* | *10.7* | *10* | *9.5* | *9.5* |
| *5* | *A1* | *10* | *7.3* | *6* | *9.8* | *9.7* |
| *6* | *A4, A2 & A3* | *1.8* | *0.5* | *0.3* | *0.5* | *0.4* |
| *7* | *½ A2* | *1.1* | *2.4* | *2.1* | *1.6* | *1.6* |
| *8* | *¾ A4* | *10.5* | *10* | *9.5* | *11.8* | *11.6* |
| *9* | *½ A2 & ¾ A4* | *0.8* | *0.9* | *0.7* | *0.9* | *0.8* |
| *10* | *A4* | *10.7* | *9.8* | *9.6* | *11.5* | *11.5* |
| *11* | *A2* | *1.5* | *1.1* | *0.5* | *0.7* | *0.7* |
| *12* | *A4 & A2* | *0.6* | *0.3* | *0.4* | *0.4* | *0.5* |
| *13* | *no restraints* | *17.5* | *24.5* | *23* | *22* | *22.3* |
| *14* | *½ A2* | *15.5* | *16* | *16* | *14.5* | *14.4* |

The values summarized in table 6.2 again emphasis's the difference between the use of $C^{\alpha}$ and CO as restraint in the Monte-Carlo simulations. Table 6.3 summarises the

approximate total distributions between the four helical regions from the different Monte Carlo simulations.

Table 6.3: Approximate average ensemble distributions between the different helical regions for the different Monte Carlo simulations:

| *Helix* | *$C^{\alpha}$ (2.7)* | *$C^{\alpha}$ (2.3)* | *$C^{\alpha}$+CO* | *CO (2.7)* | *CO (2.3)* |
|---|---|---|---|---|---|
| *A1* | *10 %* | *7 %* | *7 %* | *10 %* | *10 %* |
| *A2* | *27 %* | *25 %* | *24 %* | *21 %* | *21 %* |
| *A3* | *13 %* | *11 %* | *10 %* | *10 %* | *10 %* |
| *A4* | *40 %* | *34.5 %* | *40 %* | *40 %* | *40 %* |

Figure 6.16 illustrates the loss of helix propensity in the structures of Restraint-bin 4, where it is seen that α-helix probability in the area of helix A3 in the native protein goes down from 50 % to 46 % when the pH is lowered from 2.7 to 2.3. Again, this is only the probability for α-helical contents of helix A3 in 10 % and 11 % of the structures found during the MC simulations with $C^{\alpha}$ used as restraint at pH 2.3 and pH 2.7.

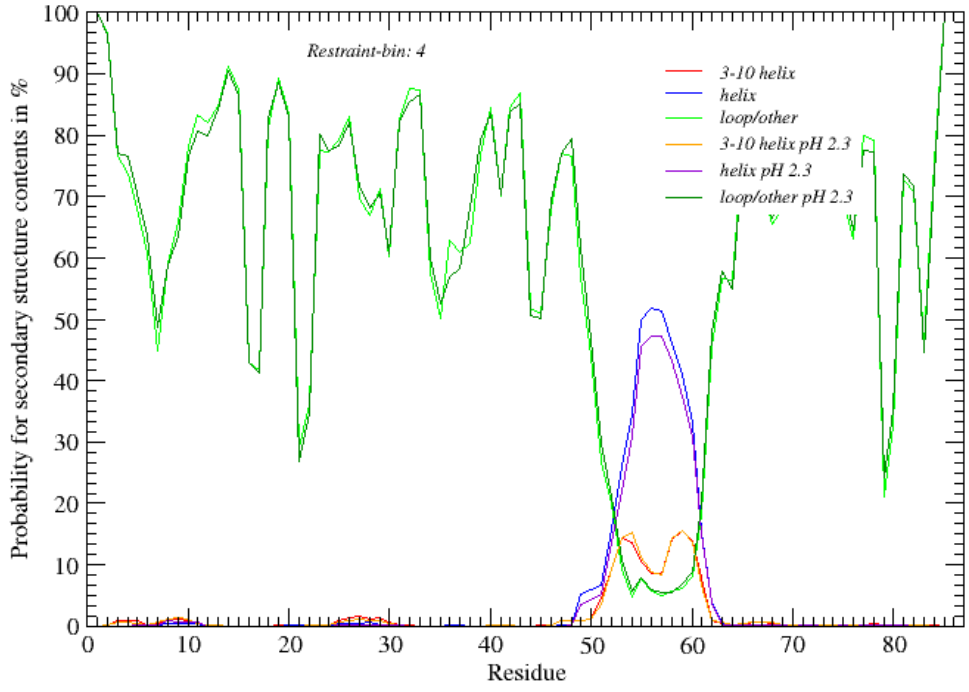


Figures 6.16: Calculated secondary structure contents for Restraint-bin 4 in percent, for simulations where $C^{\alpha}$ was used as restraint, both at pH 2.3 and pH 2.7. Orange/red: probability for 3-10 helix, Blue/violet: probability for α-helix and Light/green: probability for loop.

If one examines the probabilities for secondary structure contents as calculated by DSSPcont for all structures found during one Monte Carlo simulation, i.e. 10.000 structures, it is seen that the overall probability for α-helix in the region A4 is just below 20 %, figure 6.17. The region of helix A2 in the native structure of ACBP exhibits less than 10 % α-helix and the regions A3 and A1 represent even less. The probability for 3-10 helix in the region A4 is by DSSPcont estimated to be around 6 %, therefore the overall probability for helix is roughly 25 % for the 10.000 structures found in one MC-simulation at pH 2.3. In contrast, just below 35% of the structures originated from Restraint-bins where this region was restrained, see table 6.3.

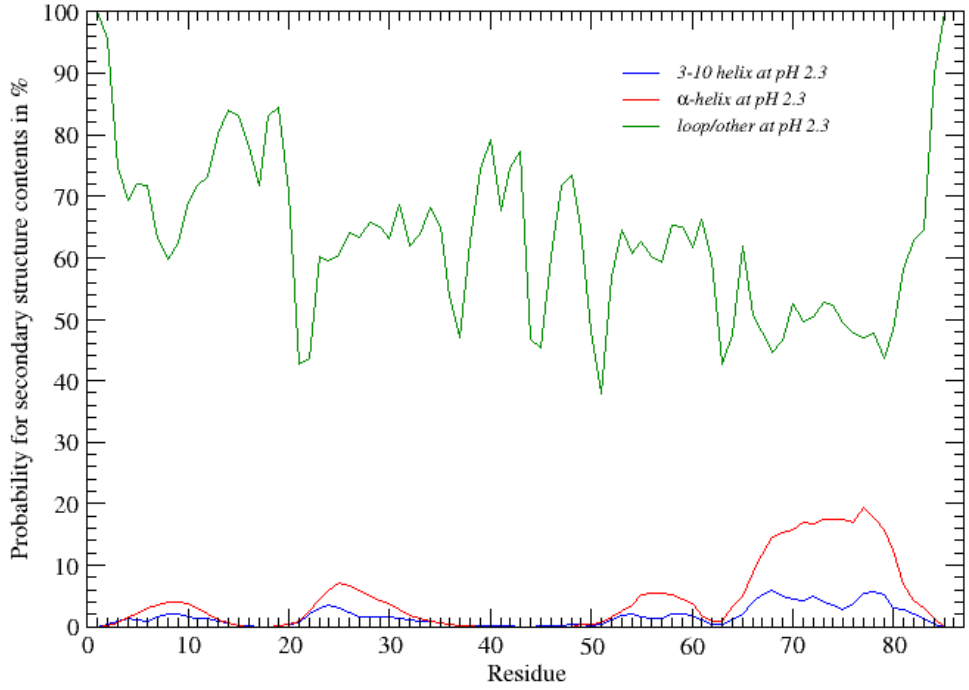


Figures 6.17: Calculated secondary structure contents in percent for all structures found in one MC-simulation, i.e. 10.000, where $C^{\alpha}$ was used as restraint at pH 2.3. Blue: probability for 3-10 helix, Red: probability for α-helix, Green: probability for loop/other.

Ideally, the ensemble found in Monte-Carlo simulations, with one chemical shift species as restraint, should be able to predict the chemical shift pattern for the other shift not used as restraint. Unfortunately, the ensemble for one run yields an absolutely different pattern for the chemical shift not used as restrained. For instant, a run with $C^{\alpha}$ as restraint yields differences between experimental and calculated chemical shift values for CO of approximately – 0.3 ppm and up to – 0.8 ppm and a pattern different from the one observed in a MC-simulation. A graphical representation can be found in Appendix B, figure B.15.

## *6.3 PALES*

The ensemble found in the Monte-Carlo simulations, with one chemical shift species as restraint, should be able to predict the chemical shift pattern for the other shift not used as restraint. Unfortunately, this was not the case, but in order to validate the predictive power of the ensembles found, they were used with the program PALES [MZweck00]. PALES calculates/predicts residual dipolar couplings (RDC) from pdb-files. That is, it predicts sterically induced alignment in dilute liquid crystalline phase. These were compared to RDCs found for ACBP at pH 2.3 by W. Fieber et al. [WFiebe04]. For each structure found in the ensembles manufactured during a Monte Carlo simulation dipolar couplings were predicted by PALES and subsequently the average of all structures was calculated. PALES needs an initial set of dipolar couplings and here the experimental values at pH 2.3 [WFiebe04] were used. For the prediction of residual dipolar coupling default simulation parameters where used. That is the orientation is simulated by an infinite wall and a standard concentration of liquid crystal. Each set of dipolar couplings were scaled by -4 in order to somewhat accommodate the alignment media used. Shortle and Ackerman [DShortle01] note that compression versus stretching yield dipolar couplings of opposite sign. Mohana-Borges et al. [RMohan04] additionally note a factor 2 between the two types. It is not expected that PALES is able to predict the exact size of the dipolar couplings, and scaling always has to be applied [AAlmon02]. In Figure 6.18 N-H experimental dipolar couplings for ACBP at pH 2.3 are seen together with predicted dipolar couplings calculated on the basis of Monte Carlo simulations were $C^{\alpha}$ or CO chemical shifts were used as restraints at pH 2.3. That is, the predicted dipolar couplings in each case represent an average over 60.000 structures. The overall magnitude of the individual N-H dipolar couplings are as expected not predicted very well on the basis of the two ensembles found in the MC-simulations. However, the overall pattern, particularly in the region of helix A4 in the native structure, is represented by both ensembles. Most couplings are negative and get smaller in magnitude or positive in areas were the observed couplings behaviour is similar, e.g. the first half of the region A2 and the loop region between helix A2 and A3 of the native structure. This is a very encouraging result supporting the validity of the ensembles found in the MC-simulations.
Figure 6.19 shows the correlation between experimental and calculated dipolar couplings of the two ensembles. The correlation coefficient lies between 0.4 and 0.44 for the predictions on the basis of the "CO-ensemble" and "$C^{\alpha}$-ensemble", respectively. That is the covariance is roughly 20 %.

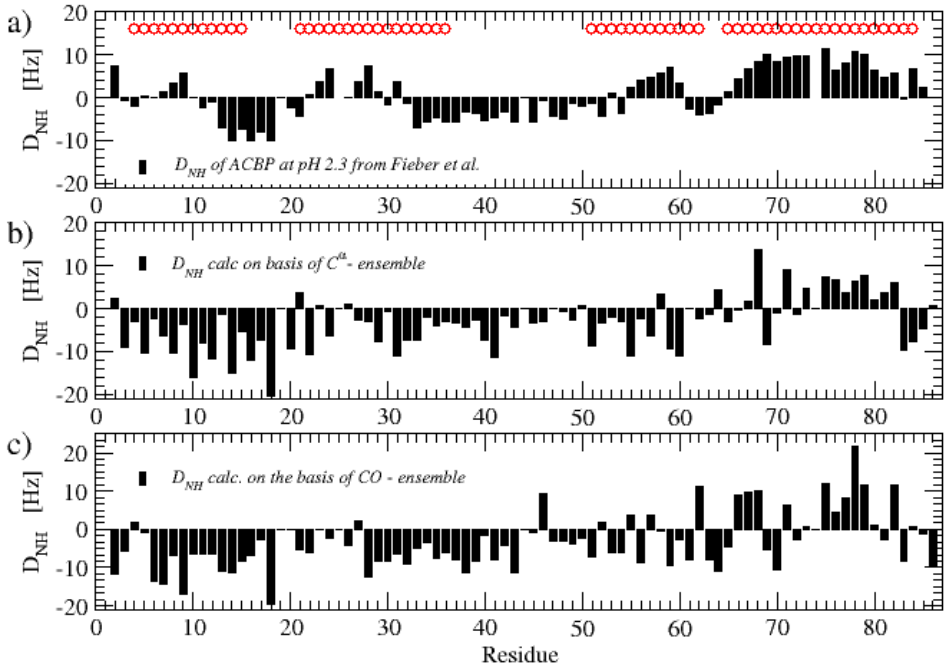


Figure 6.18: a) Experimental N-H dipolar coupling of ACBP at pH 2.3 as a function of residue position. The dipolar couplings were taken from [WFiebe04]. b) Predicted N-H dipolar couplings on the basis of the ensembles found in MC-simulations with $C^{\alpha}$ chemical shifts as restraints. c) Predicted N-H dipolar couplings on the basis of the ensembles found in MC-simulations with CO chemical shifts as restraints. The red circles represent the position of the four α-helices in the native structure of ACBP.

The relative small correlations originate from the inability to exactly model the dipolar couplings for each specific residue. The important point, however, is the ability to reproduce the overall features like the positive dipolar couplings of region A4. Another possibility for the small covariance might be that the observed RDCs sample a different ensemble than chemical shifts. RDCs measure the fractions of molecules that are restricted due to the alignment media, whereas chemical shifts represent an average of all molecules [AAlmon02].

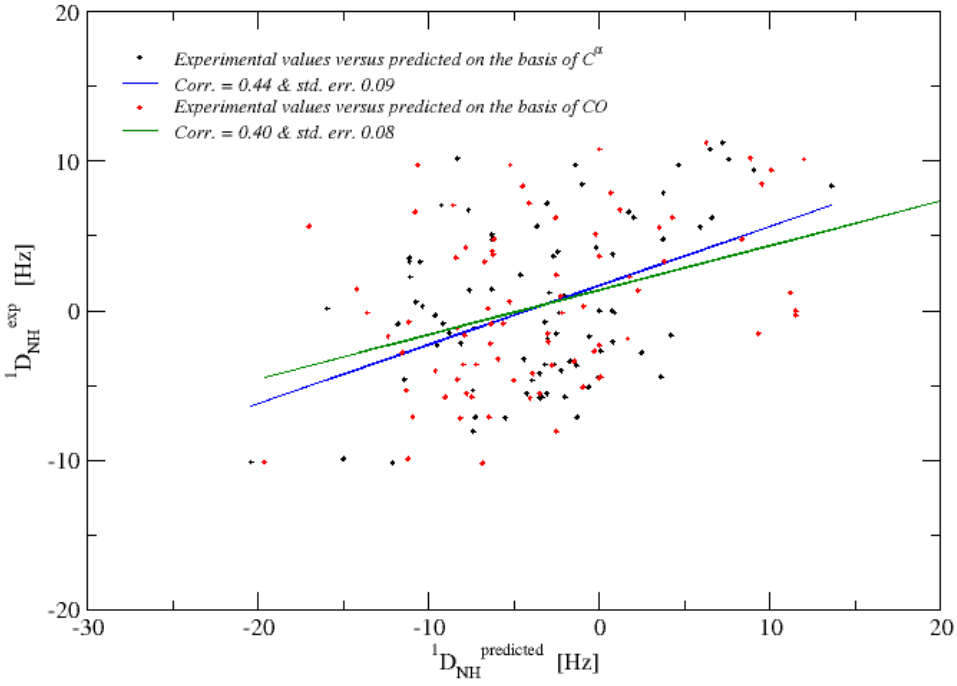


Figure 6.19: Correlation between predicted $^1D_{NH}$ values and experimentally observed [WFiebe04]. The two predicted ensembles are those found during MC-simulations at pH 2.3, where CO and $C^{\alpha}$ chemical shifts were used as restraints.

## *6.4 Discussion/Conclusion*

In order to evaluate the chemical shift data obtained in the acid denaturing titration series, Molecular Dynamic and Monte Carlo simulations where performed. It seems that it is possible to reproduce the experimental features, obtained for the unfolding of ACBP, by comparing the experimental chemical shift data to those found theoretically by SHIFTX. It was hence possible to obtain ensembles of conformations that represent the denatured state of ACBP at two pH values. It was consequently observed that the amount of structures with helical propensity decrease by around 7 % from pH 2.7 to pH 2.3. Noticeable, the largest loss of tendency for helix formation was found for the area that is helix A1 in the native protein. But also an increase in helix propensity from pH 2.7 to 2.3 in the second half of helix A2 was observed and signified a very peculiar behaviour, table 6.2 (bin 7). According to these computer simulations ACBP still contains a considerable amount of secondary helical structure at pH 2.3. The largest tendency for helix is found for the area of helix A4 in the native protein, which still accounts for roughly 34 %, followed by A2 with 25 %, A3 with 11 % and A1 with 7 %. Those ensembles, however, signify not a 100 % probability for helix, but just a percentage. For example, as was seen in figure 6.16, the combined probability for 3-10 and α-helix in the area of helix A3 of the native structure is roughly 60 % at pH 2.3. This should be seen in relation to the original MD-simulations of Restraint-bin 4, which had a probability for α-helix of just about 30 %. Therefore it is possible to find ensembles, which depict the experimentally found observation that the helix propensity for ACBP slowly decreases over the pH titration

range and residual secondary structure still exists at pH 2.3. These results fit very well with previous experimental results obtained for ACBP. As mentioned in chapter 2, these experiments suggest the early formation of helical structure in A4, which was derived from the observation that the amide hydrogens were protected against exchange. Subsequently long-range interactions are formed between A1, A2 and A4 in the transition state, where A2 and A4 interact and stabilize each other, the two helices, which have the highest propensity for helix in this study.
The simulations were nevertheless ambiguous, in a sense that the energy minimisation against carbonyl carbon chemical shifts did not behave as those made with $C^{\alpha}$ chemical shifts. Those ensembles did not reveal a change in helix propensities from pH 2.7 to pH 2.3, and also represented a slightly different percentile distribution of A2, A3, A4 and random-coil values than those found for $C^{\alpha}$ chemical shifts. As a consequence of this the ensembles obtained by using one chemical shift as restraint in the Monte Carlo simulation could not be used to predict the behaviour of the other chemical shift. This lack of cross-validation is of course problematic. It might arise from the different uncertainties by which the different chemical shifts are theoretically determined. SHFTX used empirically derived chemical shift hypersurfaces in combination with classical or semi-classical equations, that relatively accurate describe their effects, to calculate the chemical shifts from atomic coordinates [SNeal03]. The purpose of the hypersurfaces was to encapsulate effects, like nearest neighbour, dihedral angles and secondary structure, which are problematic to describe analytically and are calculated on the basis of a database of observed chemical shifts. Generally the correlation and RMS error for $^{13}C^{\alpha}$ was better than that for $^{13}CO$, which might explain the inability of the MC simulation with CO as restraint to capture the subtle differences between the different pH values. If one compares the correlation coefficients for calculated chemicals shifts found by S. Neal et al. [SNeal03] for the different carbons solely determined by physical factors (classical equations) and together with hypersurfaces, a big difference is noted. It is such that correlations factors are significantly improved for carbonyl carbon when empirical hypersurfaces are included ($\Delta$ 0.35), whereas the predictive power for $C^{\alpha}$ just is slightly increased ($\Delta$ 0.08). The hypersurfaces are constructed for folded proteins, that is the data-bases were trained against well-structured proteins of different structural classes and one could imaging that exactly the ability of the hypersurface to capture effects of statistical nature like secondary structure might be the nature of this difference. And since we look at a denatured protein the correlation coefficient for CO by SHIFTX might actually be much poorer than assumed.
Generally it should be noted that the found ensembles only represent the right conformational distributions of the experiment if the right structures are part of the original start ensemble. This is a big disadvantage of an else wise very simple approach that is easily implemented. After construction of the initial start ensemble it is not possible to add structures during a run, forcing one to manually define structures by restraining their dihedral angles and running the risk of omitting structures and guessing wrong. The small deviations between experimental and calculated chemical shifts are, however, very encouraging.
The N-H dipolar couplings predicted by PALES on the basis of the ensembles found during the Monte Carlo simulations fit relatively well with observed dipolar couplings for ACBP at pH 2.3. The ability of the chemical shift data to predict the observed pattern of dipolar couplings, via computational approaches, yields a self-consistent representation and supports the validity of the ensembles found during the Monte Carlo simulations. To my knowledge the obtained data are both novel and powerful.

The achievement is a very accurate estimate of helix formation in the acid unfolded state and a precise tracking of the loss of residual secondary structure over a pH interval.

# 7 Introduction to Met- and Leu-Enkephalin

Enkephalins are a family of neuro-peptides involved in pain-perception. They are endogenous morphine-like neurotransmitter in the mammalian brain, which bind to the opiate receptors (μ, δ, κ and τ), and they do so actually better than morphine. It is thought that this quality most probably arises due to their flexible nature. Drug designs of selective opoid agonists are difficult. Proper folding is thought of as occurring only when the peptide is in complex with the receptor [RSpada01]. To study the bioactive conformation, i.e. the peptide in complex with its receptor would be ideal, but is for solution state NMR not yet feasible, since opioid receptors are large membrane proteins. Peptides are normally void of secondary structure, but may have preferred conformations.
In this study the two pentapetides Met- and Leu-Enkephalin (Tyr-Gly-Gly-Phe-Met/Leu) are investigated in aqueous-solution by nuclear magnetic resonance spectroscopy to characterize the conformational distribution under such conditions. Enkephalins have a high affinity for δ receptors, but also bind to μ receptors.
There have previously been several experimental investigations of the structure of Enkephalins in aqueous solutions [MKhale79]. But to this time there have been no conclusive results suggesting any conformations of Met- and Leu-Enkephalin in aqueous-solution at room temperature.
The introduction of residual dipolar couplings (RDC) has improved the quality of 3D structure determination in NMR [NTjand97] significantly, but also recently helped in the characterisation of denatured states and short peptides [MLouhi03], [SOhnis03]. RDCs depend on the angle defined by internuclear single-bond vectors and the external magnetic field and give the relative orientation of the individual bond vectors [DShort01] independent on the distance between them. Here the two pentapeptides Met- and Leu-Enkephalin (Tyr-Gly-Gly-Phe-Met/Leu) are investigated in aqueous-solution by NMR spectroscopy to characterize the conformational distribution. We used RDCs to elucidate an eventual conformational change as a function of pH.

Khaled et al. [MKhale79] studied the structures of both Enkephalins in different solvents, using among others $^{1}H$ and $^{13}C$ NMR to propose the existence of a concentration-dependent folded monomeric form that exists in several conformations. They followed all carbon resonances with $D_2O$ as solvent during a pD-titration. The lowering of the apparent $pK_a$ value for the Tyr α-amino-group from 9.4 to 8, see figure D.4 in appendix D, is interpreted as the proximity of a donor proton as for instance the carboxy-terminus, which they think corroborates a head to tail conformation. Later Stimson et al. [EStims79] were unable to reproduce these results using NMR on $^{13}C$-enriched carbonyl carbons in [Leu5]-Enkephalin, and ascribed the effects to the impurities and thus rejected the model. Similarly in the mid 80'ties Gupta et al. [GGupta86] used the nuclear Overhauser effect (NOE) measurements in $D_2O$ to reveal the close proximity of the two aromatic rings in space. A result, which could not be reproduced by Motta et al. [AMotta87], who thought this to be an artefact of the method used. The only satisfactory results they obtained were measured at subzero temperatures and these were limited to intra-residue effects, in a mixture of $D_2O$ and $DMSO_{d6}$. Molecular dynamic simulations [MAburi02] showed that the conformational population distribution of Leu-Enkephalin in aqueous solutions is dependent on pH through the analysis of the glycine carbonyl oxygens and terminal groups. These simulations suggested the existents of a mixture of folded

and unfolded forms at neutral pH, but always unfolded at low and high pH. The nature of the solvent surrounding the peptide is thought to have a considerable effect on the conformation of peptides. The flexibility of linear peptides is reflected by NMR parameters, as shown by the fact that $J_{NHC\alpha H}$ scalar couplings are distributed around the average value of 6.5 Hz and, more poignantly, by the failure to observe analytical NOE's [RSpada01]. The lack of NOE's seen could be due to the unfavourable $\omega\tau_c$, due to the flexibility of the molecules and/or to the small fractional population of folded conformers. ROESY should circumvent the first problem, but only gives ROE's of low diagnostic value. Those reported in literature were only possible at low temperatures and in solvents with elevated viscosity [AMotta87]. The question of their biological relevance remains, since the environment favours these conformations, similar to crystallization conditions, which only yields a static picture of low energy conformations. Investigation in DMSO's might have its merit, since its viscosity is close to the cytoplasm, but not as high as in the synaptic cleft [RSpada01]. One of the most recent investigations is that of Met-Enkephalin in zwitterionic and negatively charged fast tumbling bicelles [IMarco04]. Contrary to polyacrylamide gel used in this study there occurs extensive binding to bicelles, but the chosen bicelles are thought to resemble membranes due to bilayer organization and the composition. Structure calculation from torsion angle and NOE-based distance constraints suggested the existence of several conformers of Met-Enkephalin selective for both $\mu$ and $\delta$ receptors, which they thought consistent with the flexibility and poor selectivity of Enkephalins.
Also investigations by other spectroscopic means than NMR, seem to corroborate the pH dependence of Met- and Leu-Enkephalin conformers [SAbdal03]. Their investigations with Raman spectroscopy showed that Leu-Enkephalin changed from a fully protonated state between pH 4 and 6, while Met-Enkephalin changed between pH 2 and 4, based on the observation of the ratio of the 850/830 wavenumbers over the pH range from 1 to 13 (the Fermi doublet of tyrosine). The same ratio indicates a total ionisation of Met-Enkephalin at pH 9, whereas Leu-Enkephalin first is fully ionised at pH 13. The $COO^-$ symmetric stretch mode (1430-1400) appears for Leu-Enk between pH 4 and 6, and might vaguely appear for Met-Enkephalin between pH 2 and 4. The absence of this band consists with the absence of $COO^-$ at this pH. A change in the tyrosine aromatic C-C stretch region (1630-1590 $cm^{-1}$) due to the change of the OH group, which was expected to occur already at pH 9 for Met-Enkephalin and not as was the case at pH 13. They conclude that the ionization of tyrosine gives a picture of the comformational state of Enkephalin, where ionization corresponds to an extended conformation with an aromatic ring/ -OH group exposed to the solvent, and a more folded structure in the state where the tyrosine ring is fully protonated. This they conclude is above pH 4 for Met- and above pH 6 for Leu-Enkephalin, though the data suggest total deprotonation at pH 13 and is inconclusive for Met-enkephalin with respect to the $COO^-$ symmetric stretch mode. The more pronounced changes in Met compared to Leu, occur due to the hydrophobic side-chain which prevents phenol and COOH deprotonation in Leu, and therefore gives are more folded structure of Leu-Enkephalin.
At present time it can be concluded that the structure of Leu- and Met-Enkephalin in aqueous solution remains unknown.

### *7.1 Residual dipolar couplings of denatured proteins*

Residual dipolar couplings (RDC) have been used to significantly improved structure determination in NMR [NTjand97], but not until recently been implemented in the characterisation of denatured states and short peptides [MLouhi03], [SOhnis03], [AAlexa03]. Weak alignment of proteins prevents the complete averaging of dipolar interactions, but preserve the solution properties of the sample. RDCs depend on the angle defined by internuclear single-bond vectors and the external magnetic field and give the relative orientation of the individual bondvectors [DShort01] independent on the distance between them.
Dipolar couplings originate from the interaction between two magnetic dipoles. The interaction energy between two point dipoles ($\boldsymbol{\mu}_1$ and $\boldsymbol{\mu}_2$) is given by:

$$\hat{\mathrm{H}}_{dd} = \gamma_1\gamma_2\hbar^2 \frac{\mu_0}{4\pi}\left\{\frac{\hat{I}_1\cdot\hat{I}_2}{r^3} - 3\frac{(\hat{I}_1\cdot\boldsymbol{r})\cdot(\hat{I}_2\cdot\boldsymbol{r})}{r^5}\right\} \qquad 7.1$$

Where $\boldsymbol{r}$ is the distance between the dipoles and $\boldsymbol{\mu} = \gamma\, h/2\pi\, \mathbf{I}$. In solution NMR dipolar couplings average to zero due to rapid isotropic tumbling. In acryl amide gel, bicelles and other anisotopic nematic liquid crystalline media the tumbling is restricted by a fraction in one direction, with is enough to ensure incomplete averaging and get measurable residual dipolar couplings.
The magnitude of the RDC is dependent on the orientation of the internuclear vector relative to the alignment tensor of the entire protein [RMohan04]. In other words, bond vectors such as $^{15}$N-$^{1}$H or $^{13}$C-$^{1}$H can be oriented relative to a global alignment tensor fixed in the molecular frame, independent of their location in the molecule. This can be deduced from equation 7.1 giving that the relative orientations between pairs of bond vectors are independent of the distance between them.

$$D_{NH} = -S\frac{\gamma_N\gamma_H}{r_{NH}^3}\frac{\mu_0\hbar^2}{4\pi}\left[A_a\left(3\cos^2\theta - 1\right) + \tfrac{3}{2}A_r\left(\sin^2\theta\cos 2\phi\right)\right] \qquad 7.2$$

S is the generalized order parameter, $\gamma_N$, $\gamma_H$ the gyromagnetic ratios and $A_a$, and $A_r$ are the axial and rhombic components of the alignment tensor.

It was previously implicitly assumed that the RDCs of a fully denatured protein would be zero. But studies have shown that even under strong denaturing conditions proteins can be aligned and dipolar couplings [DShort01] of similar composition as in the native state observed. Screening of short peptides from 2 to 15 amino acids in length revealed small RDCs for the peptides aligned in both bicelles or polyacrylamide gels [SOhnis03], inferring a non-spherical conformational ensemble. Line-broadening in the bicelles, but not in acrylamide gel, suggested the alignment here arose due to peptide binding, whereas steric hindrance was thought to be the only mechanism responsible for alignment in acryl-amide gels. The arbitrary composition of the studied peptides, except for low fraction of hydrophobic residues, reflects the intrinsic structural properties of small peptides, leading to the view of the denatured state of a protein to be composed of stiff segments with strong directional bias.

The assumption that residual dipolar couplings average to zero in denatured proteins and short peptides ignores the classical results of “random flight chain” of Kuhn

according to Louhivuori et al. [MLouhi03]. In 1934 in Kolloid-Z [MLouhi03a] Kuhn pointed out that segments of the random flight chain not are scattered spherically relative to the end-to end displacement axis. Louhivuori et al. [MLouhi03] show how this simple structure of the chain will cause nonvanishing RDCs by using the model of the random flight chain (Gaussian chain). They assume for the spatial distribution of an ensemble of conformers, that no conformational changes are induced by the obstruction itself and calculate the average orientation of each segment. They find that the probability of the internuclear vector with respect to the magnetic field for longer chains will become smaller, since the distribution of uncorrelated chain segments will go towards a more spherical one. This probability goes towards zero for the infinitely long change and simulations of the chain length in bicelles reveal dipolar couplings of the order of a few Hertz for short chains of length 10 to 100. They also observe that the couplings go towards zero towards the chain termini and hence have a very particular distribution along the peptide sequence.
Significant residual dipolar couplings have also been observed for both acid and urea denatured apomyoglobin [RMohan04], where changes in RDCs are observed in local regions with helical propensities in the acid-denatured state. Similar observations in the acid-denatured state are made for ACBP, where also mutation of a single residue in one helical area lead to large decreases of RDCs in a second helical area of the native state [WFiebe04]. The behaviour of a chain can also be described in terms of its persistence length [RMohan04]. The persistence length is a measure of the length at which the chain continues in the same direction and has been measured for denatured polypeptides to be five to seven amino acid residues long. The statistical segment lengths is approximately double the persistence length, and each statistical segment, with a propensity towards extended conformation, is highly anisotropic in shape with its own alignment tensor. Mohana-Borges et al. further suggest that RDCs in unstructured polypetides derive from transient alignment of these local regions of the chain. That is, contrary to RDCs for folded globular proteins, RDCs in denatured proteins and short peptide are not determined by the relative orientation of a bond vector to a single global alignment tensor, but arise due alignment of statistical segments or transient elements of secondary structure. Due to this local alignment tensor, it might be inferred that small peptides in extended conformation aligned with the obstructing plane have a larger contribution to the observed RDCs, as compared to more bended structures aligned with an angle. Therefore RDC measurement on denatured proteins and peptides give information on the composition of a conformational ensemble, and may for example be used for comparison with values calculated for ensembles of conformations derived during molecular dynamic simulations.

# 8 Results for Met and Leu-Enkephalin

All resonances of Met- and Leu-Enkephalin were assigned on the basis of $^{13}$CHSQC-, $^{15}$NHSQC-, TOCSY- and HMBC- experiments. In the search for inter residual NOE's that could suggest a dominating conformation ROESY-, NOESY-pulse sequences were applied, but were unsuccessful. Therefore our attention turned to residual dipolar couplings (some NOESY measurements were made on 500 MHz Brucker Instruments at Carlsberg Laboratories). The investigation were done below and above the theoretical pI of 5.52 [Expasy], in 100 mM KCl and 10 % $D_2O$ at pH 2.0, 4.04, 6.95 and 8.9 and 2.0, 4.06 and 6.95 for unlabelled Met- and Leu-Enkephalin respectively, all at T = 298K. The concentrations used for both peptides were typically from 6 mM to 16 mM. The pH interval from pH 2 to 9 was chosen in order to investigate the peptides in their cationic, zwitterionic and anionic states, since changes in the ionic state of small peptides can represent large environmental changes. The residual dipolar couplings were measured with gTOCSYNHSQC or IPAP-NHSQC on Varian Unity Inova Instruments 750 MHz and 800 MHz spectrometers at T = 298K, and for Leu-Enkephalin also encompassed in addition to the above mentioned pH-values: pH 1, 3, 5, 6 and 8.

## *8.1 NOESY*

An attempt was made to obtain inter-residual NOE's, which could suggest a dominating conformation. Several intra-residual NOE's and a few inter-residual NOE's between e.g. Gly-2 NH and $H^{\alpha}$, and $H^{\beta}$ of tyrosine, and between NH of the glysines were observed. Never the less, none were observed between the sidechains. The lack of inter-residual NOEs is most probably due to the flexibility of the molecules, where the lifetime of individual conformations is too short to allow for measurable NOE build-up. WROESY measurements with mixing times from 200 ms to 400 ms were tried, and established, where NOE build up was not eaten by exchange, to be best around 250 ms. The lack of inter-residual NOE's could also be due to a small fractional population of "folded" conformers (less than ~ 5% populated) at any given time. Nevertheless, differences in the amide proton chemical shifts at different pH-values were observed. The chemical shift of $H^N$ - of methionine changes from 8.4 ppm at pH 2 to 8.06 at pH 4, i.e. a change of -0.37 ppm, whereas $H^N$ of Phe-4, Gly-3 and Gly-2 change -0.022, +0.032 and +0.022 respectively, see figures D.1 and D.2 in Appendix D. This most probably is due to the deprotonation of the C-terminus. The fact that the effect is larger on Gly-3, which is further apart from the deprotonation centre than Phe-4, insinuates additional influences on the chemical shift changes other than deprotonation.

## *8.2 Residual dipolar couplings*

This prompted the investigation of RDCs over the pH range from pH 1 to 9, in stretched polyacrylamide gels, which are stable and inert over a broad range of conditions (for instance low pH), contrary to bicelles and phages [RMohan04]. It has been shown that alignment by strained polyacrylamide gels occurs due to steric hindrance in proteins as well as in small peptides. Contrary hereto akyl-PEG-bicelles seem additionally to mediate alignment through transient binding [SOhni03]. In these experiments 7% w/v strained polyacrylamide gel, as described in chapter 9, were used

[JChou01], [RTycko00], [HSass00]. This compression provided a deuterium quadrupolar coupling of 12-16 Hz. Unfortunately, several of the labile protons exchange beyond detection in the gel at relatively low pH. Glycine-2 exchanges beyond detection already at pH 6, Gly-3 at pH 7 and Phe-4 at pH 8 leaving just one residual dipolar coupling between $^{15}N$ and $^{1}H^{N}$ of Leucine-5 at pH 8. In Appendix D figure D.3 the theoretical calculated exchange rates for Leu-Enkephalin [YZhang], which collaborate these results, are shown. There exist several methods for obtaining RDCs by NMR. Natural abundance $^{15}N$ HSQC spectra were collected, without decoupling during acquisition time, under isotropic ($^{1}J_{NH}$) and partially aligned ($^{1}J_{NH} + D_{NH}$) (anisotropic) conditions in order to obtain RDCs, with approximately 12 h of data collection for TOCSY-NHSQC and IPAP-NHSQC spectra with roughly 6-8 hours of data collection [NTjand97]. The RDCs were calculated as the difference between scalar couplings measured in the isotropic sample and total couplings in the oriented sample [AAlexa03]. Yielding, ($^{1}J_{NH}$) - ($^{1}J_{NH} + D_{NH}$) = - $D_{NH}$.
All spectra's were analysed using NMRView software, while an in-house program (APK) was used to determine the scalar and dipolar couplings. No differences in proton linewidths between aligned and isotropic samples were observed, it was therefore interpreted that no binding to the alignment media occurred. We measured the pH-dependence of RDCs for both Enkephalins at the pH values 2, 4, 7 and 9, at pH 9, as explained above, all amide protons exchanged. For Leu-Enkephalin RDCs were additionally obtained at pH 1, 3, 5, 6, and 8, as well as reproduced at pH 2 and 3 (that is also measured with the two different methods TOCSYNHSQC and IPAP-NHSQC).
Figure 8.1, shows the J-couplings in the isotropic sample and the J-couplings together with dipolar couplings of Met-Enkephalin. It is seen that the NH J-couplings for each amino acid are constant over the pH-range, and that the difference arises in the partially aligned sample. That is, the changes in residual dipolar couplings over the pH-range are due to the changes in dipolar couplings alone. The J-couplings for each residue over the measured pH values are: $J(Hz)_{Res-2} = 94.39 \pm 0.04$ Hz, $J(Hz)_{Res-3} = 94.46 \pm 0.04$ Hz, $J(Hz)_{Res-4} = 93.25 \pm 0.3$ Hz and $J(Hz)_{Res-5} = 92.97 \pm 0.4$ Hz. This excludes variation in J-couplings that could arise due to changes in the electronic environment and hence give a picture of deprotonation rather than of conformational changes.

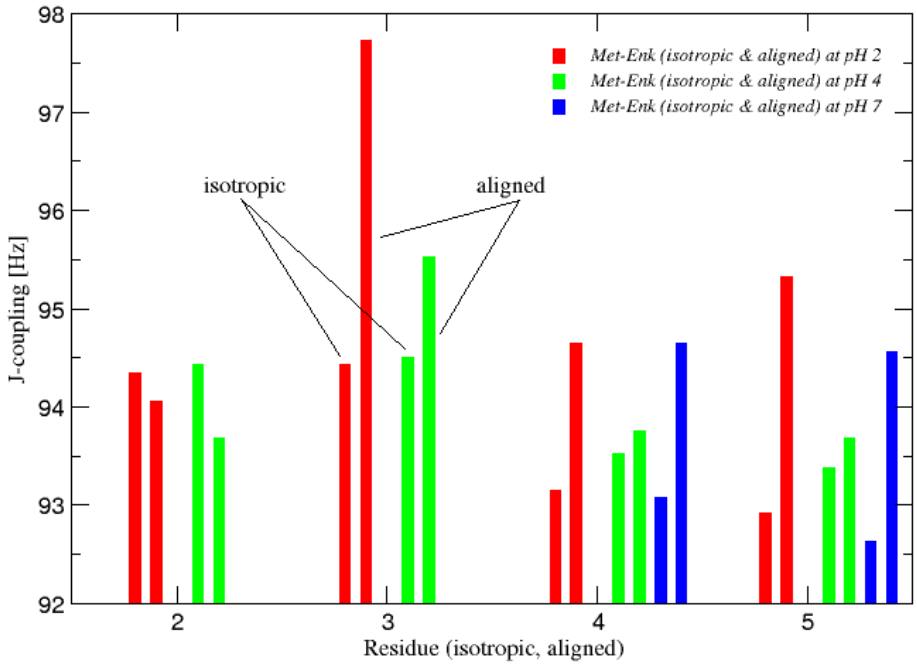


Figure 8.1: J-couplings in the isotropic sample and the J-couplings together with dipolar couplings for each residue of Met-Enkephalin at pH 2 (red), 4 (green) and 7 (blue).

The size of the RDCs for each N-H-vector changed over the pH-range for both pentapeptides. Figure 8.2 shows the RDCs for Met-Enkephalin at the three pH-values 2, 4 and 7. The amide protons for Gly-2 and -3 already exchange too fast for the NMR-timescale at pH 7, while the remaining residues exchange to fast at pH 9. The values of the RDCs are between + 0.75 and − 3.3 Hz, with the largest difference in overall RDCs between pH 2 and the higher pH-values. As pointed out in chapter 7, residual dipolar couplings from denatured proteins and short peptides cannot be used as direct restraints in structure calculations, but changes under different conditions can infer conformational changes. The data for Met-Enkephalin therefore suggests that a change in conformational ensemble occurs between pH 2 and 4.

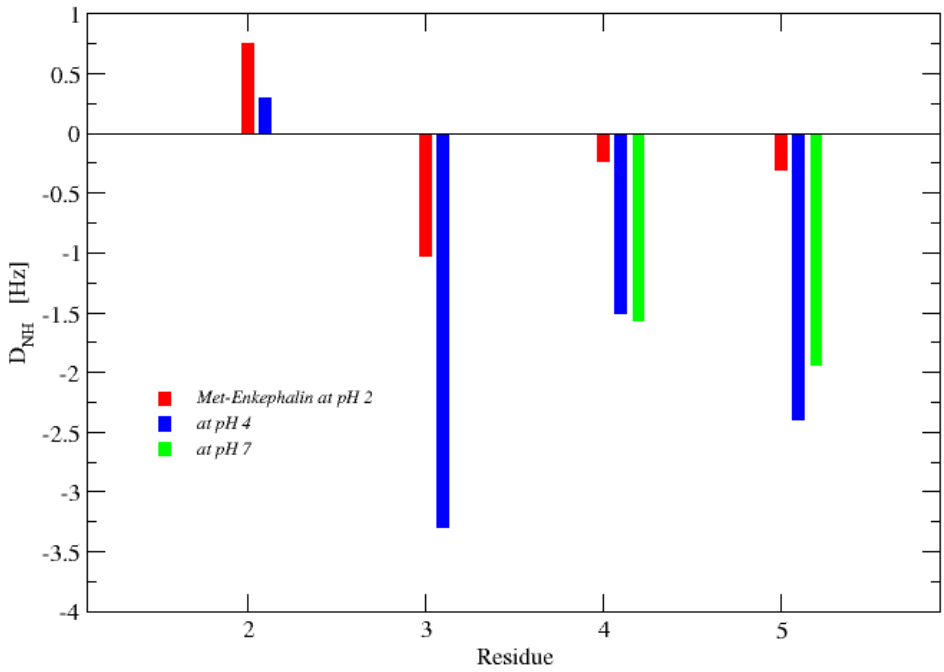


Figure 8.2: $D_{NH}$ for Met-Enkephalin at pH 2 (red), 4 (blue) and 7 (green), collected with TOCSYNHSQC for each residue.

RDCs values of Leu-Enkephalin are similar, in that Gly-2's RDC also is positive, while the remaining residues are negative. The absolute values of Leu-Enkephalins RDCs are found between + 1.2 Hz to – 5 Hz, that is slightly larger variations than those for Met-Enkephalin. It seems that Leu-Enkephalin gradually changes from pH 1 to pH 4, and a major shift occurs between 4 and 7, figure 8.3, the latter is a change that is encountered much earlier in Met-Enkephalin. However, all dipolar couplings for Leu-Enkephalin change sign between pH 1 and pH 2.

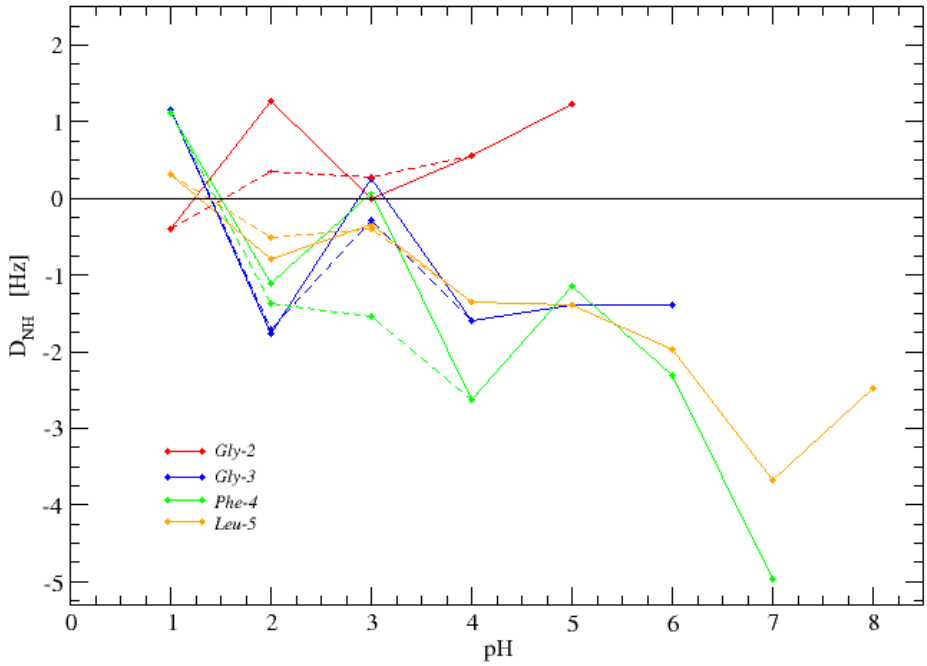


Figure 8.3: $D_{NH}$ for Leu-Enkephalin as a function pH in the interval from 1 to 8. The spectra were obtained with TOCSYNHSQC and IPAP-NHSQC. Dashed lines represent data from measurements that were repeated (pH 2 and 3).

According to Khaled et al. [MKhale79] chemical shift measurements on $^{13}CO$, both $pK_a$ values for Met- and Leu-Enkephalin have the same value of approximately 3.7, see Appendix D, figure D.4. The lower $pK_a$ value is corroborated by our own measurements, where fitting of the Henderson-Hasselbalch equation to $H^N$ chemical shifts as function of pH also yields a $pK_a$ of 3.7, see figure D.5 in Appendix D. So it seems, there exist differences between conformational distributions as a function of pH for the two Enkephalins and, which are not entirely governed by the deprotonation of the C-terminus. The $pK_a$ for isolated leucine and methionine residues [WBrown88] are raised from 2.33 and 2.28 to 3.7 in the C-terminal of Enkephalin, but changes for Leu-Enkephalin do not occur before after pH 4.
Not surprisingly the biggest similarities between Met- and Leu-Enkephalins RDCs are observed at pH 2, where both are assumed to be fully protonated and according to Abdali et al. [SAbdal03] believed to be in an extended conformation. The largest absolute RDCs for both Enkephalins are observed in the region between the two $pK_a$ values. The resolution, for the in-house program, with which the peaks can be assigned, is approximately 0.0005 ppm (0.038 Hz), but where the maximum difference for a few peaks was up to 0.0019 ppm (0.14 Hz). The digital resolution before zero-filling was 9.6 Hz and 11.7 Hz for IPAP and HSQC respectively, see chapter 9. The typical experimental uncertainties for RDCs have been reported to be around 1 Hz [AAlexa03]. Compared to the small overall sizes of the residual dipolar couplings, this is a relative large uncertainty, why the small changes around 0 Hz for some residues and their variation for the repeated measurements, cannot be attributed much significance. However, the changes ascribed to conformational changes, are

larger than those uncertainties and are hence still believed to be significant. We assumed that we in both cases investigate monomeric un-associated peptides, since we do not observe substantial line broadening over the broad range of concentrations used. Unfortunately, it was not possible to measure a Mass-spectrum of the used solution in order to be absolutely sure and regrettably it was not possible to measure RDCs at high pH.

### *8.3 Circular dichroism*

Circular dicroism also monitors conformations in peptides, the RDC data were supplemented with circular dichroism spectra acquired in the far-UV region for Met-Enkephalin (200-250 nm). A pH titration from pH 1 to 13 was made for both Met-Enkephalin and for the amino acid tyrosine alone.
The CD spectra for Met-Enkephalin show a change between pH 7 and 8. This transition can be attributed to the deprotonation of $NH_3^+$-group, which according to literature should have a $pK_a = 9.1$, see figure 8.4. This lowered $pK_a$-value is likely to be due to the formation of an H-bridge of the N-terminal proton. This $pK_a$ value is corroborated by Khaled et al. and was determined to be approximately 7.8 [MKhale79], see Appendix D, figure D.4. A possible H-bond donor is the deprotonated carboxyl-group at the C-terminus, which would require a ring-like conformation of Enkephalin. The CD spectra of the amino acid tyrosine alone, shows at 220 nm, figure 8.5, clearly changes at the literature $pK_a$-values for this residue (2.2, 9.1,10.1 [WBrown88]). The overall magnitude of these changes are however much smaller than the one observed for Met-Enkephalin in figure 8.4. This indicates that the change between pH 7 and 8 is a result of another effect than deprotonation. This could for instance be a conformational effect, since the far-UV region contains absorption bands of the backbone amide groups that are sensitive to secondary structure.

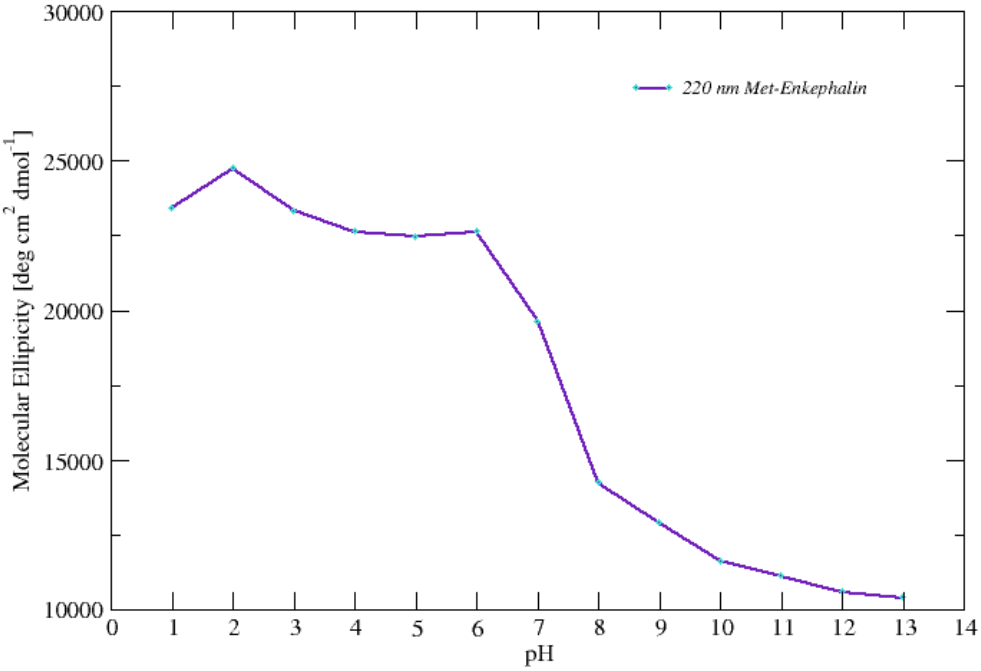


Figure 8.4: Molecular Ellipticity for Met-Enkephalin as a function of pH at 220 nm.

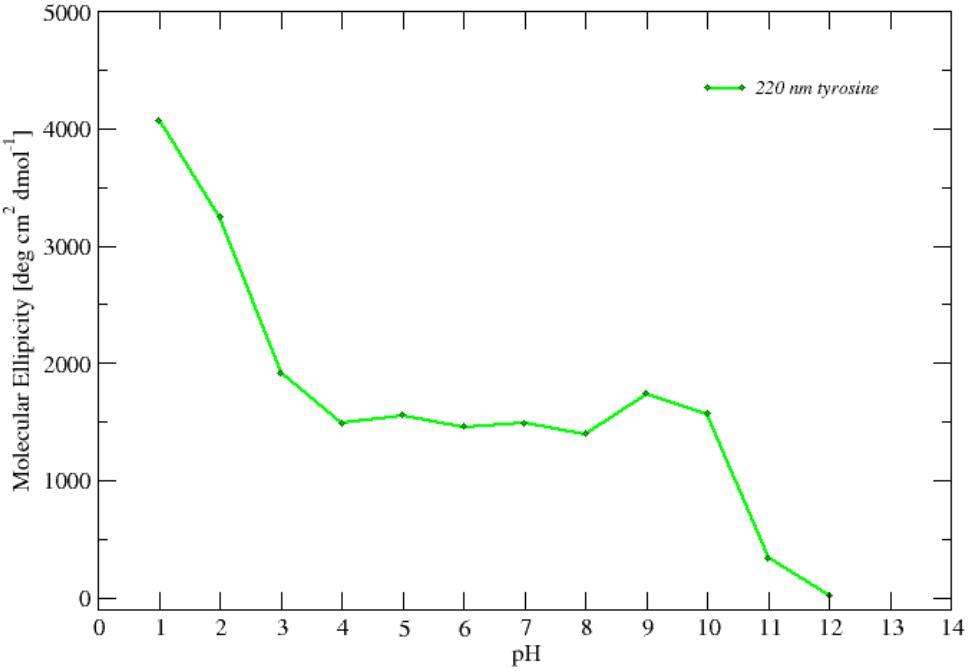


Figure 8.5: Molecular Ellipticity for tyrosine as a function of pH at 220 nm.

Interestingly, these measurements do not reveal a change for Met-Enkephalin between pH 2 and pH 4. If each CD-spectrum for each pH-value for Met-Enkephalin is subtracted from those of tyrosine, the only transition easily observed is that between pH 7 and 8, as well as the small change between pH 1 and 2, figure 8.6, which also is slightly perceptible in figure 8.4.

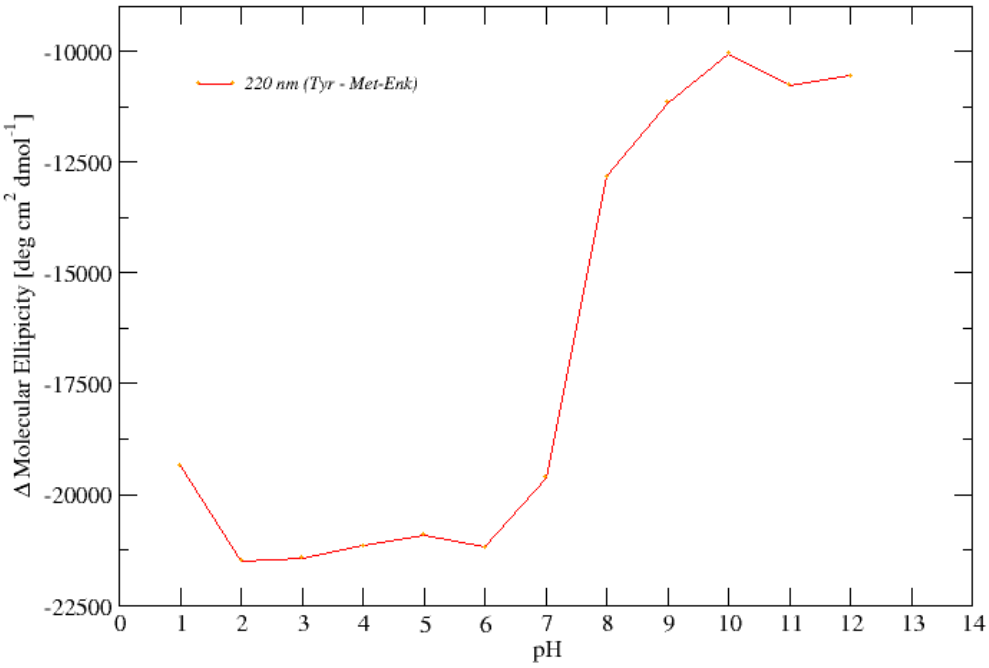


Figure 8.6: Molecular Ellipticity for Met-Enkephalin subtracted from tyrosine as a function of pH at 220 nm.

## *8.4 Discussion/Conclusion*

RDCs for unstructured peptides and proteins are, as mentioned previously, different from those of structured proteins, but they relate to the secondary structure of the backbone, and since we see changes this suggest the existence of structure in Met- and Leu-enkephalin apart from random coil.
Ohnishi and Shortle investigated several peptides (di-, tetra-, deca-, pentadeca-peptides) and found positive and negative RDC values in the range of + 5 to − 15 Hz [SOhnis03]. Louhivuori' et al. simulated a simple model of a random flight chain and showed that RDCs originate from the anisotropic structure of a chain and showed those contributions become smaller for longer chains, since large numbers of uncorrelated chain segments will go towards a more and more spherical distributions. Their simulations showed that RDCs are evenly distributed and of the same sign [MLouhi03]. This, clearly, is in contrast to our experiment, not just because the RDCs are not evenly distributed, but also due to RDCs of opposite sign for the different amino acids and the sign changes observed as a function of pH in figure 8.3. The portion of RDCs that can be attributed to the chain alone should be the same for random coil distributions at different pH-values, and since we see changes over the

pH range, this can be taken as evidence of conformational distributions other than random flight chain at different pH-values.
It was seen that the distribution of the NH-vector angles with the external magnetic field changed over the pH-range from 2 to 7 for Met-Enkephalin and pH 1 to 8 for Leu-Enkephalin. Since the angles of the NH-vectors with respect to the magnetic field can be seen as a conformational average [SOhnis03], we suggest that this implies that there exist different conformational distributions at different pH values.
The CD-measurements suggest different conformational states between pH 7 and 8 originating from the ionic state of the peptide. All together this shows that the ionic state of Enkephalin influences significantly its conformational distribution, and indicates conformational distributions different from random coil. With two different methods that track conformational changes, changes at the same pH values are observed and it is hence evident that the reason for these changes are due to changes in conformational distributions rather than due to electronic reasons.
The computation of one ore more conformations from residual dipolar couplings is difficult and would require more constraints pr. residue than measured here, but computation the other way around are feasible. Dipolar couplings calculated from an ensemble of stable conformations simulated by molecular dynamics [BNiels03] could be compared to those measured. However, more couplings would be prudent and could be obtained by measuring $C^{\alpha}$-$H^{\alpha}$, or H-H RDCs in the same system as used in these experiments.

# 9 Methods and Materials

## *9.1 NMR-spectroscopy:*

### *9.1.1 Chemical shift analysis*

The NMR spectra were recorded on recombinant $^{13}C$, $^{15}N$ double-labelled bovine ACBP on 750 MHz and 800 MHz Varian Unity Inova Instruments (T = 298K) and resonance assignments were made by triple resonance experiments; HNCA, HNCO, HNCACB, HN(CO)CA and $^{15}N$-$^{1}H$ HSQC spectra, as well as the previous sequential assignment by Jens K. Thomsen at pH 2.3. The protein was expressed and purified on (APK) by Jens K. Thomsen and Wolfgang Fieber as referred to in [WFiebe04]. All samples were prepared with 10 % $D_2O$ and the pH was adjusted with HCl or NaOH, no buffer was used except for the urea titration experiments, which contained a 10 mM Glycine buffer.
Very briefly described, these methods encompass the following:
**HNCA**, gives the correlation from the backbone amide resonances from both $^{1}H$ and $^{15}N$ to the $C^{\alpha}$ of the same residue, and most importantly to the $C^{\alpha}$ of the preceding residue. The typical values used in the data collection for HNCA spectra were; nt=2, ni=112, ni2=34, with number of points, spectral widths and transmitter/decoupler offsets; $^{1}H$: 1260, 8000 Hz, 4.773 ppm, $^{13}C$: 224, 6000 Hz, 55.998 ppm and $^{15}N$: 76, 1600 Hz, 118.013 ppm.
**HNCO**, gives the correlation from the backbone amide resonances from both $^{1}H$ and $^{15}N$ to the CO of the preceding residue. The typical values used in the data collection for HNCO spectra were; nt=2, ni=100, ni2=32, with number of points, spectral widths and transmitter offsets; $^{1}H$: 1260, 8000 Hz, 4.773 ppm, $^{13}C$: 200, 2000 Hz, 173.991 ppm and $^{15}N$: 64, 1600 Hz, 118.013 ppm.
**HN(CO)CA** experiments correlate the backbone amide $^{1}H$ and $^{15}N$ to the preceding residue $C^{\alpha}$ and the magnetization transfer takes place through the carbonyl carbon. The values used in the data collection for HN(CO)CA spectra were; nt=4, ni=112, ni2=36, with number of points, spectral widths and transmitter offsets; $^{1}H$: 1260, 8000 Hz, 4.812 ppm, $^{13}C$: 224, 6000 Hz, 56.044 ppm and $^{15}N$: 72, 1600 Hz, 118.070 ppm.
**HNCACB** correlates the same residues as HNCA, but additionally includes correlations to $C^{\beta}$. The values used in the data collection for HNCACB spectra were; nt=8, ni=116, ni2=38, with number of points, spectral widths and transmitter offsets; $^{1}H$: 1260, 8000 Hz, 4.812 ppm, $^{13}C$: 232, 16092.365 Hz, 46.042 ppm and $^{15}N$: 76, 1600 Hz, 118.070 ppm. This method was used for amino-acid type detection by means of the $C^{\beta}$ chemical shift as an additional parameter, when making the sequential assignment by HNCA and HN(CO)CA in the urea titration, while going from 0 M to 1 M urea. All NNR spectra of ACBP were transformed with nmrPipe software [FDelag95] and analysed using the program NMRView [BJohan94]. Typically the data was processed with an automated baseline correction. A squared sine-bell windows function was always used for apodization and automatic zero-filling in the first dimension and doubling of complex data points in the second dimension. Linear prediction in the indirect dimension was also used, mostly with prediction of data points before and after the complex data region.

### *9.1.2 Met and Leu-Enkephalin*

The NMR spectra were recorded on recombinant naturally abundant Met- and Leu-Enkephalin purchased as a lyophilized-powder from Bachem Feinchemikalien AG on 750 MHz and 800 MHz Varian Unity Inova Instruments (T = 298K).
**N-HSQC** recording values were typically: nt=128, ni=128, with number of points, spectral widths and transmitter offsets; $^{1}$H: 1360, 8000 Hz, 4.773 ppm and $^{15}$N: 256, 2000 Hz, 117.996 ppm.
**C-HSQC** recording values were typically: nt=128, ni=256, with number of points, spectral widths and transmitter offsets; $^{1}$H: 1360, 8000 Hz, 4.773 ppm and $^{13}$C: 512, 32000 Hz, 35.003 ppm.
**WROESY** recording values were typically: nt=8, ni=512, with number of points, spectral widths and transmitter offsets; $^{1}$H: 2730, 8000 Hz, 4.773 ppm. A mixing time of 250 ms was applied.
**HMBC** recording values were typically: nt=140, ni=256, with number of points, spectral widths and transmitter offsets; $^{1}$H: 1362, 8009 Hz, 4.773 ppm and $^{13}$C: 512, 32000 Hz, 99.991 ppm.
The data was typically processed as mentioned above for ACBP.

### *9.1.3 RDCs*

The residual dipolar couplings were measured in strained polyacrylamide gels. The polyacrylamide gels were made of 7 % w/v (acryl/bisacrylamide, 30:1 w/w) [HSass00], [RTycko00]. After polymerization in a cylindrical gel chamber with a inner diameter of 6 mm, the gels were washed with Milli-Q water for approximately 12 hours, after which they were washed with the appropriate buffer solution for at least 6 hours, the gels were after that left to equilibrate with the peptide solution in an Eppendorf tube over night, to allow the peptide to diffuse into the gel. The used concentrations in the equilibrating solution ranged from approximately 7 mM to 16 mM for both Met- and Leu-Enkephalin. The large concentration was needed for later measurements, where the cryo-probe on the NMR instruments were installed and reduced signal intensity due to the relatively high salt concentration of 100 mM KCl in the solution. The gels were transferred to the NMR-tubes by a special apparatus (NewEra Enterprise, Inc.) for the preparation of stretched polyacrylamide gels [JChou01]. The RDCs were sampled by gTOCSYNHSQC and IPAP-NHSQC spectra under isotropic ($^{1}J_{NH}$) and partially aligned ($^{1}J_{NH} + D_{NH}$) conditions on natural abundant Met- & Leu-Enkephalin purchased from Bachem AG in 100 mM KCl in 10% $D_2O$ at T = 298 K, at pH = 1 to 9, in steps of one pH unit. The RDCs were calculated as the difference between scalar couplings measured in the isotropic sample and total couplings in the oriented sample [AAlexa03]. Yielding, ($^{1}J_{NH}$) - ($^{1}J_{NH} + D_{NH}$) = - $D_{NH}$.
Collection of $^{15}$N-HSQC spectra without decoupling during acquisition leads to the evolution of NH couplings and doublet signals in the spectrum, but this setting in the standard HSQC leads to splitting in both $^{1}$H and $^{15}$N dimensions. The usage of gtocsyNhsqc pulse-sequence circumvents this problem. The IPAP-NHSQC experiment yields a $^{15}$N-{$^{1}H^{N}$} doublet in the Nitrogen-dimension.
**TOCSYNHSQC** recording values were typically: nt=512, ni=64, with number of points, spectral widths and transmitter offsets; $^{1}$H: 1366, 8000 Hz, 4.773 ppm and $^{15}$N: 128, 1700 Hz, 117.991 ppm. The data was processed with an automated baseline correction, a squared sine-bell function and automatic zero-filling in the first dimension and to a total of 1024 complex data points in the second dimension. Linear

prediction in the indirect dimension with prediction of data points before the complex data region was also applied.
**IPAP-HSQC** recording values were typically: nt=64, ni=198, with number of points, spectral widths and transmitter offsets; $^{1}$H: 1364, 8000 Hz, 4.773 ppm and $^{15}$N: 386, 1900 Hz, 117.988 ppm. The data processing was as described for TOCSYNHSQC, except with zero-filling to a total of 2048 complex data points for the indirect dimension and linear prediction before and after the complex data region.

### *9.2 CD, refractive index etc.*

All samples were prepared in 10% $D_2O$ and the pH was adjusted with HCl or NaOH without taking the H/D isotope effect into account [PGlasoe60] and in all cases measured with a glass electrode. $PK_a$ changes of side-chain groups counter balance this effect, yielding the same ionisation state of the protein in $D_2O$ and $H_2O$ [ABundi79], [GMakha95].
Concentrations were determined by far-UV absorbance at 280 nm.
Urea and guanidine hydrochloride concentrations were determined by refractive index (refractrometry) [YNozak72].
The circular dichroism measurements were made on a Jasco 810 spectra-polarimeter in the far UV region from approximately 190 to 250 nm or shorter at 298 K. Quartz cells with 0.1 cm path-length were used and typically data collection for all CD-measurements were: data point collection of 0.1 nm in continuous mode, with a scanning speed of 20 nm/min, 4 scans and a response time of 2-4 seconds.
Concentrations for CD measurements were in the 1-100 μM range.

# Appendix A

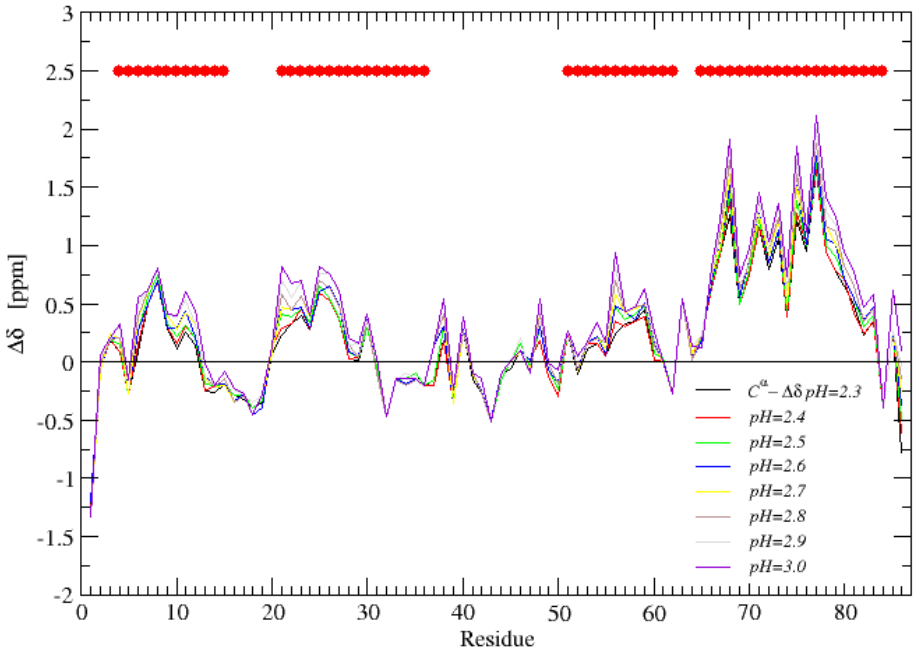


Figure A.1: Secondary $C^{\alpha}$ chemical shifts as function of residue position for pH from 2.3 to 3.0. The concentration of ACBP was 58 µM. The red circles denote the location of the four α-helices in the native structure of ACBP.

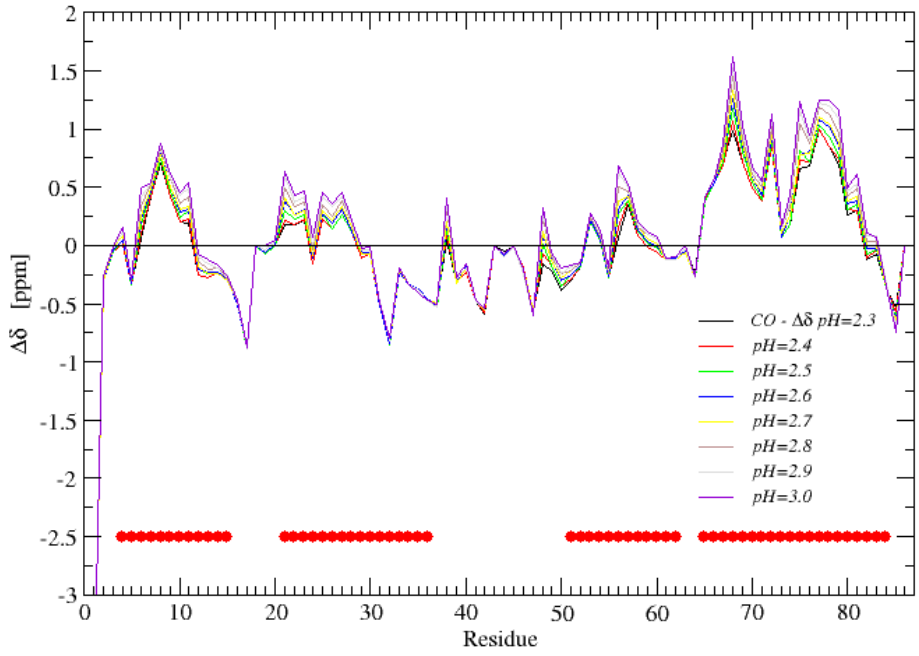


Figure A.2: Secondary CO chemical shifts for ACBP for pH values from 2.3 to 3.0. Concentration of ACBP was 58 μM. The Red circles indicate the location of the four α-helices in the native structure.

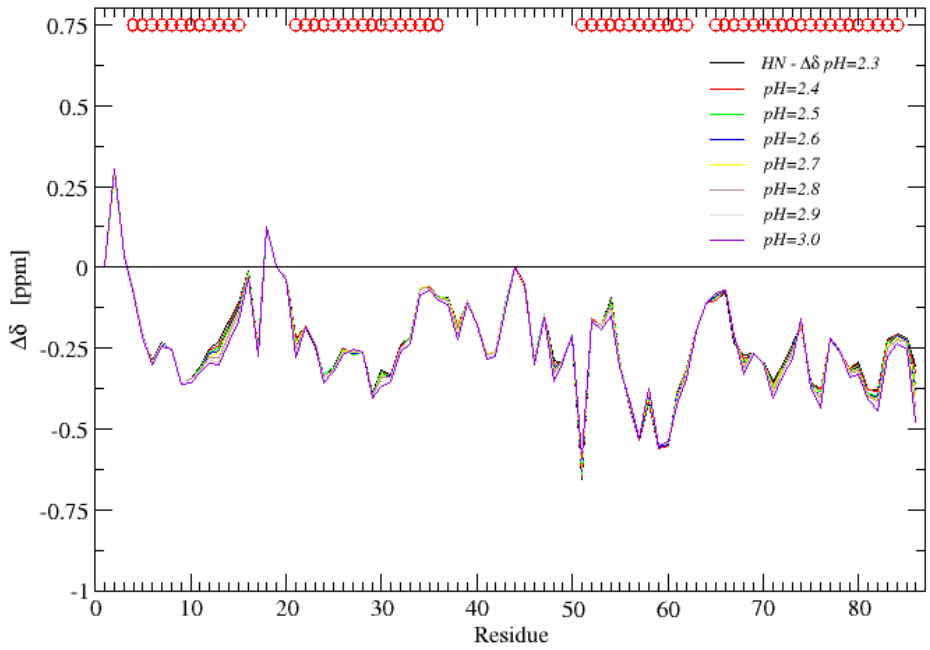

Figure A.3: Secondary $H^N$ chemical shifts for ACBP for pH values from 2.3 to 3.0. The Concentration of ACBP was 58 µM. The red circles indicate the location of the four α-helices in the native structure.

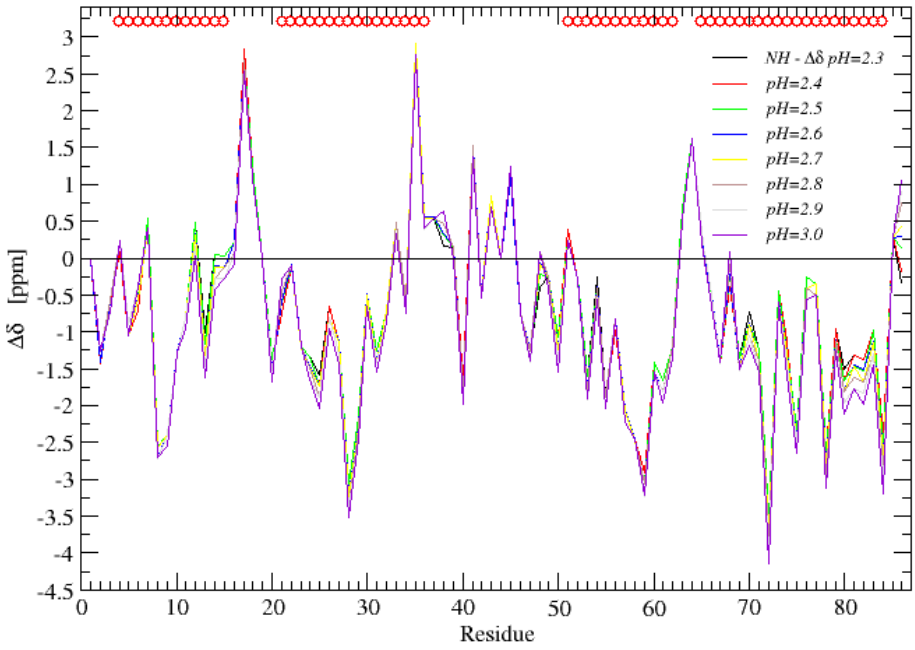


Figure A.4: Secondary NH chemical shifts for ACBP for pH values from 2.3 to 3.0. The Concentration of ACBP was 58 µM. The red circles indicate the location of the four α-helices in the native structure.

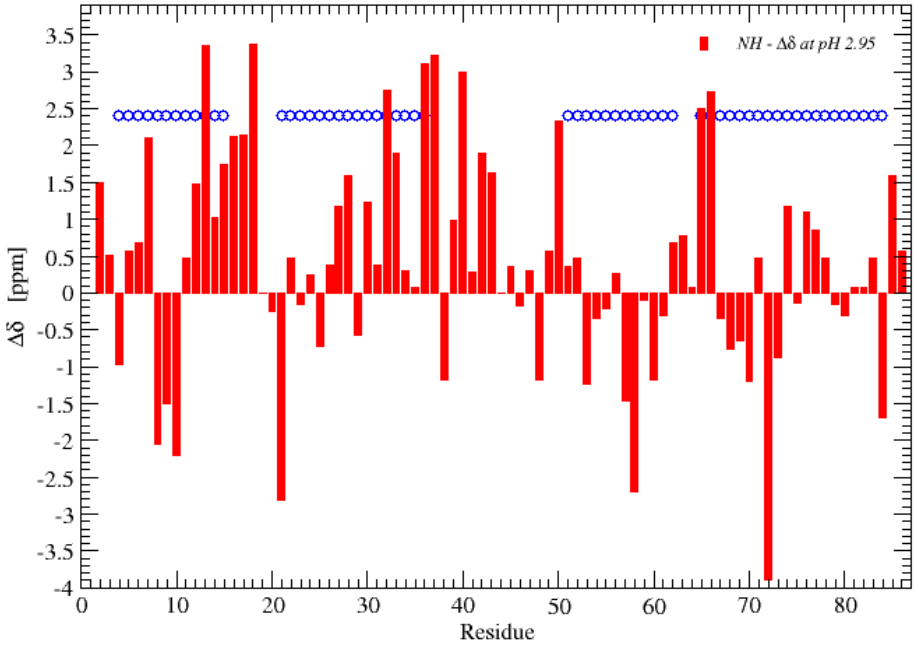


Figure A.5: Secondary NH chemical shifts for ACBP for pH 2.95. The concentration of ACBP was ~ 0.5 mM. The blue circles indicate the location of the four α-helices in the native structure.

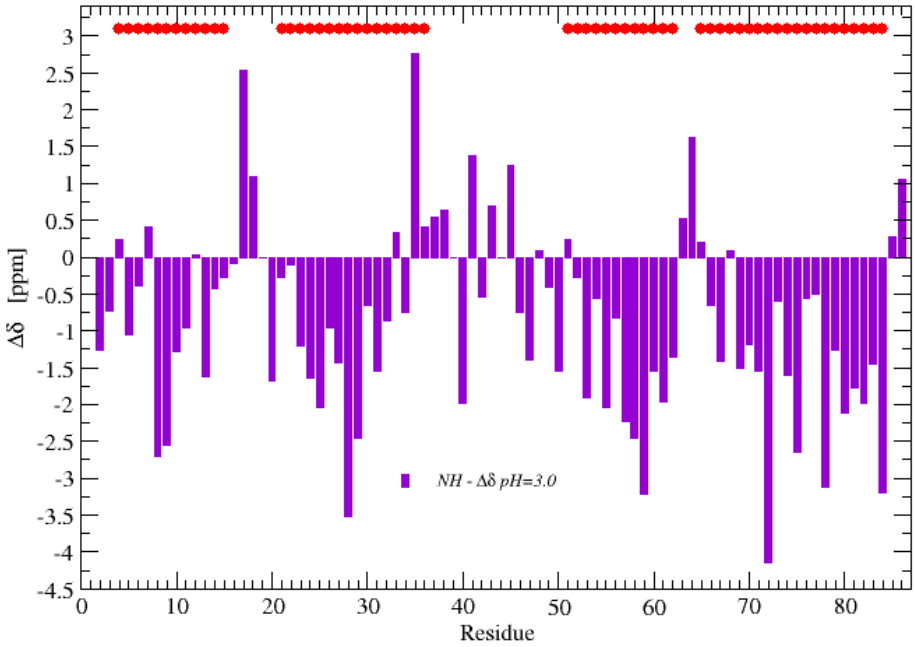


Figure A.6: Secondary NH chemical shifts as a function of residue position at pH

3.0. The concentration of ACBP was 58 µM. The red circles denote the location of the four α-helices in the native structure.

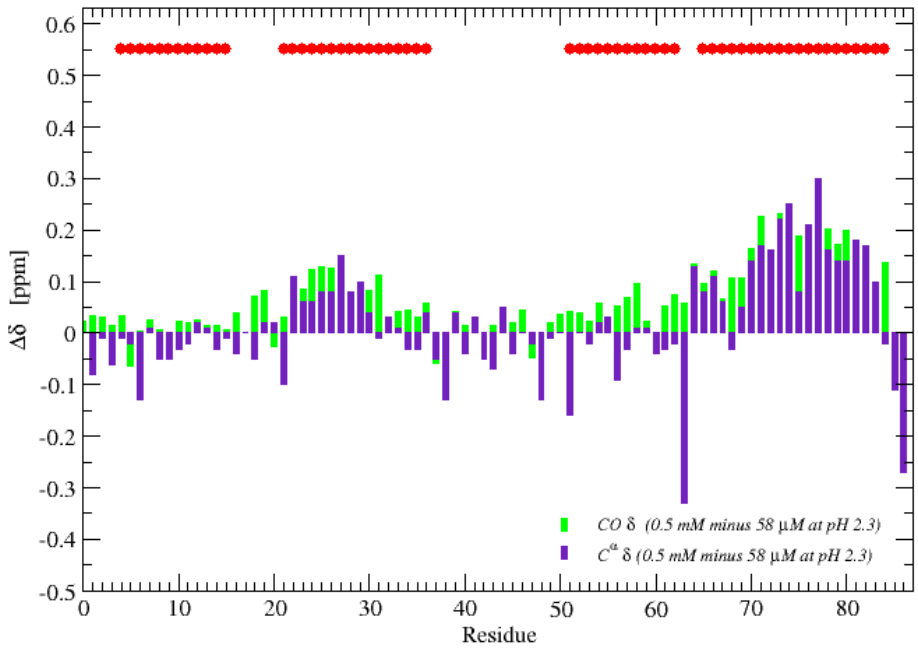


Figure A.7: CO and $C^{\alpha}$ chemical shift difference between the two measured concentrations at pH 2.3 as a function of residue position. (Data from 0.5 mM series minus 58 µM data series).

# Appendix B

Table B.1: Force constants as used for the Monte Carlo Simulations:
Force constants for chemical shifts calculated as: $\lambda=1/(a*b)$, a is the average shift over all experimental values, b is RMSD for the particular shift as given in Neal et al., J.Bio. NMR, 26: 215-240, 2003.

| RMSD / correlation coefficient | pH 2.7 | pH 2.3 |
|---|---|---|
| b=0.23 $^{1}H^{\alpha}$: 0.911 | $C^{\alpha}$: $\lambda$ = 3.7792895 | $C^{\alpha}$: $\lambda$ = 5.647036289 |
| b=0.98 $^{13}C^{\alpha}$: 0.980 | CO: $\lambda$ = 28.31487317 | CO: $\lambda$ = 27.87368493 |
| b=1.10 $^{13}C^{\beta}$: 0.996 | HN: $\lambda$ = 0.250065717 | |
| b=1.16 $^{13}$CO: 0.863 | NH: $\lambda$ = 0.0034193821 | |
| b=2.43 $^{15}$N: 0.909 | | |
| b=0.49 $^{1}$HN: 0.741 | | |
| b=0.30 $^{1}$H-sidechains: 0.907 | | |

Table B.2: Example of restraint input:

```
CONS DIHEdral BYNUM 640 642 644 653 FORCE 2.0 MIN -62.0 WIDTh 90.0
CONS DIHEdral BYNUM 642 644 653 655 FORCE 2.0 MIN -41.0 WIDTh 60.0

CONS DIHEdral BYNUM 653 655 657 663 FORCE 2.0 MIN -62.0 WIDTh 90.0
CONS DIHEdral BYNUM 655 657 663 665 FORCE 2.0 MIN -41.0 WIDTh 60.0

CONS DIHEdral BYNUM 663 665 667 672 FORCE 2.0 MIN -62.0 WIDTh 90.0
CONS DIHEdral BYNUM 665 667 672 674 FORCE 2.0 MIN -41.0 WIDTh 60.0

CONS DIHEdral BYNUM 672 674 676 678 FORCE 2.0 MIN -62.0 WIDTh 90.0
CONS DIHEdral BYNUM 674 676 678 680 FORCE 2.0 MIN -41.0 WIDTh 60.0

CONS DIHEdral BYNUM 678 680 682 687 FORCE 2.0 MIN -62.0 WIDTh 90.0
CONS DIHEdral BYNUM 680 682 687 689 FORCE 2.0 MIN -41.0 WIDTh 60.0
```

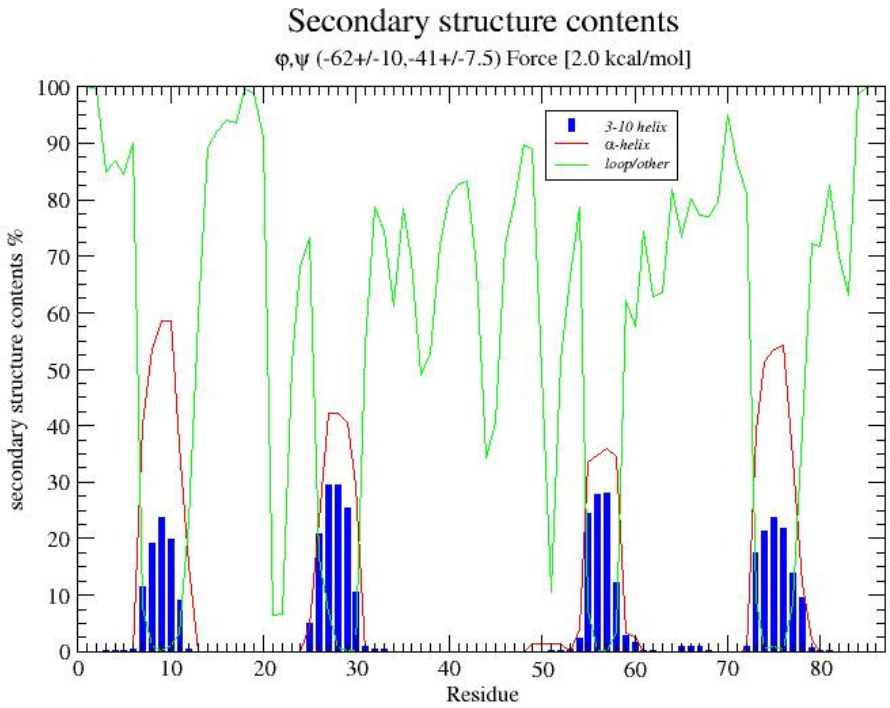


Figure B.1: Secondary structure contents at φ,ψ: [–62 ± 10], [–41 ± 7.5] and a force of 2.0 kcal/mol. Note that the amount of α-helix (red line) is slightly larger here than in the simulations used for the actual Monte Carlo simulations.

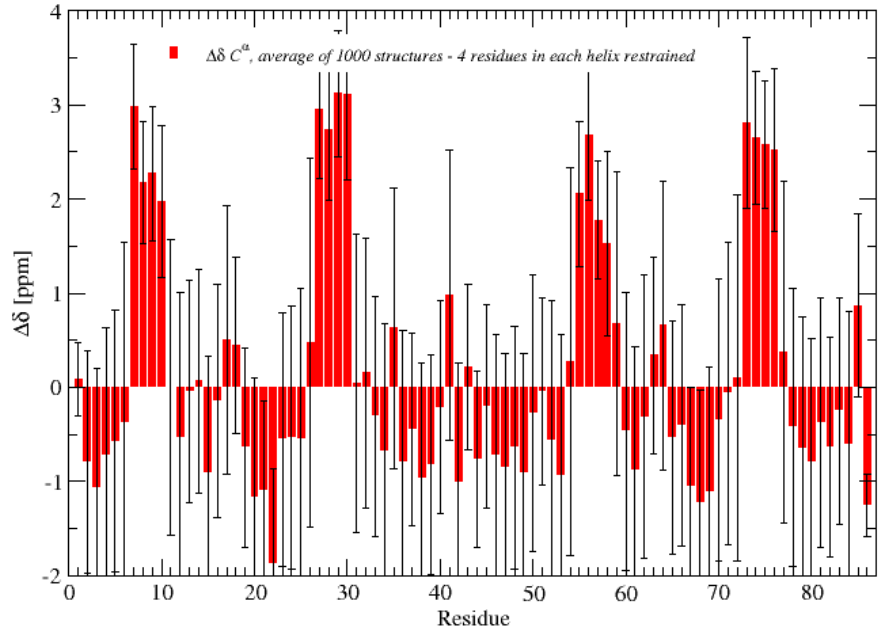


Figure B.2: $C^{\alpha}$ secondary chemical shift; φ,ψ were [-62.0±50], [-41.0±15], force was 10.0 kcal/mol and the random coils values were those from Wishart et al. 1995 [DWisha95]. The secondary chemical shifts were calculated over an average of 1000 structures.

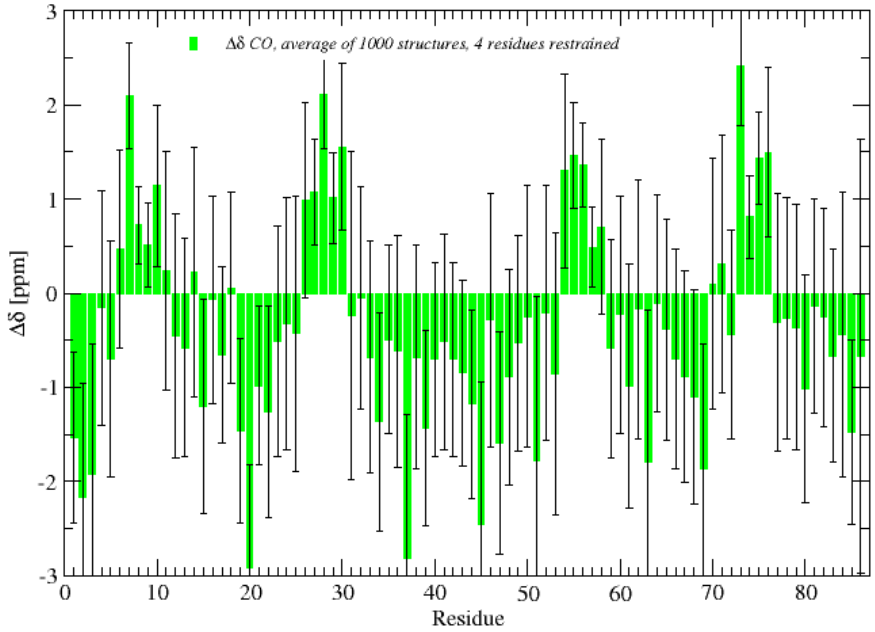


Figure B.3: CO secondary chemical shifts; φ,ψ were [-62.0±50], [-41.0±15], force was 10.0 kcal/mol and the random coils values were those from Wishart et al. 1995 [DWisha95]. The secondary chemical shifts were calculated over an average of 1000 structures.

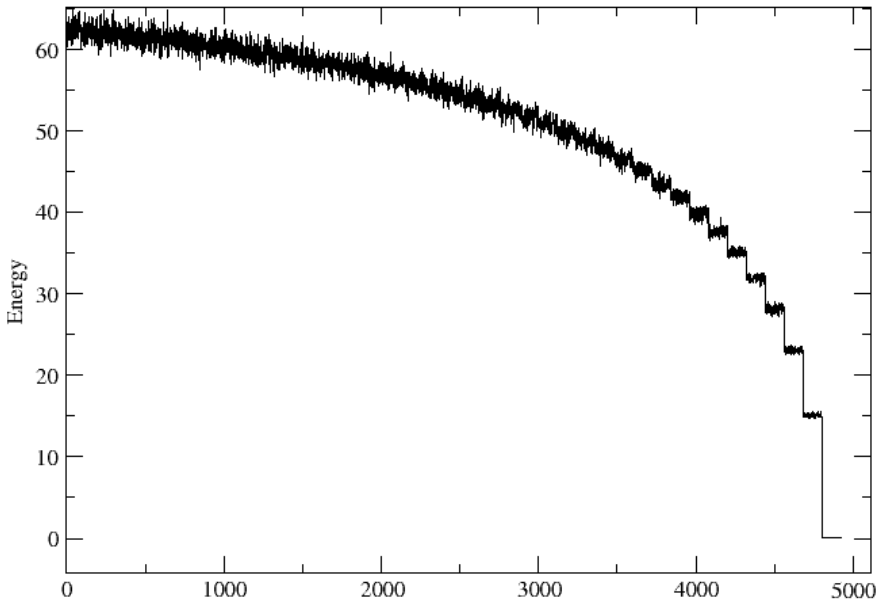


Figure B.4: Trajectory of the energy saved at every 100000 step over the course of the temperature interval [0.1, 0.00001][b].

[b:] for MC-simulations where $C^{\alpha}$ chemical shifts at pH 2.7 were used as restraints.

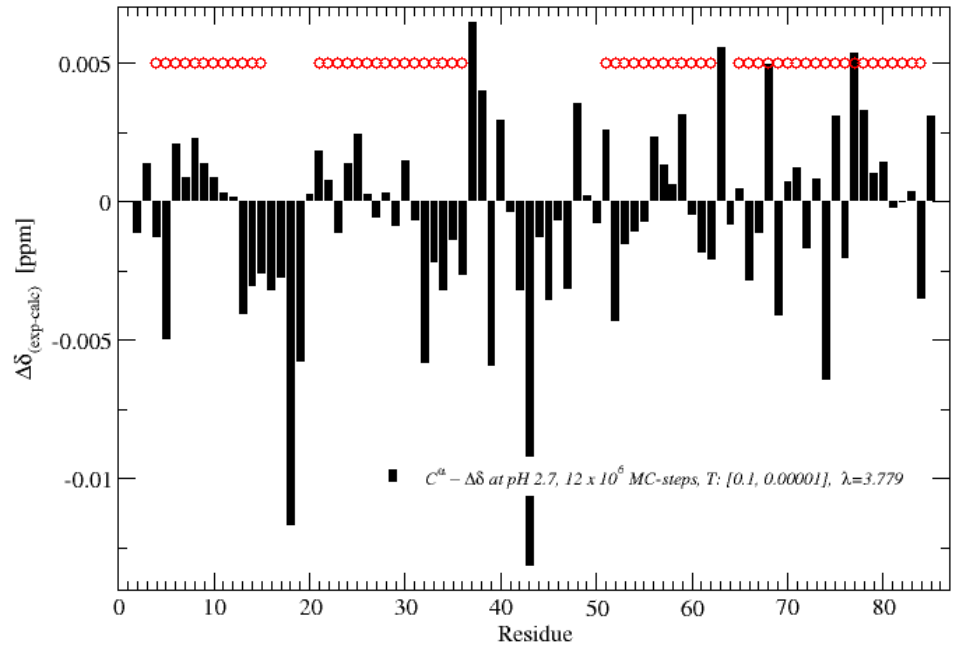


Figure B.5: The difference between experimental and calculated secondary chemical shifts for $C^{\alpha}$ at pH 2.7. The temperature interval was 0.1 to 0.00001 K, with 40 temperature decreases and 12 million Monte Carlo steps at each temperature. The red circles denote the location of the four α-helices in the native structure of ACBP.

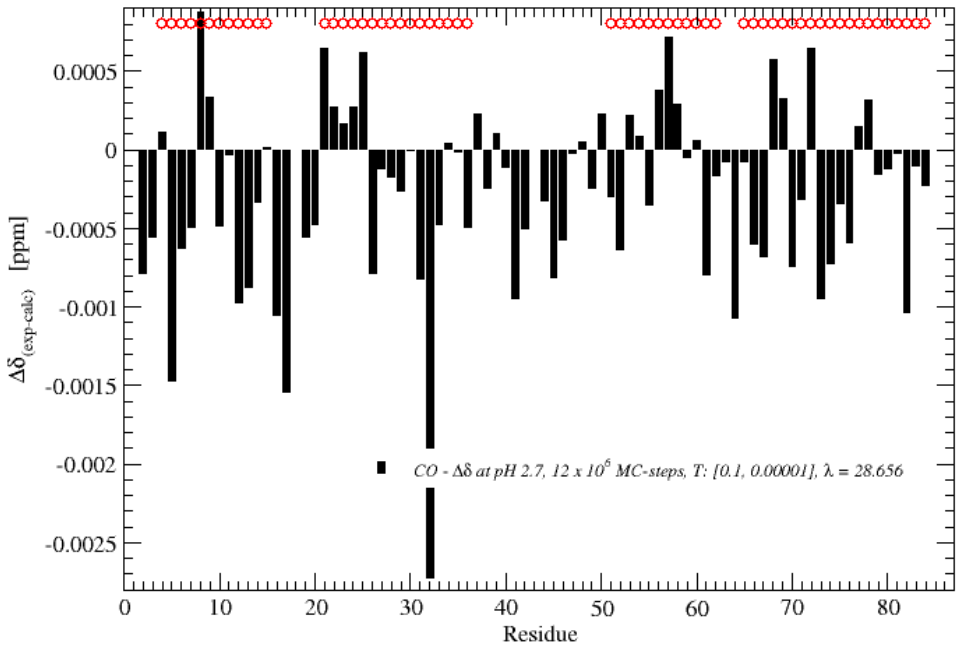


Figure B.6: The difference between experimental and calculated secondary

chemical shifts for CO at pH 2.7. The temperature interval was 0.1 to 0.00001 K, with 40 temperature decreases and 12 million Monte Carlo steps at each temperature. The red circles denote the location of the four α-helices in the native structure of ACBP.

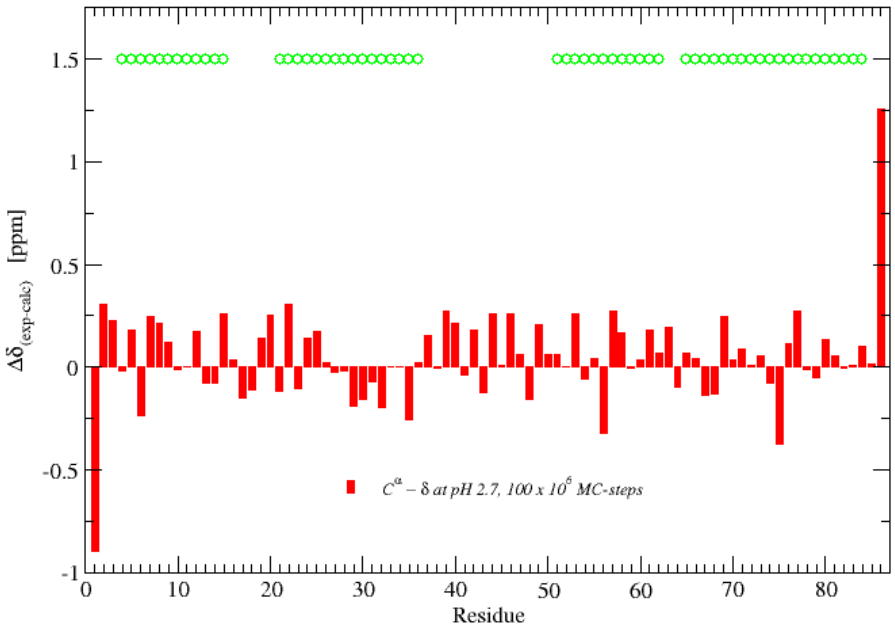


Figure B.7: Difference between the absolute experimental and calculated chemical shifts for $C^{\alpha}$ at pH 2.7. Note the relative large absolute difference in ppm as compared to the differences in e.g. figure B.5.

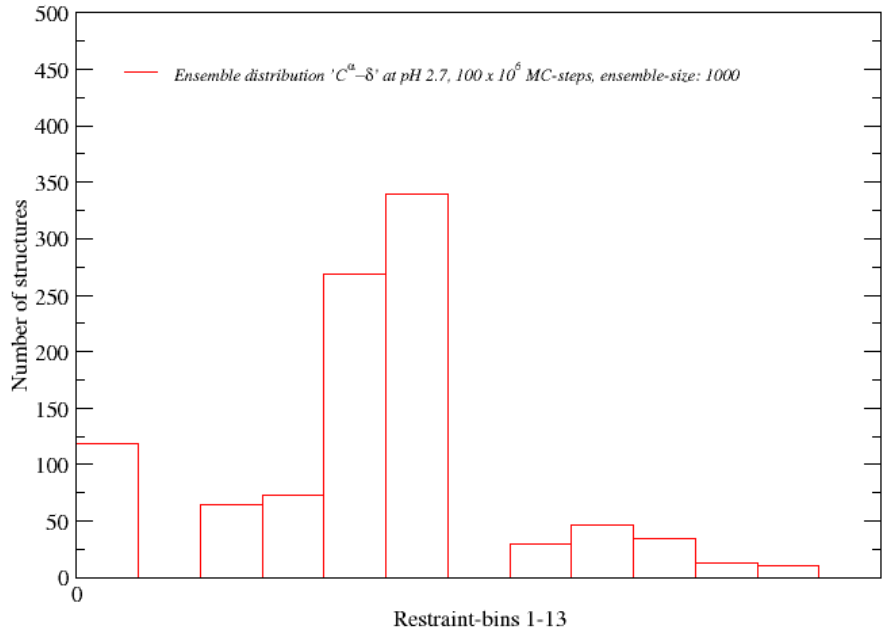


Figure B.8: Distribution between the different Restraint-bins from table 6.1 for $C^{\alpha}$ at pH 2.7 where absolute chemical shifts were used for the energy minimization. It was noted that no structures from Restraint-bin 13 were present, indicating no random coil structures present in the ensemble. The total number of structures in this simulation was 1000.

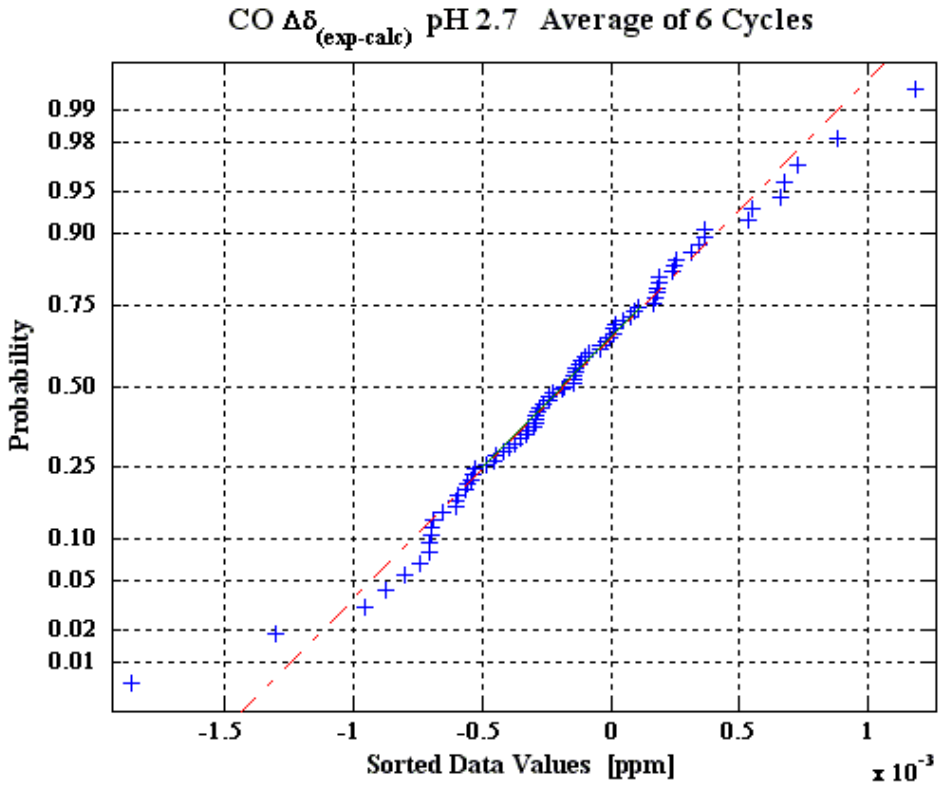


Figure B.9: Normal probability plot for MC-simulation with CO chemical shifts used as restraint at pH 2.7. In the case of a random distribution, the data (blue crosses) should be evenly distributed around the straight line and not diverge from

it at the ends.

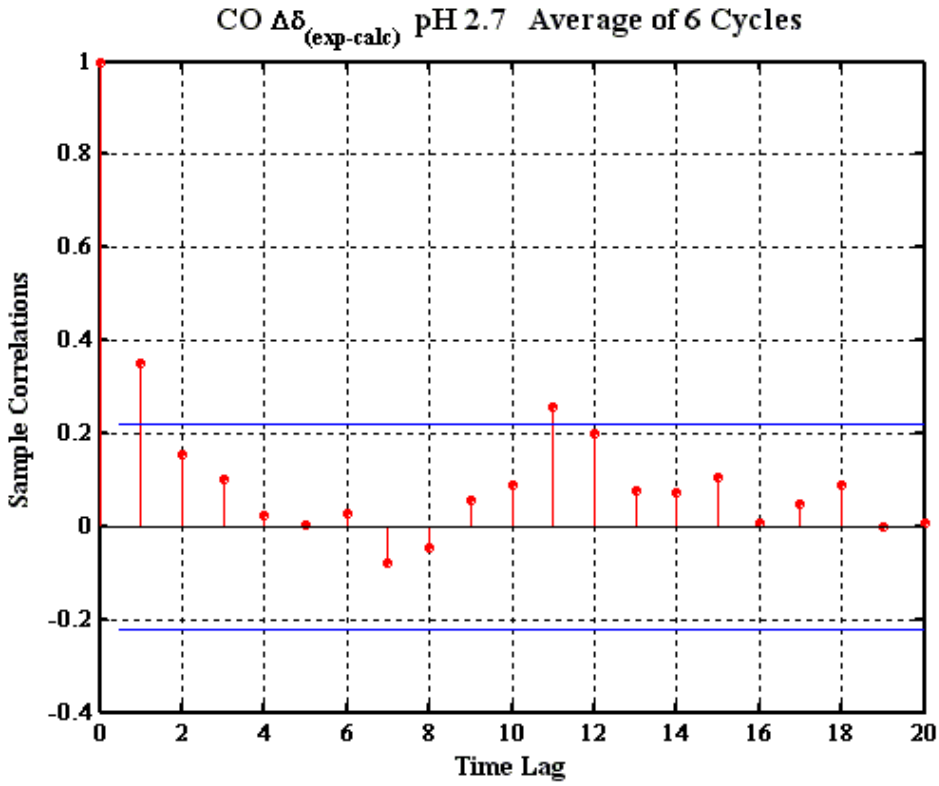


Figure B.10: Autocorrelation plot for CO at pH 2.7. The autocorrelation plots periodicity exposes the non-randomness. The two red lines at approximately ± 0.2 are 2 times the standard deviation of the correlation. If the lag fails to converge under this value within a few lags, this would be another indication for non-randomness. Here the data fall under this line quite fast, but strictly speaking this value can just be used if the data is random.

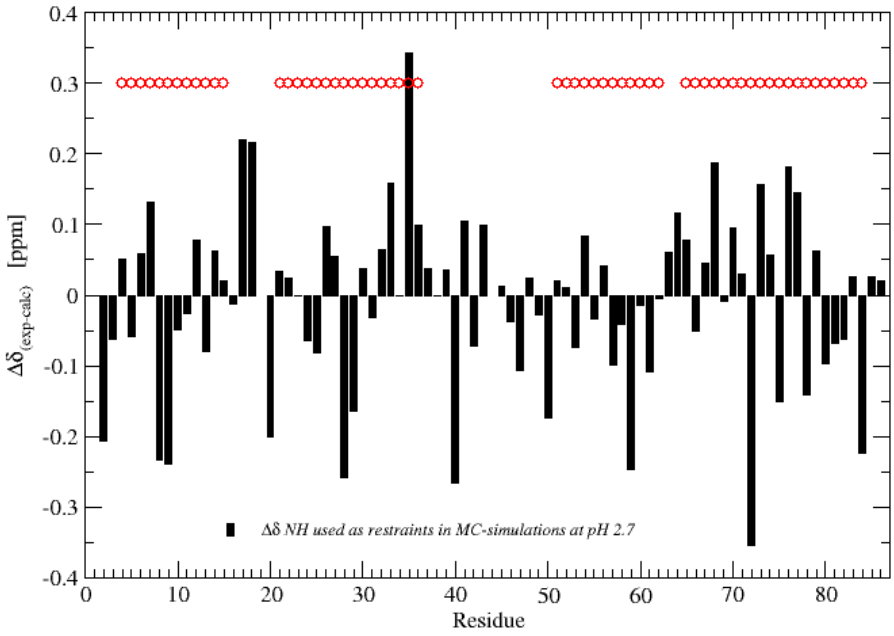


Figure B.11: Difference between the NH secondary experimental and calculated chemical shifts at pH 2.7. Note the relative large difference in ppm as compared to the differences in e.g. figure B.5.

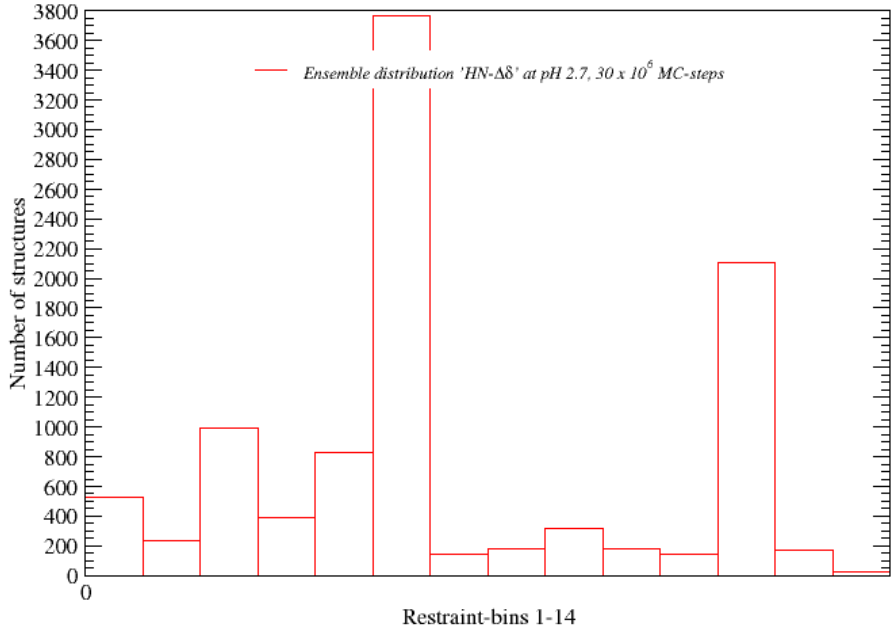


Figure B.12: Distribution of the ensemble found during MC simulations where HN chemical shifts were used as restraints at pH 2.7. Note the small contents of Restraint-bin 13, which is approximately 2%.

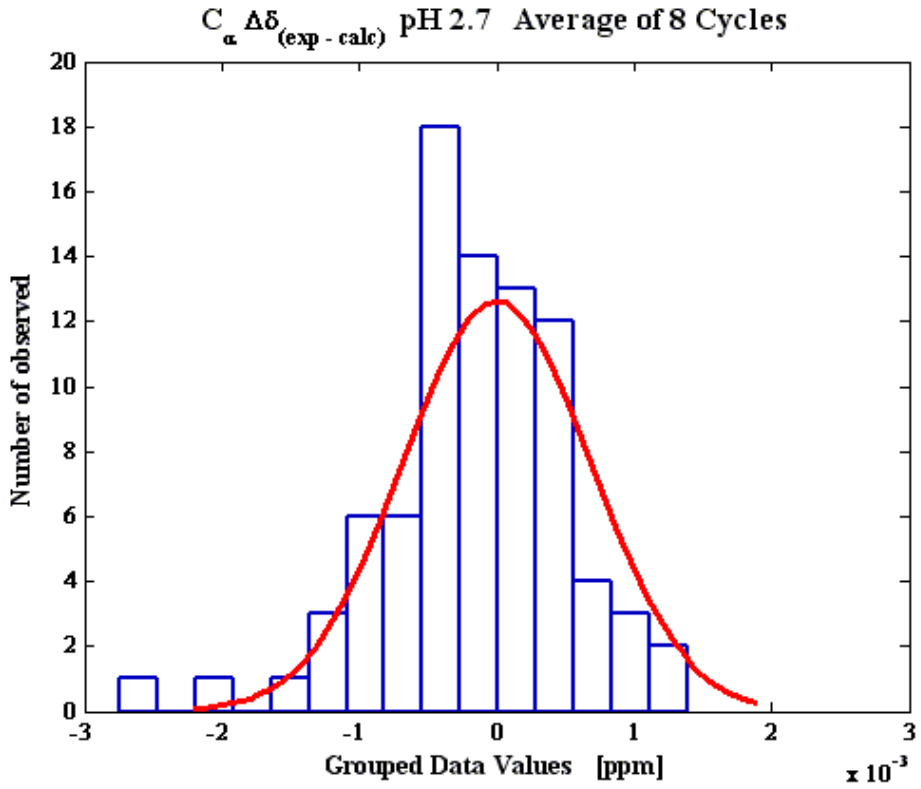


Figure B.13: Histogram of the spreading of data ($C^{\alpha}_{experimental}$ - $C^{\alpha}_{calculated}$) from 8 MC simulation cycles. The overlay is a Normal distribution, where it is noted that the differences not follow a normal distribution.

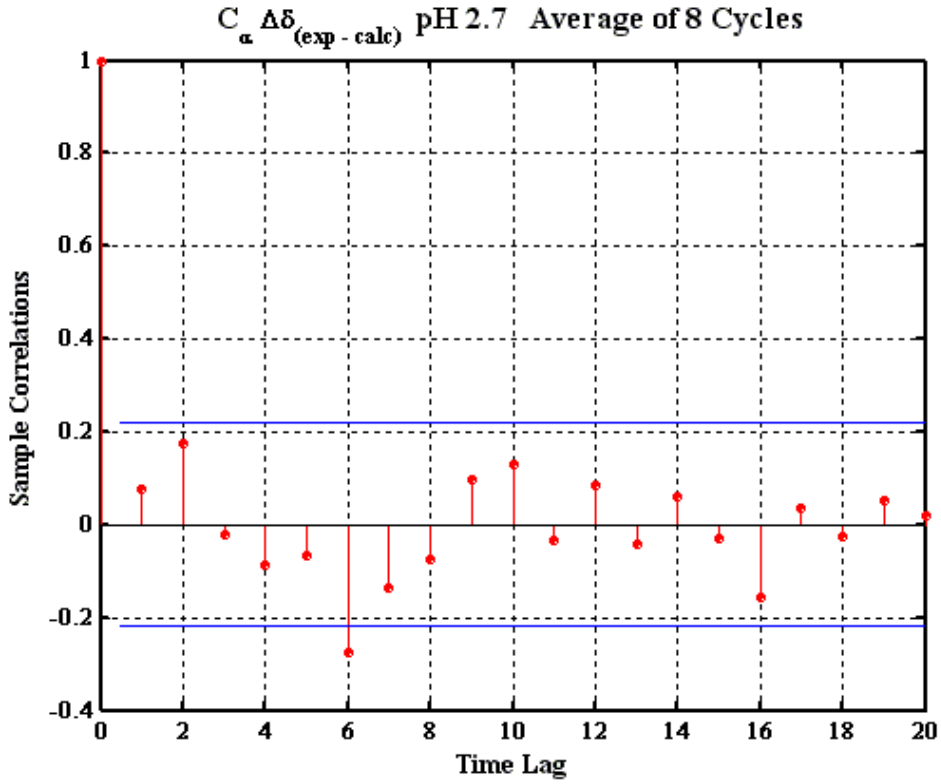


Figure B.14: Autocorrelation plot of the data from 8 MC simulation cycles ($C^{\alpha}_{,experimental}$ - $C^{\alpha}_{,calculated}$). The autocorrelation plots periodicity exposes the non-randomness. The two red lines at approximately ± 0.2 are 2 times the standard deviation of the correlation. If the lag fails to converge under this value within a few lags, this would be another indication for non-randomness.

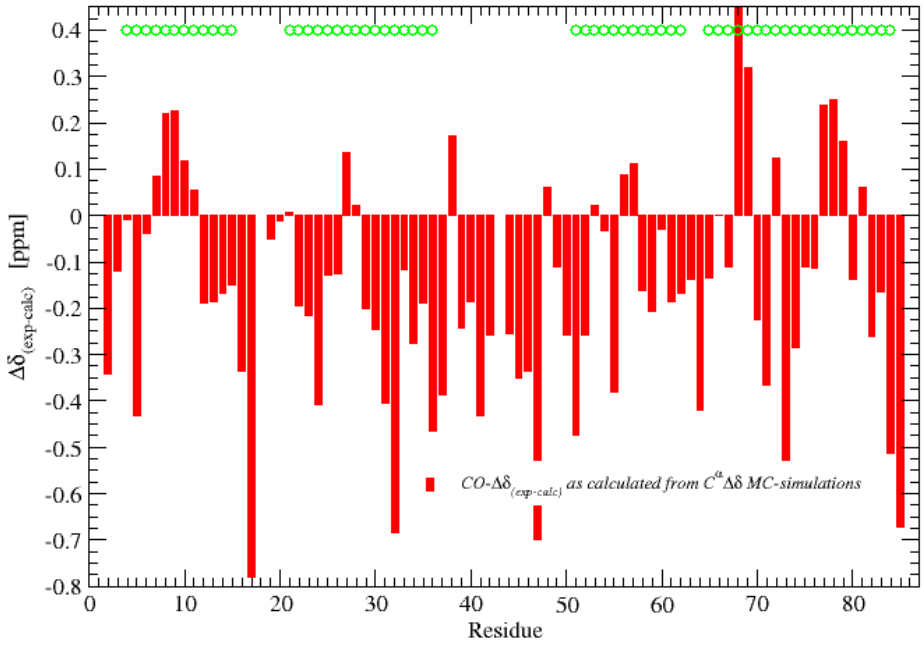


Figure B.15: Difference between experimental CO secondary chemical shifts and calculated chemical shifts produced on the basis of an ensemble of structures found during a MC-simulation where $C^{\alpha}$ chemical shifts were used as restraint at pH 2.7.

# Appendix C

Table C.1: Measured and adjusted reference values for all urea concentrations.

| Urea concentration | Transmitter offset | Tof-adjusted |
|---|---|---|
| 1.097 | 4.773 | 4.812 |
| 2.188 | 4.773 | 4.836 |
| 3.083 | 4.773 | 4.860 |
| 4.102 | 4.773 | 4.892 |
| 5.093 | 4.773 | 4.931 |

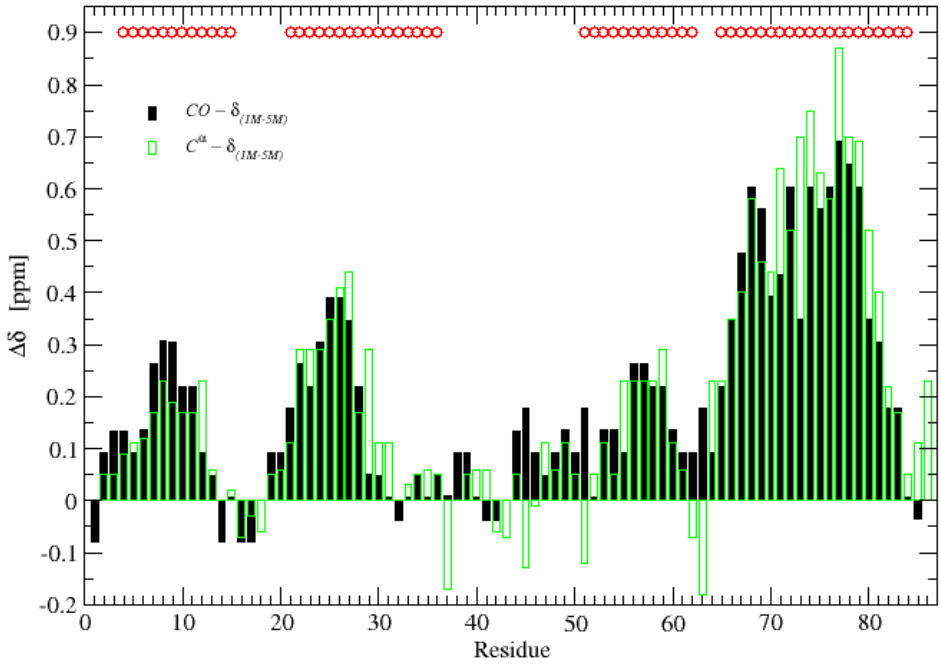


Figure C.1: Difference of the $C^{\alpha}$ and CO chemical shifts between 1M and 5M urea as a function of residue. Black: $C^{\alpha}$-δ at 1M minus 5M urea. Green: CO-δ at 1M minus 5M urea. Note that there might exist a factor like binding, which could influence distinct areas of the peptide sequence differently.

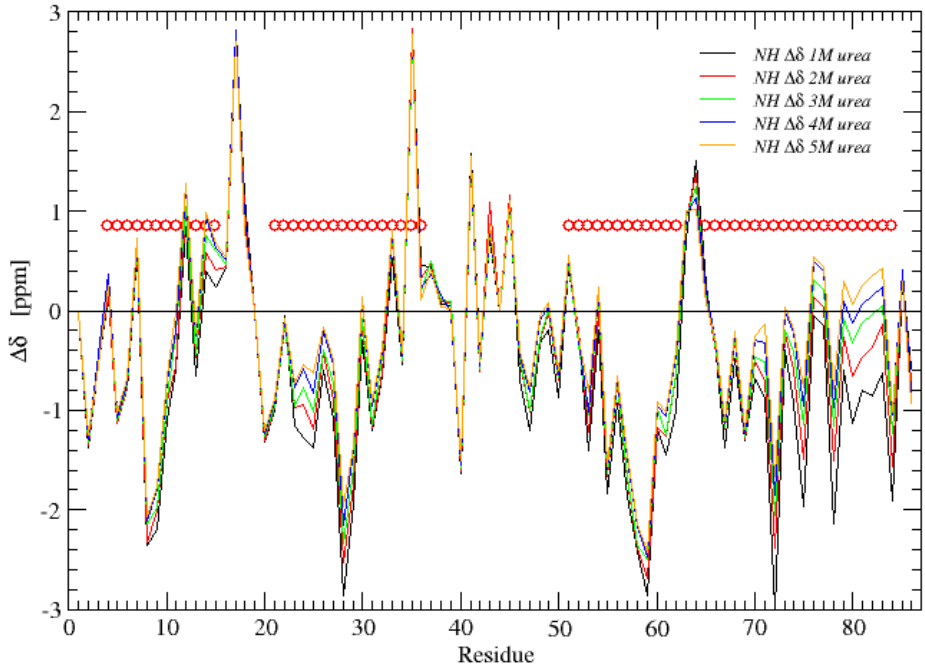


Figure C.2: $^{15}N$ secondary chemical shifts for urea concentrations from 1.1 to 5.1. The amide nitrogen doesn't change much over the range of urea concentrations, but exhibit large offsets up to ± 3 ppm from the random coil. Note that the loop residues seem to be responsible for the largest positive off sets.

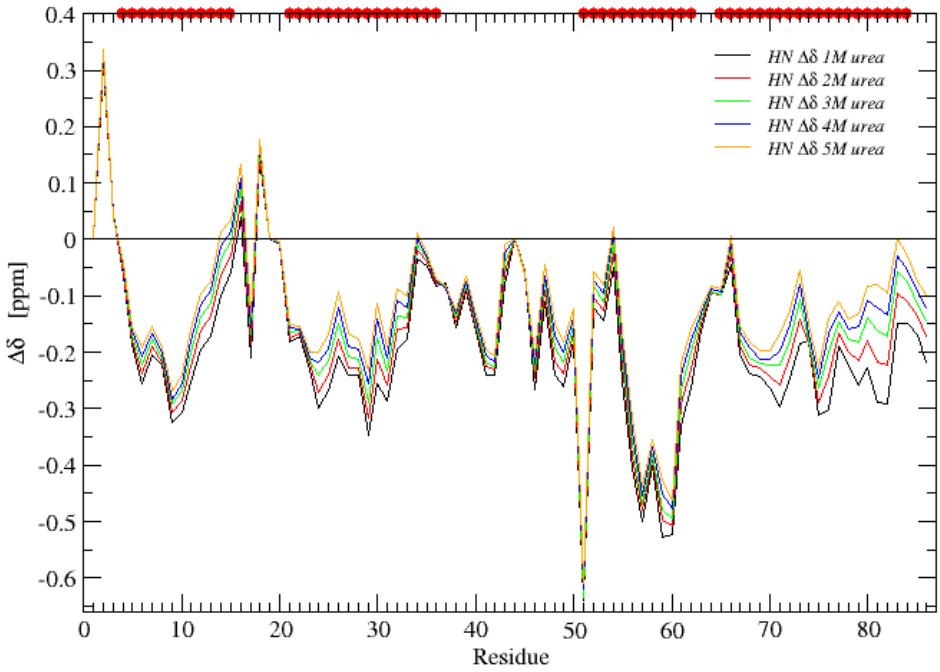


Figure C.3: $^{1}$H secondary chemical shifts for urea concentrations from 1.1 to 5.1. Largest offsets from random coil values are seen in the segments of the peptide sequences corresponding to helices A4, part of A3, A2 and A1 in the native structure. The changes are minimal over the interval form 1 to 5 M urea, with the greatest changes occurring in the regions A4, A2 and A1.

# Appendix D

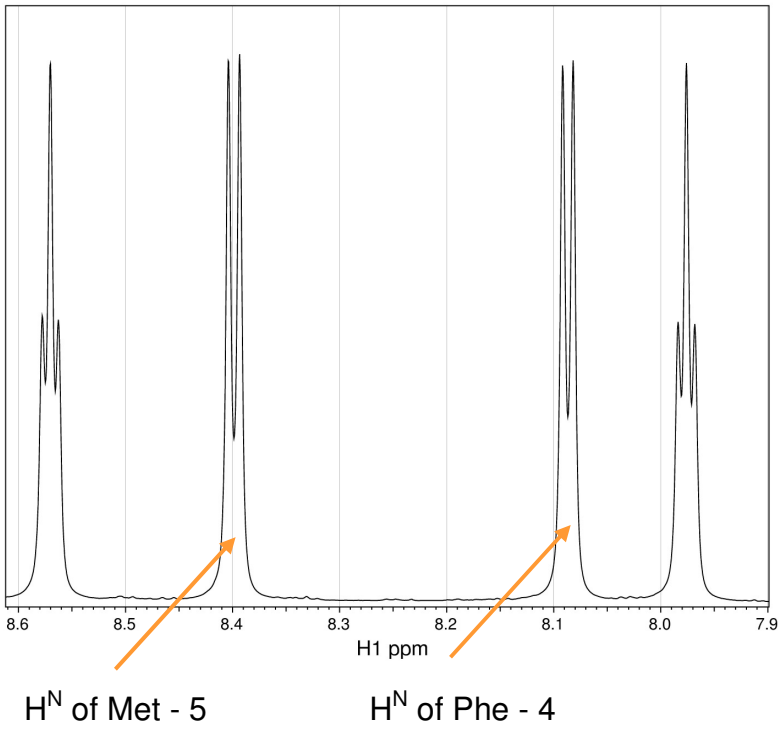


Figure D.1: $^{1}$H-spectrum of the amide region of Met-Enkephalin at pH = 2.

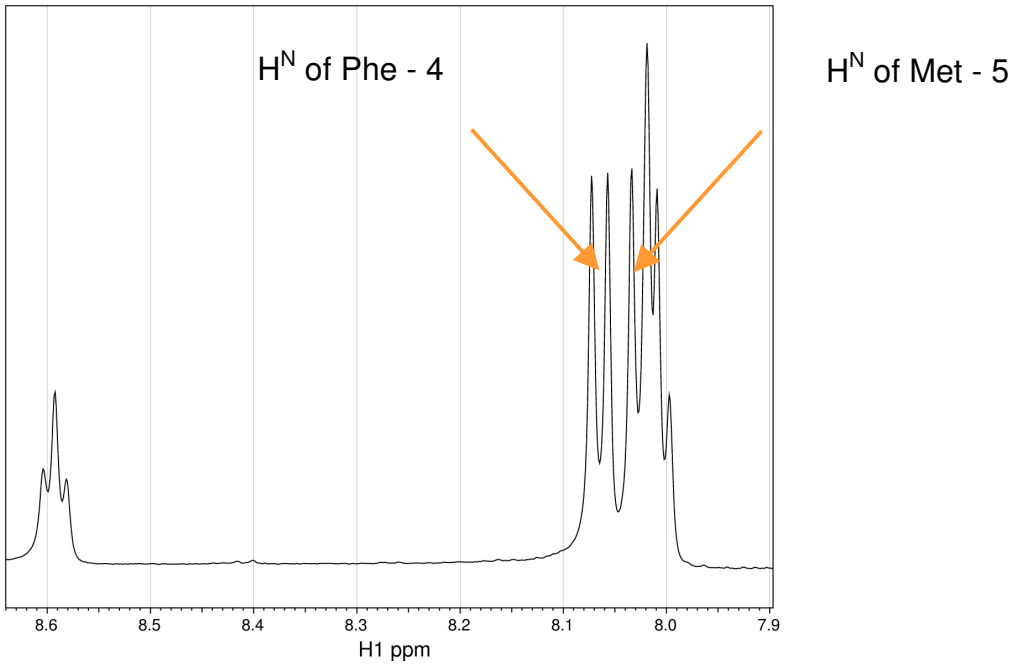


Figure D.2: $^{1}$H-spectrum of the amide region of Met-Enkephalin at pH = 4.

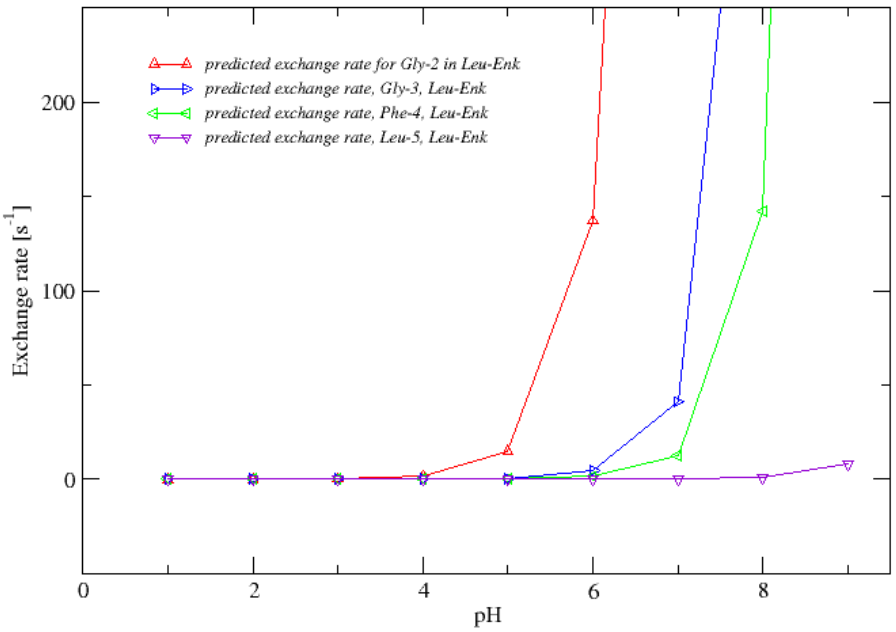


Figure D.3: Calculated exchanges rates for Leu-Enkephalin, with the program SPHERE [YZhang]. It can be seen that the Gly-2 exchange rate already is increased at pH 5, and cannot be measured at pH 6, whereas the remaining residues follow at subsequent pH values

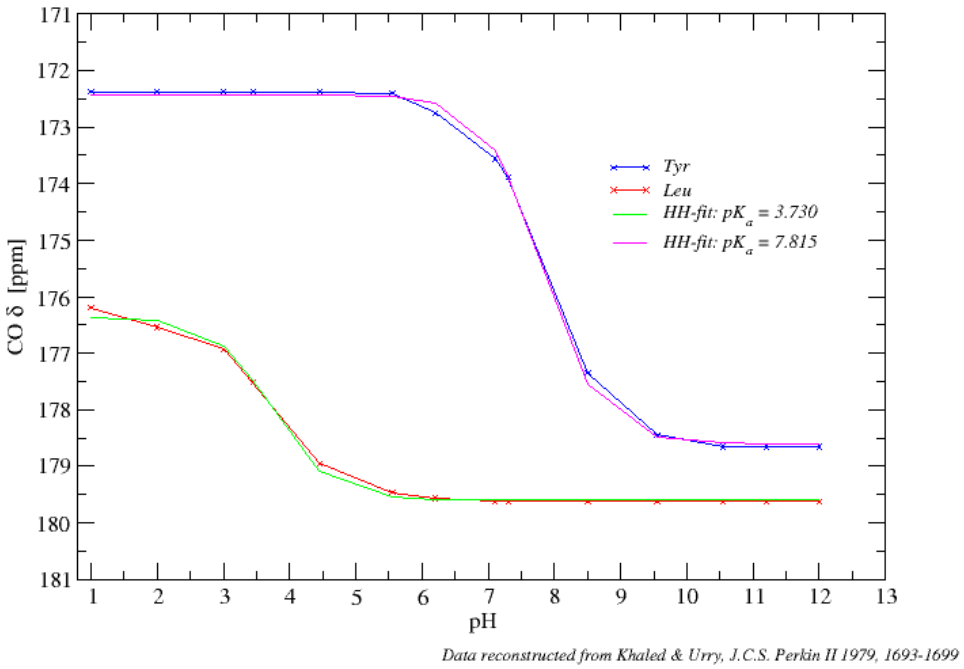


Figure D.4: $pK_a$ –values for Leu-Enkephalin as reconstructed from the data of carbonyl chemical shifts from Khaled et al. [MKhaled79] fitted with the Henderson–Hasselbalch equation yielding $pK_a = 3.7$ and $pK_a = 7.8$.

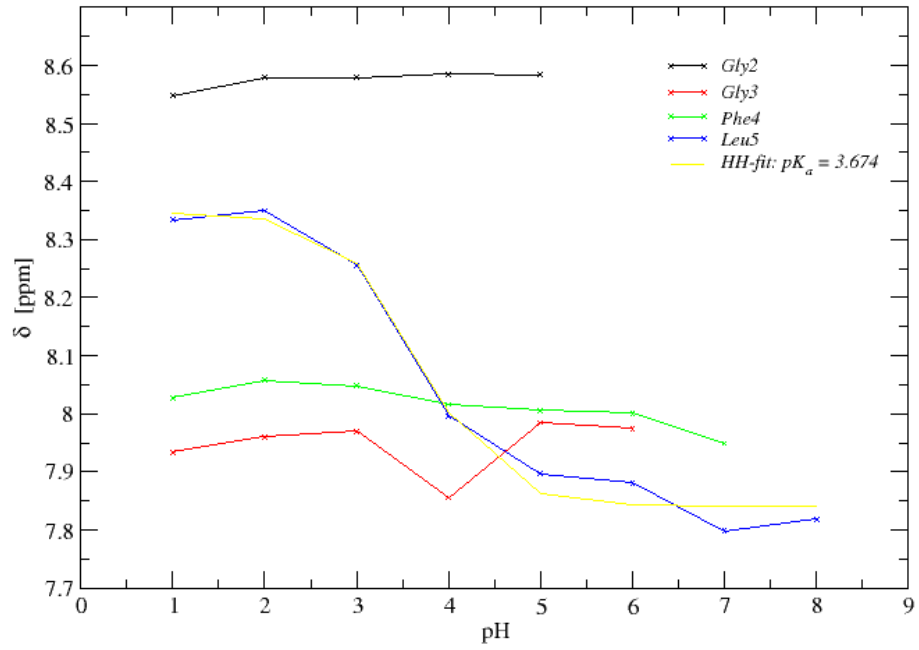


Figure D.5: $pK_a$ –value for Leu-Enkephalin. Fitted by Henderson–Hasselbalch equation to $H^N$ chemical shifts as function of pH, yielding a $pK_a$ of 3.7. Chemical

shifts at pH values 1, 2, 3, 5, 6 and 8 were measured with IPAP_NHSQC, whereas chemical shift values at pH 4 and 7 were measured by TOCSYNHSQC.

# Bibliography

[AAlexa03] A. Alexandrescu & R. A. Kammerer, (2003) Structure and disorder in the ribonuclease S-peptide probed by NMR residual dipolar couplings, Protein Science, 12, 2132-2140.

[AAlmon02] A. Almond & J. B. Axelsen, (2002) Physical Interpretation of Residual Dipolar Couplings in Neutral Aligned Media, JACS, 124, 34, 9986-9987.

[ABundi79] A. Bundi & K. Wüthrich, (1979) $^{1}$H NMR parameters of the common amino acid residues measured in aqueous solutions of the linear tetrapeptides H-Gly-Gly-X-L-Ala-OH, Biopolymers, 18, 285-297.

[ACabal05] A. Caballero-Herrera et al., (2005) Effect of Urea on Peptide Conformation in Water: Molecular Dynamics and Experimental Characterization, Biophysical Journal, 89, 842-857.

[ALeach01] A. R. Leach, Molecular Modelling, Principles and Applications, Pearson Education Limited, 2$^{nd}$ edition, 2001.

[AMotta87] A. Motta et al., (1987) Nuclear Overhauser effects in linear peptides A low-temperature 500 MHz study of Met-enkephalin, FEBS 215, 2, 215-218.

[AMögli05] A. Möglich et al., (2005) Molecular Basis for the Effect of Urea and Guanidinium Chloride on the Dynamics of the Unfolded Polypeptide Chains, J. Mol. Biol., 345, 153-162.

[ASimon03] A. Cohen Simonsen et al., (2003) Acyl-coenzyme A organizes laterally in membranes and is recognized specifically by acyl-coenzyme A binding protein, FEBS Letters, 552, 253-258.

[BBKrag93] B. B. Kragelund et al., (1993) Three-dimensional Structure of the Complex between Acyl-Coenzyme A Binding Protein and Palmitoyl-Coenzyme A, J. Mol. Biol., 230, 1260-1277.

[BBKrag95] B. B. Kragelund et al., (1995) Folding of a Four-Helix Bundle: Studies of Acyl-Coenzyme A Binding Protein, Biochem., 34, 7217-7224.

[BBKrag96] B. B. Kragelund et al., (1996) Fast and One-step Folding of Closely and Distantly Related Homologous Proteins of a Four-helix Bundle Family, JMB, 256, 187-200.

[BBKrag99] B. B. Kragelund et al., (1999) Acyl-coenzyme A binding protein (ACBP), BBA, 1441, 150-161.

[BBKrag99*] B. B. Kragelund et al., (1999) The formation of native-like structure containing eight conserved hydrophobic residues is rate limiting in two-state protein folding of ACBP, Nat. Struct. Biol., 6, 6, 594-601.

[BBKrag99†] B. B. Kragelund et al., (1999) Conserved Residues and Their Role in Structure, Function, and Stability of Acyl-Coenzyme A Binding Protein, Biochem., 38, 2386-2394.

[BGaigg01] Gaigg et al. (2001) Depletion of acyl-coenzyme A-binding protein affects sphingolipid synthesis and causes vesicle accumulation and membrane defects in Saccharomyces cerevisiae, Mol. Biol. Cell, 4, 11, 47-60.

[BJohns94] B. A. Johnson & R. A. Blevins, (1994) NMRView: a computer program for the visualization and analysis of NMR data, J. Biomol. NMR, 4, 603-614.

[BNiels03] B. G. Nielsen et al., (2003) The Probability Distribution of Side-Chain Conformations in [Leu] and [Met] enkephalin Determines the Potency and Selectivity to μ and δ Opiate Receptors, Biopolymers (Peptide Science) 71, 5, 577-592.

[CAnder02] C. A. F. Andersen et al., (2002) Continuum secondary structure captures protein flexibility, Structure, 10, Is. 2, 175-184.

[CPace86] C. N. Pace, (1986) Determination and Analysis of Urea and Guanidine Hydrochloride Denaturation Curves, Methods in Enzymology, Vol. 131, 266-280.

[CTanfo68] C. Tanford, Protein Denaturation, Advances in Protein Chemistry, (1968) Vol. 23, 121-282.

[DBaker00] D. Baker, (2000) A surprising simplicity to protein folding, Nature, 405, 39-42.

[DLanda02] D. P. Landau & K. Binder, A Guide to Monte Carlo Simulations in Statistical Physics, Cambridge University Press, 2002.

[DShort96] D. Shortle, (1996) The denatured state (the other half of the folding equation) and its role in protein stability, FASEB J., 10, 27-34.

[DShort96$^{+}$] D. R. Shortle, (1996) Structural analysis of non-native states of proteins by NMR methods, Current Opinion in Structural Biology, 6, 24-30.

[DShort01] D. Shortle & M. Ackerman, (2001) Persistence of Native-Like Topology in a Denatured Protein in 8 M Urea, Science, 293, 487-489.

[DvAalt01] D. M. van Aalten et al., (2001) Binding site differences revealed by crystal structures of Plasmodium falciparum and bovine acyl-CoA binding protein, J. Mol. Biol., 309, 1, 181-192.

[DWisha94] D. S. Wishart & B. D. Sykes, (1994) The $^{13}$C Chemical-Shift Index: A simple method for the identification of protein secondary structure using $^{13}$C chemical-shift data, J. Biomol. NMR, 4, 171-180.

[DWisha95] D. S. Wishart et al., (1995) $^{1}$H, $^{13}$C and $^{15}$N random coil NMR chemical shifts of the common amino acids. I. Investigations of nearest-neighbour effects, J. Biomol. NMR, 5, 67-81.

[EAlm99] E. Alm and D. Baker, (1999) Matching theory and experiment in protein folding, Current Opinion in Structural Biology, 9, 189-196.

[edDReid97] Protein NMR techniques, ed. By D. Reid, Human Press 1997

[ELiepi94] E. Liepinsh & G. Otting, (1994) Specificity of Urea Binding to Proteins, J. Am. Chem. Soc., 116, 9670-9674.

[EStims79] E. R. Stimson et al., (1979) Solution conformation of enkephalin. A nuclear magnetic resonance study of 13C-enriched carbonyl carbons in [Leu5]-enkephalin, Biochemistry 18, 1661-1671.

[Expasy] Calculated by the program “Primary structure analysis (pI/M.W.)” on ExPASy www.expasy.org Wilkins M. R, Gasteiger E, Bairoch A, Sanchez J. C, Williams K. L, Appel R D and Hochstrasser D. F., 1998 Protein Identification and Analysis Tools in the ExPASy Server in: 2-D Proteome Analysis Protocols. Editor Link AJ Humana Press New Jersey. Last access-date 28-11-05.

[FChiti99] F. Chiti et al., (1999) Acceleration of the folding of acylphosphatase by stabilization of local secondary structure, Nat. Struct. Biol., 6, 4, 380-387.

[FDelag95] F. Delaglio et al., (1995) NMRPipe: a multidimensional spectral processing system based on UNIX pipes, J. Biomol. NMR, 6, 277-293.

[GGupta86] G. Gupta et al., (1986) NOE data at 500 MHz reveal the proximity of phenyl and tyrosine rings in enkephalin, FEBS 198, 2, 245-250.

[GMakha95] G. I. Makhatadze et. al., (1995) Solvent isotope effects and protein stability, Nat. Struct. Biol., 2, 852-855.

[HSass00] H. Sass et al., (2000) Solution NMR of proteins within polyacrylamide gels: Diffusional properties and residual alignment by mechanical stress or embedding of oriented purple membranes, J. Biomol. NMR, 18, 303-309.

[IMarco04] I. Marcotte et al., (2004) A Multidimensional $^{1}$H NMR Investigation of the Conformation of Methionine-Enkephalin in Fast-Tumbling Bicelles, Biophysical Journal, 86, 1587-1600.

[JChou01] J. J. Chou et al., (2001) A simple apparatus for generating stretched polyacrylamide gels, yielding uniform alignment of proteins and detergent micelles, J. Biomol. NMR, 21, 377-382.

[JKohn04] J. E. Kohn et al., (2004) Random-coil behaviour and the dimensions of chemically unfolded proteins, PNAS, Vol. 101, no. 34, 12491-12496.

[JSchel02] J. A. Schellman, (2002) Fifty years of solvent denaturation, Biophys. Chem., 96, 91-101.

[JThoms02] J. K. Thomsen et al., (2002) Transient Intermediary States with High and Low Folding Probabilities in the Apparent Two-State Folding Equilibrium of ACBP at Low pH, JMB, 318, 805-814.

[KLLars04] K. Lindorff-Larsen et al., (2004) Determination of an Ensemble of Structures Representing the Denatured State of the Bovine Acyl-Coenzyme A Binding Protein, JACS, 126, 10, 3291-3299.

[KModig03] K. Modig er al., (2003) Water and urea interactions with the native and unfolded forms of a β-barrel protein, Protein Science, 12, 2768-2781.

[KPlaxc97] K. W. Plaxco et al., (1997) The effects of guanidine hydrochloride on the ´random coil` conformations and NMR chemical shifts of the peptide series GGXGG, J. Biomol. NMR, 10, 221-230.

[KTeilu00] K. Teilum et al., (2000) Formation of Hydrogen Bonds Precedes the Rate-limiting Formation of Persistent Structure in Folding of ACBP, JMB, 301, 1307-1314.

[KTeilu02] K. Teilum et al., (2002) Transient Structure Formation in Unfolded Acyl-coenzyme A-binding Protein Observed by Site-directed Spin Labelling, JMB, 324, 349-357.

[KTeilu05] K. Teilum et al., (2005) Different Secondary Structure Elements as Scaffolds for Protein Folding Transition States of Two Homologous Four-Helix Bundles, Proteins, 59, 80-90.

[KVAnde91] K. V. Andersen et al., (1991) The Secondary Structure in Solution of Acyl-Coenzyme A Binding Protein from Bovine Liver Using $^{1}$H Nuclear Magnetic Resonance Spectroscopy, Biochem., 30, 10654-10663.

[KVAnde93] K. V. Andersen & F. M. Poulsen, (1993) The three-dimensional structure of acyl-coenzyme A binding protein from bovine liver: structural refinement using heteronuclear multidimensional NMR spectroscopy, J. Biomol. NMR, 3, 271-284.

[LSmith96] L. J. Smith et al., (1996) The concept of a random coil Residual structure in peptides and denatured proteins, Folding & Design, Vol. 1, no. 5, R95-R106.

[MAburi02] M. Aburi & P. E. Smith, (2002) A conformational Analysis of Leucine Enkephalin as a Function of pH, Biopolymers, 64, 177-188.

[MDtuto] http://www.ch.embnet.org/MD_tutorial/ & http://www.charmm.org/document/Charmm/ Last access-dates 28-11-05.

[MKhale79] M. A. Khaled & D. W. Urry, (1979) pH and Solvent Titrations of Enkephalins by Carbon-13 Nuclear Magnetic Resonance Spectroscopy: Complete Assignment of Resonances, J. Chem. Soc., Perkin Transactions II, p1693.

[MKjærK94] M. Kjær et al., (1994) Automated and semiautomated analysis of homo- and heteronuclear multidimensional nuclear magnetic resonance spectra of proteins: the program Pronto, Methods in Enzymology, 239, 288-307.

[MLouhi03] M. Louhivuori et al., (2003) On the Origin of Residual Dipolar Couplings from Denatured Proteins, J. Am. Chem. Soc. 125, 15647-15650.

[MLouhi03a] Reference in [MLouhi03]; Kuhn W. Kolloid-Z. 1934, 68, 2.

[MReily92] M. D. Reily et al., (1992) Structure-Induced Carbon-13 Chemical Shifts: A Sensitive Measure of Transient Localized Secondary Structure in Peptides, J. Am. Chem. Soc., 114, 6251-6252.

[MZweck00] M. Zweckstetter & A. Bax, (2000) Prediction of Sterically Induced Alignment in Dilute Liquid Crystalline Phase: Aid to Protein Structure Determination by NMR, J. Am. Chem. Soc., 122, 3791-3792.

[NFitzk04] N. C. Fitzkee & G. D. Rose, (2004) Steric restrictions in protein folding: An α-helix cannot be followed by a contiguous β-strand, Protein Science, 13, 633-639.

[NFitzk04$^{+}$] N. C. Fitzkee & G. D. Rose, (2004) Reassessing random-coil statistics in unfolded proteins, PNAS, Vol. 101, no. 34, 12497-12502.

[NTjand97] N. Tjandra & A. Bax, (1997) Direct Measurements of Distance and Angles in Biomolecules by NMR in a Dilute Liquid Crystalline Medium, Science 278, 1111-1113.

[PGlaso60] P. K. Glasoe & F. A. Long, (1960) USE OF GLASS ELECTRODES TO MEASURE ACIDITIES IN DEUTERIUM OXIDE, Journal of Physical Chemistry, 64, 1, 188-190.

[RMohan04] R. Mohana-Borges, N. Goto, G. Kroon, J. Dyson, P. Wright, (2004) Structural Characterization of Unfolded States of Apomyoglobin using Residual Dipolar Couplings, J. Mol. Biol. 340, 1131-1142.

[RPain00] R. H. Pain, edited by, Mechanism of Protein folding, (Frontiers in Molecular Biology) Oxford University Press, 2$^{nd}$ edition, 2000.

[RSpada01] R. Spadaccini & P.A. Temussi, (2001) Natural peptide analgesics: the role of solution conformation, Cell. Mol. Life Sci. 58, 001-11.

[RTycko00] R. Tycko et al., (2000) Alignment of Biopolymers in Strained Gels: A New Way To Create Detectable Dipole-Dipole Couplings in High-Resolution Biomolecular NMR, J. Am. Chem. Soc., 122, 9340-9341.

[RZwanz92] R. Zwanzig et al., (1992) Levinthal's paradox, Proc. Natl. Acad. Sci., 89, 20-22.

[SAbdal03] S. Abdali et al., (2003) Enkephalins; Raman Spectral Analysis and Comparison as a Function of pH-value from 1 to 13, Biopolymers, 72, 5, 318-328.

[SKazmi01] S. L. Kazmirski et al., (2001) Protein folding from highly disordered denatured sate: The folding pathway of chymotrypsin inhibitor 2 at atomic resolution, PNAS, 98, 2, 4349-4354.

[SKelly97] S. M. Kelly & N. C. Price, (1997) The application of circular dichroism to studies of protein folding and unfolding, BBA, 1338, 161-185.

[SKim98] S. Kim & J. Baum, (1998) Electrostatic interactions in the acid denaturation of α-lactalbumin determined by NMR, Protein Science, 7, 1930-1938.

[SKirkp83] S. Kirkpatrick et al., (1983) Optimization by Simulated Annealing, Science, 220, 4598, 671-680.

[SKrist05] S. Kristjansdottir et al., (2005) Formation of Native and Non-native Interactions in Ensembles of Denatured ACBP Molecules from Paramagnetic Relaxation Enhancement Studies, JMB, 347, 1053-1062.

[SNeal03] S. Neal et al., (2003) Rapid and accurate calculation of protein $^{1}H$, $^{13}C$ and $^{15}N$ chemical shifts, J. of Biomol. NMR, 26, 215-240.

[SOhnis03] S. Ohnishi & D. Shortle, (2003) Observations of Residual Dipolar Couplings in Short Peptides, Proteins: Structure, Function and Genetics 50, 546-551.

[SSchwa00] S. Schwarzinger et al., (2000) Random coil chemical shifts in acidic 8 M urea: Implementation of random coil shift data in NMRview, J. Biomol. NMR, 18, 43-48.

[SSchwa01] S. Schwarzinger et al., (2001) Sequence-Dependent Correction of Random Coil NMR chemical shifts, J. Am. Chem. Soc, 123, 2970-2978.

[SSpera91] S. Spera and A. Bax, (1991) Empirical Correlation between Protein Backbone Conformation and Cα and Cβ $^{13}C$ Nuclear Magnetic Resonance Chemical Shifts, J. Am. Chem. Soc., 113, 14, 5490-5492.

[TLazar] T. Lazaridis & M. Karplus, (1999) Effective Energy Function for Proteins in Solution, PROTEINS: Structure, Function, and Genetics 35, 133-152.

[VDagge03] V. Daggett and A. Fersht, (2003) The present view of the mechanism of protein folding, Nature Reviews Mol. Cell Biol., 4, 497-502.

[WBrown88] William H. Brown, (1988) Introduction to Organic Chemistry, Brooks/Cole Publishing Company, fourth edition.

[WChoy01] W. Choy and J. Forman-Kay, (2001) Calculation of ensembles of structures representing the unfolded state of an SH3 domain, JMB, 308, 5, 1011-1032.

[WFiebe04] W. Fieber et al., (2004) Short-range, Long-range and Transition State Interactions in the Denatured State of ACBP from Residual Dipolar Couplings, J. Mol. Biol., 339, 1191-1199.

[WFiebe05] W. Fieber et al., (2005) Reversible dimerization of acid-denatured ACBP controlled by helix A4, Biochemistry, Feb 8; 44(5):1375-84.

[WKabsc83] W. Kabsch & C. Sander, (1983) How good are predictions of protein secondary structure? FEBS Lett., 155, 179-182.

[WPeti01] W. Peti et al., (2001) Chemical shift in denatured proteins: Resonance assignments for denatured ubiquitin and comparison with other denatured proteins, J. Biomol. NMR, 19, 153-165.

[YGoto90] Y. Goto et al., (1990) Mechanism of acid-induced folding of proteins, Biochem. 29, 14, 3480-3488.

[YLiFPi05] Y. Li, Frances Picart & Daniel Raleigh, (2005) Direct Characterization of the Folded, Unfolded and Urea-denatured States of the C-terminal Domain of the Ribosomal Protein L9, J. Mol. Biol., 349, 4, 839-846.

[YNozak72] Y. Nozaki, (1972) The preparation of guanidine hydrochloride, Methods Enzymol., 26, 43-50.

[YZhang] Yu-Zhu Zhang, Protein and peptide structure and interaction studied by hydrogen exchange and NMR. Ph.D. Thesis, Structural Biology and Molecular Biophysics, University of Pennsylvania, PA, USA &
Bai, Milne, (1993) Mayne & Englander, Proteins, 17, 75-86.
The rates are calculated with the program SPHERE available on the web-page: http://www.fccc.edu/research/labs/roder/sphere/sphere.html
Last access-date 28-11-05.

# 10 Introduction to tri-L-serine

The characteristic features of the amide modes in vibrational spectra, like vibrational absorption (VA), vibrational circular dichroism (VCD), Raman and Raman optical activity (ROA) spectra, have been shown to be sensitive to secondary structural changes [RSchwe01] in protein and peptides and can be measured on these molecules both in solution and in the solid state. Ab intio calculations on small peptides [KJalka03], [MKnapp99], [PBour02] have been able to explain and predict the experimental spectra. These calculations yield the optimised structures, spectroscopic transitions and intensities. The modes responsible for the spectroscopic activity provide an insight into the secondary structural changes of the investigated molecules. Quantum mechanical calculations can yield a detailed description of the electronic distribution in molecules, enabling the extraction of properties dependent on the distribution. In particular, they can facilitate a detailed picture of chemical reactions in which bonds are formed and broken [ALeach01]. Density functional theory (DFT) is an alternative approach for the calculations of the electronic structure of atoms and molecules, which considers the total electronic energy as a function of the electron density rather than the electronic wavefunction. A theory made possible by the proof of Hohenberg and Kohn that the energy of a system can be expressed as a function of the electron probability densities and that all other electron densities than the true ground state electron density would lead to higher energies. Hence, DFT is a variational method operating on the squared norm of the wavefunction (probability density) instead on the wave function it self.

## *10.1 Density functional theory*

In DFT the energy functional is written as a sum of two terms, where the first term is the interaction of the electrons with an external potential energy and the second represents the kinetic energy and the contribution from inter-electronic interactions. The theory it self does not yield the energy functional dependence on the probability density, but one approach has been given by Kohn and Sham (KS). Here, the total system energy is given by three parts. The systems kinetic energy, which is dependent on orbitals and defers KS from being a true density functional. In practice these are chosen as linear combinations of basis sets like for instance 6-31G*, thus resembling the Linear Combination of Atomic Orbitals (LCAO) method known from Hartree-Fock theory. The second term contains the electron nuclear Coulomb attraction between the i'th nuclei and the electron, and finally the Coulomb repulsion between all electrons. One of this method's shortfalls is that, the Hartree electrostatic energy assumes uncorrelated movement of the electrons. To some measure this term can be alleviated by the last term. The last term is the exchange-correlation functional, and corrects for the exchange and the correlations between electrons as well as containing contributions due to the discrepancy between the true and the calculated electronic kinetic energy. The energy within the Kohn-Sham scheme is then solved be assuming a functional form of the exchange-correlation functional and a trial density and solving for a self-consistent electron density. The success of the DFT methods is hence dependent on the choice of exchange-correlation functional one chooses, with the simplest being the local density approximation (LDA or LSDA). LDA is a model based on a uniform electron gas in which the electron density is invariable through space. This gives a mean value of the exchange-correlation energy at a given point in

space. If the expansion of the density, as which LDA can be regarded, is supplemented with gradients of the density, a more complete description for molecules is achieved. A widely used gradient corrected exchange functional is the one proposed by Becke, which leaves the choice of correlation functional open. Here, corrections like the Lee-Yang-Parr correlation functional (LYP) can be used. The main method used in these calculations is the B3LYP, which is semi-empirically determined hybrid method. The B3 exchange includes three different expressions for the exchange with appropriate weight, determined by fitting to experimental data, thus enabling a better fit to experiment and being applicable for the systems for which the experimental data were (are) available. "The B3LYP hybrid method has also been shown to give good results for systems which were not included in the parameterization."

### *10.2 Calculation of the vibrational spectra*

At the basis of the theoretical treatment of spectroscopic features lies the ability to predict transitions between different states. After the identification of ground state it is possible to generate exited states by exposing the ground state to different radiations fields. These excited states can have different origins, for example vibrational, electronic, rotational or nuclear or electronic spin. By measurement of absorption of incident light of a given frequency, polarisation and intensity it is possible to infer something about the structural features of the investigated system [ASen84], [MDiem84], [PBour02]. The main purpose of vibrational analysis is to assign spectral features to structural features or units in the molecule. By comparing theoretical and experimental spectra it should in theory be possible to determine the best candidate for a structure in cases where only one conformer and species is present. However, several conformers and species might be present, obscuring the interpretation. Additionally pH effects, solvent polarity, solute concentration, and ionic strength might need to be investigated as they all can influence and changes the molecule and hence its spectra.
The assignment of frequencies to specific vibrational modes is important, in that it connects the fluctuation in the 3-dimensional structure of the molecule. Molecular properties, such as magnetic or electric dipole moments, can be defined as the response of a wavefunction to an external perturbation. The description of the perturbation of the energy can be made within the wavefunction picture, since it is energy that is perturbed regardless of the perturbation which is applied. The perturbation can for instance be due to an external electric field, an external magnetic field or a change in the nuclear geometry.

The minimum energy structure is due to the fluctuations not fixed in space, and it is therefore convenient to describe the molecular system by mass weighted coordinates. This allows the potential energy to be Taylor expanded around the optimised structure and giving a solution of the nuclear displacement in terms of internal coordinates. The normal modes for the 3N-6 vibrational modes (for a non-linear molecule) can be described in terms of linear combinations of these internal coordinates. A normal mode calculation yields a description for the observed vibrations and the nuclear displacements that is dependent on the optimised structure, the force field and atomic masses. Mass-weighted coordinates can be transformed to normal coordinates, but this still is not a convenient way to describe displacement like e.g. bond stretching. Therefore normal coordinates are transformed to an internal coordinate system. The

association of chosen internal coordinates and a frequency is made via the force constants contribution to that frequency. This is called the potential energy distribution (PED), which is a convenient way of assigning frequencies to vibrational modes. Additionally one can use molecular visualization programs like Gauss View and Molden to graphically display the molecular vibrations, but the PEDs are quantitative descriptions, which depend on the choice of internal vibrational coordinates. These are different from simple valence internal coordinates normally used for Z-matrices in geometry optimizations or in molecular mechanic force fields.

In this study one conformer of the nonionic neutral and zwitterionic species of L-serinyl L-serinyl L-serine (SSS or tri-L-serine), together with its cationic and anionic species and the capped N-acetyl tri-L-serine N'- methylamide (NALSLSLSNMA) analog were optimized with density functional theory with the Becke 3LYP hybrid exchange correlation (XC) functional and the PW91 GGA XC functional and the 6-31G* and aug-cc-pVDZ basis sets. Subsequently the vibrational absorption (VA), vibrational circular dichroism (VCD), Raman and Raman optical activity (ROA) spectra were simulated in order to compare them to experimentally measured spectra. A comparison of the various ways to treat the effects of the environment and solvation on both the structure and the spectral properties has been thoroughly investigated for one conformer, with the goal to determine which level of theory is appropriate to use in the systematic search of the conformational space for this and other small peptides in aqueous solution, at low, medium and high pH levels. In addition, the effects of the counterion, here $Cl^-$ anion, are also investigated.

## *10.3 Bibliography*

[RSchwe01] R. Schweitzer-Stenner, (2001) J. Raman Spectrosc., 32, 711-732.

[KJalka03] K. J. Jalkanen et al., (2003) Vibrational Analysis of Various Isotopomers of L-Alanyl-L-Alanine in Aqueous Solution: Vibrational Absorption, Vibrational Circular Dichroism, Raman, and Raman Optical Activity Spectra, International Journal of Quantum Chemistry, 92, 239-259.

[MKnapp99] M. Knapp-Mohammady et al., (1999) Chem. Phys., 240, 63-77.

[PBour02] P. Bour et al., (2002) Ab initio quantum mechanical models of peptide helices and their vibrational spectra, Biopolymers, 65, 1, 45-59.

[ALeach01] A. R. Leach, Molecular Modelling, Principles and Applications, Pearson Education Limited, 2nd edition, 2001.

[ASen84] A. C. Sen & T. A. Keiderling, (1984) Vibrational Circular Dichroism of Polypeptides. III. Film Studies of Several α-Helical and β-sheet Polypeptides, Biopolymers, 23, 1533-1545.

[MDiem84] M. Diem et al., (1984) Determination of Peptide Conformation via Vibrational Coupling: Application to Diastereoisomeric Alanyl Dipeptides, Biopolymers, 23, 1917-1930.

INSTITUTE OF PHYSICS PUBLISHING PHYSICAL BIOLOGY

Phys. Biol. **3** (2006) S63–S79 doi:10.1088/1478-3975/3/1/S07

# The VA, VCD, Raman and ROA spectra of tri-L-serine in aqueous solution

**V Würtz Jürgensen**[1] **and K Jalkanen**[1,2,3]

[1] Quantum Protein (QuP) Centre, Department of Physics, Technical University of Denmark, Bldg 309, DK-2800 Kgs Lyngby, Denmark
[2] Laboratory of Physics, Helsinki University of Technology, PO Box 1100, 02015 TKK, Otakaari 1, Espoo, Finland
[3] Nanochemistry Research Institute, Department of Applied Chemistry, Curtin University of Technology, GPO Box U1987, Perth, Western Australia 6845, Australia

Received 9 December 2005
Accepted for publication 16 January 2006
Published 22 February 2006
Online at stacks.iop.org/PhysBio/3/S63

**Abstract**
The structures of one conformer of the nonionic neutral and zwitterionic species of L-serinyl L-serinyl L-serine (SSS or tri-L-serine), together with its cationic and anionic species and the capped *N*-acetyl tri-L-serine *N*′-methylamide analog were optimized with density functional theory with the Becke 3LYP hybrid exchange correlation (XC) functional and the PW91 GGA XC functional and the 6-31G* and aug-cc-pVDZ basis sets. Subsequently, the vibrational absorption, vibrational circular dichroism, Raman and Raman optical activity spectra were simulated in order to compare them to experimentally measured spectra. In addition, we compare to previously reported studies for both structural determination and spectral simulations and measurements. A comparison of the various ways to treat the effects of the environment and solvation on both the structure and the spectral properties is thoroughly investigated for one conformer, with the goal to determine which level of theory is appropriate to use in the systematic search of the conformational space. In addition, the effects of the counterion, here $Cl^-$ anion, are also investigated. Here we present the current state of the art in nanobiology, where the latest methods in experimental and theoretical vibrational spectroscopy are used to gain useful information about the coupling of the nuclear, electronic and magnetic degrees of freedom and structure of tri-L-serine and its capped peptide analog with the environment.

S This article has associated online supplementary data files

## Introduction

One approach for the determination of protein and peptide secondary structure from the spectroscopic data is to optimize the geometry for all possible low energy structures of the system with density functional theory (DFT) using the appropriate exchange correlation (XC) functional and appropriate treatment of the environment, and for these optimized structures simulate the spectra measured. This is especially important for new novel flexible peptides, which can assume various structural and functional states depending on small changes in the environment. For the conformers with the lowest energies and predicted to be present under the conditions of the experiment, the vibrational absorption (VA), vibrational circular dichroism (VCD), Raman and Raman optical activity (ROA) spectra can be simulated and compared to the experimental data. The best match is, in theory, the candidate for the structure in cases where only one conformer and species is present. In some cases, more than one conformer or species may be present at the given temperature in the solution for which the intensity measurements were made. This will complicate the interpretation of the measured spectra and, therefore, temperature-dependent studies may be required. In addition, the effect of pH, solvent polarity, solute concentration and ionic strength may all also have to be investigated. In many cases due to the pKas of the *N*-terminal, *C*-terminal and side chain groups, the solution's pH needs to be carefully controlled by buffering conditions.

  

The aim for the present study is to optimize the structures of the various species of tri-L-serine (neutral nonionic and zwitterionic, anionic and cationic) for a representative conformer and to simulate the VA or infrared (IR) intensities, VCD intensities, Raman intensities and ROA intensities and nuclear magnetic resonance (NMR) shielding tensors for these four species. Additionally, one conformer of tri-L-serine's capped analog (NALSLSLSNMA) has also been determined. The start configuration (conformer) was chosen to be the linear structure since a crystal structure for the peptide is not available. A search for the lowest energy conformer and other low energy conformers will be performed for all species once the adequate level of theory to do so is determined. The level of theory to adequately treat the effects due to the environment, solvation, hydrogen bonding and pH on the structures, vibrational frequencies, and VA, VCD, Raman and ROA intensities needs to be documented before one undertakes the very expensive systematic potential energy surface search. It is not feasible to perform systematic searches at all levels of theory at this time, nor is scientifically expedient.

The two neutral species of tri-L-serine that were investigated are the nonionic $NH_2$–···–COOH and the zwitterionic $NH_3^+$–···–$COO^-$ forms. This allows one to compare the spectroscopic features of the various species with each other and also with the experimental spectra of the tri-peptide in solution. One generates spectra that can be compared to those measured on tri-L-serine in solutions of nonpolar and polar solvents and those measured on tri-L-serine in the gas phase, in the powdered state or *dissolved* in a KBr pellet. With the recent increased use of mass spectroscopy and molecular beam experiments, the vibrational spectra of many peptides and their fragmentation products have been measured under a variety of experimental conditions. It is necessary to simulate spectra for the conditions relevant for these experiments, and not strictly for the measurements on aqueous solutions. Simulated spectra can be used to determine whether the peptide's most dominant species is the zwitterion, anion or cation in the solution measured, and whether the chosen geometry (structure or conformer) is the dominant conformer present for the given species. In many cases, the measurements are made for solutions where the exact pH is not known. Here, by analyzing the spectra, one may actually be able to determine the pH by determining the species present. This will extend the use of VA, VCD, Raman and ROA measurements to determine pH and ionic strength of aqueous solutions of amino acids and peptides. This is extremely important when many species are all present, and not a single conformer and single species.

The possibility of more than one species and conformer being present for the experimental conditions of the measurement further complicates the spectral interpretation. Therefore, calculations on the anionic and cationic species of tri-L-serine were made in order to be able to distinguish the species present under conditions present in the experiments. In addition to the continuum model calculations, we have additionally solvated the cation/$Cl^-$ counterion complex with explicit water molecules. Here one seeks to determine how well the Onsager and PCM continuum models are able to represent/reproduce the effects due to explicit hydrogen bonds. Finally, we have embedded this complex within both a spherical cavity (Onsager model) and a molecular complex cavity (PCM model), to see how well the combined hybrid model does, that is, how well the explicit water model simulates the effects due to the strongly interacting hydrogen bonded water molecules and how well the continuum models (Onsager or PCM) simulate the effects due to the bulk water molecules and the water molecules near the hydrophobic groups, but not strongly interacting with the peptide. Finally, the results at all levels of theory are compared to other reported theoretical results for tri-L-serine and the available experimental data, which is the ultimate benchmark for all simulations which seek to model real biological systems in their native environments. The last species for which calculations were performed is the capped analog: *N*-acetyl tri-L-serine *N*′-methylamide. To determine the spectra of the tri-L-serine sequence as it occurs in a large protein one simulates the spectra of the tripeptide's capped analog.

## Materials and methods

### *Density functional theory*

The calculations were performed with Gaussian 98 and 03 at the DFT level of theory with the Becke 3LYP hybrid XC functional (DFT-B3LYP) and the Perdew Wang generalized gradient approximation (GGA) XC functional (DFT-PW91) with the 6-31G* and aug-cc-pVDZ basis sets. At these levels of theory we have additionally calculated the Hessian, the atomic polar tensors (ATP) and the atomic axial tensor (AAT), which allows us to calculate the dipole- and rotational strengths required to simulate the VA and VCD spectra. Furthermore, the electric dipole electric dipole polarizability derivatives (EDEDPD) were calculated in order to simulate the Raman scattering spectra. In addition, geometry optimizations were performed at the DFT-B3LYP and DFT-PW91 levels with the Onsager continuum model for the neutral zwitterionic species and its anionic and cationic forms. The Onsager continuum is a reaction field model, which allows one to simulate the solvation effects on the properties of the solute without considering explicit solvent molecules [1]. It represents the effects due to the bulk solvent, but does not include the direct interactions between the solute and the solvent. A thorough description of both DFT and its extension to simulate vibrational spectra can be found in [2–10]. At the optimized Onsager geometry, atomic axial tensors (AAT) were calculated without the Onsager model. The DFT-B3LYP level of theory has been shown to be able to reproduce the VA and VCD spectra for the alanine dipeptide quite well. This level of theory with the 6-31G* basis set was chosen as a compromise between high accuracy and computational cost for treating the effects due to explicit water molecules and the combined hybrid approach [8, 9]. Additionally, the VCD spectra have been simulated using the PCM model, a more sophisticated continuum solvent model, to represent the effects due to the solvent. Our previous work involved using the Onsager continuum model [8, 9]. Here one wishes to

test the more elaborate PCM model for treating the effects due to the aqueous environment. In addition, the structure of NALSLSLSNMA with the 6-31G* basis set at the DFT-B3LYP level has been determined. Previously, we have recommended the large aug-cc-pVDZ basis set for high quality Raman and ROA spectral simulations for phenyloxirane [11], but in this work the smaller basis set (6-31G*) that we have previously used for our modeling studies on LA and NALANMA, which gave us qualitative agreement with the experimentally measured ROA spectra for these two molecules in an aqueous environment, has been used [8, 9]. Additionally, the VA, VCD, Raman and ROA spectra of NALSLSLSNMA with the 3-21G split valence basis set and at the DFT-B3LYP level have been simulated. Here one documents how well this split valence basis set does. Previously a minimal basis set for the semi-empirical based DFT method, the so-called SCC-DFTB method, has been used to determine the optimized structures and Hessians for NALANMA, oxirane, thiirane and Leu-enkephalin [12]. Unfortunately the tensors required to simulate the VCD, Raman and ROA spectra are not yet implemented, and it is not even yet known whether the tensors calculated with a minimum basis set would be even worth pursuing, but from previous studies, the prospects appear to be very low. A more practical and feasible alternative is to use a split valence basis set like the 3-21G basis set, but this level of theory may also be inadequate. The inclusion of polarization functions is most likely to be important for even qualitatively representing the linear response properties due to the time varying electric and magnetic fields. Here the VA, VCD, Raman and ROA spectra for NALSLSLSNMA have been simulated with the 3-21G level of theory to document whether this level of theory is actually worth pursuing in the context of extending the SCC-DFTB method for the simulation of the VA, VCD, Raman and ROA intensities. It is very important to extend the current SCC-DFTB theory to treat the electronic and magnetic response properties of the molecule in biological systems in their native environment. The tensors and their derivatives with respect to nuclear displacements and velocities are not only important for simulating the intensities of the vibrational transitions, but also for deriving the forces which bind the molecules to each other (complex and aggregation phenomena) and to ligands (drug molecules, be they inhibitors or substrate analogs). Hence theoretical vibrational spectroscopy can not only add to the understanding for experimental spectroscopists, but also for molecular biologists, physical biologists and biochemists, who seek new theoretical and experimental methods to understand the structure, function and mechanism of action of their nanomachines (proteins, self-assembling aggregates of proteins, protein/nucleic acid complexes and glycosolated proteins).

By using DFT-PW91 GGA XC functionals the nonlocal exact exchange from the DFT-B3LYP XC functional is not used. This saves on computational expense and programing and has been recommended by many solid state physics groups for this reason. Additionally, the optimized effective potential (OEP) method has been suggested as an alternative to exact nonlocal exchange [13]. The OEP method allows one to develop a local exchange functional that satisfies many criteria which are not satisfied by nonOEP local exchange functionals, one criterion being that an electron does not interact with itself (self interaction). The exact exchange term is nonlocal and expensive to calculate hence the search for exchange terms which are local. The exact exchange and Coulomb terms exactly cancel for a one-electron system, but for many local exchange functionals used, a self-interaction (SI) term exists, which is clearly in error. Recently the group of Bartlett has extended the OEP method, which was originally developed to generate local exchange functionals for atoms, to generate local OEP correlation functionals based on MP2 correlation energies and potentials and subsequently based on coupled cluster correlation energies and potentials. They have called this methodology *ab initio* DFT since it allows for a systematic improvement of the XC functionals, in contrast to the previously developed XC functionals. The OEP exchange and correlation functionals are systematically better with respect to their convergence properties, a problem noted by the Bartlett group which previously prevented the general use of the OEP method [14]. This methodology presents a way to systematically improve upon the XC functionals used within the DFT method. An approximation to the rigorous OEP method developed by Krieger, Li and Iafrate is also very accurate and computationally feasible [15]. This has really greatly improved the previous limitations of DFT. The problems with calculating charge transfer excitations have been addressed by the Handy group [16]. The problems with calculating excited state energies by the static limit and by including dynamical effects have been addressed by the groups of Gross, Aldrichs and Berands among others [17]. Finally, the problem of the treatment of dynamic and static correlation and van der Waals forces (interactions) and hydrogen bonding, very important for modeling biological systems, have also recently been addressed [18, 19]. Hence the latest DFT implementations are fast approaching the highly correlated wavefunction methods in accuracy and applicability, but with less cost than the full wavefunction based methods, but of course with more cost than the originally formulated DFT methods. The synergistic relation between wavefunction and density functional based quantum mechanics has never been more fruitful than it now is and it appears to be evolving with an ever increasing rate. Additionally, Green's function integral approaches, like the GW method, are also contributing to the picture, especially with respect to the treatment of excited electronic states [20]. Here the time-dependent extension of DFT still has its problems. What remains to be done is for these new *ab initio* DFT XC functionals to be implemented in open source DFT codes such as SIESTA [21] and ABINIT [22] and also for the linear response properties to be implemented which will allow for the calculation of all of the properties required to simulate the VA, VCD, Raman and ROA spectra. This will allow for the promulgation of these methods to the full research communities.

To treat the effects due to the environment (solvent) the polarized continuum model (PCM) incorporates electrostatic, dispersion–repulsion contributions to the molecular free energy and cavitation energy [23]. However, at the optimized

geometries obtained with the PCM model with the Gaussian program for the charged species, some of the Hessians gave us negative eigenvalues. It was originally postulated that this problem originated due to the lack of an origin-independent definition of the electric dipole moment for charged systems. Subsequently calculations were performed with the $Cl^-$ counterion in close proximity to the positively charged ammonium group to give us a well-defined neutral species for the tri-L-serine cation–$Cl^-$ anion complex. The developers of the PCM model have also noted that this model may have problems for charged systems [23]. Here we made the system neutral by adding the $Cl^-$ anion to the tri-L-serine cation. Initially we did not solvate the system, but performed geometry optimizations for the salt bridge (ion pair state) complex. This did not solve the problem, and the cation/anion complex was subsequently explicitly solvated with '22' water molecules. In addition to the explicit water treatment, we have additionally embedded the tri-L-serine cation/$Cl^-$ anion complex (solvated system) within a spherical cavity (Onsager continuum model) and a cavity that encloses (has the shape of ) the hydrated complex (PCM continuum model). Due to convergence problems with the geometry optimizations with the PCM for the complex, we do not present the complex/PCM results here. Note that the effects due to the solvent have been hypothesized to be small, but in the case of the hydrogen bonding this approximation is not the case.

The goal here has been to determine the level of theory and solvent treatment to use for the future systematic potential energy search (scan) for this molecule and its various species, but along the way we have encountered some fundamental problems with the treatment of the solvent environment. What has further complicated this work is that, in addition to having multiple conformers present under the conditions of the experiment, there may also be multiple species, and if the concentration is too high, aggregate formation. In addition to the problem of conformational sampling and averaging, one is faced with the additional problem of species sampling and averaging and finally the sampling and averaging of the solvent degrees of freedom. With the proton possibly moving back and forth between two atoms to interconvert between species, the conformational equilibrium is not just thermodynamically determined, as assumed by many, but also kinetically determined. Hence the ideas of thermodynamic averaging may need to be re-explored and the idea of kinetic averaging may need to be explored. The whole idea of a mean field approach may also need to be re-thought. Hence one must be very careful when analyzing the distribution of all of the species and conformers of the species when one is analyzing the spectra of a biological sample. In addition, the time scale of the measurement and the physics of the process need to be considered, whether one determines an average structure or one determines a superposition of structures. Here in addition to the solvent molecules which are strongly hydrogen bonded with the polar portions of the peptides, we also have to properly sample and average the solvent molecules which form the cages around the nonpolar groups (the so-called hydrophobic effect) and the counterions; the solvent molecules which are in contact with these solvent molecules, and whose motions are strongly coupled with the aforementioned, also need to be considered. Hence, there is lack of real progress in this area, even though the basic ideas and formulation of the problem are relatively straightforward! In this work, we also have not completely solved all of these problems, but have addressed the question of how to couple the explicit and continuum solvent models to be able to simulate the VA, VCD, Raman and ROA spectra of biomolecules in the aqueous media. This is an extension of our previous work on NALANMA where we showed to simulate the VA, VCD, Raman and ROA spectra of this molecule we needed to include explicit water molecules [9, 10]. In addition, the structure found, the $P_{II}$ structure, is not even a minimum on the gas phase potential energy surface. Hence the NALANMA plus four water molecule complex is the real species of interest. That this is the case has been verified by recent NMR experiments, which previously could not be interpreted. This new paradigm has not only allowed for the interpretation of the VA, VCD, Raman and ROA spectra of NALANMA [9], but also of the NMR spectra [24]. In the next section, we give a brief overview of the theory required to calculate the tensors required to simulate the VA, VCD, Raman and ROA spectra of tri-L-serine. For the equations the reader can see our previous works on NALANMA [8–10].

*Theoretical treatment of spectroscopic features*

At the basis of the theoretical treatment of spectroscopic features lies the ability to predict transitions between different states. After the identification of the ground state, it is possible to generate exited states by exposing the ground state to different radiations fields. These excited states can have different origins, for example vibrational, electronic, rotational or nuclear or electronic spin. By measurement of absorption of incident light of a given frequency, polarization and intensity, it is possible to infer something about the structural features of the investigated system [25–27]. The main purpose of vibrational analysis is to assign spectral features to structural features or units in the molecule. Molecular properties such as the electric dipole moment can be defined as the response of the wavefunction (or electron density) to an external perturbation [7, 11].

The description of the perturbation of the energy can be made within the wavefunction picture, since it is energy that changes regardless of the perturbation that is applied. The perturbation can for instance be due to an external electric field, an external magnetic field or a change in the nuclear geometry. Extensive treatment of the theory behind spectral simulations, i.e. obtaining the tensors required to simulate the VA, VCD, Raman and ROA spectra, can be found in various books and journals [7–11]. The theory for VA and VCD spectral simulations is thoroughly discussed in [28–43], whereas the theory behind Raman scattering and ROA spectral simulations previously have been covered in [8–10].

*Experimental infrared or vibrational absorption, vibrational circular dichroism and Raman spectral measurements at Bruker AG, Ettlingen, Germany*

L-serinyl-L-serinyl-L-Serine (SSS or tri-L-serine) was purchased as a lyophilized powder from Bachem

Feinchemikalien AG (>98% purity TLC) and was not dissolvable in pure deionized $H_2O$. The theoretical pI for SSS was calculated to be 5.24 [44]. The FTIR spectra were recorded at room temperature with a Bruker IFS 66/S instrument. A liquid cell with a $CaF_2$ window and 6 mm path length was used for the solution VA spectroscopy. The VCD spectra were measured at room temperature with a Bruker IFS 66/S, PMA 37 instrument and obtained at 4 $cm^{-1}$ and 6 $cm^{-1}$ resolutions and a photo-elastic modulator (PEM) set to 1/4 wave at 1500 $cm^{-1}$. VCD and VA spectra were measured against pure solvent and against pure KBr, respectively. The tri-peptide was dissolved in approximately 0.1% HCl solution with 50 mg $ml^{-1}$, i.e., 179 mM for the VA measurements. Tri-L-serine was also mixed with KBr, 1 mg substance in 201 mg KBr and compressed into a solid pellet, which was used for both the VA and VCD spectral measurements.

The frequency range for VA spectra of tri-L-serine in HCl obtained in the $CaF_2$- cell had a range from 1000 to 1800 $cm^{-1}$ and spectral resolution 4 $cm^{-1}$. Due to low optical density of SSS in HCl, it was not possible to obtain a VCD spectrum of this solution. The frequency range for the VA spectrum for tri-L-serine in KBr pellet was 500–4000 $cm^{-1}$ with a spectral resolution of 4 $cm^{-1}$. For the VCD spectrum of the pellet the range was 1000–1800 $cm^{-1}$, with a spectral resolution of 6 $cm^{-1}$. Finally a saturated solution of tri-L-serine in $CCl_4$ was prepared for both VA and VCD measurements, though the optical density for VCD was not high enough.

*Experimental infrared or vibrational absorption, vibrational circular dichroism and Raman scattering spectral measurements at Thermo Electron Corporation, Madision, WI, USA*

Raman scattering: spectra were obtained at Thermo Electron Corporation, Madison, WI, USA. For the experiments at Thermo Electron Corporation 25.32 mg tri-L-ser powder was dissolved in 500 ml of 0.25 M HCl, yielding a pH of 0.93 and a concentration of 180 mM. Only Raman scattering measurements were able to be measured on the solutions. The concentration was too high to allow for good VA and VCD measurements. The Raman measurements were made at two different wavelengths, as shown on the experiment spectra.

*DFT with the Becke 3LYP hybrid XC functional*

All the peptides were built using either the program GaussView [45] or Molden [46] with all backbone atoms lying in the same plane, i.e., the all-trans configuration with side groups alternately pointing up and down. Bond angles were initially checked so that they corresponded to ideal $sp^2$ and $sp^3$ hybridizations. The bond lengths were set to standard values obtained from a built in library in GaussView. These structures Cartesian coordinates were used as input for Gaussian 98 and 03. Geometry optimization rendered an optimized structure and corresponding electronic energy. The VCD intensities are calculated with Gaussian 98 and 03, in addition to the normal mode frequencies and VA or IR intensities. To get the VA spectra the APT were calculated, as well as the AAT additionally necessary for the VCD spectra. Raman intensities were computed with Gaussian 98 and 03 as well, and for the simulation of the Raman spectra, the EDEDPD needed to be calculated. Raman intensity calculations are default for SCF frequency calculation, but can be specified for DFT and MP2 calculations to produce the intensities by numerical calculations via finite field perturbation theory.

## Results and discussion

The optimized structures represent only a local energy minimum for each species. The most important dihedral angles, which determine the conformer for tri-L-serine, of all the species investigated are given in supplementary (sup) table S1(*b*) together with all calculated bond lengths in sup table S1(*a*) (available from stacks.iop.org/PhysBio/3/S63). The atom numbering in the tables for the structural parameters is shown in sup figures S1(*a*)–S1(*h*) and in figures 1(*a*) and (*b*). There are not large differences in the bond lengths calculated for the different tri-L-serine species. The species for which the values diverge the most from the mean values is the zwitterionic species calculated without the Onsager continuum model. For instance, the length of the CO bond differs from the mean value by 0.012 Å, while the bond lengths for the other CO bonds differ by not more than 0.002 Å from the mean value. This can be understood in light of the fact that all other ionic species were calculated within the two continuum models (Onsager and PCM).

*Assignment and description of the vibrational modes*

The interaction of electromagnetic radiation with molecular vibrations is generally described in terms of normal modes of the system investigated. The normal modes belonging to the peptide group are the so-called amide modes: amide I, II and III (AI, AII and AIII). AI is usually described as a pure CO stretching mode, where (CO s) is the dominant contribution to the eigenvector, but can also contain, for instance, some mixture of CCN deformation (CCN d). AI is normally accredited to the region around 1600–1700 $cm^{-1}$ [47–49]. AII is generally considered less structure sensitive than AI and AIII, and is generally attributed as the out-of-phase combination of CN s and NH in-plane bend (ib). AII is normally found around 1550 $cm^{-1}$. AIII is reported more structure sensitive than AI, and in general described as an in-phase combination of CN stretch and NH ib. AIII is commonly found around 1250 $cm^{-1}$. To assign the modes one must define a set of internal coordinates which can be used in the so-called vibrational analysis. One can then use these internal coordinates to assign modes based on the potential energy distributions (PEDs). In sup table S2 we define the internal coordinates and in sup tables S2(*a*), S2(*b*) and S2(*c*) we give the vibrational frequencies ($\nu_i$), the PEDs based on the internal coordinates given in sup table S2, the dipole strengths ($D_i$), the rotational strengths ($R_i$) and the Raman scattering intensities (Ram) for the zwitterionic species. The atom numbering is as given in sup figure S1(*b*). In sup table S3 we define the internal coordinates and in sup table S3(*a*) we give the

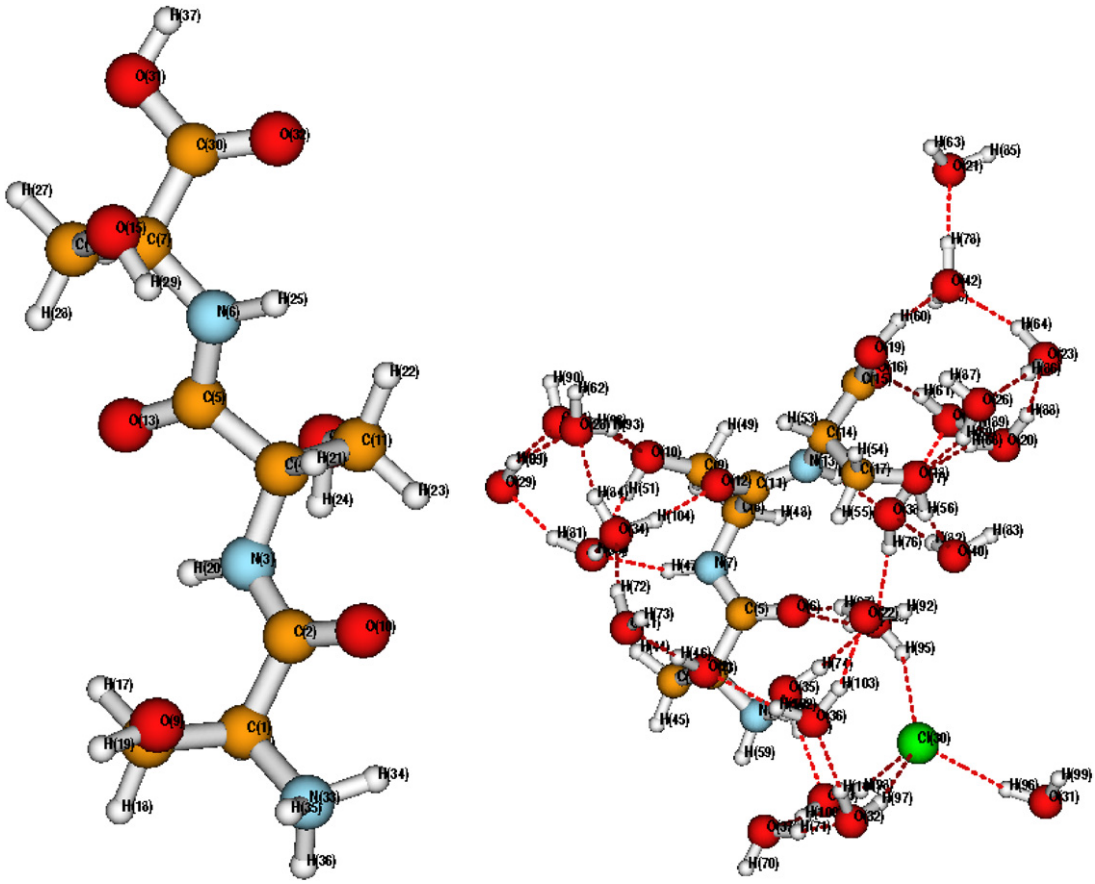

(*a*) (*b*)

**Figure 1.** (*a*) Tri-L-serine cation II, (*b*) tri-L-serine cation II + $Cl^-$ anion solvated with 22 water molecules + Onsager continuum model (best model).

vibrational frequencies $\nu_i$, the PEDs based on the internal coordinates given in sup table S3, the $D_i$, the $R_i$, and the Ram for the nonionic neutral species, atom numbering given in sup figure S1(*a*).

In sup table S4 we define the internal coordinates and in sup table S4(*a*) we give the $\nu_i$, the PEDs based on the internal coordinates given in sup table S4, the $D_i$, the $R_i$ and the Ram for the capped species, atom numbering given in sup figure S1(*g*). In sup table S5 we define the internal coordinates and in sup tables S5(*a*) and S5(*b*) we give the $\nu_i$, the PEDs based on the internal coordinates given in sup table S5, the $D_i$, the $R_i$ and the Ram for the anionic species, atom numbering given in sup figure S1(*d*). In sup table S6 we define the internal coordinates and in sup tables S6(*a*)–S6(*e*) we give the $\nu_i$, the PEDs based on the internal coordinates given in sup table S6, the $D_i$, the $R_i$ and the Ram for the cationic species, atom numbering given in sup figure S1(*f*). In sup table S7 we define the internal coordinates and in sup tables S7(*a*)–S7(*c*) we give the $\nu_i$, the PEDs based on the internal coordinates given in sup table S7, the $D_i$, the $R_i$ and the Ram for the cationic/Cl-anioinic solvated species, atom numbering given in sup figure S1(*h*). Figures 1(*a*) and (*b*) show the structures of two different ways to model the cationic species of tri-L-serine: (a) cation II + PCM continuum model and (b) cation II + $Cl^-$ anion solvated water complex embedded within an Onsager solvation sphere. In sup figures S1(*a*) neutral, S1(*b*) zwitterion, S1(*c*) zwitterion with Onsager, S1(*d*) anion I, S1(*e*) anion II, S1(*f*) cation I, S1(*g*) capped tri-L-serine and S1(*h*) cation II, solvated and $Cl^-$ anion are shown for the other species found to date. Note that for the solvated species, the positions of the water molecules may change (the hydrogen bonded water–peptide–$Cl^-$ anion network is variable). Hence the internal coordinates of the cation and the individual water molecules are stable, but the other internal vibrational coordinates may change. Hence which set of internal coordinates to use for these complexes is an open area of research, which we are investigating. For each snapshot (local minimum), the set of internal coordinates is clearly defined, but not necessarily the same with the previous step. Hence in sup table S7 not all internal coordinates are labeled, and hence the PEDs in sup tables 7(*a*), 7(*b*) and 7(*c*) are not all labeled, but $\nu_i$, $D_i$, $R_i$ and Ram are all given.

For the calculated species the amide modes are not all pure modes, but contain mixing to different degrees, see sup tables S8–S11. Amide I for anion I and II contains also mixtures from stretching of the carboxyl group ($R_{19,20}$), while cation II's AI mode contains mixing with a CN stretch and a CNN deformation, consistent with the definition of the

coordinate $R_{76}$ in sup table S6 as assigned in sup table S8. The capped species has mixtures of different C=O stretches and one mixed with a CN stretch. The neutral species has just pure C=O stretches, where $R_{20}$ is a CO stretch of the carboxyl group. For the zwitterionic species without the Onsager continuum model, the AI mode consists of a C=O stretch together with a CN stretch, except for $R_{20}$ and $R_{21}$ which again is the stretching mode of the carboxyl group. The zwitterionic species within the Onsager solvation sphere is made up of pure C=O stretches except for the carboxyl group. AII modes for all calculated types (species) are as given by their PEDs in sup table S9. For most species the amide modes are pure, expect for the cations, where there is considerable mixing with, for instance, $R_{52}$, which is a H–C–H scissor. One exception is given by the amide modes for the cationic species calculated at the higher level of theory or larger basis sets, see sup tables S8, S9 and S10, as well as sup table S6(*c*) (B3LYP/aug-cc-pVDZ, PCM), sup table S6(*d*) (PW91/aug-cc-pVDZ, PCM) and sup table S6(*e*) (B3LYP/6–31G*, PCM). AIII modes for all conformers, given by PEDs and the definition of in-phase combination of CN stretching and NH in-plane bend, are found in sup table S10. The C–H deformation of methine is sometimes also considered an AIII mode and can for all calculated species be found in sup table S11. All amide III modes show extensive mixing, for both types of modes, except for the in-phase combination of CN stretching and NH in-plane bend of the cationic species calculated with the larger basis set (aug-cc-pVDZ), sup table S10. Diem and coworkers have shown that the amide III mode is only pure amide III in the model compound *N*-methyl acetamide [26]. In their pioneering work on isotopomers of L-alanyl-L-alanine, they showed that the two CH methine deformation modes on the *N*- and *C*-termini strongly couple with the amide III modes, mixing to such an extent that there are actually 5 modes, two methine for each $C^{\alpha}$–H group and what had been called the amide III mode. Subsequently, we confirmed this assignment in our theoretical investigation on the isotopomers of L-alanyl-L-alanine [50].

Comparison of the calculated zwitterionic species, sup figures S4–S6, shows substantial differences in peak positions and intensities of the IR spectra, see sup tables S2(*a*)–S2(*c*) and sup table S8–S10. The IR intensities are found to be larger using the Onsager model. The experimental IR spectrum of water has intense modes at 3500 and 1700 $cm^{-1}$ that the Onsager continuum model does not treat explicitly [1]. The solvent water is treated as a spherical dielectric cavity of radius $a_o$ with the dielectric constant $\varepsilon = 78$ representing the solvent polarity in which the molecule is embedded. Note that the interaction term in the Onsager model is a function of the electric dipole moment of the molecule, molecules with no electric dipole moment will not experience a solvent effect. This could explain the intensity difference seen between the two models, as the shapes of the cavities are different and the interaction Hamiltonians are different. For more details see [23]. The zwitterionic species calculated with a larger basis set (aug-cc-pVDZ) and with the PCM model sets itself apart from the previously calculated spectra, see sup figure S6. The amide I modes are shifted substantially towards lower frequencies and are located around 1600 $cm^{-1}$, see sup table S8, and are considerably more intense.

As expected the intensity of AIII is smaller than AII, which is as intense as AI or more dominant. AII is the least sensitive to structure of the three amide modes and the largest differences are observed for AIII as would be expected for structural changes seen for the dipolar ion calculated with the two different methods. A more extended structure, sup figure S1(*c*), is observed for the zwitterion optimized within the Onsager continuum model, compared to a much more bent conformation, sup figure S1(*b*), for the method which does not treat the solvent. By analyzing the vibrational modes with the GaussView program, one can see that the vibrational modes of the zwitterion computed with the Onsager continuum model are more due to displacements all over the molecule (delocalized modes) than of the zwitterion computed in 'pure' gas phase where the modes are due to a single or a few dominating displacements (localized modes) [45].

The VCD spectra differ to the same extent as the IR spectra. The Onsager continuum model without the inclusion of explicit water molecules does not appear to be adequate to model the spectra tri-L-serine in aqueous solution. In addition, the spectra appear to be greatly modified by the continuum model. One of the problems inherent in the Onsager continuum model is the shape of the cavity. The recommended procedure to determine the cavity radius is to perform a volume calculation. We have followed the recommended procedure and then noted that the cavity does not appear to enclose the whole molecule or complex when we have combined the Onsager continuum with our explicit water model. By using the Molden program, one is able to see the size of the box which fully encloses the molecule or complex. Here we have seen that the problems that some groups have reported with this model may be due to part of the molecule and (or) complex (explicit water molecules) lying outside the cavity. We recommend that the previously reported Onsager results should be checked to see that either the molecule and (or) molecular complex was fully enclosed with the spherical cavity. If not, these calculations should be repeated with larger cavity radii. But in this case there is probably a large percentage of the cavity that is now not filled with solvent. Here one has two possibilities, to go to a more physical cavity, for example the PCM model, or to fill the spherical cavity so that the cavity is filled with water molecules. Another possibility is to develop a model with a rectangular cavity, to match the periodic boundary conditions and shapes which have been utilized in the solid state physics and condensed matter physics community. Here the two groups of researchers can really learn from each other. Indeed we have initiated a project where we are now modeling and implementing new cavity models to treat the problem of solvation and solvent effects. In this report, we only present our results utilizing the Onsager and PCM continuum models alone and in combination without explicit water model.

Comparing the spectra of all calculated species, sup figures S4–S11, one sees quite different spectra, where both peak frequencies and intensities are distinct. The most remarked changes occur for higher frequencies

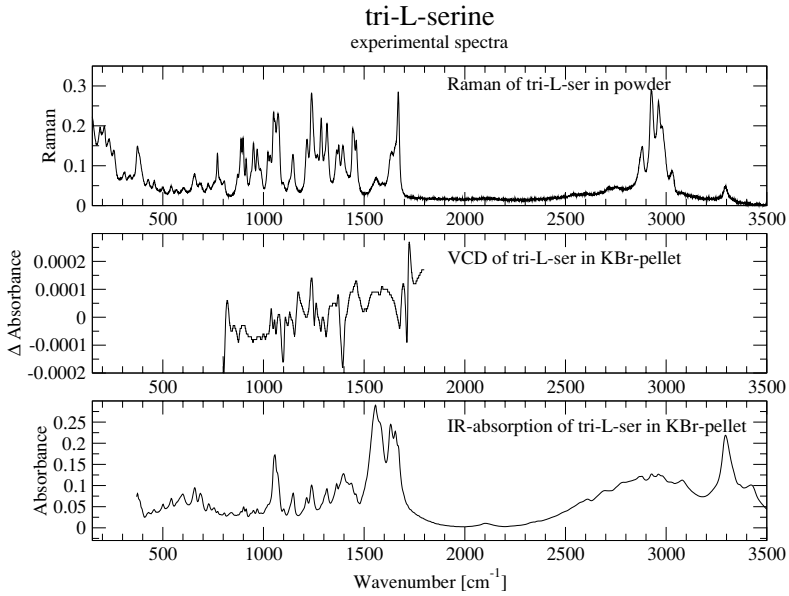


**Figure 2.** Experimental VA, VCD and Raman spectra for tri-L-serine in KBr pellet and powder.

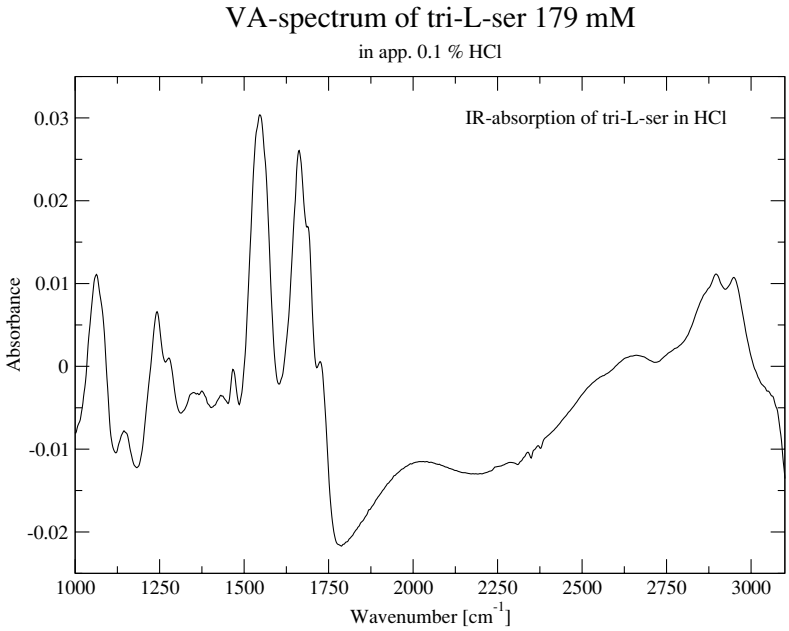


**Figure 3.** IR absorption spectra of tri-L-ser in approximately 0.1% HCl.

(above 2000 $cm^{-1}$), where all ionic-species peak intensities are lower than those from the capped-, neutral- and zwitterionic-species (without Onsager). That is, peak intensities for higher frequencies are dampened within the Onsager solvation sphere, something that does not apply at all for the zwitterionic species calculated within the PCM model. All AI modes are relatively similar by exhibiting intensities around 500–600, and are found in the same frequency range between 1800 and 1700 $cm^{-1}$, sup table S8. Both anions constitute exceptions, by having AI modes with intensities around twice that value, sup figures S7 and S8, sup tables 5(*a*) and (*b*), as well as all species calculated by PCM. The frequency of AI of the cation calculated with PW91 is, however, considerably lower at 1627 $cm^{-1}$. The amide II is the most prominent peak below 2000 $cm^{-1}$ in all calculated spectra, except for the capped and the neutral species where the amide I region has the same intensity. But also for the cation II and anion II, amide I is more intense than AII, sup tables S6(*b*) and S5(*b*), as well as the spectra calculated with the PCM model, here AII and AI are equally intense or AI is the dominating mode, sup tables S6(*c*)–S6(*e*).

*VA spectrum of tri-L-serine in KBr and in HCl solution*

The peaks of VA spectra for the tri-L-serine/KBr pellet and the compound in solution coincide, see figures 2 and 3. There are,

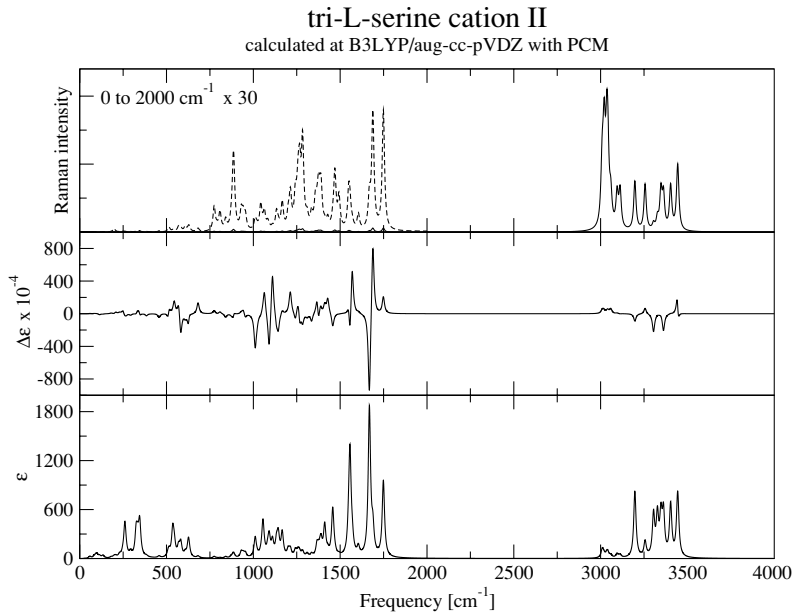


**Figure 4.** Calculated VA, VCD and Raman spectra for cation II with B3LYP/aug-cc-pVDZ and PCM.

however, some differences: solution peaks are much broader and slightly shifted towards higher wave numbers, except for 1556 $cm^{-1}$ in KBr pellet, which is shifted down to 1546 $cm^{-1}$ in solution (blow-up of the amide I region can be found in sup figure S2). Tri-L-serine is expected to have strong solvent interactions due to the three OH groups in the side chains. The side chain OH groups can also H-bond with the backbone $NH_3^+$, amide C=O and NH, and $CO_2^-$ groups. Broadening is noticed at 1060 $cm^{-1}$, which is attributed to CCO out of plane stretch of $C^{\alpha}$–$C^{\beta}$–O of serine. The AI region would be expected to be broader in solution due to the C=O stretch, which indeed is observed.

*Comparison between the calculated and measured VA and VCD spectra*

In the following, the major features of the VA spectra of solid (KBr pellet) and solution tri-L-serine are compared to the calculated spectra for all species. Internal coordinates together with the potential energy distributions for the calculated modes can be found in sup tables S2–S6(*e*) in the supplementary data (available from stacks.iop.org/PhysBio/3/S63). The KBr pellet spectrum exhibits a very weak peak around 950 $cm^{-1}$, a peak that normally is attributed to a COOH stretch, none of the calculated spectra can explain this peak in the experimental spectrum. A very prominent peak is seen at 1057 $cm^{-1}$, KBr pellet figure 2, corresponding to 1063 $cm^{-1}$ for tri-L-serine in solution. All calculated spectra have peaks in the vicinity due to stretches of the side chains, see sup tables S5, S5(*b*), S2, S2(*a*), S6–S6(*e*), but none of which are comparable to the intensity of the experimental spectra. One exception might be given by cation II calculated at PW91, sup table S6(*d*), which exhibits a fairly prominent peak at 1025 $cm^{-1}$, as well calculated with the larger basis set aug-cc-pVDZ (1055 $cm^{-1}$, see sup table S6(*c*)). Both can be attributed to the $C_{14}$–$O_{15}$ side chain stretch. In figures 4 and 5, we present the simulated spectra with the B3LYP hybrid XC functional and PW91 GGA XC functional with the large aug-cc-pVDZ basis set for the cationic species and the PCM continuum solvent model. In figure 6, we present the simulated spectra with the B3LYP hybrid XC functional and the smaller 6-31G* basis set for the cationic species and the PCM continuum solvent model. This basis set and XC hybrid functional were used for the explicit water cation/anion complex simulations, so it is important to show the two simulations at the same levels.

**Table 1.** Experimental vibrational modes.

| Experiment | ($cm^{-1}$) | ($cm^{-1}$) | ($cm^{-1}$) |
|---|---|---|---|
| KBr pellet | 1655, 1632 | 1556, 1435 | 1398, 1364, 1315, 1239, 1214 |
| HCl solution | 1725, 1688, 1662 | 1546, 1467 | 1277, 1242 |

The amide modes for all calculated species assigned with internal coordinates and the PEDs are given in sup tables S8–S11 while the major vibrational modes found in the same area for tri-L-serine measured in the KBr pellet and in HCl solution are given in table 1. The difference in number of peaks obtained from the two experiments is due to the broadening of the modes. It was seen that the calculated *amide I* modes are between 1788 and 1714 $cm^{-1}$ (lower level of theory), while the experimental values are considerably lower for the tri-L-serine both in the pellet and in solution. The results in solution are however a little bit closer to the calculated ones. It seems, however, that the *amide I* modes of all the species calculated with the PCM model are much closer to those experimentally observed, particularly the zwitterion and the cation calculated at the B3LYP/aug-cc-pVDZ level, as seen in sup table S8 and table 1.

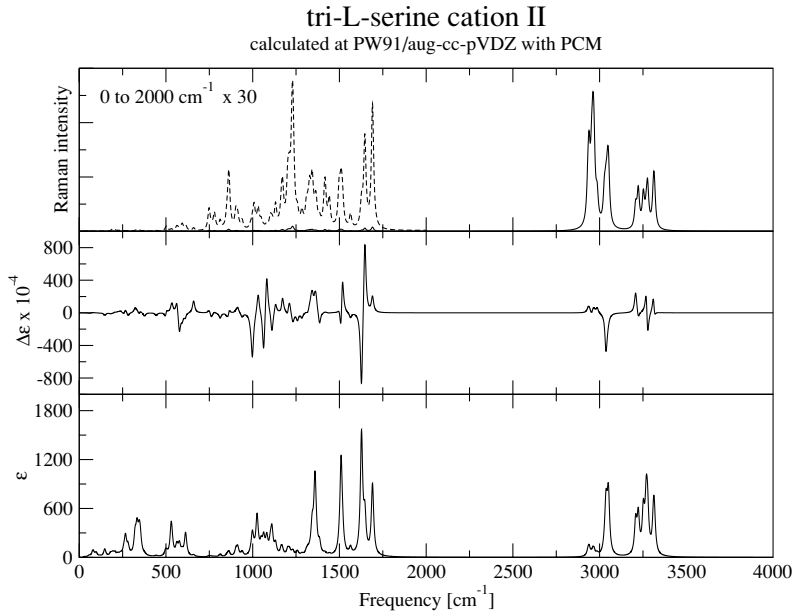


**Figure 5.** Calculated VA, VCD and Raman spectra for cation II with PW91/aug-cc-pVDZ and PCM.

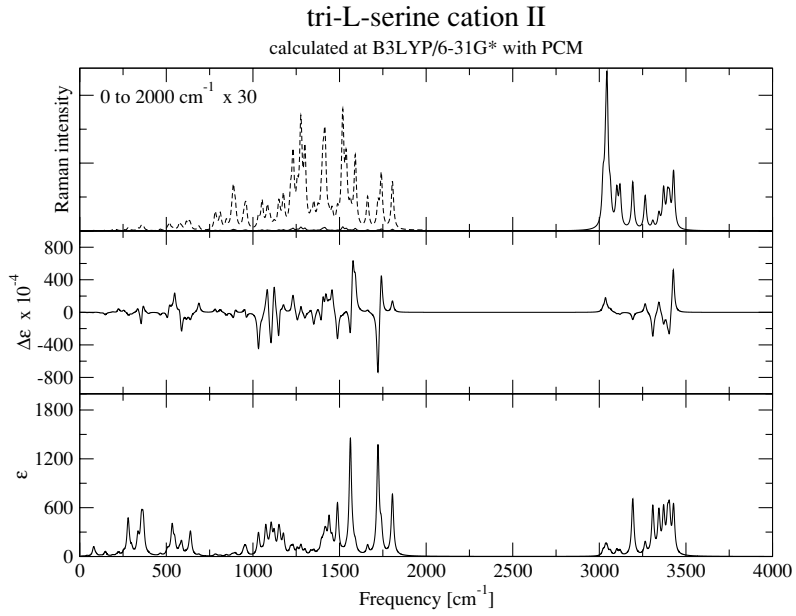


**Figure 6.** Calculated VA, VCD and Raman spectra for cation II with B3LYP/6-31G* and PCM.

For the *amide II* region of the experimental spectra, the frequencies of the bands in the HCl solution spectra (figure 3) are again in closer agreement with those in the calculated spectra than those of the bands in the KBr spectrum. It is noticeable that the peak 1556/1546 $cm^{-1}$ is larger in intensity than the peaks that constitute the AI-region, a feature that is seen in almost all calculated spectra, especially the ions (not anion I). Closest to this feature comes the zwitterion calculated with the Onsager model and cation II. For the spectra calculated with the PCM model, it seems that only the zwitterion is able to reproduce this feature. Cation II calculated at B3LYP/6–31G*, PCM, might have a more intense AII than AI, but AI lies unfortunately at too high frequencies, see sup tables S8, S9 and table 1 as well as figures 2 and 6. It is difficult to estimate if the spectral feature between AI and AII is reproduced by any of the calculated spectra, since the amide I and II regions are much closer together in the experimental spectra.

The calculated *amide III* modes fit equally poorly or well with respect to the peaks observed in the experiment. However, it seems again that cation II represents the features a little better, especially with respect to the spectral features around

the peak 1298 $cm^{-1}$, which is absent in all other calculated species. Generally the intensity of AII vibrations is larger than that of the AI vibrations, except for the neutral, capped, anion II and cation II species. It seems odd that the AII modes have more intensity, since the AI modes in the other systems are more intense, but this seems also to be the picture for the experimentally obtained spectra. Here rather than having the COOH species, we have the $COO^-$ modes. There exist the symmetric and antisymmetric combinations of the CO bond strengths. Also depending on the bond lengths and force constants for these modes in different environments, the two modes can change their nature, and hence both the vibrational frequencies, and the VA, VCD, Raman and ROA intensities. We note that the modes in the amide II region are enhanced, but they may actually not be amide II modes, but the $COO^-$ modes or other modes which strongly couple with these modes and with or via the explicit or implicit water models. This is a very interesting topic and requires more investigation, which is beyond the scope of this work. We will present a full report on this topic in the near future. In addition to varying the environment for the parent species, we also will investigate isotopic substitution with $^{13}C$, $^{18}O$ and $^{2}H$ isotopes. Here by changing the mass we will be able to decouple the modes that are strongly coupled. As mentioned before, this has also been the case for the amide III modes. They are actually strongly coupled to the CH modes on the adjacent *N*- and *C*-terminal modes. To decouple them, one must perform isotopic substitution at $C^{\alpha}$ centers to get pure amide III modes. Clearly this is much easier to do theoretically than experimentally. But Diem and coworkers have shown experimentally that the information gained from such work is well worth the experimental effort [26].

The experimental spectrum, figure 2, has a peak of weak intensity at 2101.83 $cm^{-1}$. This peak does not exist in neither of the calculated spectra. It is an overtone of the vibration at 1056.64 $cm^{-1}$ (half the wave number is 1050.915 $cm^{-1}$, where a vibration is found), this correlates to the fact that overtones are not considered in the calculations. A lot of peaks, on broad background, exist in the region from 2500 to 3500 $cm^{-1}$, where the most intense peaks are 3295 and 2927 $cm^{-1}$. This region does not resemble any of the calculated spectra; this might be due to moisture and $CO_2$ in the air during the experiment or its preparation. The calculated spectra have vibrational modes up to almost 3800 $cm^{-1}$, except for the zwitterionic species (without Onsager), and those calculated with the PCM model, which just exhibits vibrations up to 3533 $cm^{-1}$. The vibrations in this region are due to OH stretching and the neutral and cationic species should have more due to the acid group COOH, nevertheless, none of the calculated spectra reproduce the very prominent peak at 3592 $cm^{-1}$ of the experimental spectrum. The calculated vibrations, in this upper vibrational region, extend for all calculated species down to 3000 $cm^{-1}$. One exception is the zwitterion calculated without Onsager continuum model that exhibits a single mode at 2697 $cm^{-1}$. This vibration is due to an elongated NH stretch of $N_{33}$–$H_{34}$, since $H_{34}$ comes in close proximity to $O_{10}$ with a distance of 1.6577 Å arising as a result of the gas phase, see sup table S1(*a*), S2, S2(*b*).

For the experimentally obtained VCD spectrum, see figure 2 and sup figure S2, it can be said, other than the fact that the features between the VA and VCD coincide, that the region around 1700 wave numbers first assumes a positive value before going towards negative values (seen from the left). This feature is imitated by most of the calculated spectra, see sup figures S4–S11 or sup tables S2–S6.

All in all it can be said that the larger basis set (aug-cc-pVDZ compared to 6–31G*) and the polarized continuum model had a considerably better accordance with the experimental data. The major features were reproduced quite well in the infrared-absorption spectra, especially for the cation II species in the frequency regions between 1000–1100 and 1550–1700 $cm^{-1}$. The reproduction of the Raman spectra was not as good, but better than the reproduction of the VCD spectra. The frequency agreement measures the accuracy of the eigenvalues of the Hessian while the infrared absorption, Raman and VCD intensity agreement measures the accuracy of the eigenvectors, the atomic polar tensors, the electric dipole polarizability derivatives and the atomic axial tensors.

The Raman scattering spectra are presented in figures 2 and 7. As one can see in figure 2 the Raman spectra are not as affected by the solvent water, as are the VA and VCD spectra. This is due to water being a stronger absorber of IR radiation, and not a good Raman scatterer at the wavelengths used in our Raman experiments. In figure 7 one can see that the Raman spectra for the aqueous solution are not as well resolved as the Raman spectra for the powder. We have measured the Raman spectra with laser sources of 633 nm and 1064 nm. As one can see in our Raman spectral simulations for the various species of tri-L-serine, the implicit solvent models do quite well for the Raman spectral simulations, where the water does not show a strong signal, that is, for the powder. But with respect to the measurements for the aqueous solution spectra, the explicit water model and the hybrid explicit water + Onsager continuum model does better, sup figure S3 and figures 8–10. Here both sets of calculations appear to be useful and important. What is important is to have the explicit water molecules which are responsible for stabilizing the structure of the peptide, and which compete with the intramolecular hydrogen bonds between the side chain OH groups and the backbone carbonyl oxygen of the amide and carboxylate groups. With the explicit water model these hydrogen bonds are less important.

### *N-acetyl tri-L-serine N′-methylamide (NALSLSLSNMA) results*

At the Becke 3LYP level with the 3-21G and 6-31G* basis sets, we have optimized the geometry starting from the linear structure. In sup figure S1(*g*) we show our Becke 3LYP/6–31G* optimized structure for NALSLSLSNMA. Here we end up with the intramolecular hydrogen bonding between the serine side chain OH group with the backbone carbonyl C=O group. The backbone torsional angles $\phi_i$ and $\psi_i$, the side chain torsional angles $\chi_{ij}$, and the peptide torsion angle $\omega_i$ for NALSLSLSNMA for the various levels of theory are given in table 2. Here one can see that the local minimum at the

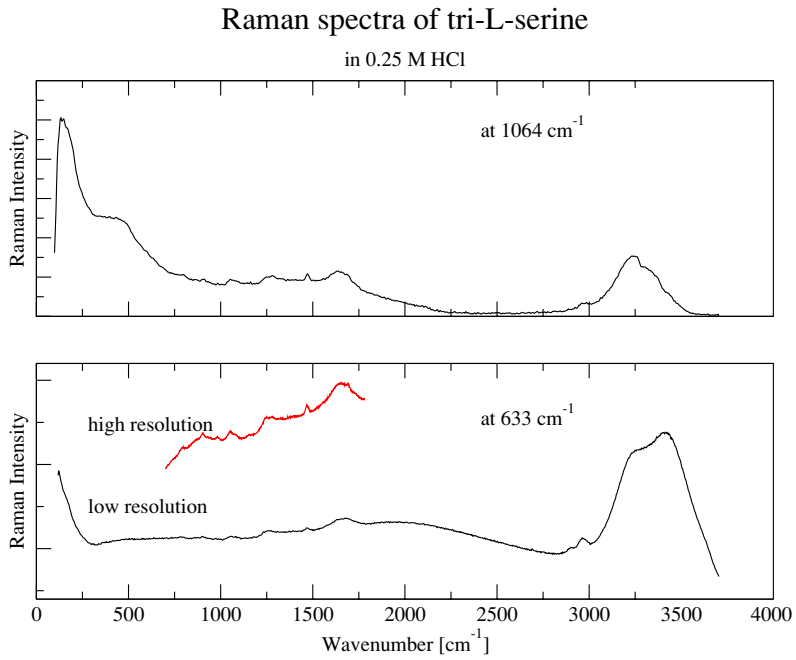


**Figure 7.** Raman spectra of tri-L-serine 0.25 M HCl.

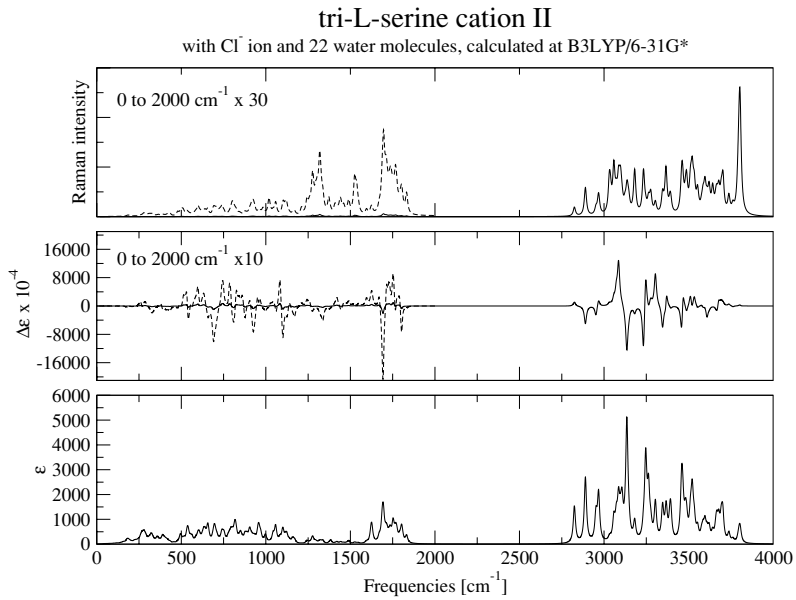


**Figure 8.** Calculated VA, VCD and Raman spectra for cation II with B3LYP/6-31G*, explicitly solvated with 22 water molecules and $Cl^-$ ion.

lower basis set level is also a minimum for the higher basis set level. This is not always the case, also with respect to the XC functional within DFT and also with the level of treatment of electron correlation for the correlated levels. This is especially true with respect to dispersion forces which stabilize van der Waals complexes and dispersion forces which are responsible for base stacking in DNA and the interactions between the aromatic side chains in proteins, for example, the tyrosine and phenylalanine side chains in Leu-enkephalin. Hence even though it is nice to use a smaller basis set and (or) level of theory on preliminary studies, and the use of continuum models to treat solvation effects, in many cases one is misled if one only uses the local minimum at these 'lower levels', when one goes to a more sophisticated level of theory, basis set, treatment of the solvent and other environmental factors and perturbations.

The VA, VCD and Raman spectra for NA-triLser-NMA at the Becke 3LYP/6–31G* level of theory, figure 11, are presented below and compared with that at the Becke 3LYP/3-21G level of theory, figure 12. As one can see

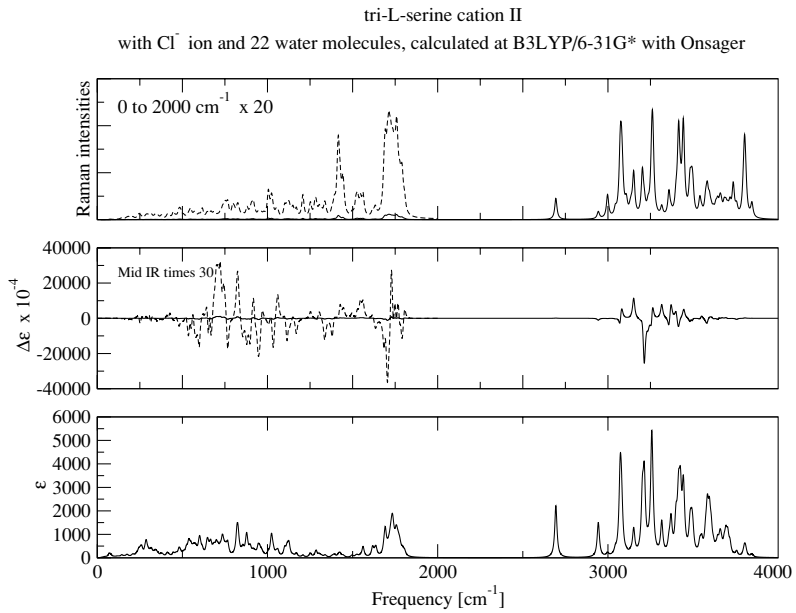


**Figure 9.** Calculated VA, VCD and Raman spectra for cation II with B3LYP/6-31G*, explicitly solvated with 22 water molecules and a $Cl^-$ ion, within Onsager solvation sphere (except AAT).

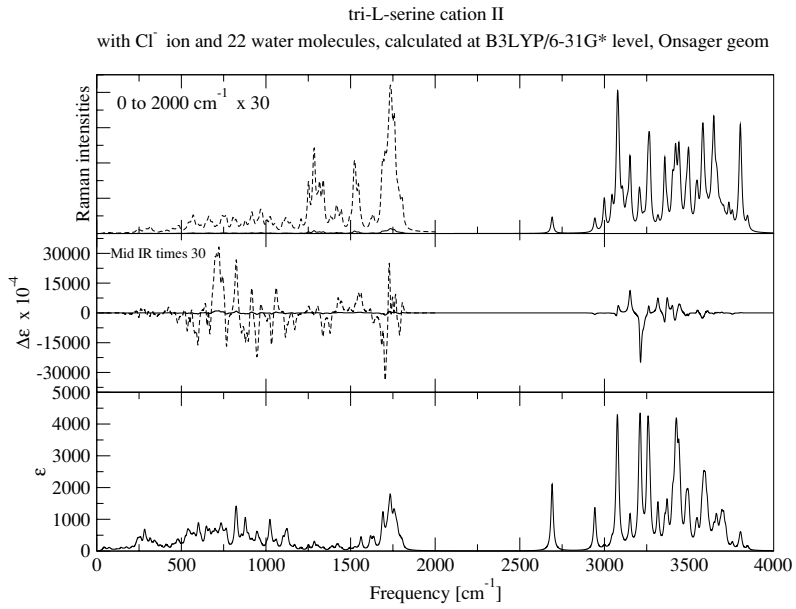


**Figure 10.** Calculated VA, VCD and Raman spectra for cation II calculated at B3LYP/6-31G*, explicitly solvated with 22 water molecules and a $Cl^-$ ion, geometry optimized within Onsager solvation sphere (i.e. AAT, Hessian, APT and EDEDPD calculated without).

**Table 2.** Torsional angles for NALSLSLSNMA at Becke 3LYP level with the 6-31G* and 3-21G basis sets.

| B3LYP | $\phi_1$ | $\psi_1$ | $\chi_{1,1}$ | $\chi_{1,2}$ | $\omega_1$ | $\phi_2$ | $\psi_2$ | $\chi_{2,1}$ | $\chi_{2,2}$ | $\omega_2$ | $\phi_3$ | $\psi_3$ | $\chi_{3,1}$ | $\chi_{3,2}$ |
|---|---|---|---|---|---|---|---|---|---|---|---|---|---|---|
| 3-21G | −171 | 179 | 176 | −100 | 158 | −96 | 179 | 180 | −100 | 158 | −104 | −170 | −169 | −178 |
| 6-31G* | −157 | 169 | −180 | −91 | 159 | −82 | 170 | −176 | −91 | 160 | −96 | −171 | −167 | −176 |

there are very large differences in the VA, VCD and Raman spectra using the Becke 3LYP hybrid XC functional and the two different basis sets. Hence it is clear that the 3-21G level of theory which has been advocated for simple organic compounds, does not appear to be adequate to represent peptide systems. Also shown are the ROA spectra for the NA-triLser-NMA with the Becke 3LYP hybrid XC functional and 6–31G* and 3-21G basis sets, figure 13. We present the simulated results for the ROA spectra to document the feasibility of these calculations and also to show how the

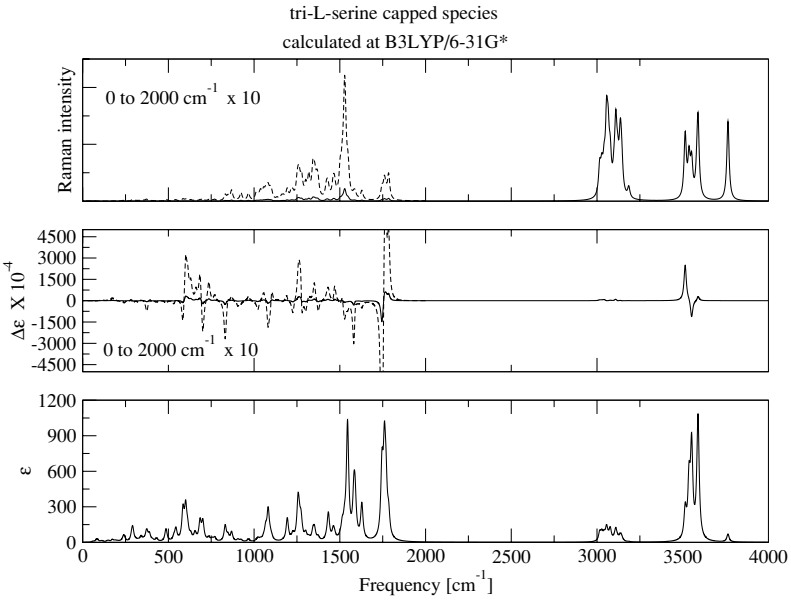


**Figure 11.** Calculated VA, VCD and Raman spectra for the capped peptide.

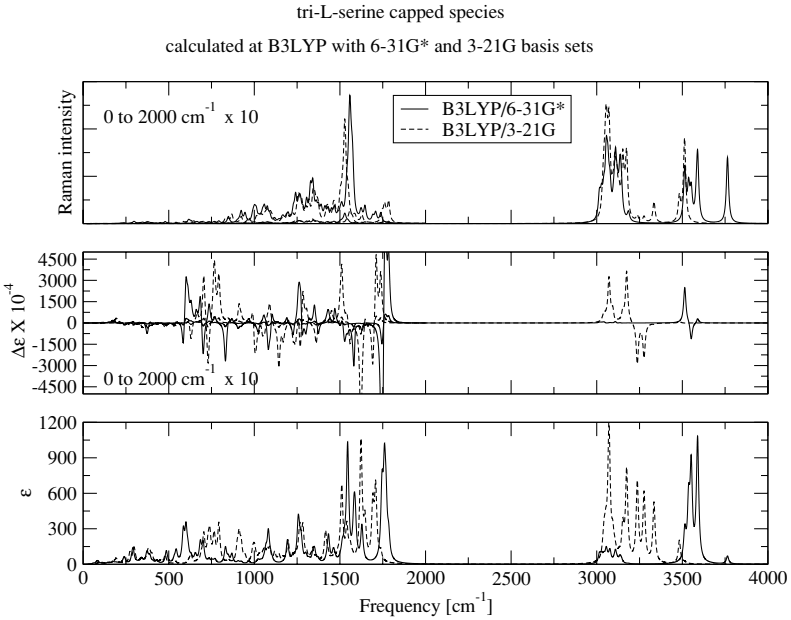


**Figure 12.** Calculated VA, VCD and Raman spectra for NALSLSLSNMA calculated at B3LYP/ 3-21G and B3LYP/6-31G*.

signed nature of the ROA adds information to the spectra not present in the Raman, similar to the additional information provided by the VCD in addition to the VA. Here one can get absolute configuration information, which has made VCD and ROA spectroscopy extremely important in the pharmaceutical industry, where the enantiomeric purity is of importance, and more important the identification of which enantiomer is present. By monitoring the VCD and ROA spectra during a biological process, one can also monitor the extent that the molecule either racemizes or to what extent the process is stereo selective and stereo specific. Hence the applications of these two relatively new spectroscopies have greatly benefited from the development of theoretical methods to fully interpret and understand the spectra. As one can see in figure 11, the 3-21G basis set does not appear sufficient to simulate the ROA spectra, and hence the SCC-DFTB method will require the use of an extended basis set for the calculation of the tensors required to simulate the vibrational intensities.

## Discussion

The differences between the experimental and calculated spectra are most certainly due to the fact that the calculated species are for tri-L-serine molecules either in the gaseous phase, where the aqueous environment is only treated by

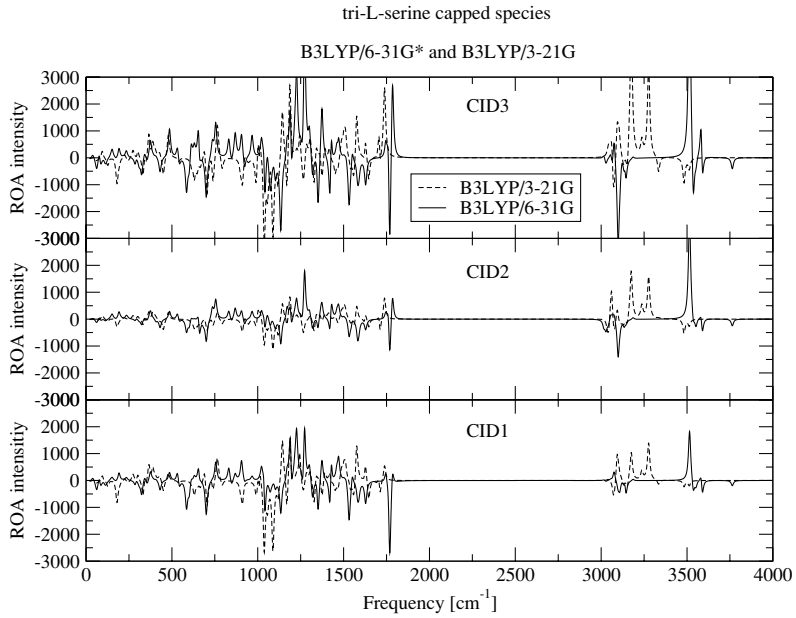


**Figure 13.** Calculated ROA spectra for NALSLSLSNMA calculated at B3LYP/3-21G and B3LYP/6-31G*.

continuum models, where we only treat a small number of the water molecules, or where we combine the small cluster of explicit water molecules hydrogen bonded to tri-L-serine with the continuum solvent models. Even though the solvent medium of the species is simulated with either the Onsager or PCM continuum models, this cannot be regarded as in aqueous solution, since strong solvent interaction from the side-chain serine groups is expected but not considered at all with the continuum solvent models. Another possibility for the discrepancies between experiment and calculations, which is equally important, is the fact that the spectra are not calculated at a global energy minimum, as we know of, since no systematic energy minimization was done. We have tried to improve upon the gas phase and continuum models by including the explicit water molecules which are hydrogen bonded with the cationic species and also which solvate the $Cl^-$ anion. This clearly treats the direct interactions much better than the two continuum models, but does not treat the effects due to bulk water. Hence we have embedded our tri-L-serine cation plus the $Cl^-$ anion within the two cavities, either spherical in the case of the Onsager model, or shape of the cluster in the case of the PCM model. This clearly appears the way to go. Since the point of this work was to document the various ways to treat the effects due to the aqueous environment, counterions and pH on both the structural and vibrational properties, we feel we have accomplished that with our last set of calculations. A future publication shall present our results at this level of theory for all species and also perform a systematic potential energy surface (PES) at this level of theory. This will require a lot of computer time and hence the programs which we have used must also be very efficient to be able to do this. Hence we are also in the process of modifying the programs to make such calculations feasible for not only tripeptide systems, but also much larger peptide systems. This is clearly also a criterion if we wish to perform the required sampling and averaging required to simulate the VA, VCD, Raman and ROA spectra for all species and conformers for biological molecules, here peptides in solution and bound to proteins.

For the experimentally obtained VCD spectrum it can be said, other than features between VA and VCD spectra coincide, that the region around 1700 wave numbers almost exhibits the same $\pm/+$ pattern as the calculated spectrum.

Eker *et al* have presented a combined Raman, VA and VCD study of tripeptides in aqueous solution, similar to our previous works on LA, NALANMA and LALA [8, 9, 50]. In their study they also present the results for the anionic species of tri-L-serine. This was the only species for tri-L-serine for which they were able to obtain the backbone torsion angle ($\phi_1$,$\psi_1$) and ($\phi_2$,$\psi_2$). Their reported values were (–135, 178) and (–175, 135), respectively. They found a very large pD dependence of the VA, VCD and Raman spectra for tri-L-serine, much larger than for the other tripeptides studied. This is not surprising due to the nature of the side chains of tri-L-serine, all being OH groups, which allow for both hydrogen bonding and protonation. Here the explicit water model and our hybrid explicit water model combined with the continuum solvent models are very applicable. The results we have to date suggest that our model should be able to answer the outstanding questions left unanswered in the study of Eker *et al*. In a future publication, we will present our complete set of results from our hybrid for the complete set of the species for tri-L-serine, which is beyond the scope of this work.

In the article of Eker *et al* the amide I bands of several species were measured, but due to purely signal to noise issues, only the spectra of the anionic species were presented. A quick comparison between our calculated and their measured spectra shows that our calculated amide I band is shifted towards higher wave numbers, around 1700–1790 $cm^{-1}$, while the measured values lay a little bit lower around 1630–1730 $cm^{-1}$.

Hence, our experimental peaks are closer to the experimental results of Eker *et al*, which lie around 1650 $cm^{-1}$ [51]. The overall features are very hard to compare, but do not seem similar, except for the lower frequency peak being higher in intensity than the next. Our calculated VCD spectra, though again shifted towards higher wave numbers, seem to show the overall features of their measured VCD spectrum for the acidic species rather than the alkaline.

## Conclusions and outlook

In this work, we have utilized the B3LYP DFT level of theory to model various species of tri-L-ser and NA tri-L-ser NMA. In this work, we have added explicit water molecules, and have also tested the ability or capabilities of one of the newly developed continuum models, the so-called PCM model. Previously, the Onsager continuum has been shown to be inadequate to treat amino acids and small peptides due to its not taking into account the specific hydrogen bonded interactions. This also appears to be the case for the PCM model. Even the developers of this model have come to similar conclusions on other simpler systems. But this level of theory needs to be further tested on larger systems such as the two presented here, that is, tri-L-serine and NA tri-L-ser NMA. It appears that even for larger peptides and capped peptides, the inclusion of explicit water molecules to treat the water molecules in the first hydration shell that directly interact with the polar parts of the molecule is extremely important. The treatment of these waters is important for many reasons. Firstly if they are not included, the structures with intermolecular hydrogen bonds are almost always lowest in energy due to the stabilization energy generated by these interactions. But in aqueous solution it is the total energy of the whole system, which must be a minimum and not just the lowest energy of the individual parts. Hence the cooperativity effects and synergistic interactions must be treated. The hope is that only the strongly hydrogen bonded interactions are necessary for these calculations, but the definitive answer to this question is still open and we are still working on this problem in this system and others, where we hope to be able to develop an automated way of answering this question. In addition, the structures that include the explicit water molecules are in many cases not even local minimum on the PES for the isolated molecule, so one has no chance of even finding them without explicitly adding waters. Also if one wishes to simulate the VA, VCD, Raman and ROA spectra, as is our goal, then one needs not only to find the correct local minimum for the peptide + N explicit water molecules but also to treat the coupling of the modes of the solvent with the water molecules in this local hydration shell environment. The process of energy transfer, redistribution and charge transfer are also very important in understanding the function of biomolecules, so these are also goals of our studies, we not only want the structure, as many studies do, but we want the VA, VCD, Raman and ROA spectra and the electric, magnetic and nuclear properties of the molecule and its hydration shell, since they are also very important for our goal of understanding the structure and function of biomolecules via probing with electromagnetic radiation in the various environments where the molecules are present in their native states, but also under non-native conditions which may arise and which may for instance be responsible for illness. Hence the goal is to be able to understand medicine at a molecular level, and here one requires not only just the structures of the various molecules in aqueous solution, but also their interactions with each other, with the solvent and ultimately as a function of the environmental stresses which cause illnesses, so that we can develop possible safeguards and cures.

## Acknowledgments

The Danish Research Council is acknowledged for its financial support for the Quantum Protein Centre and VWJ's PhD stipendium (grant). The authors would like to thank J Sonne, T H Pedersen (QuP-Centre) for their part in the calculations and H H Drews from Brucker Optik GMBH, FT-IR applications Marketing, Rudolf-Plank-Str. 23, D-76275 Ettlingen, Germany for the help with the experimental measurements, as well as other staff members. We would also like to thank the German Cancer Research Center (the DKFZ) in Heidelberg, Germany for providing computer resources, which allowed the large solvated systems to be calculated on the HP Cluster at the DKFZ. In addition, we would like to thank the staff at Thermo Electron, Madison, WI, USA for help with the Raman measurements. We would also like to thank the Laboratory of Physics at Helsinki University of Technology and the Finnish Academy of Science for supporting this research project during KJJ's many visits to the Laboratory of Physics and for the fruitful discussions with Risto Nieminen and Ivan Degtyarenko. In addition, KJJ would like to thank Julian Gale for fruitful discussions and the Government of Western Australia for funding under the Premier Research fellow program.

## References

[1] Onsager L 1936 *J. Am. Chem. Soc.* **58** 1486–93
[2] Gill P M W Density functional theory (DFT) *Hartree–Fock (HF) and Self-consistent Field in Encyclopedia of Computational Chemistry* (New York: Wiley) pp 678–88
[3] Frisch M J *et al* 2001 (Pittsburgh, PA: Gaussian Inc.) *Gaussian 98 and 2003*
[4] Atkins P W and Friedman R S 2004 *Molecular Quantum Mechanics* 4th edn (Oxford: Oxford University Press)
[5] Kohn W 1999 *Rev. Mod. Phys.* **71** 1253–66
[6] Jalkanen K J, Bohr H G and Suhai S 1997 Density functional and neural network analysis: hydration effects and spectroscopic and structural correlations in small peptides and amino acids *Theoretical and Computational Methods in Genome Research* ed S Suhai (New York: Plenum) pp 255–77
[7] Jensen F 1999 *Introduction to Computational Chemistry* (New York: Wiley)
[8] Jalkanen K J, Nieminen R M and Bohr J 2000 Simulations and analysis of the Raman scattering and differential Raman scattering/Raman optical activity (ROA) spectra of amino acids, peptides and proteins in aqueous solution *Vestn. Mosk. Univ. Khim.* **41** 4–7

Jalkanen K J, Nieminen R M, Frimand K, Bohr J, Bohr H, Wade R C, Tajkhorshid E and Suhai S 2001 *Chem. Phys.* **265** 125–51
Tajkhorshid E, Jalkanen K J and Suhai S 1998 *J. Phys. Chem.* B **102** 5899–913
Frimand K, Bohr K, Jalkanen K J and Suhai S 2000 *Chem. Phys.* **255** 165–94
[9] Han W G, Jalkanen K J, Elstner M and Suhai S 1998 *J. Phys. Chem.* B **102** 2587–602
[10] Jalkanen K J and Suhai S 1996 *N*-acetyl-*L*-alanine *N*′-methylamide: a density functional analysis of the vibrational absorption and vibrational cirkular dichroism spectra *Chem. Phys.* **208** 81–116
Deng Z, Polavarapu P L, Ford S J, Hecht L, Barron L D, Ewig C and Jalkanen K J 1996 *J. Phys. Chem.* **100** 2025–34
[11] Jalkanen K J, Jürgensen V W and Degtyarenko I M 2005 *Adv. Quantum Chem.* **50** 91–124
[12] Bohr H, Jalkanen K J, Elstner M, Frimand K and Suhai S 1999 *Chem. Phys.* **246** 13–36
Frimand K and Jalkanen K J 2002 *Chem. Phys.* **279** 161–78
Abdali S, Niehaus T, Jalkanen K J, Ciao X, Nafie L A, Frauenheim Th, Suhai S and Bohr H 2003 *Phys. Chem. Chem. Phys.* **5** 1295–300
Jalkanen K J *et al* 2006 *Int. J. Quantum Chem.* **106** 1160–98
[13] Talman J D and Shadwick F W 1976 *Phys. Rev.* A **14** 36–40
[14] Hirata S, Ivanov S, Grabowski I, Bartlett R J, Burke K and Talman J D 2001 *J. Chem. Phys.* **115** 1635–49
[15] Krieger J B, Li Y and Infrate G J 1992 *Phys. Rev.* **A45** 101–26
[16] Yanai T, Tew D P and Handy N C 2004 *Chem. Phys. Lett.* **393** 51–7
[17] Bauernschmitt R and Ahlrichs R 1996 *Chem. Phys. Lett.* **256** 454–64
Dreuw A and Head-Gordon M 2004 *J. Am. Chem. Soc.* **126** 4007–16
Gritsenko O and Baerends E J 2004 *J. Chem. Phys.* **121** 655–60
Tawada Y, Tsuneda T, Yanagisawa S, Yanai T and Hijaro K 2004 *J. Chem. Phys.* **120** 8425–33
Hirata S, Ivanov S, Grabowski I and Bartlett R J 2002 *J. Chem. Phys.* **116** 6468–81
Neiss C, Saalfrank P, Parac M and Grimme S 2003 *J. Phys. Chem.* **A107** 140–7
[18] Engel E and Bonetti A F 2001 *Int. J. Mod. Phys.* **B 15** 1703–13
[19] Hirata S, Ivanov S, Bartlett R J and Grabowski I 2005 *Phys. Rev.* **A 71** 032507-1-7
[20] Onida G, Reining L and Rubio A 2002 *Rev. Mod. Phys.* **74** 601–59
Reining L, Olevano V, Rubio A and Onida G 2002 *Phys. Rev. Lett.* **88** 066404
Ismail-Beigi S and Louie S G 2003 *Phys. Rev. Lett.* **90** 076401
Zhukov V P, Chulkov E V and Echenique P M 2004 *Phys. Rev. Lett.* **93** 096401
Botti S, Sottile F, Vast N, Olevano V, Reining L, Weissker H-C, Rubio A, Onida G, Sole R D and Godby R W 2004 *Phys. Rev.* B **69** 155112
[21] Soler J M, Artacho E, Gale J D, Garcia A, Junquera J, Ordejon P and Sanchez-Portal D 2002 *J. Phys.: Condens. Matter* **14** 2745–79
[22] Gonze X *et al* 2002 *Comput. Mater. Sci.* **25** 468–92
[23] Tomasi J, Mennucci B and Cammi R 2005 *Chem. Rev.* **105** 2999–3093
Cramer C J and Truhlar D G 1999 *Chem. Rev.* **99** 2161–200
Tomasi J and Persico M 1994 *Chem. Rev.* **94** 2027–94
Miertus S, Scrocco E and Tomasi J 1981 *Chem. Phys.* **55** 117–29
[24] Poon C-D, Salulski T, Weise C F and Weisshaar J C 2000 *J. Am. Chem. Soc.* **122** 5642–3
Weise C F and Weisshar J C 2003 *J. Phys. Chem.* B **107** 3265–77
[25] Sen A C and Keiderling T A 1984 *Biopolymers* **23** 1533–45
Carney J R and Zwier T A 1999 *J. Phys. Chem.* A **103** 9943–57
Mons M, Dimicoli I, Tardivel B, Piuzzi F, Brenner V and Millie P 1999 *J. Phys. Chem.* **A103** 9958–65
[26] Diem M, Oboodi M R and Alva C 1984 *Biopolymers* **23** 1917–30
[27] Bour P, Kubelka J and Keiderling T A 2002 *Biopolymers* **65** 145–59
[28] Stephens P J 1985 *J. Phys. Chem.* **89** 748–52
[29] Amos R D, Handy N C, Jalkanen K J and Stephens P J 1987 *Chem. Phys. Lett.* **133** 21–6
[30] Stephens P J 1987 *J. Phys. Chem.* **91** 1712–15
[31] Buckingham A D 1987 *Chem. Phys.* **112** 1–14
[32] Amos R D, Jalkanen K J and Stephens P J 1988 *J. Phys. Chem.* **92** 5571–75
[33] Bak K L, Jørgensen P, Helgaker T, Ruud K and Jensen H J Aa 1993 *J. Phys. Chem.* **98** 8873–87
[34] Bak K L, Jørgensen P, Helgaker T, Ruud K and Jensen H J Aa 1994 *J. Chem. Phys.* **100** 6621–27
[35] Bak K L, Delvin F J, Ashvar C S, Taylor P R, Frisch M J and Stephens P J 1995 *J. Phys. Chem.* **99** 14918–22
[36] Jalkanen K J, Stephens P J, Amos R D and Handy N C 1988 *J. Phys. Chem.* **92** 1781–5
[37] Stephens P J, Jalkanen K J, Amos R D, Lazzeretti P and Zanasi R 1990 *J. Phys. Chem.* **94** 1811–30
[38] Hansen A, Stephens P J and Bouman T D 1991 *J. Phys. Chem.* **95** 4255–62
[39] Bak K L, Hansen A E and Stephens P J 1995 *J. Phys. Chem.* **99** 17359–63
[40] Ditchfield R 1972 *J. Chem. Phys.* **56** 5688–91
[41] Epstein S T 1973 *J. Chem. Phys.* **58** 1592–95
[42] Ditchfield R 1974 *Mol. Phys.* **27** 789–807
[43] Bouman T D and Hansen A E 1988 *Chem. Phys. Lett.* **159** 510–15
[44] Wilkins M R, Gasteiger E, Bairoch A, Sanchez J C, Williams K L, Appel R D and Hochstrasser D F 1998 Calculated by the program primary structure analysis (pI/M.W.) *Protein Identification and Analysis Tools in the ExPASy Server in: 2-D Proteome Analysis Protocols* ed A J Link (New Jersey: Humana Press) on ExPASy www.expasy.org
[45] GaussView a visualization and analysis program from Gaussian Inc. [3]
[46] Schaftenaar G and Noordik J H 2000 Molden: a pre- and post-processing program for molecular and electronic structures *J. Comput.-Aided Mol. Des.* **14** 123–34
[47] Schweitzer-Stenner R 2001 *J. Raman Spectrosc.* **32** 711–32
[48] Mirkin N G and Krimm S 1991 *J. Mol. Struct.* **242** 143–60
[49] Faurskov Nielsen O 1995 Anvendelse af IR, Raman, UV, VIS, Flourescens, Phosphorescens i Biofysisk Kemi *Lecture Notes* (Copenhagen: HCØ Tryk)
[50] Jalkanen K J, Nieminen R M, Knapp-Mohammady M and Suhai S 2003 *Int. J. Quantum Chem.* **92** 239–59
Knapp-Mohammady M, Jalkanen K J, Nardi F, Wade R C and Suhai S 1999 *Chem. Phys.* **240** 63–77
[51] Eker F, Cao X, Nafie L and Schweitzer-Stenner R 2002 *J. Am. Chem. Soc.* **124** 14330–41